UNIVERSITA' DEGLI STUDI DI PADOVA

Centro Interdipartimentale di Studi e Attività Spaziali (CISAS)

SCUOLA DI DOTTORATO DI RICERCA IN SCIENZE TECNOLOGIE E MISURE SPAZIALI (XX Ciclo)

Sede Amministrativa: Università degli Studi di Padova

Indirizzo: Astronautica e Scienze da Satellite
Curriculum: Esplorazione del Sistema Solare

Tesi

COMPOSITION AND MECHANISMS OF ACCUMULATION OF ICES OVER THE MARTIAN POLAR CAPS THROUGH ANALYSIS OF PFS/MEX OBSERVATIONS

Studio dei ghiacci e dei meccanismi di formazione delle calotte polari marziane dalle osservazioni di PFS/MeX

Dottorando: Marco Giuranna

Supervisore:
Prof. Pierluigi Bernacca (Università di Padova)

Co-Supervisore:
Prof. Vittorio Formisano (IFSI/INAF)

Coordinatore dell'Indirizzo: Prof. Pierluigi Bernacca
Direttore della Scuola: Prof. Pierluigi Bernacca

31 Gennaio 2008

A mia madre,
che anche essendomi dottorato
mi considera ancora uno sfaticato.

A mio padre,
dal quale ho ereditato questo
utilissimo, insopportabile carattere.

A mio fratello,
fonte di ispirazione,
al quale va tutta la mia stima.

Al Prof. Formisano,
per il suo inestimabile contributo,
senza il quale questa tesi non esisterebbe.

Ai miei Amici, quelli veri,
che mi accettano per quello che sono,
che mi accettano nonostante quello che sono.

A Chiara,
la mia ex ragazza,
sempre presente nei tanti momenti di bisogno.

A tutti coloro,
figuranti, nemici ed amanti,
che hanno contribuito a farmi diventare ciò che sono.

Table of contents

SUMMARY (ITALIAN)

Marte è forse il pianeta più affascinante del nostro Sistema Solare. Nonostante le sue ridotte dimensioni (il suo diametro è circa la metà di quello terrestre), Marte ospita il vulcano più grande (*Olympus Mons*, alto circa 22 km, con un diametro di base di oltre 550 km) ed il bacino d'impatto più profondo ed esteso (*Hellas Basin*, con i suoi 2300 km di diametro e 9 km di profondità) di tutto il Sistema Solare.

Nel passato, la pressione e la temperatura di Marte erano probabilmente più elevate di quanto non siano ora e tali da permettere la presenza di acqua liquida sulla superficie del pianeta. Erano presenti fiumi, laghi e forse anche un oceano nell'emisfero settentrionale, battezzato *Oceanus Borealis*. Ci sono indizi a favore di un simile scenario: sulla superficie di Marte sono ancora ben visibili i segni lasciati dallo scorrimento di fluidi, canali sinuosi con sistemi di affluenti e fondi di laghi asciutti con depositi di detriti portati dai fiumi. Recenti studi mostrano che quella che sembra essere la costa di un antico oceano (l'*Oceanus Borealis*, appunto) si trova, dal punto di vista gravitazionale, lungo una equipotenziale ad altimetria costante.

Dove c'è acqua, ci può essere la vita. Questo spiega il crescente interesse mostrato sia dell'Europa che dagli Usa verso il pianeta rosso, obiettivo quest'ultimo di numerose missioni spaziali. Tra le ultime ricordiamo: Mars Global Surveyor (missione NASA lanciata nel settembre del 1997), Mars Odyssey (missione NASA lanciata nell'aprile 2001), Mars Exploration Rover e Mars Express (rispettivamente missioni NASA ed ESA lanciate nel giugno del 2003), quest'ultima con un payload di 13 strumenti, fra i quali figura il Planetary Fourier Spectrometer (PFS), uno spettrometro di Fourier di concezione italiana operante nelle regioni spettrali dell'infrarosso termico e del vicino infrarosso.

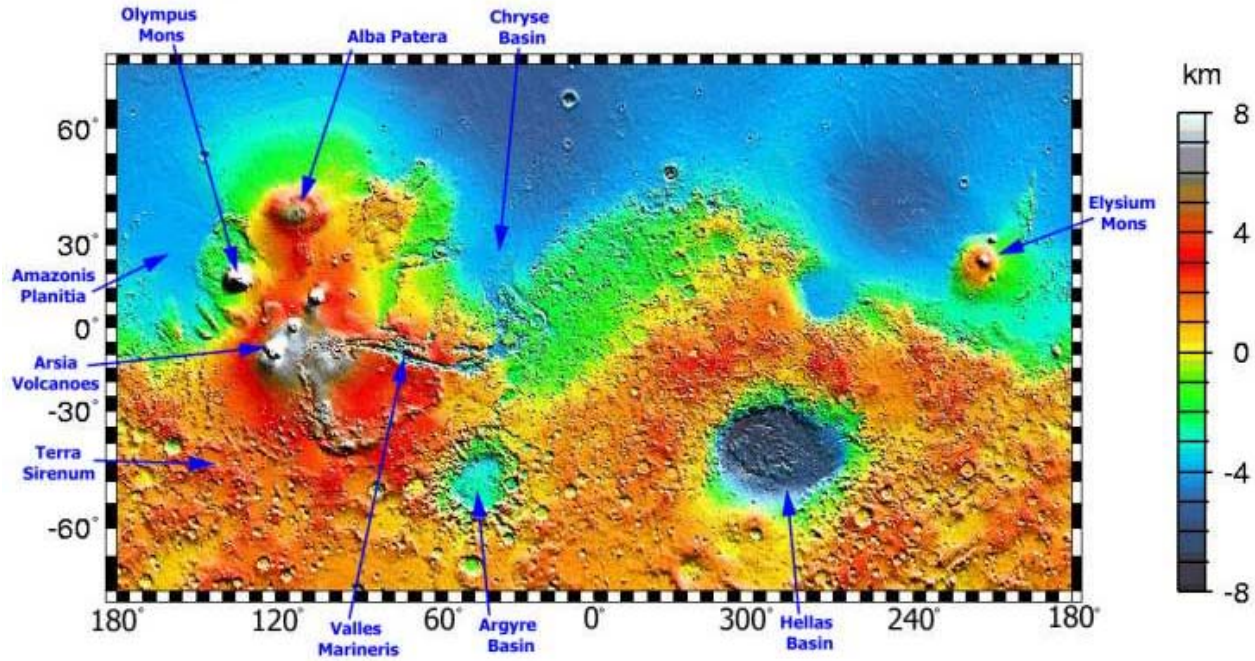

Fig. 1 Topografia marziana, compilata nell'estate del 1999 con i dati del Mars Orbiter Laser Altimeter (MOLA) a bordo della Mars Global Surveyor (MGS) – NASA.

L'esistenza di una tenue atmosfera su Marte è nota fin dalle prime osservazioni telescopiche. Il pianeta mostra chiaramente due calotte polari brillanti, il cui aspetto varia con le stagioni, ed una serie di fenomeni legati alla presenza di nubi che erano già noti agli astronomi del XIX secolo. Le prime missioni spaziali hanno mostrato che i 6.1 millibar di pressione superficiale media sono dovuti quasi esclusivamente alla presenza del biossido di carbonio. Tuttavia, informazioni attendibili sull'atmosfera marziana sono state ottenute solo con l'avvento delle esplorazioni spaziali e, nonostante il considerevole sforzo sia teorico che sperimentale, ci sono ancore moltissime questioni aperte circa i più importanti fenomeni atmosferici.

Le calotte polari sono un aspetto estremamente importante di Marte, in quanto rappresentano la forza principale che guida e regola il clima marziano. Poiché una considerevole porzione dell'atmosfera marziana condensa e sublima ogni anno nelle regioni polari (un processo noto come il *ciclo della CO_2*), i depositi di ghiaccio giocano un ruolo significativo nella circolazione regionale e globale. Comprendere la natura delle calotte polari è essenziale se vogliamo comprendere l'attuale clima di Marte, e la sua evoluzione passata e futura.

Fino al 30% dell'atmosfera marziana condensa ogni anno per formare le calotte polari in entrambi gli emisferi, inducendo enormi variazioni nella pressione superficiale su tutto il pianeta. Ad un primo sguardo, questo fenomeno può sembrare chiaro, ma in realtà è il risultato di una serie di eventi dinamici complessi che si verificano in entrambi gli emisferi nei rispettivi inverni. Vortici transienti, disturbi termici in alta quota di larga ampiezza, onde planetarie stazionarie, sono solo alcuni dei complessi fenomeni dinamici che caratterizzano le regioni polari marziani la cui origine, natura ed evoluzione sono ancora ignote, o parzialmente ignote.

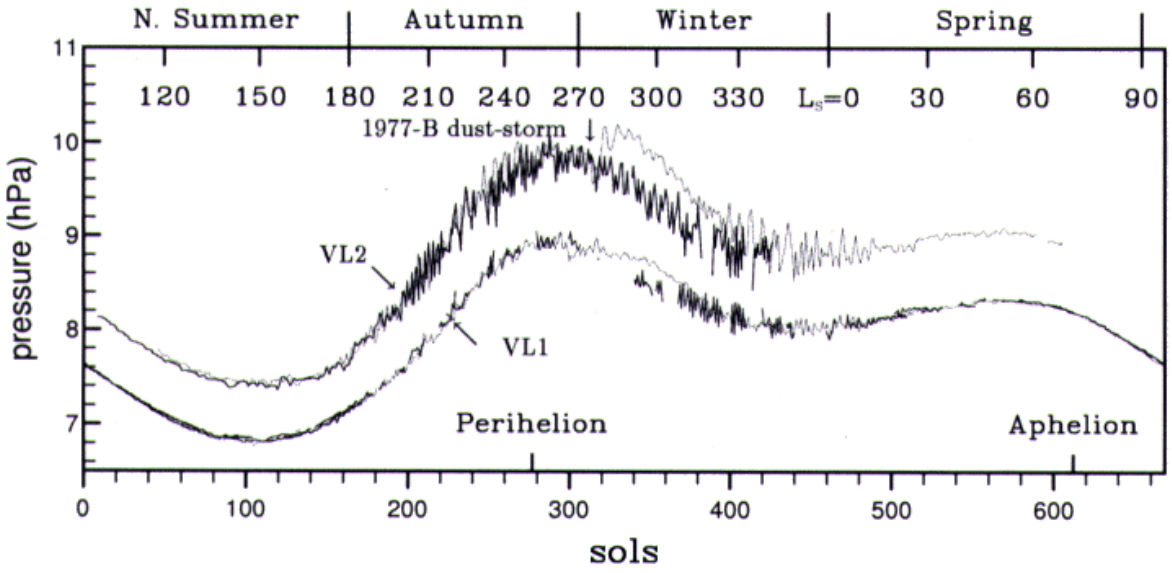

Fig. 2 Evoluzione temporale della pressione superficiale registrata dalle due sonde Viking nei primi tre anni marziani: anno 1 (*puntinata*), 2 (*continua*) e 3 (*tratteggiata*) sono sovraimpressi sullo stesso grafico. La grande variazione stagionale della pressione superficiale è dovuta principalmente alla condensazione della CO_2 atmosferica nelle calotte polari stagionali.

Tanti sono gli interrogativi ancora senza risposta. Non è facile capire se l'accumulo di ghiaccio di CO_2 nelle calotte polari è il risultato della condensazione diretta del vapore al suolo (brina), o una conseguenza della condensazione atmosferica e successiva precipitazione della CO_2 (neve). I meccanismi di formazione di nubi di ghiaccio secco e di nevicate nelle notti polari di Marte sono tutt'altro che chiari, e la condensazione diretta del principale costituente atmosferico (il biossido di carbonio) nelle regioni polari durante l'autunno e l'inverno è un aspetto della meteorologia marziana che non ha una controparte terrestre.

Nonostante siano stati effettuati molti studi sulla recessione della calotta polare sud durante la primavera e l'estate, sia mediante osservazioni da satellite che da terra, solo un ridottissimo numero di lavori sull'evoluzione (espansione) stagionale della calotta sud in autunno ed inverno è presente in letteratura; inoltre, il più di questi fa uso di predizioni da parte di modelli teorici piuttosto che di misurazioni effettive.

Uno degli interrogativi che i planetologi si pongono fin dalle prime osservazioni da telescopio riguarda la calotta meridionale residua: in estate, essa appare decentrata rispetto al polo geografico di circa 3° di latitudine (vedi Fig. 3). Tale asimmetria non può essere spiegata tramite modelli di inerzia termica o di bilancio radiativo, né può essere associata a variazioni locali della topografia. È un mistero che avvolge Marte da diverse decadi.

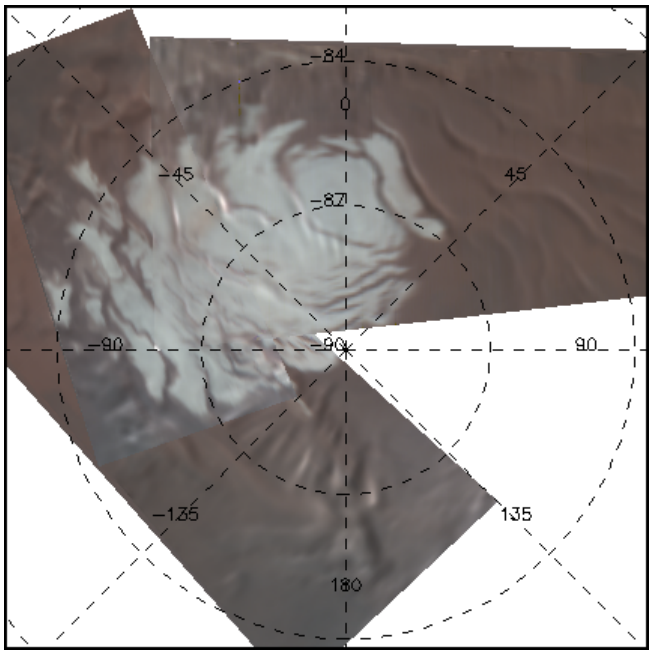

Fig. 3 La calotta polare meridionale residua, decentrata rispetto al polo geografico.

L'acqua è di fondamentale importanza per l'interesse umano nell'esplorazione di Marte, ed è dunque necessario minimizzare ogni confusione tra la presenza di ghiaccio d'acqua e di CO_2. Questi due ghiacci hanno riflettanze molto simili che rende difficile la loro distinzione mediante immagini monocromatiche o multi banda. Le osservazioni nell'infrarosso termico (5-50 μm) possono risolvere parzialmente la composizione delle calotte stagionali e permanenti, poiché le temperature di condensazione del ghiaccio di CO_2 e H_2O differiscono di alcune decine di gradi. Così, le mappe di temperatura

superficiale possono essere utilizzate per determinare la composizione dei ghiacci, ma solo nell'ipotesi che non ci siano misture spaziali di suolo/giaccio d'acqua/ghiaccio secco nel campo di vista. Per risolvere completamente e senza ambiguità la composizione dei ghiacci delle calotte polari di Marte, le dimensioni dei grani e la contaminazione da polveri è necessario studiare la regione spettrale del vicino infrarosso (~ 1-5 μm). Inoltre, sono necessarie risoluzioni spettrali elevate (~ 1 cm^{-1}) per risolvere molte delle sottili righe spettrali del ghiaccio di CO_2.

Una panoramica generale di Marte e degli interrogativi legati alle calotte polari marziane è presente nel Capitolo 1.

In questo lavoro abbiamo cercato di colmare, almeno parzialmente, le attuali lacune circa la conoscenza della composizione e dei meccanismi di formazione delle calotte polari di Marte, attraverso l'analisi dei dati forniti da PFS. Il Planetary Fourier Spectrometer è attualmente l'unico strumento in grado di misurare gli spettri di Marte sia nell'infrarosso termico che nel vicino infrarosso, con una elevata risoluzione spettrale senza precedenti (~ 1.3 cm^{-1}). Una descrizione globale dello strumento è fornita nel Capitolo 2. Gli ultimi sviluppi sulle procedure calibrazione dei dati di PFS, che sono parte integrante di questo lavoro, sono riportati nel Capitolo 3.

Molti dei risultati scientifici ottenuti in questo lavoro sono stati pubblicati (o sono in fase di pubblicazione) su riviste scientifiche internazionali, quali *Planetary and Space Science* ed *Icarus*. Tali pubblicazioni sono allegate in Appendice. I principali risultati scientifici ottenuti sono riportati nelle varie sezioni del Capitolo 7.

Le informazioni che si possono ottenere dagli spettri di Marte nell'infrarosso termico e nel vicino infrarosso sono molte, e grazie ad esse è possibile studiare molti dei problemi legati alle calotte polari, quali:

1. la composizione dei ghiacci delle calotte perenni e stagionali;
2. la dimensione dei grani e lo spessore dei depositi di ghiaccio;
3. la distribuzione e la variazione spaziale dei depositi e la contaminazione con polveri;
4. il bilancio radiativo delle notti polari;
5. la composizione delle superfici polari non ghiacciate;
6. la presenza e la composizione delle nubi;
7. i meccanismi di accumulo del ghiaccio di CO_2;
8. i campi termici, i venti e la circolazione nell'atmosfera polare;
9. la asimmetria della calotta meridionale residua.

Nel capitolo 4 vengono analizzate le regioni spettrali più diagnostiche per lo studio di tali problematiche e le informazioni che da esse si possono ottenere. Nello stesso capitolo vengono inoltre discussi i requisiti che uno strumento deve possedere affinché tali studi possano essere effettivamente condotti ed i limiti delle precedenti missioni. Ne risulta che PFS è uno strumento ideale per lo studio dei problemi legati alle calotte polari marziane e che una quantità notevole di informazioni può essere ricavata grazie all'acquisizione simultanea di spettri nell'infrarosso termico e nel vicino infrarosso, quest'ultima essendo una caratteristica unica di PFS rispetto alle precedenti missioni spaziali a Marte.

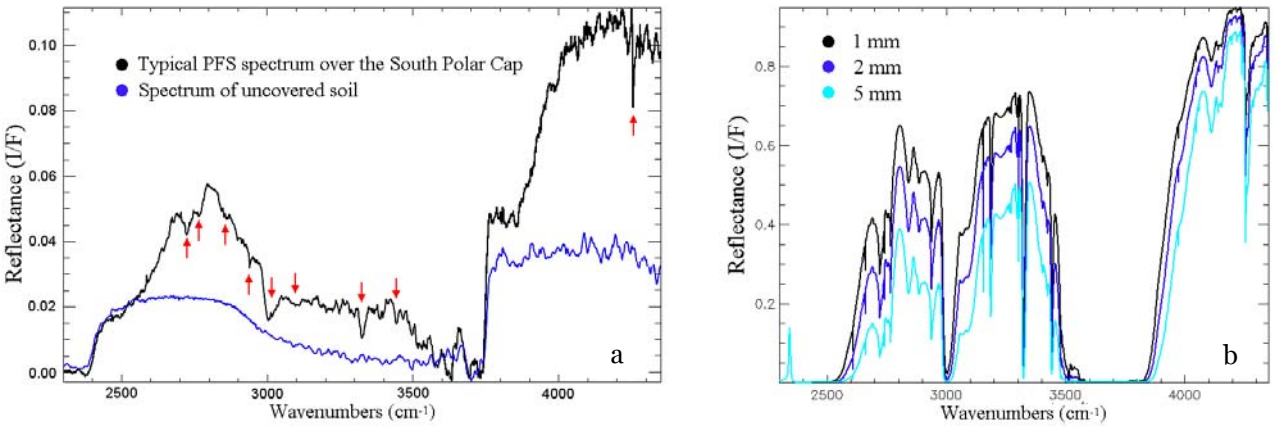

Fig. 4 *a*. Gli spettri delle calotte polari marziane misurati da PFS nel vicino infrarosso mostrano chiaramente le caratteristiche spettrali del ghiaccio di CO_2, compresa una serie di piccole bande di assorbimento attorno a 2720, 2770, 2850, 2940, 3000, 3320 e 3440 cm-1 (frecce rosse). *b*. Albedo spettrale del ghiaccio di CO_2 puro calcolata per diverse dimensioni dei grani.

Ma per ottenere effettivamente le informazioni sopra elencate è spesso necessario ricorrere al confronto tra gli spettri di Marte misurati da PFS e quelli calcolati da modelli teorici. Per fare questo è necessario fare uso della teoria del trasferimento radiativo. Il calcolo della riflettanza bi-direzionale del ghiaccio d'acqua o del ghiaccio ci CO_2 è possibile tramite l'utilizzo di soluzioni numeriche o approssimate dell'equazione del trasporto radiativo. I principi della teoria del trasferimento sono discussi nel Capitolo 5. Dopo aver ricavato la forma generale dell'equazione del trasporto radiativo, viene analizzato il caso di un mezzo a stratificazione orizzontale. A tale equazione vengono poi collegate le proprietà ottiche di un mezzo e vengono introdotti gli algoritmi per il calcolo delle proprietà di singolo scattering di una particella di tale mezzo mediante la teoria di Mie, con particolare attenzione al calcolo della funzione di fase che descrive l'andamento angolare di tali quantità. Tali calcoli vengono poi estesi al caso più realistico di una distribuzione statistica delle dimensioni delle particelle. Infine, vengono analizzate le più comuni tecniche risolutive (numeriche ed approssimate) dell'equazione del trasporto radiativo, con particolare riferimento alle tecniche utilizzate in questo lavoro (metodo delle *ordinate discrete*, e algoritmi *two-stream*). I pacchetti software di pubblico dominio attualmente disponibili per risolvere il problema del trasferimento radiativo sono stati collezionati e riassunti in una apposita tabella.

Il problema della modellazione delle proprietà spettrali dei ghiacci viene discusso nei dettagli nel capitolo 6. Indipendentemente dall'algoritmo risolutivo scelto, e se si tratti di soluzioni numeriche o approssimate dell'equazione del trasporto, quando si vogliono calcolare le proprietà di scattering multiplo di un mezzo particolato non si può prescindere dall'aver calcolato precedentemente le proprietà di singolo scattering. Per il calcolo di queste ultime, ad una certa lunghezza d'onda λ, occorre conoscere solamente

(1) il *size parameter* $x = 2\pi r/\lambda$, cioè il rapporto tra la circonferenza della particella e la lunghezza d'onda;

(2) l'*indice di rifrazione complesso* m a quella lunghezza d'onda; $m = m_{re} - i m_{im}$, dove m_{re} è l'indice di rifrazione ordinario e m_{im} è collegato al coefficiente di assorbimento lineare K_{abs} tramite la relazione $K_{abs} = 4\pi m_{im}/\lambda$.

m_{re} e m_{im} vengono insieme dette *costanti ottiche*.

Se si vogliono calcolare gli spettri di riflettanza di qualunque superficie, è dunque necessario collezionare dapprima le costanti ottiche dei materiali di interesse. Una fase importante del lavoro svolto è stata dunque la ricerca e la raccolta delle costanti ottiche del ghiaccio d'acqua e di CO_2, e della polvere marziana. Una serie di requisiti deve essere soddisfatta affinché le costanti ottiche di un mezzo possano essere accettate nel nostro studio. Tra queste la risoluzione spettrale con la quale sono state calcolate, e le temperature alle quali tali quantità rappresentano effettivamente il comportamento ottico del materiale in esame (le costanti ottiche di un materiale dipendono dalla temperatura del mezzo stesso). La temperatura do condensazione della CO_2 a Marte è di circa 150 K ed è questa la temperatura alla quale ci si aspetta di trovare tale ghiaccio su Marte. Ma per l'acqua è diverso. Ci si aspettato variazioni della temperatura del ghiaccio d'acqua approssimativamente nell'intervallo 150-210 K. Seguendo questi ed altri criteri, sono state scelte le costanti ottiche ottimali per perseguire i nostri studi. In Figura 5 sono raffigurate le costanti ottiche del ghiaccio di CO_2 a 150 K. Una discussione completa delle costanti ottiche dei ghiacci e delle polveri marziani, assieme ad un'analisi critica delle distribuzioni di dimensioni attese su Marte per tali composti è presente nel paragrafo 6.2.

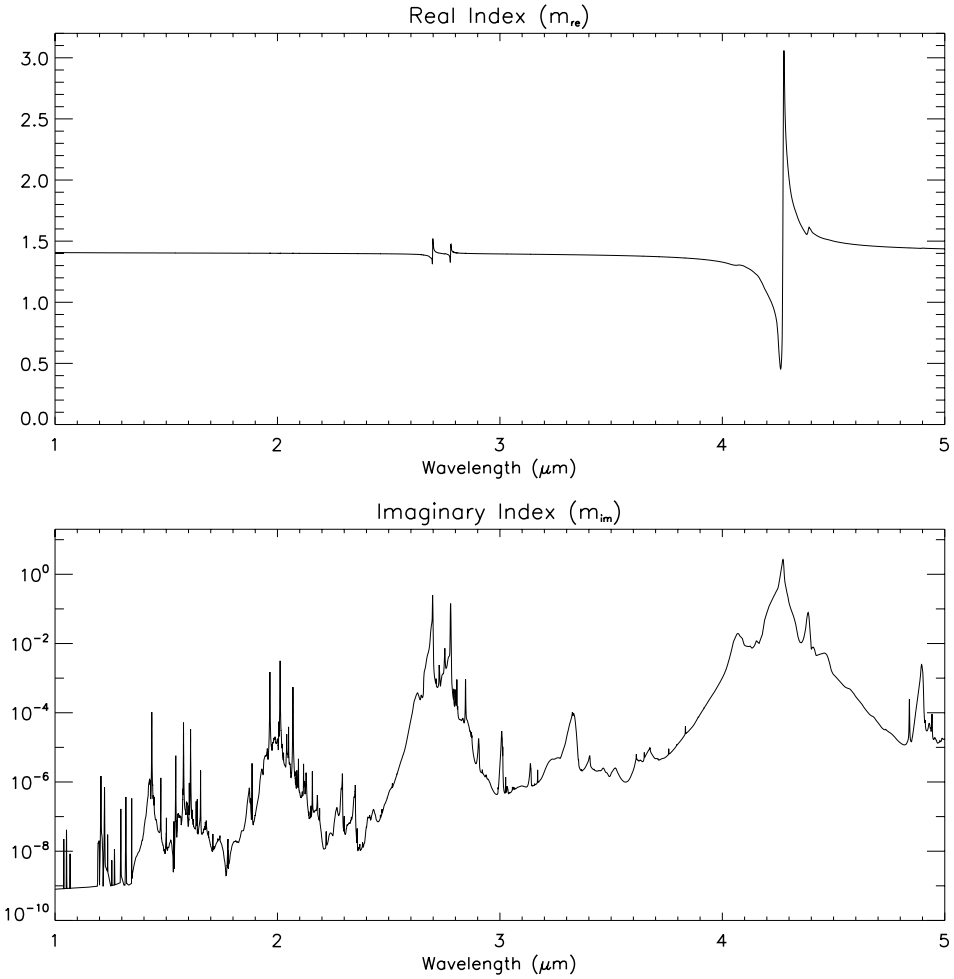

Fig. 5 Costanti ottiche del ghiaccio di CO_2 a 150K.

Una volta note le costanti ottiche di un materiale, è possibile calcolare l'albedo di singolo scattering di tale materiale seguendo la teoria di Mie. Dovendo studiare la

composizione dei ghiacci delle calotte polari marziane è ragionevole presumere che il ghiaccio d'acqua e quello di CO_2, entrambi possibili date le condizioni te pressione e temperatura marziane nelle notti polari, siano miscelati tra di loro e questi, a loro volta, contaminati dalle polveri atmosferiche. Per poter riprodurre fedelmente le osservazioni è quindi necessario calcolare le proprietà spettrali di misture di questi tre elementi. Esistono diversi modi di miscelare fra di loro diverse sostanze. Nelle *intimate mixtures*, le molecole dei singoli costituenti sono considerate estremamente vicine tra di loro. In questo caso, il processo di media avviene a livello delle particelle individuali e i parametri che compaiono nell'equazione del trasporto radiativo solo le medie delle proprietà dei vai tipi di particelle nella mistura, pesate dalla loro sezione d'urto geometrica. Esempi di albedo di singolo scattering del ghiaccio di CO_2 per diversi livelli di contaminazione da parte di ghiaccio d'acqua e polvere sono mostrati in figura 6.

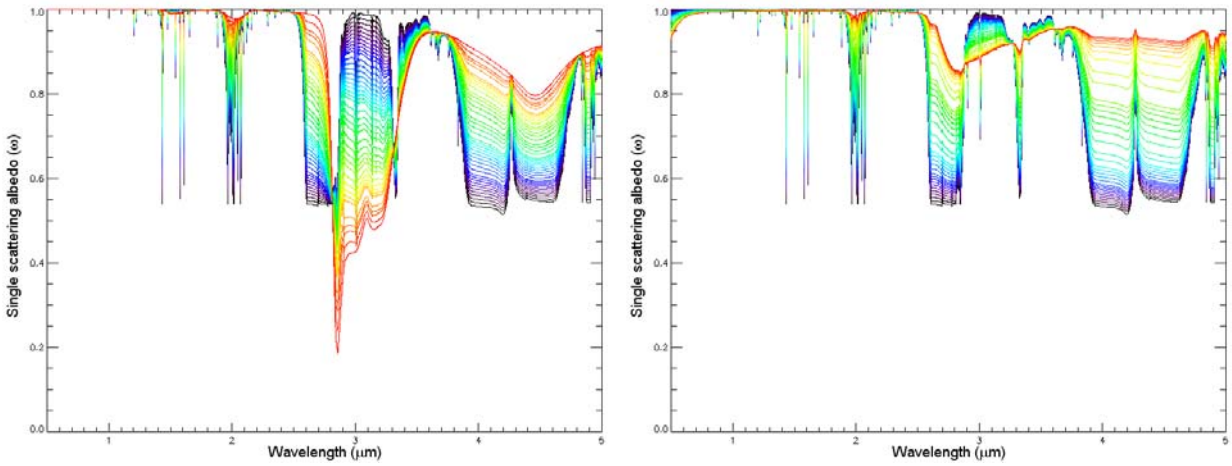

Fig. 6 Albedo di singolo scattering di una particella di CO_2 (r = 5mm) per diversi livelli di contaminazione con ghiaccio d'acqua e polvere. *Sinistra*: in nero, Ghiaccio di CO_2 puro; in rosso, 0.9 wt% di ghiaccio d'acqua. *Destra*: in nero, Ghiaccio di CO_2 puro; in rosso, 0.9 wt% di polvere.

Come già accennato, una volta note le quantità di singolo scattering di un mezzo, è possibile calcolare il suo spettro di riflettanza spettrale in funzione delle diverse geometrie di osservazione (angolo di incidenza, di emissione e di fase). Per fare questo è necessario risolvere la parte di scattering multiplo contenuta nell'equazione del trasporto radiativo, sia pure numericamente o con diversi livelli di approssimazione.

Tra le soluzioni approssimate, di rilevante importanza per il nostro studio è stato un algoritmo sviluppato da Wiscombe e Warren (1980) in grado di calcolare la riflettanza emisferico-direzionale del ghiaccio d'acqua e del ghiaccio di CO_2 una volta nota l'albedo di singolo scattering, utilizzando l'approssimazione *delta-Eddington* (si veda Tabella 5.2), una delle approssimazioni *two-stream* discusse nel paragrafo 5.3.3. Tale algoritmo permette anche di calcolare la riflettanza emisferico-direzionale per diversi valori della profondità ottica τ; specificando l'albedo della strato inferiore è quindi possibile studiare l'effetto dei diversi spessori dello strato superiore di ghiaccio, dal caso "otticamente sottile" al caso "semi-infinito". Un esempio è mostrato in Figura 7, dove è raffigurata la riflettanza spettrale di un sottile strato di ghiaccio di CO_2, puro e contaminato da polvere e ghiaccio d'acqua, per diverse profondità dello strato, sopra una superficie di ghiaccio d'acqua. Questo modello è stato utilizzato nel nostro lavoro per studiare la composizione della calotta meridionale residua (paragrafo 7.2)

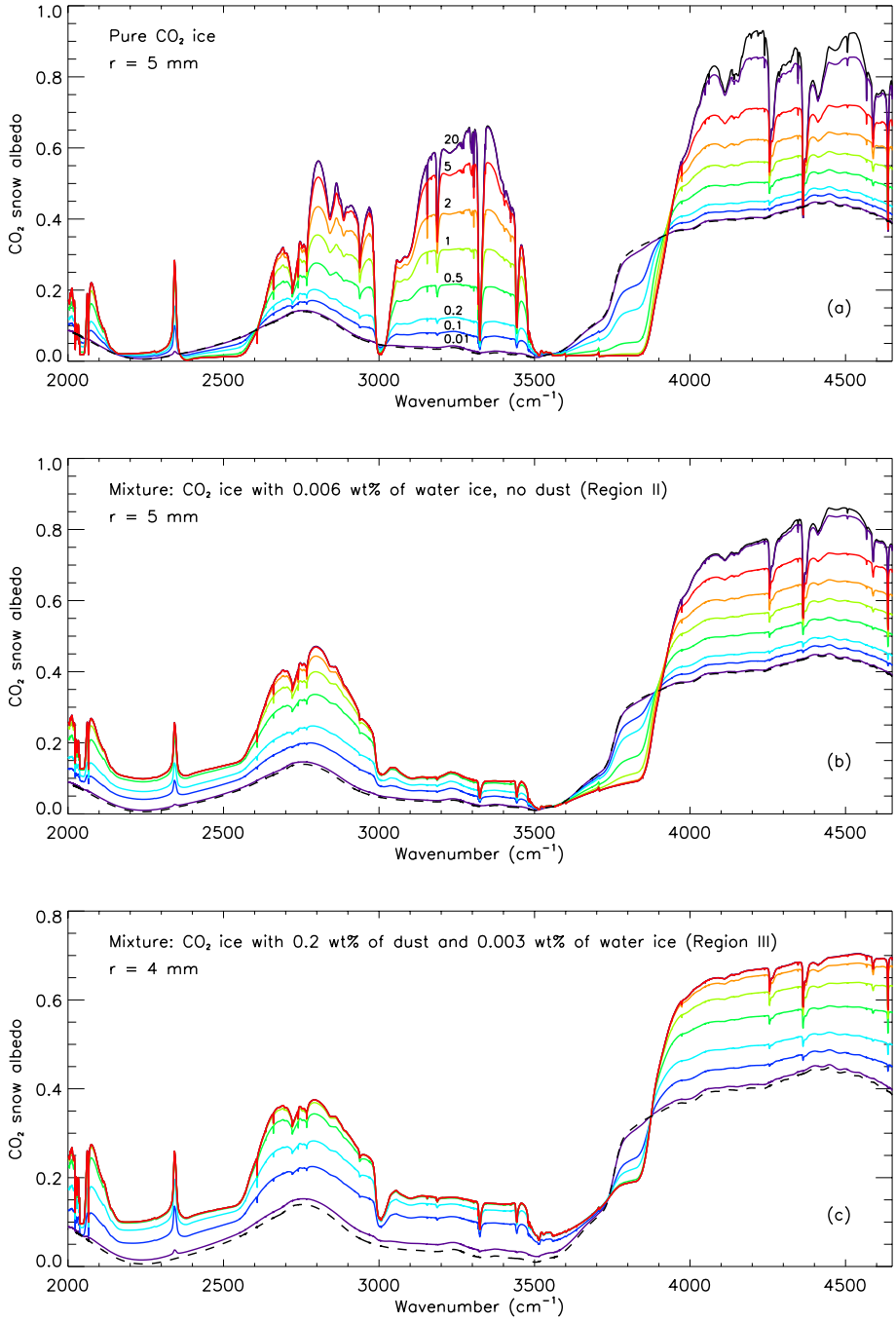

Fig. 7 Riflettanza spettrale emisferico-direzionale del ghiaccio di CO_2, calcolata con l'approssimazione *two-stream delta-Eddington* per un sottile strato di ghiaccio di CO_2, puro e contaminato da polvere e ghiaccio d'acqua, per diverse profondità dello strato, sopra una superficie di ghiaccio d'acqua (linea tratteggiata). Le curve nere rappresentano il caso di profondità semi-infinita. I numeri nel pannello superiore indicano la profondità dello snowpack, espressa in massa per unità di area (g cm^{-2}). Stessi colori indicano stesse profondità.

Un altro modello di riflettanza largamente usato in questo lavoro, appartenente alla categoria delle soluzioni approssimate dell'equazione del trasferimento radiativo è il

modello di Hapke della riflettanza bi-direzionale (Hapke 1993, 2002). Tale modello esiste in due versioni, quella isotropa e quella anisotropa, che differiscono tra di loro per una diversa implementazione della parte di scattering multiplo, più accurata nel secondo caso e comprendente il *coherent backscatter opposition effect* (si veda il paragrafo 6.2.1.2 per una trattazione dettagliata di tale effetto e delle differenza tra le due implementazioni). Alcuni esempi sono riportati in Figura 8. Gli effetti distinti delle dimensioni dei grani e dei livelli di impurità sulla riflettanza del ghiaccio di CO_2 consentono di ricavare simultaneamente ed accuratamente tali parametri mediante il *fit* degli spettri misurati.

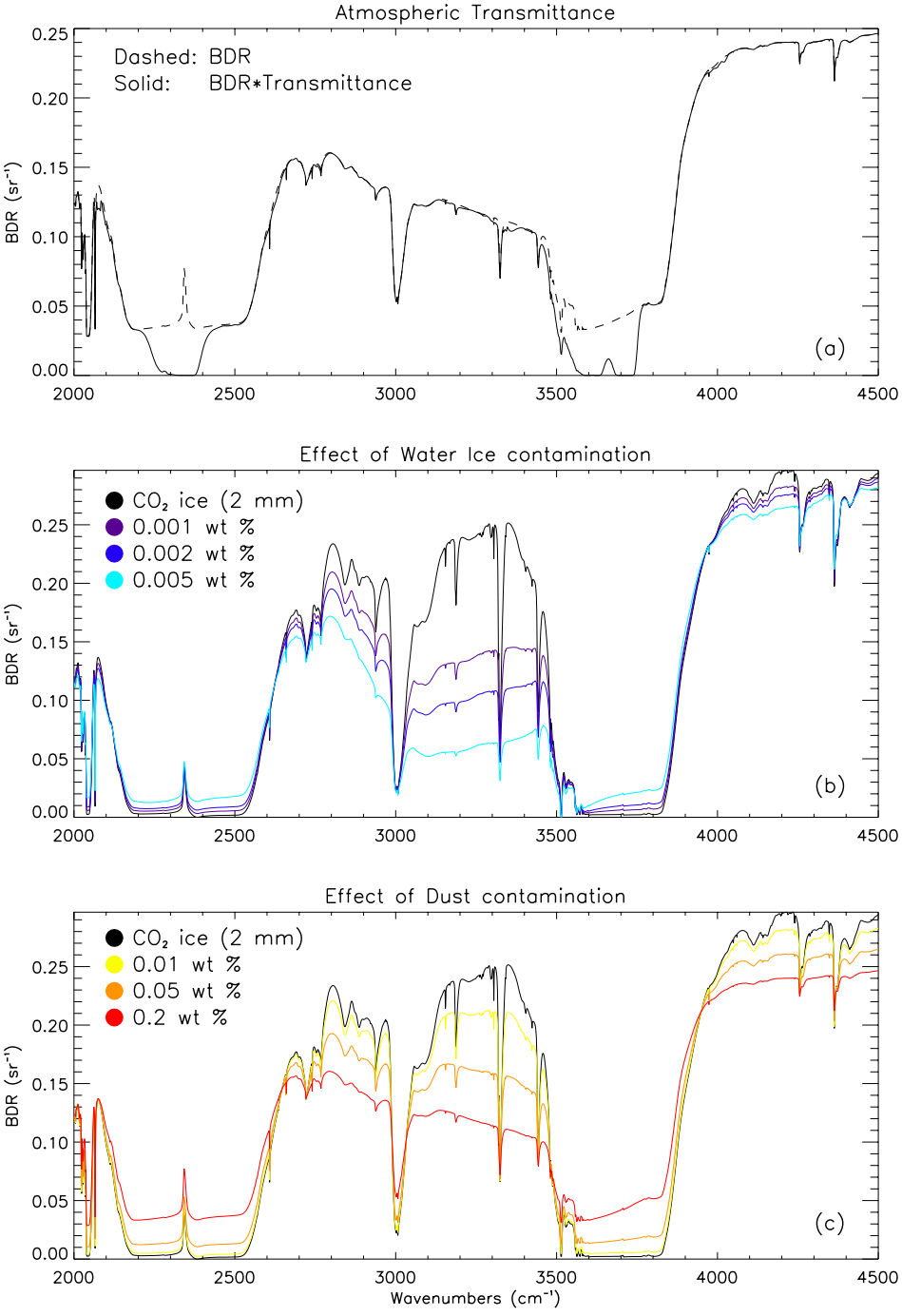

Fig. 8 (a) Effetto della trasmittanza atmosferica marziana. (b) Riflettanza calcolata di miscele CO_2/H_2O. (c) Riflettanza calcolata di miscele di CO_2/polvere.

Questo modello è molto più accurato del precedente ed è stato utilizzato per studiare la composizione della calotta polare Nord in primavera (paragrafo 7.4).

Tra gli algoritmi in grado di fornire soluzioni numeriche dell'equazione del trasporto radiativo segnaliamo DISORT (Stamnes *et al.* 1988), originariamente sviluppato ed utilizzato per problemi di scattering di nubi, ma che si è dimostrato estremamente valido anche nel calcolo di riflettanze angolari dei ghiacci ed altre superfici, ed il codice Fortran *refl.f* sviluppato recentemente da Mishchenko *et al.* (1999) per il calcolo della riflettanza bi-direzionale dei ghiacci ed altre superfici. Tali algoritmi hanno il vantaggio di fornire soluzioni molto accurate del problema del trasferimento radiativo, ma hanno il grande svantaggio di richiedere tempi di calcolo molto lunghi, inutilizzabili in pratica per modellare grandi quantità di osservazioni. Tuttavia, si sono rivelati uno strumento indispensabile per poter validare e rifinire i modelli approssimati utilizzati in questo lavoro.

La radianza osservata nell'infrarosso termico dipende da molteplici parametri dell'atmosfera e della superficie di Marte, come descritto dalla teoria del trasferimento radiativo: la temperatura superficiale, la densità di colonna degli aerosol di polvere e ghiaccio d'acqua presenti in atmosfera, le temperature dell'aria in funzione dell'altezza, la pressione superficiale, e la densità di colonna del vapor d'acqua e del monossido di carbonio. Adottando il formalismo generale dell'analisi Bayesiana, è stato sviluppato un algoritmo per l'analisi scientifica delle singole misure calibrate di PFS, permettendo di ricavare simultaneamente i suddetti parametri. Una descrizione completa di questo metodo è riportata da Grassi *et al.* (2005). Come risultato, da una singola misura di PFS è possibile ricavare:

a) la temperatura superficiale;
b) il profilo verticale di temperature (nell'intervallo indicativo 1-50 km);
c) il contenuto integrato di polvere;
d) il contenuto integrato di ghiaccio d'acqua.

Alcuni esempi della qualità del modello sono riportati in Figura 9.

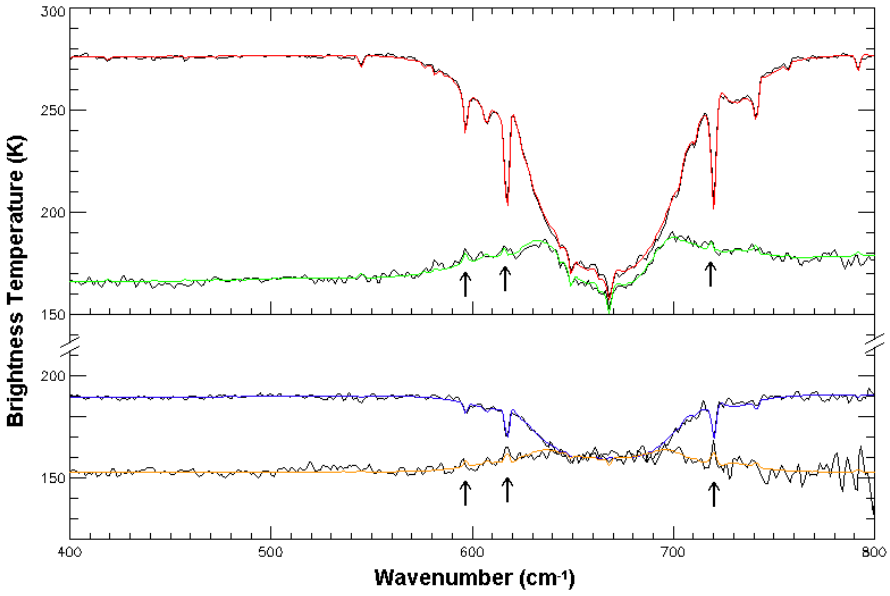

Fig. 9 *Curve in nero*: Spettri di PFS misurati. *Curve colorate*: spettri sintetici. Le frecce indicano le Q-branches della CO_2.

L'alta risoluzione spettrale di PFS consente di individuare differenti gradienti termici nell'atmosfera, come dimostrato dall'effettivo modellamento, nello stesso spettro, di Q-branches in emissione ed in assorbimento (curve verde e arancione in figura 9).

Dalle misure di temperatura superficiale è possibile tracciare i confini della calotta polare sud durante il suo periodo di espansione (vale a dire durante l'autunno e l'inverno) sfruttando il rapido aumento (diminuzione) della temperatura superficiale che si ha quando il ghiaccio di CO_2 viene rimosso (depositato). Un tale approccio è già stato utilizzato in precedenza per studi simile, ma i nostri risultati hanno dimostrato che, se si definiscono i confini della calotta in espansione (o in ritiro) come quelle zone in cui la temperatura superficiale scende al di sotto di (o supera) certe temperature fissate a priori, si possono avere errori considerevoli nella latitudine di tali confini. Tali errori sono dovuti al fatto che la temperatura di condensazione al suolo della CO_2 varia in funzione della pressione superficiale locale che, a sua volta, varia con l'altimetria. Per uno studio rigoroso di tale problema è necessario utilizzare come temperature di soglia, piuttosto che dei valori fissi, il valore effettivo della temperatura di condensazione al suolo della CO_2 che corrisponde all'effettiva pressione parziale al suolo. Questo è possibile utilizzando l'equazione di Clausius–Clapeyron che, per i nostri scopi può essere scritta come:

$$(1) \qquad T_{cond}^{surf}(h) = \frac{b}{a - \ln(P^{surf}(h) \cdot m)}$$

dove $T_{cond}^{surf}(h)$ è la temperature di condensazione al suolo della CO_2 (espressa in Kelvin) in funzione dell'altimetria h; a e b sono i coefficienti di Clausisus-Clapeyron per la CO_2 (a = 23.102; b = 3148 K); P^{surf} è la pressione superficiale (espressa in millibar), ed m è il mixing ratio della CO_2.

I confini della calotta in espansione sono quindi definiti come le zone in cui la temperatura superficiale scende al di sotto della temperatura di condensazione al suolo della CO_2 per gli effettivi valori della pressione superficiale. In questo modo è stato possibile mettere in evidenza come l'espansione della calotta polare meridionale è asimmetrica, per il fatto che all'interno dei maggiori bacini di impatto marziani (*Hellas* ed *Argyre*) la pressione parziale della CO_2 è maggiore rispetto alle zone limitrofe più elevate, consentendo alla CO_2 di condensare a temperature maggiori e permettendo al ghiaccio di CO_2 di essere stabile anche a latitudini minori (fino a 30° Sud ed oltre).

I dettagli ed i risultati di questo studio sono trattati nel paragrafo 7.1, e mostrati in Figura 10. Il lavoro è stato pubblicato sulla rivista *Planetary and Space Science* e l'articolo è allegato in Appendice A.4. La calotta si espande con una velocità costante di circa 10° di latitudine per 15 gradi di L_s durante gran parte dell'autunno (fino ad L_s ~ 70°) indipendentemente dalla longitudine (triangoli neri e verdi in Figura 10). La massima estensione della calotta si raggiunge nell'intervallo 80°–90° L_s, quando i bordi della calotta si estendono fino a –40° di latitudine. Dopo il solstizio d'inverno, la calotta sud di CO_2 inizia e recedere con un tasso di circa 5° di latitudine ogni 25 gradi di L_s durante tutto l'inverno. All'interno dei bacini di *Hellas* e *Argyrae* (triangolo rossi in Figura 10), grazie alle maggiori pressioni, la temperatura di condensazione della CO_2 è diversi gradi più alta di quella del resto della regione polare, cosicché il ghiaccio di CO_2 è stabile a latitudini (e temperature) maggiori, estendendosi fino a (e occasionalmente al di sopra di) –30° di

latitudine, rendendo la calotta asimmetrica. Le asimmetrie longitudinali si riducono man mano che la calotta recede, come conseguenza del fatto che il ghiaccio all'interno dei bacini sta sublimando, e scompare definitivamente attorno ai 145° di Ls. Dopodichè la calotta continua a ritirarsi simmetricamente.

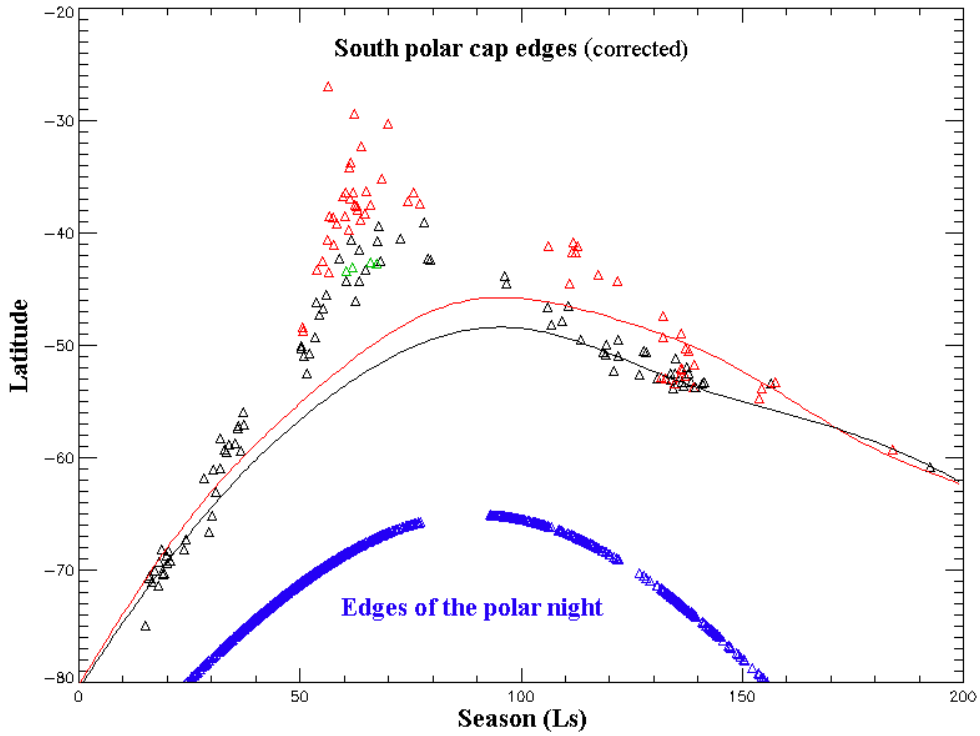

Fig. 10 Latitudine dei confini della calotta Sud in funzione della stagione.

PFS ha iniziato ad osservare Marte durante la fine dell'estate meridionale. In questo lavoro abbiamo analizzato le osservazioni dei ghiacci del polo Sud in tre delle prime 100 orbite di Mars Express: 30, 41, e 61. Le osservazioni durante le orbite 30 e 41 mostrano chiaramente le features spettrali della calotta (Fig. 4°). Più di 25 anni fa, il Viking orbiter notò per la prima volta che le calotte residue Nord e Sud hanno composizioni diverse; la prima consiste di ghiaccio d'acqua, mentre la seconda di ghiaccio di CO_2.

La presenza di ghiaccio di CO_2 nella calotta meridionale residua fu proposta solo sulla base delle basse temperature di brillanza osservate, poiché le caratteristiche spettrali della calotta nel vicino infrarosso non sono mai state pubblicate da nessuna delle precedenti missioni.

Grazie alle osservazioni di PFS ed al lavoro svolto in questa tesi è stato finalmente possibile dimostrare la presenza di ghiaccio di CO_2 nella calotta residua meridionale di Marte.

Gli spettri di riflettanza misurati da PFS sono stati modellati e riprodotti in tutti i dettagli spettrali dai nostri modelli. La superficie è descritta come uno strato semi-infinito di mezzo particolato. Lo scattering è l'assorbimento delle singole particelle è stato calcolato utilizzando la teoria di Mie, mentre per l'intero strato è stata utilizzata la teoria dello scattering multiplo nell'approssimazione *two-stream delta-Eddington* precedentemente

descritta. La calotta polare è stata modellata come *intimate mixture* di ghiaccio di CO_2, e polvere e ghiaccio d'acqua con raggi dell'ordine di 1–2 μm.
Un esempio di *fit* dei dati di PFS è mostrato in figura 11. Il *fit* è molto buono e tutte le caratteristiche spettrali osservate sono state riprodotte dal modello, permettendo di ricavare la composizione della calotta meridionale residua in termini di dimensioni dei grani di CO_2, presenza di ghiaccio d'acqua e polveri, e variazioni spaziali. In questo esempio, il modello è stato calcolate per grani di CO_2 di 3.5 mm, intimamente miscelati con una frazione di massa dello 0.001 wt% per il ghiaccio d'acqua, e dello 0.01 wt% per la polvere. Il modello prevede anche una percentuale di suolo non ricoperto da ghiaccio pari al 30%.

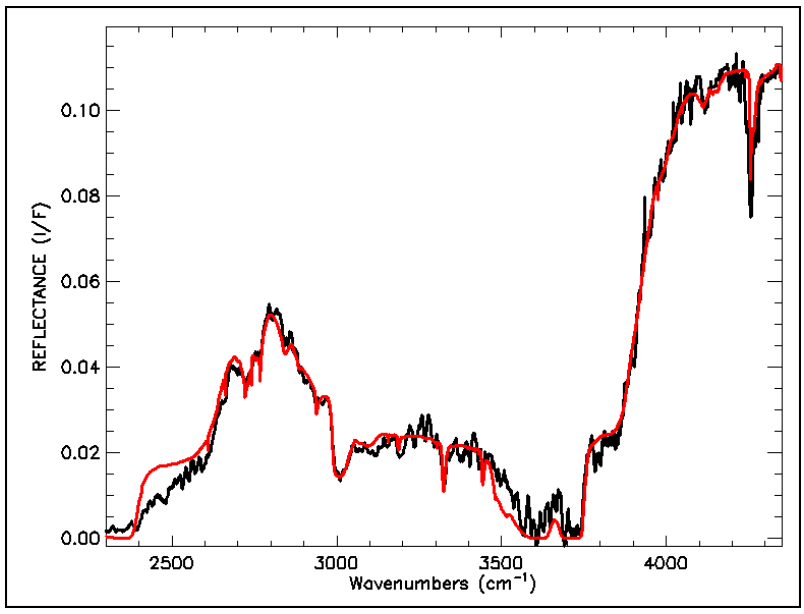

Fig. 11 Spettro medio misurato da PFS durante l'orbita 30 (*curva nera*) e riflettanza emisferico-direzionale calcolata (*curva rossa*).

I risultati di questo lavoro mostrano che il costituente principale dei ghiacci della calotta residua è effettivamente il biossido di carbonio, ma è sempre presente una percentuale di ghiaccio d'acqua dell'ordine di alcune decine di ppm in massa. Le dimensioni effettive dei grani sono tipicamente 5–10 mm, e il contenuto di polvere è pari a $1–6 \cdot 10^{-4}$. I dettagli di questo studio sono riportati nel paragrafo 7.2. Il lavoro è stato pubblicato sulla rivista *Planetary and Space Science* e l'articolo è allegato in Appendice A.3.

Lo studio più innovativo ed originale svolto durante i tre anni di questo lavoro di dottorato è senz'altro l'analisi dei meccanismi di formazione della calotta polare Sud. Abbiamo già accennato che durante gli inverni marziani, complessi fenomeni dinamici si instaurano nell'atmosfera delle notti polari. Analizzando i campi termici misurati da PFS nelle regione polare sud è stato possibile analizzare nei dettagli alcuni di questi fenomeni, e dare finalmente una spiegazione al perché la calotta residua appare decentrata rispetto al polo geografico (Fig. 3).

Dall'analisi dei dati risulta chiaramente che agli inizi dell'autunno meridionale la calotta stagionale in espansione appare già simmetrica e centrata attorno al polo. In altre parole, poco dopo la fine dell'estate, l'asimmetria mostrata dalla calotta è già svanita a causa dei nuovi depositi di ghiaccio. Ci siamo quindi chiesti se tali depositi siano il risultato di condensazione diretta al suolo (brina) o in atmosfera con successive precipitazioni (neve). I campi termici misurati da PFS mostrano chiaramente che le temperature atmosferiche nella regione polare nei primi mesi dell'autunno (fino ad $L_s \sim 30°$) sono nettamente al disopra del profilo di condensazione della CO_2 atmosferica (Figura 12). Di conseguenza il biossido di carbonio non può condensare in atmosfera ed i depositi osservati sono necessariamente il risultato di una condensazione in superficie.

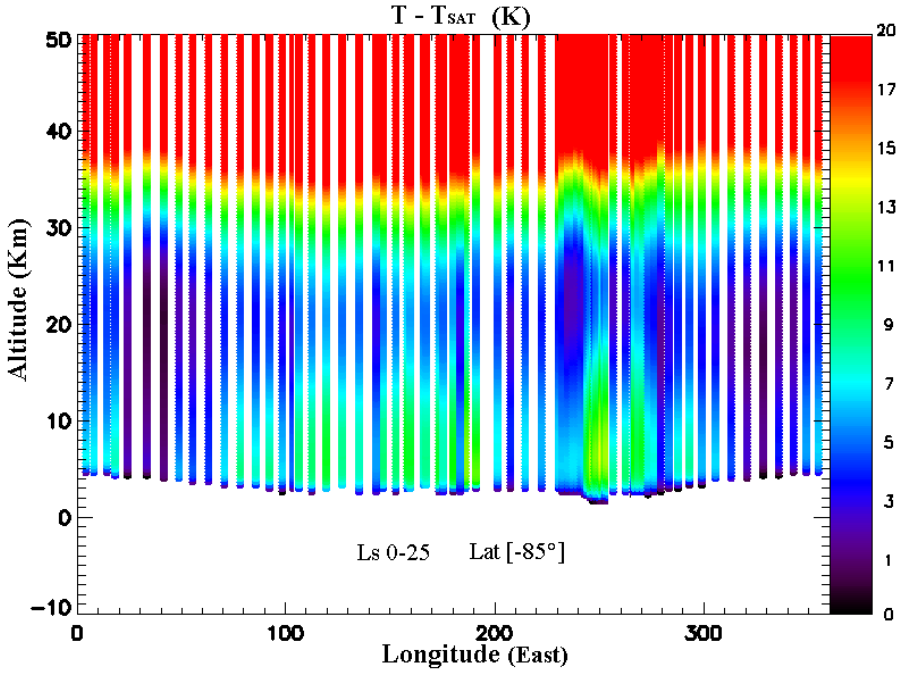

Fig. 12 Ls 0°–25°. Sezione longitudinale a –85° di latitudine che mostra T – T_{sat} in funzione dell'altitudine. Il colore rosso è utilizzato per T – $T_{sat} \geq 20$ K.

Decisamente diversa e più complicata è la situazione osservata durante la seconda metà dell'autunno meridionale (Figura 13). Nell'intervallo 50°–70° L_s la regione polare è chiaramente caratterizzata da due climi regionali distinti. Le precipitazioni di ghiaccio di CO_2 sono ora consentite, ma possono aver luogo esclusivamente nell'emisfero occidentale. Nell'emisfero orientale (più precisamente, nell'intervallo 30°–210° longitudine Est), l'intera colonna atmosferica è diversi gradi al di sopra della temperature di saturazione T_{sat}; qui, la deposizione diretta del vapore è l'unico meccanismo consentito per l'accumulo di ghiaccio di CO2 nella calotta. Nell'emisfero Occidentale, invece, la condensazione in atmosfera è consentita fino ad altezze di 30 km e l'accumulo di ghiaccio è probabilmente dominato dalla precipitazione. Quanto detto è particolarmente vero in due regioni particolarmente fredde, centrate attorno a 260° e 320° longitudine Est, dove la condensazione della CO_2 in atmosfera è consentita in ampie regioni, a partire dalla superficie, fino a quote di 20-30 km.

È particolarmente interessante notare che le regioni più fredde (frecce blu in Figura 13a) sono localizzate proprio attorno al centro della calotta residua (linea blu tratteggiata in Figura 13b).

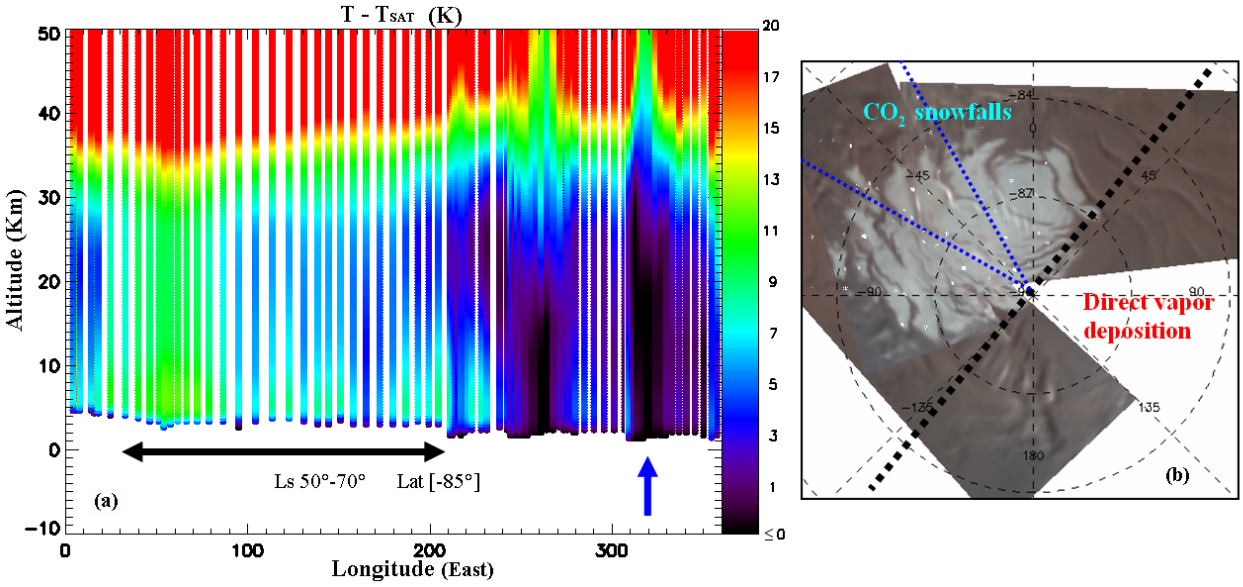

Fig. 13 (a) Ls 50°-55°. Sezione longitudinale a –85° di latitudine che mostra T – T_{sat} in funzione dell'altitudine. Sono chiaramente visibili due climi regionali, uno più caldo nell'emisfero orientale, uno più freddo in quello occidentale. (b) Nevicate di CO2 sono consentite solo nell'emisfero occidentale. Le regioni più fredde (frecce blu in Figura 13a) sono localizzate proprio attorno al centro della calotta residua.

A questo punto ci siamo chiesti come è possibile che si possano formare due climi regionali così diversi nella regione polare. Dai campi termici abbiamo calcolato i venti. Come risultato, abbiamo ottenuto che, durante la seconda metà dell'autunno Sud, la circolazione marziana alle medie latitudini è caratterizzata da forti venti termici (*eastward winds*). Questi venti si originano proprio in corrispondenza delle latitudini degli enormi bacini di *Hellas* ed *Argyre*. L'interazione di questi venti con una tale topografia locale eccita un'onda planetaria (Rossby) quasi-stazionaria di numero d'onda uno, in grado di generare zone di alta pressione (e quindi temperature più elevate) in gran parte dell'emisfero orientale, impedendo alla CO_2 di condensare in atmosfera, e zone di bassa pressione (dunque temperature più fredde) nell'emisfero occidentale, che consentono alti tassi di condensazione atmosferica della CO_2. A questa onda sono associati movimenti ascendenti e discendenti che generano, rispettivamente, raffreddamento e riscaldamento adiabatico. Quello del raffreddamento adiabatico è un fenomeno dinamico molto efficiente, in grado di creare ampie zone di sovra-saturazione nelle quali la condensazione è molto probabile.

Il confronto con i modelli di circolazione globale di Marte supportano l'idea di questa onda planetaria, eccitata dai grandi bacini, che risulta quindi responsabile della asimmetria osservata per la calotta meridionale residua.

Questi e molti altri risultati di questo lavoro sono riportati nel paragrafo 7.3 di questa tesi. Il lavoro è stato inviato alla rivista scientifica *Icarus* ed è attualmente in fase di stampa.

La calotta polare Nord è stata ampiamente osservata da PFS. Il periodo migliore per tali osservazioni è a metà primavera, nell'intervallo 20°-50° L_S. In questo periodo, infatti, le nubi che usualmente circondato la calotta sembrano scomparire. PFS ha osservato la calotta Nord in L_S = 39.9° durante l'orbita 452. Tali misurazioni sono state utilizzate per studiarne la composizione, lo stato microfisico, i modi di coesistenza e lo spessore, mediante il confronto con i modelli di riflettanza bi-direzionale calcolata utilizzando la teoria di Hapke precedentemente descritta.

I dati sono stati raggruppati in cinque diversi gruppi, che corrispondono ad altrettante regioni spaziali della calotta, mostrate in figura 14. Gli spettri appartenenti ai diversi gruppi mostrano caratteristiche estremamente simili, tali da consentirne la media. Un esempio del fit dei dati è mostrato in figura 15.

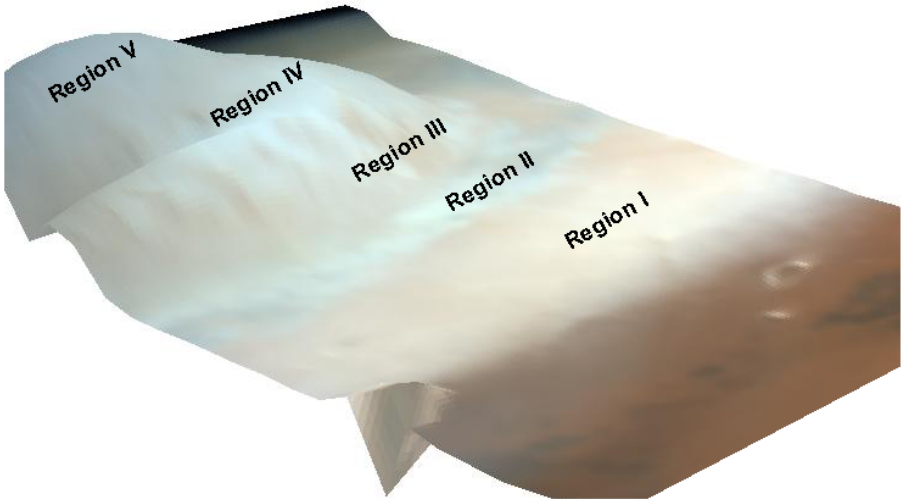

Fig. 14 Grafico tridimensionale della calotta polare Nord, così come osservata durante l'orbita 452. Sono segnate le cinque regioni investigate in questo lavoro.

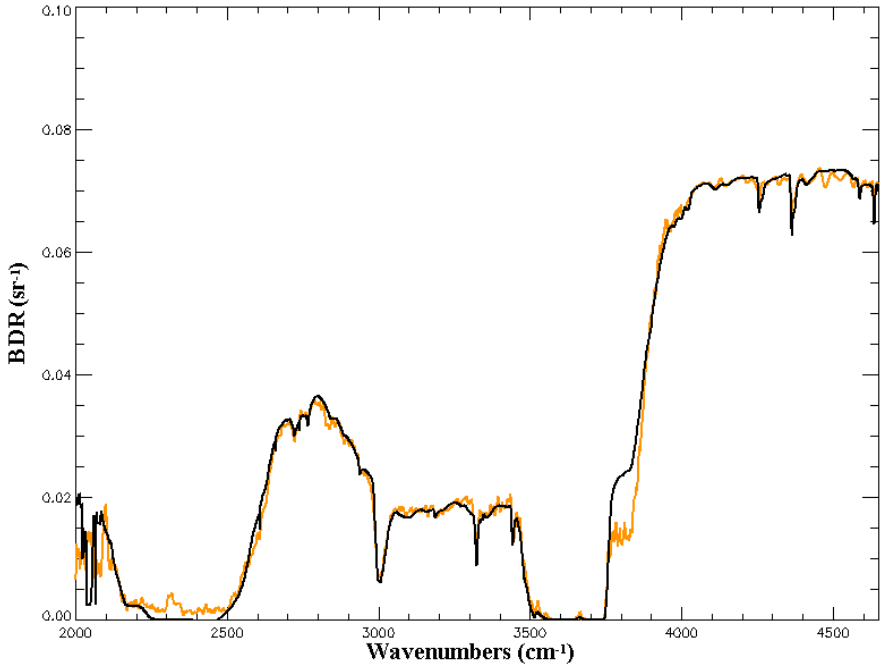

Fig. 15 Best-fit (curva nera) delle osservazioni (curva arancione) nella regione IV.

I dettagli ed i risultati di questo studio sono discussi nel paragrafo 7.4, e riassunti in Tabella 1. Il lavoro è stato pubblicato sulla rivista *Planetary and Space Science* e l'articolo è allegato in Appendice A.5.

Tabella 1

Description	composition	Grain size	Dust content (wt%)	H2O ice content (wt%)	Thickness
Region I (65° N – 72° N)	H2O ice	20 μm	0.15	-	Decreases with latitude
Region II (76°N – 79°N)	CO2 ice	5 mm	0	0.006	0.5–1 g cm-2 (1–2 cm)*
Region III (79°N – 81°N)	CO2 ice	3.7 mm	0.23	0.003	0.2–0.5 g cm-2 (0.4–1 cm)*
Region IV (81°N – 84°N))	CO2 ice	3 mm	0.02	0.0018	1–2 g cm-2 (4–10 cm)*
Region V (≥ 84°N)	CO2 ice	5 mm	0	0.003	> 20 g cm-2 (≥ 60–80 cm)*

*Assumendo una densità di 0.5 g cm^{-3}

INTRODUCTION

Mars, fourth planet from the Sun. Perhaps the most fascinating planet of the entire Solar System, surely the planet that most excites the interest of the international space agencies, with huge employments of scientists and resources involved in several international space missions. Not only does Mars have the largest volcanoes and deepest canyons in the entire Solar System, it also shows evidence for the most catastrophic floods. Large channels carved by these floods drain into the northern plains, lending support for the existence of an ancient ocean over most of the northern hemisphere.

Where there's water, there could be life. Meteorites from Mars that have landed on Earth show clear evidence that conditions appropriate to life did exist on the planet, including in the recent past.

Both Europe and USA have shown an increasing interest in the red planet, which has been the target of several missions. Among the latest, we remind: Mars Global Surveyor (NASA mission launched in September 1997), Mars Odyssey (NASA mission launched in April 2001), Mars Exploration Rover and Mars Express (respectively, NASA and ESA missions launched in June 2003), the latter with a payload of 13 instruments including the Planetary Fourier Spectrometer (PFS).

The existence of a thin atmosphere on Mars is known since the first observations with telescopes. The first space missions shown how the 6.1 millibar average pressure at the surface is due almost exclusively to carbon dioxide. The planet clearly shows two polar caps, whose aspect varies with seasons, and a series of phenomena related to the presence of clouds which were known already to the astronomers of the XIX century. Nevertheless, reliable information in the atmosphere have only been obtained with the advent of space explorations and, despite considerable theoretical and experimental efforts, remarkable questions still arise from the most important atmospheric phenomena.

The polar caps have gained significance in that they are one of the driving forces of the Martian climate. Because a large portion of the atmosphere condenses in and sublimes from the seasonal caps in a cyclic way during the year, the frost deposits play a significant role in the regional and global atmospheric circulation. Understanding the nature of the seasonal polar caps is essential if we want to understand the current Martian climate with high degree of confidence.

As much as 30% of the Martian atmosphere condenses every year to form polar caps in both hemispheres, inducing large variations of the surface pressure over the entire planet. At first glance, this phenomenon may seem straightforward, but this event is actually very complex, especially in the southern hemisphere. Traveling weather systems (transient eddies) are prominent in both hemispheres, while the large-amplitude and strongly upper-level disturbances observed for the first time in the northern hemisphere by the Viking Meteorology Experiment have yet to be observed in the south, despite the prediction by Mars Global Circulation Model (GCM) experiments. A peculiar and very prominent component of the southern winter circulation is a large-amplitude quasi-stationary wave pattern.

Whether the CO_2 ice accumulation in the polar caps is the result of a direct vapour condensation at the ground (frost), or of atmospheric condensation and precipitation (snow), cannot be easily addressed. The formation of CO_2 ice clouds and snowfall in the Martian polar night is far from being completely understood, and the direct condensation of the main atmospheric constituent (carbon dioxide) in the polar regions during fall and winter is one aspect of the Martian meteorology that has no terrestrial counterpart.

Despite the large number of studies on the southern spring and summer polar cap recession, with both satellite and ground-based observations, only few studies are available in the literature describing the seasonal progression of the Martian south polar cap (SPC) during the fall and winter seasons; in addition, most of them make use of model predictions rather than measurements.

Water has a great importance to human interest in exploration of Mars, making it important to minimize any confusion between the occurrence of CO_2 and H_2O ice. The similarity in reflectance of fresh CO_2 and H_2O snow makes them difficult to distinguish in monochrome or multiband reflectance imaging. Thermal infrared observations may partially resolve the composition of the seasonal and permanent polar caps on Mars: the condensation temperatures of CO_2 and H_2O differ by several tens of degrees, thus measurements of surface temperatures may be used to determine the ice composition, providing no spatial mixtures are present in the field-of-view (FOV). To unambiguously and comprehensively resolve the Mars' polar cap ice composition, the CO_2 snow/frost grain sizes as well as the water ice and dust contamination, it is necessary to investigate the near-infrared spectral region. Spectral resolutions as high as ~ 1 cm^{-1} are also required to resolve many of the narrow CO_2–ice absorption lines.

In this work we try to fill, at least partially, the lack of information about the composition and the mechanisms of accumulation of ices over the Martian polar caps, through the analysis of PFS observations. The Planetary Fourier Spectrometer has the unique, unprecedented capability of measure both the thermal and the Near Infrared radiation with a high spectral resolution. We also review, discuss and optimize practical methods for quantitative remote spectroscopy of icy surfaces.

Most of the scientific results presented in the last Chapter of this thesis have been published on international scientific journals. Three papers on the composition of the South Residual polar Cap, the evolution of the Seasonal South Polar Cap, and the composition and thickness of the North Polar Cap in mid-spring have been published on *Planetary and Space Science*. A fourth, robust paper on the condensing CO_2 South Polar Cap of Mars is in press on the scientific journal *Icarus*. Two additional technical papers on the spectral and radiometric calibration of the two spectral channels of PFS have been published on *Planetary and Space Science*. The published papers are available in the Appendix of this book.

This thesis is structured in three main sections. In the first section we provide general information and discuss open issues about Mars and its polar caps (**Chapter 1**), and present an overview of the PFS experiment (**Chapter 2**) and the latest developments on calibrations, which come not only before, but *during* our work, as a part of it (**Chapter 3**).

In the second section we first discuss on how, from a theoretical point of view, is it possible to obtain quantitative information about Martian polar caps from infrared spectroscopy, by examining the most diagnostic spectral regions, the instrumental

requirements, and the limitations of the previous missions (**Chapter 4**). We then derive the Radiative Transfer Equation and discuss the most common numerical and approximate solution techniques, as well as the computation of the main quantities involved in the Radiative Transfer Model (**Chapter 5**). Finally, we present the single-scattering properties of Martian ices (H_2O and CO_2) and dust, and review the reflectance model we selected to model the spectral properties of ices (**Chapter 6**).

In the third, last section, we present the most interesting scientific results achieved in the triennial work of this thesis (**Chapter 7**). PFS observations of both the North and South polar caps have been analyzed and compared with theoretical reflectance spectra and model predictions. As a result, new, original, and valuable scientific results have been obtained and published on international scientific journals. A total of five papers have been already published, plus one that is in press on *Icarus* at the moment of writing. Published papers are available in the **Appendix** of this book.

1 MARS AND THE POLAR CAPS

Mars, the fourth planet from the Sun, is the last of the inner, terrestrial planets. With an average distance from the Sun of $227.9 \cdot 10^6$ km and a significant orbital eccentricity (e=0.093), it has a minimum distance from the Sun of $206.7 \cdot 10^6$ km at the perihelion, while it is $249.1 \cdot 10^6$ km away from the central star at the aphelion. Thus, its orbital period is longer than that of the Earth: it takes about 687 days (1.88 terrestrial years) for a complete revolution around the Sun. Remarkable is the analogy between the terrestrial and the Martian day, the latter being of 24h 37min 22s. The rotation axis of Mars has an inclination close to that of the Earth: 25.19° with respect to the 23.45° of the terrestrial one. Mars' dimensions are notably lower than those of the Earth; its equatorial diameter is 6787 km, about the half of the Terrestrial one. It has a mass of $6.4 \cdot 10^{23}$ kg, which is about 0.107 times that of the Earth and its average density is 3.96 g/cm^3, lower than that of the Earth (5.52 g/cm^3) and similar to that of the Moon (3.34 g/cm^3). This suggests that Mars has a lower percentage of heavy elements with respect to the Earth and, consequently, a smaller nucleus which, in turn, reflects the near absence of a global magnetic field. Due to its small mass, the gravitational acceleration at the surface is of only 3.7 m/s^2 (38% of the terrestrial one) and the escape velocity is rather low: 5.03 km/s. This value is not sufficiently high to prevent the atmospheric gases to escape the planet, and this is one of the causes of the rarefied Martian atmosphere. The shape of Mars is far from being a perfect sphere: the southern hemisphere appears several kilometres embossed with respect to the northern one, so that its flattening (~1/170) is higher than that of the Earth (~1/298). The difference of about 20 km between the polar and the equatorial radius is mainly due to the rotation of the planet, with a small contribute (~ 5%) by the volcanic region of *Tharsis*, which is located close to the equator at 105° W longitude (see Fig. 1.2). Mars has two small satellites, Deimos and Phobos. In Table 1.1 we summarize the main geodetic and orbital parameters of Mars.

With the only use of a telescope it is possible to distinguish on the Martian surface broad regions of a bright orange colour, some reddish and some other dark areas, and bright regions at the poles whose edges vary following the cycle of the Martian seasons (Fig. 1.3). Due to the inclination of its rotation axis and the orbital eccentricity, the red planet is characterized by short and relatively hot southern summers, and lengthy cold winters. The reddish colour is due to the presence of iron oxides in the surface, while the dark areas are probably composed by rock similar to terrestrial basalts, with a surface oxidised and altered by the atmospheric agents. The bright areas appear to have a similar composition and are covered by fine dust. The bright regions at the poles are the polar caps, apparently composed by CO_2 and H_2O ices, whose edges expand and regress according to the seasons (see Subsection 1.3.1). Broad yellowish clouds, transporting dust lifted by winds, are particularly evident during the southern summer.

In the following sections we will briefly describe the characteristics and the composition of the Martian surface and atmosphere (Sections 1.1 and 1.2), and review what we know about the Martian polar caps, their physics and open issues (Section 1.3).

Table 1.1 Summary of Mars geodetic and orbital parameters

Parameter	Value
Mass (kg)	$6.42 \cdot 10^{23}$
Mean density (kg/m^3)	3940
Mean radius (km)	3389.508 ± 0.003
Mean equatorial radius (km)	3396.200 ± 0.160
North polar radius (km)	3376.189 ± 0.050
South polar radius (km)	3382.580 ± 0.050
Volume of north polar cap (10^6 km^3)	1,2 to 1,7
Volume of south polar cap (10^6 km^3)	2 to 3
Escape velocity (m/s)	5,000
Minimum surface temperature (K)	150
Maximum surface temperature (K)	310
Triaxial ellipsoid:	
a (km)	3398.627
b (km)	3393.60
c (km)	3376.200
Flattening	1/(169.8 ± 1)
Average distance from Sun (UA)	1.524
Rotation period (terrestrial days)	1.026
Orbital period (terrestrial days)	686.98
Obliquity (inclination of rotation axis respect to orbital plane)	25.19°
Orbital inclination	1.85°
Orbital eccentricity	0.093

1.1 The surface

The Martian surface is similar to that of terrestrial deserts; its yellow-reddish colour is due to the presence of iron oxides. Generally, the soil appears covered by dust and spread by rock with various sizes and shapes (Fig. 1.1). Martian rocks are richer of volatile elements with respect the terrestrial counterparts, and show a higher iron/magnesium ratio.

Fig. 1.1 An image of the Martian surface taken by Viking Lander I, landed on Mars on 20th July 1976.

The main characteristic of the Martian topography is the difference in altitude (~ 5 km) between the plains of the northern hemisphere and the terrains of the southern hemisphere. The dichotomy of the two hemisphere is the results of two different geological

stories. The crust of the southern hemisphere is heavily craterized (old) while that of the northern hemisphere has a much smaller count of craters. Reasonably, it must have undergo some sort of superficial rejuvenating process, perhaps due to volcanic activity or aeolian erosion. The *Tharsis* region is a vast volcanic area which interrupts the dichotomy between the two hemispheres. According to the craterizzation rate, the *Tharsis* plateau has an age between 4.1 and 3.3 Gy, while the three volcanoes there raising (*Arsia Mons*, *Pavonis Mons* e *Ascraeus Mons*) are younger, with an extimated age between 3 and 2.5 Gy. North-West from *Tharsis* is the highest volcano of the whole Solar System, *Olympus mons* (18°N latitude, 225° E longitude). A map of the Martian topography is shown in Figure 1.2.

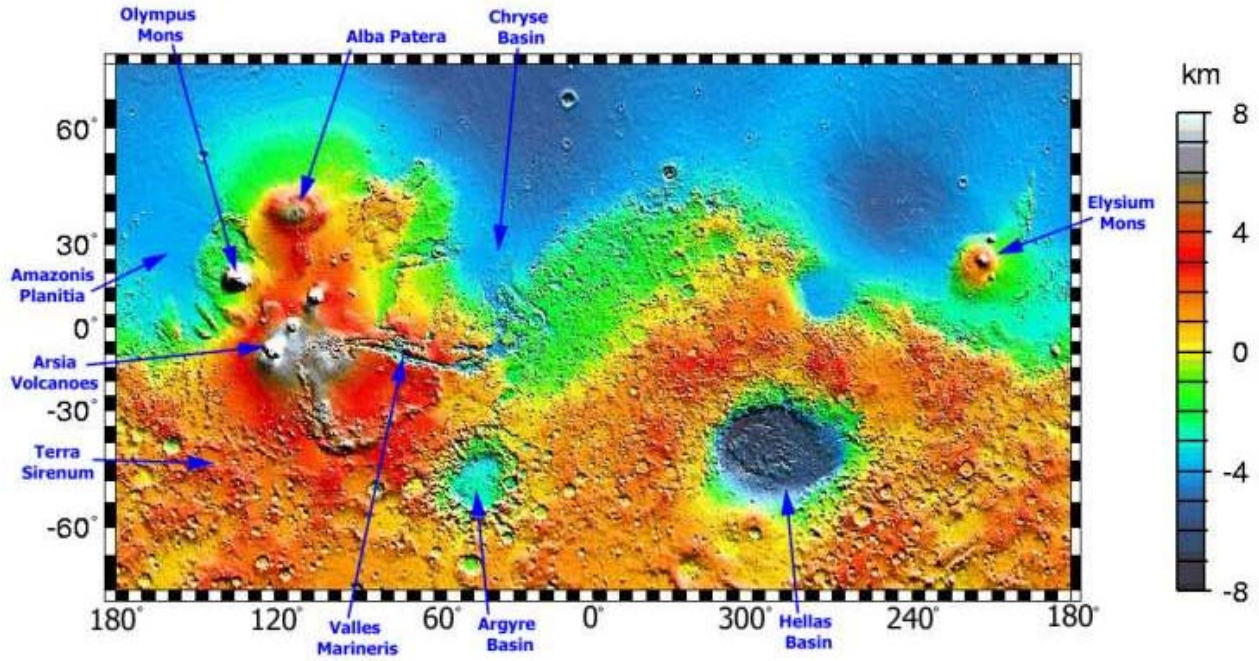

Fig. 1.2 Martian topography, compiled in the summer of 1999 with Mars Orbiter Laser Altimeter (MOLA) data aboard Mars Global Surveyor (MGS) – NASA.

Close to the equator, for about 4000 km eastward from the center of the *Tharsis* region, is the *Valles Marineris*, a crack in the crust of Mars which extends for about a fifth of the entire Martian perimeter, up to 600 km wide and about 7 km deep. It is about 27 times more extended, seven times wider and three times deeper than the Grand Canyon. Its origin is still not clear: MGS high-resolution images revealed layered sediments which make the fluvial nature very likely, although other explanations have been proposed.

In the southern hemisphere, with a 2300 km diameter and 9 km depth, is the largest impact crater of the whole Solar System, *Hellas Basin* (45° S latitude, 70° E longitude), whose bottom represents the lower-altitude area of the entire planet. It is surrounded by a series of mountains and volcanoes, generated after the impact process, and it is a place where fog and frost usually form. It is clearly visible from the Heath as a whitish circular spot in the southern hemisphere of the planet. A general discussion about the Martian topography can be found in Smith *et al.*, 1999.

The chemical composition of the Martian surface has been investigated through three main methods: direct analysis from Landers, study of SNC meteorites, and spectroscopic observations. In this field, the study of emissivity in the Thermal Infrared has a great

relevance, and important results has been achieved by the TES experiment aboard the *Mars Global Surveyor* NASA mission.

The two Viking Landers were not conceived for a complete analysis of surface compounds. Important indications on the abundance of elements in the fine materials come from X-rays fluorescence observations. The results are summarized in Table 1.2. The composition, surprisingly similar in the two sites and for different samples, cannot be related to any terrestrial mineral, although the relatively low content of Silicon and high content of iron and Magnesium suggest a mafic or ultramafic nature. The high concentrations of Sulfur and Chlorine, which indicate the presence of salts, were also unexpected.

Table 1.2 Composition of Martian surface measured by Viking Landers

Sample type	Covered fine materials		Uncovered fine materials		Duricrust
Site	VL1	VL2	VL1	VL2	VL1
Constituent	Weight percentage				
SiO_2	44	43	43	43	42
Al_2O_3	7.3	-	7.3	-	7
Fe_2O_3	17.5	17.3	18.5	17.8	17.6
MgO	6	-	6	-	7
CaO	5.7	5.7	5.9	5.7	5.5
K_2O	<0.15	<0.15	<0.15	<0.15	<0.15
TiO_2	0.62	0.54	0.66	0.56	0.59
SO_3	6.7	7.9	6.6	8.1	9.2
Cl	0.8	0.4	0.7	0.5	0.8

The above elements allow for about 90% of the total weight; the remaining fraction may be formed by Nitrogen and Carbon compounds (particularly carbonates and nitrates), which cannot be detected with this technique, or may be due to errors in the measurements.

The analysis carried on by the X-spectrometer Pathfinder only partially confirmed the above results. By comparing the two datasets, Aluminium and Magnesium are more abundant, while Iron, Chlorine and Sulfir are much less abundant. In this case, the rocks that have been analysed are similar to *andesites*, terrestrial materials derived by the fractionation of basalt in intrusive conditions. The mafic nature of the surface, which appeared to be consolidated, has then been, at least partially, called into question.
Another puzzling result is the total absence of carbonates, especially when considering the primordial atmospheric composition, which should have privileged its synthesis. Nevertheless, it important to note that both experiments performed an analysis of the content of the simple elements, not of the compounds.

Remote sensing spectroscopic techniques, both from spacecraft and Earth-based, may grant a global coverage of the planet, but may be biased by the presence of atmosphere and aerosols. They may also be difficult to interpret. Nevertheless, several reflectance spectra of Mars show a deep feature that may be interpreted as the tail of two absorptions due to the charge transfer between Fe^{3+} and O^{2-}. Such absorptions are centered in the near UV (0.34 μm) and are responsible for the classic red colour of the planet. It is not easy to understand which compounds may lead to the formation of the ferric ion. Crystal-shaped oxides (*hematite*) or hydroxides (*goethite*) show the above-mentioned band in the UV, but they also show a series of features that have never been observed in Martian spectra. To justify

the Fe_2O_3 abundance as measured by the Viking Landers (18%) one may assume the presence of nanocrystalline oxides, with very small grain sizes (~ 10 nm) and thus with an almost featureless spectrum, as observed at Mars. Among the terrestrial materials which contain nanocrystalline oxides we find the *palagonites*. This term indicates the products of the chemical alteration at low temperatures (in particular hydratation) of vitreous basalts. Beside the oxides, they have a strong concentration of clays. Soderblom and Wenner (1987) first suggested *palagonite* as a main constituent of the Martian soil, and infrared spectra of terrestrial samples support this hypothesis (Fig. 1.3).

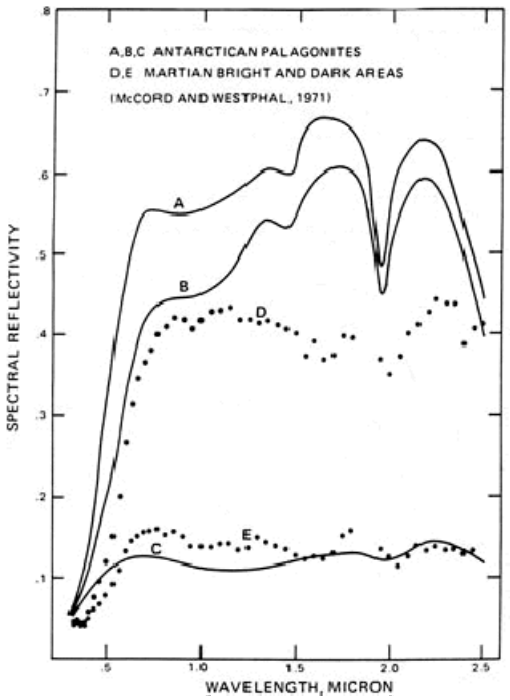

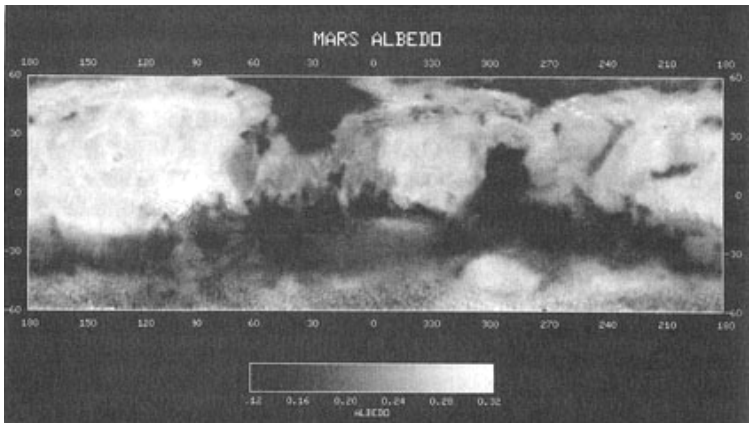

Fig. 1.3 **Top**: Martian albedo in the 0,3÷3 μm spectral region. Note the bimodal distribution of the bright (0,37÷0,4) and dark (0,1) regions, which are known since the first telescopic observations.

Left: Comparison between the reflectance spectrum of Mars and that of three different Antarctic palagonites.

Important concentrations of *Hematite* and *Augtite* in the North-West limit of *Syrtis Major* have also been pointed out by TES data analysis. The general aspect of the dark areas has been successfully modelled by Singer (1980). By the assumptions that the bright areas are sites of dust deposition and that a significant percentage of dust likely contaminates the dark areas, he determined the spectral shape of an ideally-clean dark area by subtraction of spectra. The result was surprisingly similar to a sample of basalt covered by a thin film of *plagonite* (about 30 μm). Superficial oxides become transparent around $\lambda = 0.8$ μm, where the spectral features of the underlying mafic material become predominant and the spectrum shoes the bands of the present minerals (*pyrossens*). Presence of clay minerals has been suggested by many authors, for they are one of the most common product of the chemical weathering in terrestrial environments. This idea is supported by several studies which have identified the *montmorillonite* (a aluminium-rich clay) as the most likely constituent for suspended dust observed in the IRIS spectra, thanks to the absorption band observed between 800 and 1100 cm^{-1}. Many authors investigated the presence of minerals different from silicates, such as carbonates, sulphates and nitrates. In particular, the presence of carbonates have been extensively investigate, but the results in the near-infrared (they have a characteristic band around 2.55 μm) are inconclusive. Such minerals have the most intense bands in the thermal infrared (characteristic vibrational modes of

CO_3^{2-} group are around 1500 cm^{-1}) but no clear evidence of such bands have been observed in the IRIS and TES spectra.

1.2 The atmosphere

The existence of an atmosphere on Mars is known since the first observations with telescopes. The planet clearly shows two polar caps, whose aspect varies with seasons, and a series of phenomena related to the presence of clouds which were known already to the astronomers of the XIX century. Nevertheless, reliable information in the atmosphere have only been obtained with the advent of space explorations and, despite considerable theoretical and experimental efforts, remarkable questions still arise from the most important atmospheric phenomena. A highly-dynamical system such the atmosphere of a planet needs a series of high-quality, long-term measures to be studied. It is a typical example of chaotic system in which a little perturbation may originate significant effects in the long-term behaviour. The development of atmospheric models, able to satisfactorily predict the behaviour of the Martian atmosphere, is an ambitious task. At the same time, this long-term scientific work is one of the most important in planetology science, for the results obtained on Mars may provide useful information to much more complex systems, such as the atmosphere of the Earth itself.

Before the space era, spectroscopy has been the only tool to investigate the composition of the Martian atmosphere. Early estimates of the atmospheric pressure based on measurements of the diffusion of the solar radiation predicted values around 100 millibar, and the carbon dioxide was thought to be a minor component of the atmosphere. The firsts space missions shown how the Martian atmosphere is actually much thinner that predicted and that the 6.1 millibar on average at the surface were due almost exclusively to carbon dioxide. The absolute amount of CO_2 in the atmosphere varies significantly during a Martian year (see Section 1.3): during the winter the atmospheric temperature drops below the CO_2 condensation temperature on mars (~ 150 K) and the carbon dioxide tends to condense on the surface, forming the seasonal polar caps. Seasonal variations of the pressure, measured by the two Viking Landers, confirm that as high as 30% of the atmosphere is involved in this process every year. The other species are much less abundant, but may be very important in the total energetic balance of the atmosphere and may give us indications about the processes here involved. The main constituents of the lower Martian atmosphere are summarized in Table 1.3.

Water has a partial pressure at the surface which is far below that of the triple point, and cannot exist in the liquid state, but just as water vapour or ice. The absorption lines of water vapour are well visible in the thermal and near infrared, between 200 and 400 cm^{-1} and above 1300 cm^{-1}. Systematic observations of this parameter has been performed by a devoted instrument of the Viking orbiter, the Mars Atmospheric Water Detector (MAWD). Such observations highlighted important systematic trends of water content, which varies with season and latitude. Relevant quantities are involved in the condensation and sublimation processes in the polar caps. Atmospheric vapour (CO_2 and H_2O), under certain conditions, may condense directly in the atmosphere, leading to the formation of clouds and precipitations.

Molecular Oxygen is present in relatively low quantities, as predicted in the absence of a biological source. Oxygen can be detected on Mars thanks to a series of lines, either in

absorption or emission, the strongest being at 7883 cm^{-1} (*Oxygen glow*). As all the homopolar diatomic molecules, O_2 does not have a permanent electric dipole moment and other lines than the above-mentioned one may be very difficult to be observed with infrared spectroscopy.

Table 1.3 Composition of Martian lower atmosphere

Gas	Abundance in volume
CO_2	95.32 %
N_2	2.7 %
Ar	1.6 %
O_2	0.13 %
CO	0.07 %
H_2O	0.03 % (a)
Ne	2.5 ppm
Kr	0.3 ppm
Xe	0.08 ppm
O_3	0.04÷0.2 ppm (a)

(a) varies with season and latitude

Table 1.4 Minor species in the Martian atmosphere

Gas	Measured band (cm^{-1})	Upper limit (ppm in volume)
C_2H_2	729	0,002
C_2H_4	1443	0,5
C_2H_6	821	0,4
CH_4	1306	0,02
N_2O	1258	0,1
NO_2	1621	0,01
NH_3	968	0,005
PH_3	1122	0,1
SO_2	1362	0,1
OCS	859	0,01

Carbon monoxide was first identified in 1967 on the basis of the absorption bands in the near infrared associated to the vibrational transitions. Significant variations of the CO abundance in the Martian atmosphere have not yet been reported.

Ozone is only present as traces. It was detected for the first time in the Ultra Violet spectra of Mariner 7 as an intense absorption at 2550 Angstrom, associated to its photo-dissociation. The synthesis of O_3 is, by any means, inhibited by the presence of water vapour and thus the abundances of the two components are anti-correlated.

Viking Landers have also provided an additional and fundamental amount of information, such as very accurate isotopic ratios, and the abundance of molecular Nitrogen N_2 and noble gases. If we assume that Mars initially had a C/N ratio of the same order of magnitude of that observed for Venus and the Earth, the red planet should have had an original pressure between 100 and 1500 millibar due to the CO_2 content. If this is true, Mars experienced strong climatic variations, as proved by the many traces of liquid water flows on the surface. The origin itself of the Martian atmosphere is not clear: if, from one side, the *T-Tauri* phase of the Sun must have eliminated any primordial gaseous hull, the degassing by volcanic emissions and the contribution of volatiles by impacts of comets

and meteorites in the following eras must have contributed in a conspicuous manner to the formation of an atmosphere. In particular, the degassing must have been a dominant factor, for the nature of atmospheres of the terrestrial planets is directly related to the surface activity. The thin atmosphere of Mars seems then adequate to the low endogen activity, but substantial questions still arise on the processes that occurred in the different planetary environments.

The minor species in the Martian atmosphere are summarized in Table 1.4. The low concentration of Methane indicates, once again, the present absence of a large-scale biological activity.

1.3 The polar caps

In this section we summarize what we know about the Martian polar caps and their physics. In Subsection 1.3.1 we discuss on the extension, mass and thickness of the polar caps. Since the condensation and the sublimation phases differ in the processes involved and in the kind of observations available, we will first examine the formation of the polar caps (Subsection 1.3.2) and then their sublimation phase (Subsection 1.3.3). In the much shorter last three Subsections, we briefly discuss microphysical state of CO_2 ice (Subsection 1.3.4), the interannual variability of the seasonal polar caps (Subsection 1.3.5) and the implications and the problems raised by the possibility that there is permanent CO_2 ice in the Martian polar regions (Subsection 1.3.6).

The Martian Polar caps have been observed for more than two centuries by terrestrial observers. Following the first observations by J. Cassini and C. Huygens, Herschel (1784) first described their seasonal characteristics. From Earth, they appear like white bright features waxing and waning over a Mars year. Because of the 25.19° inclination of Mars' equator to its orbit plane, the seasons on Mars are much like their terrestrial counterparts.

By analogy with the Earth, most observers assumed that the Martian polar caps were composed of water frost, until the first space probes to Mars. Following the Mariner 4 mission in 1965, Leighton and Murray (1966) used a simple thermal model to reveal the processes which control the Martian seasonal polar caps: during the fall and winter seasons at high latitudes, the local surface and atmospheric temperatures become cold enough to reach the frost point of CO_2, the major constituent of the thin Martian atmosphere. Spectroscopic observations later confirmed the CO_2 composition (Herr and Pimentel, 1969; Larson and Fink, 1972, Fig. 1.4).

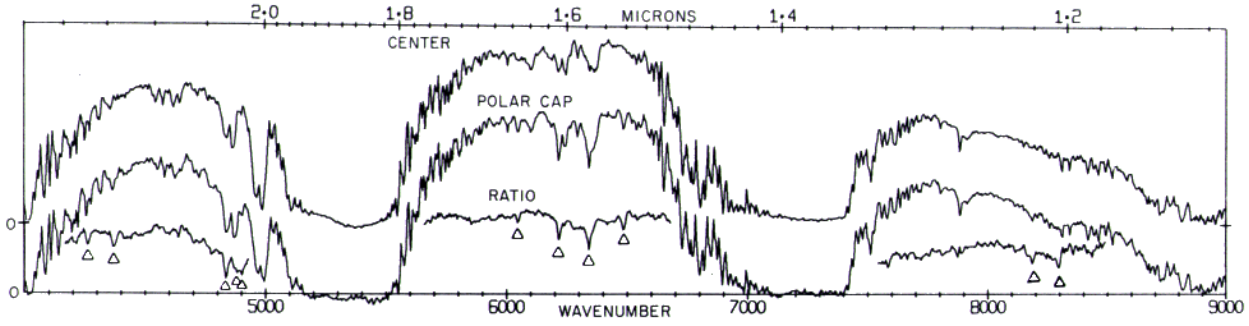

Fig. 1.4 The first identification of Carbon Dioxide frost on the Martian polar caps (Larson and Fink, 1972) – Spectra of the center of the planet Mars (*top*), the polar cap (*middle*), and the ratio of polar cap divided by the center (*bottom*). *Triangles*: detected CO_2 frost absorption features.

This "CO_2 cycle" causes the global atmospheric mass to vary by several tens of percent. Surface pressure measurement made from the two Viking probes which landed in the northern hemisphere of the planet in 1976 clearly showed these enormous seasonal variations (Fig. 1.5). Although these seasonal oscillations are also influenced by the atmospheric circulation (Hourdin et al., 1993), they reflect the variation of the global mass of the atmosphere; the first minimum of pressure near sol 100 occurs during southern winter when a large part of the atmosphere is trapped in the seasonal south polar cap, and the secondary minimum corresponds to the northern winter, shorter than the southern winter because of the high eccentricity of the Martian orbit. The CO_2 cycle also affects the Martian climate by creating a strong planet-wide atmospheric circulation called the "condensation flow" which transports heat, momentum and mass from the subliming cap toward the region of the forming polar cap. It is also coupled in several ways (described in this chapter) to the seasonal cycles of H_2O and dust.

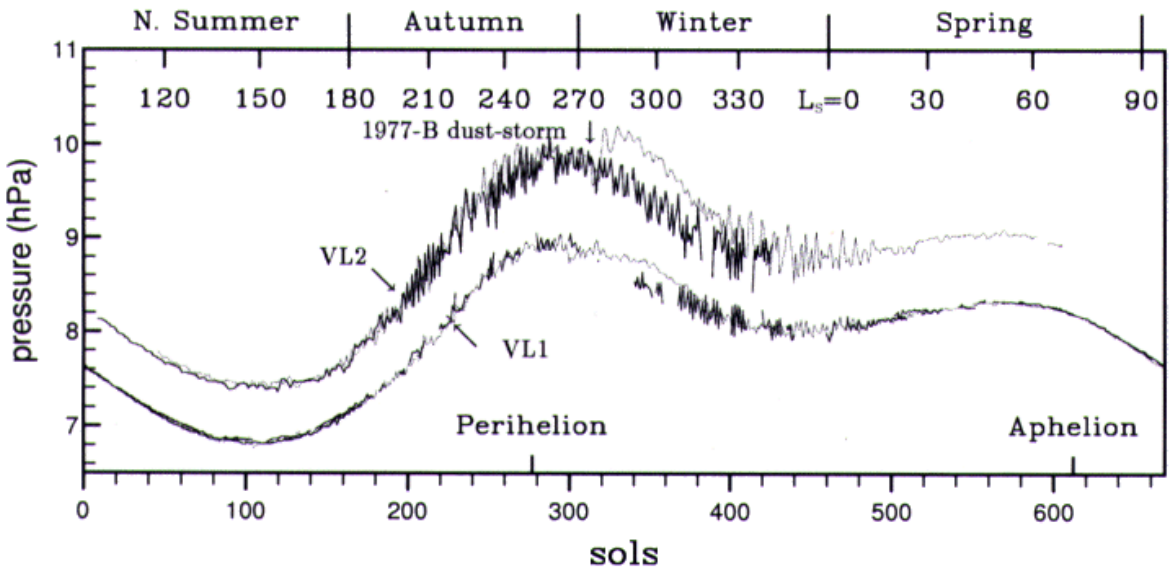

Fig. 1.5 Time evolution of the surface pressure recorded by the two Viking Landers during the first three Martian years: year 1 (*dotted*), 2 (*solid*) and 3 (*dashed*) are superimposed on the same graph. The large seasonal variation of the surface pressure are primarily due to the condensation of the atmospheric CO_2 in the seasonal polar caps. Figure from Hourdin et al (1993), data from Tillman and Guest (1987).

The influence of the Martian seasonal caps is not restricted to the high Martian latitudes, and understanding the processes that control the CO_2 cycle is important for understanding the past and current Martian climate. The process of condensation and sublimation of the polar caps described by Leighton and Murray (1966) is rather simple, but the observations of the polar caps by the spacecraft missions of the 70's (Mariner 9 and Viking) gave unexpected results and even raised some of the most puzzling questions about the planet. As an important part this thesis, we have investigated the CO_2 condensing south polar cap of Mars and the mechanisms of CO_2 ice accumulation. The regional and global circulation of the planet, as well as the middle-latitude topography of Mars play an important role in the processes of condensation, and the available Global Circulation Models are not able to predict in detail the complexity of the atmospheric dynamical phenomena that occur in the polar region. The results will be presented in Section 7.3.

1.3.1 Extension, mass and thickness of the polar caps

Extension: The locations of the polar caps boundaries during their condensation phases and their maximum extensions are not very well known for several reasons. First, since during the fall and winter seasons Martian poles are by definition tilted away from the Sun -and thus from Earth-, telescopic observations have been difficult to obtain. Moreover both spacecraft and telescopic observations in the visible are complicated by the near coincidence of the terminator with the edge of the cap. Viking observations of the south polar cap (Briggs et al., 1977; James P. B., 1983) confirm terrestrial observations that the surface frost extends to between -50° and -55° latitude and reaches as far north as -40° latitude in the relatively low-elevation Hellas and Argyrae basins which are covered preferentially by the frost as expected from energy balance consideration (low elevations have higher pressures, corresponding to higher frost formation temperatures).

In the northern hemisphere, observations of the cap boundaries are even more difficult. These regions are usually obscured by clouds during fall, winter and early spring to latitudes as low as +40°. These clouds, generally referred to as "polar hood", have been studied for decades by telescopic observers who were able to distinguish them from the ground ice because of their high variability and their higher opacity in images obtained with blue and violet filters. The polar hood has also been observed in details by Mariner 9 and Viking (Briggs and Leovy, 1974; Briggs et al., 1977). The camera aboard Mariner 9 showed that the hood is diffuse at latitude higher than 60°, but that it exhibits complex wave structures at lower latitudes. A southern polar hood also exists but is much less prevalent than the northern one (James et al., 1979).

Analysis of images of the north polar cap acquired with various filters from Earth (e.g. James et al., 1987) and by Viking (James, 1979; 1982) suggest that the cap extends to roughly 55° in late winter. This is supported by the IRTM data analyzed by Christensen and Zurek (1984).

During the late fall and winter seasons, the second Viking Lander located at 48° N latitude observed thin surface frost deposits (Jones et al., 1979; Wall, 1981). There has been considerable debate about whether the frost was composed of CO_2 or H_2O ice, although the most recent studies have favored a H_2O ice composition (Hart and Jakosky, 1986; Svitek and Murray, 1990).

Mass: The mass of the polar caps cannot be observed remotely, although future gamma-ray spectrometers could come close by measuring remotely the effect of the CO_2 on the gamma-ray and neutron emissions. Nevertheless, the amount of CO_2 which gets globally trapped in the seasonal polar caps can be estimated from the seasonal surface pressure variations measured by the Viking Landers (Fig. 1.2). This is not straightforward, since these variations are not only due to condensation and sublimation of atmospheric carbon dioxide in the polar caps, but are also strongly influenced by internal mass redistribution associated with the atmospheric circulation (Talagrand et al., 1991; Hourdin et al., 1993; Pollack et al., 1993). For this reason, the surface pressure cycle depends on the location on the planet and is not simply related to the global atmospheric mass cycle. Hourdin et al. (1995) used a global circulation model to estimate the local meteorological component and thus the global atmospheric mass budget from the Viking data, with a rather good accuracy except for the fact that global Martian topography is not very well known. Corresponding model results showed that for a consistent total seasonal cap +

atmospheric carbon dioxide budget of about 6.8 mbar, an equivalent pressure up to 1.0 mbar and 1.7 mbar gets trapped every year in the north and south polar cap respectively.

Thickness: The thickness of the CO_2 ice layer is thought to be highly variable (James et al., 1979): as explained above, the local condensation and sublimation rate depends on latitude and on the local topography, winds, and surface properties. Wind redistribution also plays a significant effect, for instance accumulating frost in the lee of craters (Thomas et al., 1979). Using the Viking IRTM data to determine annual radiation budget and infer the annual carbon dioxide frost budget of the Martian north and south residual cap regions, Paige and Ingersoll (1985) calculated that during the winters observed by Viking, there was about 75 g cm^{-2} of CO_2 frost deposited at the north pole and about 110 g cm^{-2} deposited at the south pole. This corresponds to maximum cap thickness of the order of 0.5 and 0.7 m, respectively, in the fully dense state (~1.6 g cm^{-3}). Such results are consistent with most polar cap models, including the pioneering works by Leighton and Murray (1966) and more recent and sophisticated models (e.g. Hourdin et al., 1995). Thomas et al. estimated that the maximum winter accumulation of frost in some observed frost streaks lying in the lee of craters was of the order of 100-150 g cm^{-2}.

In section 7.1 we present a detailed study of the south polar cap boundaries as a function of season and longitude for the fall and winter seasons. Our results show a much more irregular and extended cap than previously reported by Viking and terrestrial observations. The results have been published in the scientific journal *Planetary and Space Science* (Giuranna *et al.*, 2007a); the paper is available in the Appendix of this book, Section A.4. In the section devoted to the North Polar Cap results of our work (Section 7.4) we also discuss about the extension, the snowpack density and thickness of the NPC in mid-spring. Our results have been published in the scientific journal *Planetary and Space Science* (Giuranna *et al.*, 2007b); the paper is available in the Appendix of this book, Section A.5.

1.3.2 The condensing Martian polar caps

1.3.2.1 Energy balance and modelling of the condensing polar caps

The condensation of the Martian polar caps start in fall, when the polar regions are shrouded in continual darkness during the polar night. Almost all that is known about the condensing polar caps has therefore come from the infrared observations. Because actual observations are limited, significant advances in our understanding of the formation of the seasonal polar caps have been obtained through thermal balance modelling. The amount of CO_2 which condenses in the polar caps is controlled by the energy balance of the Martian polar regions: the total net flux of energy into a region at its boundaries must be equal to the rate at which energy is stored inside the region. Since condensation can occur both in the atmosphere and on the surface, the combined atmosphere + surface column energy balance equation must be considered.
To first order, it gives

(1.1) $$C_{CO_2} = \left[F_{IR}^{\uparrow} - Adv - Cond - (1-A)F_{solar}^{\downarrow}\right] / L$$

where C_{CO_2} is the total CO_2 condensation rate (kg m^{-2} s^{-1}); L the latent heat of CO_2 ($5.9 \cdot 10^5$ J kg^{-1}); $F_{IR}^{\uparrow}$ the thermal infrared flux of the system toward space; *Adv* the heating rate due to heat transport by the atmosphere to the system (advection); *Cond* the subsurface heat conduction flux (positive when the subsurface is warmer than the surface); A is the planetary albedo at solar wavelengths; $F_{solar}^{\downarrow}$ the solar flux at the top of the atmosphere. This last term is of course equal to zero at night and especially during the polar night, when most of the condensation occurs.

Outgoing infrared emission: Under regular conditions (i.e. outside the dust storm period), the thermal infrared flux toward space $F_{IR}^{\uparrow}$ is usually the major term (Pollack et al., 1990; Hourdin et al., 1995). It can be determined from spacecraft observations. In particular, the Viking IRTM observations have been used to determine the seasonal evolutions of $F_{IR}^{\uparrow}$ during the first Viking year for the core regions of the residual cap (Paige and Ingersoll, 1985), and more recently for the entire seasonal caps during the polar night seasons (Forget and Pollack, 1996). $F_{IR}^{\uparrow}$ was primarily affected by low brightness temperatures events (see subsection 1.2.1), especially in the northern atmosphere (Forget and Pollack, 1996).

Polar caps surface temperatures and thermal emission: When the atmosphere is clear, $F_{IR}^{\uparrow}$ is usually close to the infrared flux emitted by the surface. In models, this flux can be computed as $F_{surf\uparrow} = \varepsilon \sigma T_{surf}^4$, with σ, the Steffan-Boltzmann constant ($5.67\ 10^{-8}$), ε the spectrally averaged emissivity and T_{surf} the surface temperature. The CO_2 ice surface temperature T_{surf} only depends on the local atmospheric pressure p, through the CO_2 vapour pressure curve, described by the Clausius-Clapeyron's law, which for our purposes can be written as $T = 3148/(23.102 \ln p)$ with T in Kelvin and p in millibars (see James et al., 1992). In spite of this relation, the cap surface temperatures are poorly known because of the large uncertainties in the available Martian topographic data used to derive the surface pressure. This is a serious obstacle to modelling and understanding the physics of the caps. Estimating directly the ground ice temperatures from infrared observations is difficult because of the anomalous brightness temperature observed during the polar night (see subsection 1.2.1) and because of the strong emission of the dust particles warmer than the surface cap when the atmosphere is sunlit. Actual "thermodynamic" ground ice temperatures have been estimated at the pole by Paige and Ingersoll (1985), and more recently mapped for the global polar caps by Forget and Pollack (1996). Interestingly enough, these temperatures seems to be colder than the expected frost point of CO_2 for the topography of the polar regions which is usually used in the models. In both hemispheres, there is an apparent systematic decrease of the temperature toward the pole, but the southern polar cap is globally 4 K colder than the northern cap. Near winter solstice, temperatures at the pole are about 145.5 K in the north and 141.5 K in the south, corresponding to pressures of respectively 4.3 mbar and 2.3 mbar.

Atmospheric radiative effects: $F_{IR}^{\uparrow}$ can be affected by the presence of other aerosols such as airborne water ice or dust, and by the absorption and emission of the gaseous atmosphere in the 15-μm band. In the southern hemisphere, model results (Pollack et al., 1990; Hourdin et al., 1995) and available infrared observations (Martin and Kieffer, 1979; Martin, 1981) suggest that the winter polar atmosphere is approximately isothermal. Its net effect on the total outgoing radiation should thus be negligible. This is not valid for the northern fall and winter seasons observed by Viking during which two global dust storms occurred. The second storm caused a strong increase of the infrared emission measured by all the IRTM channels,
especially in the 9-μm and 11-μm channel. This dust storm warming was particularly strong near the cap edge. It decreased with latitudes but was still observable in the polar region (Martin, 1981). This second storm, and to a lesser extent the first one were accompanied by a more durable and particularly intense warming of the upper atmosphere in high northern latitudes thought to be caused by complex atmospheric dynamical processes (Martin and Kieffer, 1979; Jakosky and Martin, 1987). Despite the fact that the clear upper Martian atmosphere only radiates in the the 15-μm gaseous CO_2 band, this polar warming considerably increased the total infrared emission toward space of the polar regions (Forget and Pollack, 1996).

Atmospheric heat advection: During the dust storms, the strong increase of the infrared emission toward space $F_{IR}^{\uparrow}$ does not imply that more CO_2 condensed during these periods: this increase is nothing but the observable consequence of a much larger advection of energy toward the pole by the atmosphere. In equation 1.1, the observed increase of $F_{IR}^{\uparrow}$ was certainly correlated with a much larger increase of *Adv*, causing the CO_2 condensation to decrease or even stop during these periods (Martin and Kieffer, 1979). The heat advected above the caps during the upper atmosphere polar warming events only directly affects atmospheric levels located above the expected level of condensation but it inhibits the condensation rate indirectly by its radiative effect (Martin and Kieffer, 1979; Forget and Pollack, 1996).

More generally, theoretical studies conducted with atmospheric general circulation models (Pollack et al., 1990; Hourdin et al., 1995) confirm that the heat advection by the atmosphere *Adv* plays a fundamental role near the cap edge (up to 20-30 Wm^{-2}), especially for enhanced dust loading. This role is probably much smaller near the center of the seasonal cap (a few Wm^{-2}), as suggested by the heat budget studies by Paige and Ingersoll (1985).

Subsurface heat conduction: The subsurface conduction *Cond* accounts for the energy stored in the subsurface material during the year. Thus, it is positive and non negligible, especially when the caps start condensing, and where the thermal inertia is high. Actual values of the subsurface thermal inertia are poorly known below the diurnal skin depth on Mars. This uncertainty must be taken into account when modelling the polar caps (Wood and Paige, 1992). The highest thermal inertia should be found on the water ice north residual cap, where the subsurface conduction could reach 20-30 Wm^{-2} (Paige and Ingersoll, 1985). On the other hand, *Cond* is probably close to zero on the south residual cap where the temperature is constant all year long. This difference between the North and

South caps may be important in explaining the polar caps asymmetry (Jakosky and Haberle, 1990).

Application: polar cap models. Since Leighton and Murray (1966), many models have been developed to simulate the formation of the Martian polar caps by examining their energy balance (e.g. Briggs, 1974; Davies et al., 1979; James and North, 1982; Wood and Paige 1992; Pollack et al., 1990, 1993; Hourdin et al., 1993, 1995). Most recent models are able to reproduce the annual variations in atmospheric pressure shown in Fig 1.2, but most studies concluded that it was necessary to use artificially low values for the modelled caps emissivities to account for a condensation rate lower than expected. This confirms that in these models major processes have not yet been taken into account or properly treated (e.g. CO_2 clouds and snow, heat advection during the dust storm, upper atmosphere polar warming) and that the available datasets used for the topography and for the seasonal thermal inertia may not be accurate.

1.3.2.2 Observations in the thermal infrared

As introduced in the previous paragraph, almost all that is known about the condensing polar caps come from the infrared observations, the polar regions being shrouded in continual darkness during the polar night. The observations by two orbiting spacecraft missions to Mars, Mariner 9 and Viking, gave surprising results. Scientists predicted almost isothermal polar caps at about 145-148 K in vapour pressure equilibrium with the atmosphere. The Viking Infrared Thermal mapper (IRTM) which was expected to measure such surfaces temperatures with its 11-μm and 20-μm channels found considerable structure with minimum brightness temperatures far below the CO_2 frost point, often below 135 K (Kieffer et al., 1977). The location and brightness temperatures of these anomalously “cold” areas were highly variable, sometimes on time scales of days. There were observed at most polar latitudes in the northern hemisphere unlike in
the southern hemisphere where they were less frequent, especially equator- ward of 80° S (Forget and Pollack, 1996, Kieffer et al., 1977). In particular, an exceptionally high frequency of occurrence of extremely low brightness temperatures was reached near the north pole right after the first phase of the second global dust storm observed by Viking, a few days after the northern winter solstice.

The Mariner 9 IRIS spectrometer polar night observations - analysed by Paige et al. (1990a) - show that these areas exhibit a complex spectral signature (Figure 1.6), at least in the northern polar region in late winter (the only period and region for which relevant IRIS spectra are available). Hypotheses for explaining these observations include a strong enrichment in lighter, non-condensable gases in the winter polar atmosphere allowing the partial pressure of CO_2 to be less than that at low latitude (Kieffer et al., 1977), low surface emissivities for carbon dioxide frost (Ditteon and Kieffer, 1979), and the presence of carbon dioxide clouds (Hunt, 1980). Hess (1979) cast doubt on the feasibility of the non-condensable gas enrichment by showing that vertical and horizontal gradients in the average molecular weight of the Martian polar atmosphere could be stable only under very special circumstances. The last two hypotheses have been supported or studied by various authors. They are reviewed in the next two paragraphs.

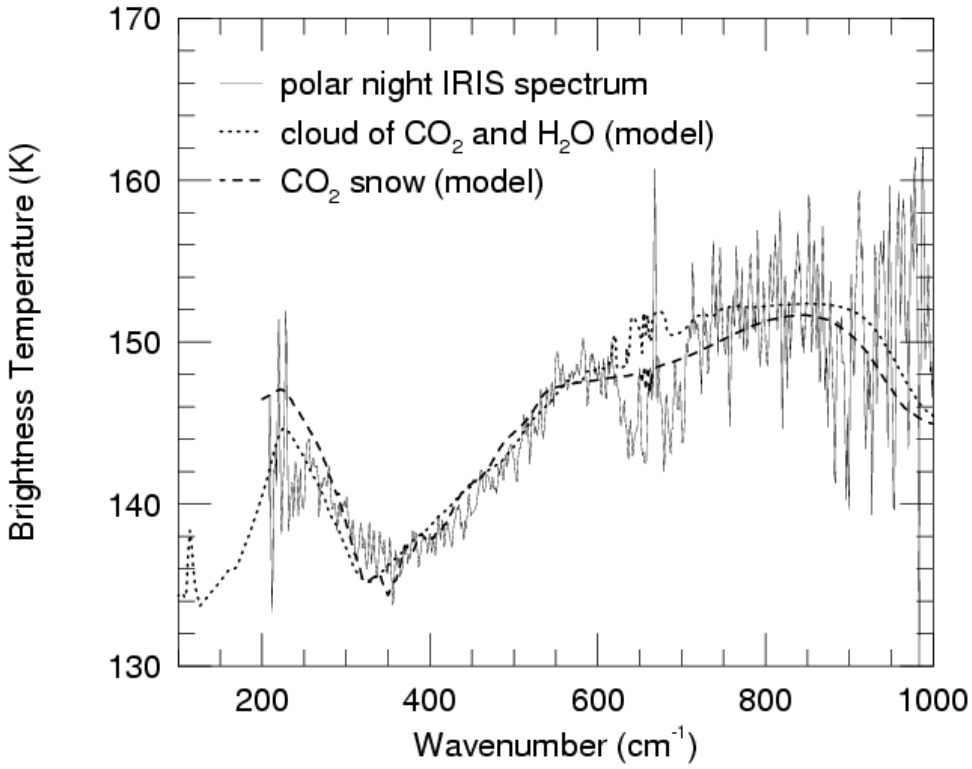

Fig. 1.6 Typical Mariner 9 IRIS spectrum of the northern polar cap during the polar night (75° N, 150° W, Ls=331°). Data below 225 cm^{-1} and above 750 cm^{-1} are very noisy and thus not reliable. The prominent feature extending from about 600 to 800 cm^{-1} is due to absorption and emission by gaseous CO_2. Outside the CO_2 gas band, the spectra can be matched by simulated spectra of precipitating CO_2 cloud (r = 50 μm) mixed with water ice particles (dotted line) as well as simulated spectra of CO_2 snow (r = 2.5 mm) contaminated by 0.05 % of dust and 0.05 % of water ice (dashed line). Figure from Forget et al., 1995.

Although many disparate effects have been offered to explain these features, the current consensus is that they are caused by regions of relatively fine-grained CO_2 frost, probably the result of snowfall (Hansen, 1999; Titus et al., 2001), and occurring often in regions of high topographic slopes, implying dynamic atmospheric processes (Forget et al., 1998b). Recently, an additional explanation of cold-spots in the Martian winter polar caps and their evolution has been proposed by Hansen, 2003a, involving the mobility of dust grains (subparagraph 1.3.2.2.3). In the following subparagraph we review the explanations offered for the low brightness temperatures observed in the IRIS Mariner 9 spectra.

1.3.2.2.1 Radiative properties of the CO_2 frost in the thermal infrared

Most natural planetary surfaces have emissivities above 90% in the thermal infrared. In particular snow and sea-ice on Earth always have emissivities near 99% (Warren et al., 1990). However, CO_2 ice has the property that its inter-band absorption in the infrared is much smaller than, for example, that of H_2O ice. This is apparently due to the lack of hydrogen-bonding in CO_2 ice (Warren, 1986). The interband absorptions were first measured in the laboratory by Ditteon and Kieffer (1979) who suggested that CO_2 snowflakes and frost could be efficient scatterers and thus have a low emissivity. Accurate

laboratory measurements by Hansen (1993) indicate that in the spectral regions on either side of the strong 15 μm absorption, the CO_2 ice is actually a factor of ten more transparent than reported by Ditteon and Kieffer. Using such laboratory data, the emissivity of pure CO_2 ice deposits can be estimated using radiative transfer models (Warren et al., 1990; Forget et al., 1995). These models have confirmed that Martian CO_2 frost could theoretically have an emissivity much lower than one in the thermal infrared. At any wavelength the primary variable controlling the radiative transfer properties is the snow grain size: the emissivity strongly increases with grain size. Contamination by dust and especially water ice can also raise the emissivity especially near their respective absorption bands. The emissivity could also depend on other properties not accounted for in the models, such as the grain shape. For instance, it seems reasonable that, if the growth can proceed in alternative ways, the form which maximizes the emissivity will be favoured since such particles will cool, and grow at the maximum rate (James et al., 1992).

On Mars, outside the observed anomalously low brightness temperatures areas, and especially in early fall, late winter and spring where no specific spectral signature was detected, the Martian polar cap emissivity is likely to be high (Paige, 1985; Forget et al., 1995). According to the models, that would require very large grain sizes, or more precisely spectroscopic path lengths on the orders of centimetres. Water ice and dust contamination could help but unrealistic amounts would be required to raise the emissivity above 0.9 (Warren et al., 1990). Large spectroscopic path lengths are also suggested by near-infrared observations of the subliming cap (subparagraph 1.3.3.3.3) and implications are discussed in Subsection 1.3.4.

Can the low brightness temperatures be explained by spatial variations in surface emissivity? The observed spectral features in the IRIS and IRTM data can be reproduced by modelled millimetre-sized grains CO_2 snow deposits mixed with small amounts of water or dust (Fig. 1.6; Forget et al., 1995). The high spatial and temporal variability of the brightness temperatures would suggest a scenario based on the different properties of CO_2 snow originating from the atmosphere and ice formed on the ground, as explained below.

1.3.2.2.2 Carbon dioxide ice clouds and snow

As first suggested by Gierash and Goody (1968) , further studied by Paige (1985) using a one-dimensional polar radiative model, and more recently modelled and analyzed with an atmospheric General Circulation Model (Pollack et al., 1990), atmospheric CO_2 condensation could occur at most altitudes in high latitudes during the fall and winter seasons. CO_2 ice particles are likely to form clouds in the polar night atmosphere.

Only limited observational evidence of CO_2 clouds exists. Clouds in the polar regions of Mars have been known for decades, especially in the northern hemisphere, and are referred to as “polar hoods” (see Briggs and Leovy, 1974; Briggs et al., 1977), but Mariner 9 IRIS showed that the northern winter hood was composed of water ice, at least south of 65° N. However, Briggs and Leovy (1974) observed at higher latitudes some cloud lines formed at the CO_2 ice temperature, with very distinct fine structure. They showed that water ice clouds could not have exhibited such structure because of the slow condensation and sublimation rates of water ice at low temperature, and that these clouds were likely to be composed of CO_2 ice. Also, three of the Mariner 6 and 7 infrared spectrometers limb

spectra have been interpreted as a reflection on thin CO_2 clouds because of characteristic spikes at 4.26 μm (Herr and Pimentel, 1970).

Kieffer et al. (1976) first suggested that CO_2 clouds could create the anomalously low IRTM brightness temperatures, among other possibilities. Pollack et al. (1990) showed that the spatial and temporal variabilities of the modelled atmospheric condensation rate were consistent with those exhibited by the low 20-μm brightness temperatures mapped by the Viking IRTM. In particular, the fact that the second Viking dust storm was followed by a period of maximum frequency and intensity of low brightness temperature events is consistent with model results: by its radiative effect, dust strongly increases the atmospheric emissivity, its cooling rate, and thus the atmospheric condensation rate (Pollack et al., 1990). Model calculations indicate that increasing the dust optical depth from 0 to 5 in the winter polar atmosphere produces a transition from a situation in which almost all the carbon dioxide condenses on the ground to one in which it nearly all condenses in the atmosphere. It also seems likely that the dust particles can serve as cloud condensation nuclei, along with H_2O ice particles.

CO_2 ice clouds are expected to affect the infrared emission of the polar caps mainly by scattering the radiation emitted by the surface back to the surface, if their particles are not too small (Hunt, 1980; Forget et al., 1995). Non-precipitating CO_2 clouds, composed of particles smaller than a few micrometers should be transparent in the infrared, whereas precipitating CO_2 clouds with particle radii larger than 10 μm should effectively scatter the infrared radiation. The hypothesis of opaque CO_2 clouds emitting higher in the atmosphere in a colder layer (Paige et al., 1990a) seems to be incompatible with the observations (Forget et al., 1995).

As for the CO_2 ice deposits, such clouds are able to produce the observed infrared features if the CO_2 ice particles are mixed with small amounts of water or dust (Fig. 1.3; Forget et al., 1995). In fact, the signature of CO_2 ice clouds and deposits are rather similar in that they both rely on the fact that intermediate size CO_2 ice grains can be efficient scatterers at infrared wavelengths, whether they are airborne or on the ground. CO_2 ice deposits composed of much larger grains or nonporous solid ice having directly condensed on the ground or having undergone frost metamorphism should have an emissivity close to unity, and, in any case, much higher than that of small CO_2 ice particles originating from atmospheric condensation. Besides, if the solid CO_2 ice layer is thin enough, it is likely that it will be transparent in the infrared and that the ground beneath will radiate through (with a high emissivity). On the basis of these results, Forget et al. (1995) suggested that the low brightness temperatures were likely to be created by CO_2 snow falls, and that both falling snow particles and fresh snow deposits could contribute to create the observed features.

1.3.2.2.3 Mobility of dust grains

The dynamic nature of these cold-spots has been demonstrated by repeated TES observations of the same locations (Eluszkiewicz and Titus, 2002). The apparent grain coarsening observed has been explained as a process of “continued condensation” (Forget et al., 1998b) or a sintering process starting from micron-sized grains (Eluszkiewicz and Titus, 2002) based on theoretical study by Eluszkiewicz, 1993. Recent mappings of the

polar cap composition and properties (Hansen, 2001) has suggested another possible process: the movement of dust condensation nuclei from the centre of newly fallen snow grains (where they are largely optically hidden) to grain boundaries (where they are fully optically active). This process was suggested by the modelling of low-emissivity spots in which the CO_2 ice grain size is little different from, while the apparent dust content is much smaller than in the surrounding regions. The seasonal polar caps of Mars are composed primarily of solid CO_2, likely mixed with some micron-sized Martian dust and water ice. Many of these dust and water ice grains may be brought in as condensation nuclei for CO_2 snow grains. In Hansen 2001, each TES spectra from revolution 214 has been analyzed by fitting to model spectra of ternary CO_2-H_2O-dust intimate mixtures, including partial spatial coverage, surface temperatures, and water ice clouds. The results of this analysis show that the central polar cap is 100% covered by CO_2 deposits, and that the temperature usually varies as expected (as a function of altitude). Nevertheless, several low-emissivity regions in the central polar cap has been found, normally indicated by a large brightness temperature difference between 25 and 18 μm.

A detail of the brightness temperature difference, CO_2 grain size, and dust mass mixing ratio over one of these regions is shown in figure 1.7.

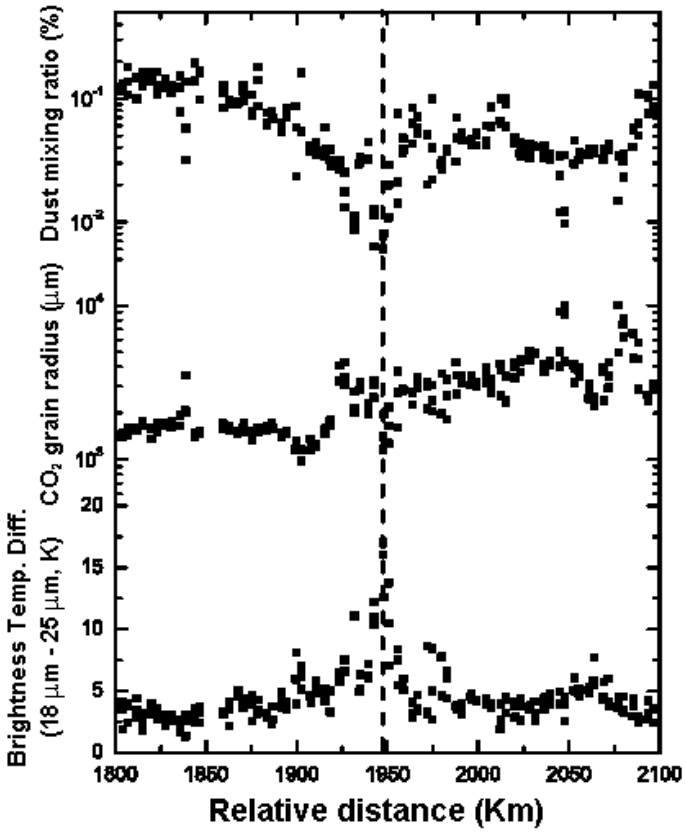

Fig. 1.7 Brightness temperature difference, CO_2 grain size, and dust mass mixing ratio over one of the low-emissivity regions (figure from Hansen, 2003a).

The typical behaviour shown here is that the large brightness temperature difference is reflected mostly in the dust mixing ratio, and not the CO_2 grain size, as has been assumed previously (Hansen, 1999; Titus et al., 2001). This observation suggests a different process

for the temporal and spatial variation of low-emissivity regions. These regions are most likely initiated by fresh CO_2 snowfall from atmospheric dynamic interactions with topographic obstacles. If the CO_2 grains are formed around dust condensation nuclei, the optical properties of the dust are subdued or absent (depending on the ratio of grain size to nucleus size). If the dust nuclei subsequently migrate to the grain boundaries as the deposit matures, the optical effect of the dust will approach the intimate mixing formulation of the models. The effective CO_2 grain size may not change significantly as it matures.

The condensing south polar cap has been extensively studied in this thesis (Section 7.3). Our results show that CO_2 snowfall are likely to occur in the polar night during the fall and winter season, making the carbon dioxide ice clouds and snow explanation given in subparagraph 1.3.2.2.2 the most favourable one. The results have been submitted to *Icarus*.

1.3.3 The subliming Martian polar caps

1.3.3.1 Energy balance of the subliming and residual polar caps

Similarly to the condensation rate, the sublimation rate of the CO_2 ice
frost is controlled by the energy balance of the polar regions. However, the sublimation phase is different since it only occurs at the polar cap surface. To first order, equation 1.1 in subsection 1.2.1 remains valid, although the subliming rate C_{CO_2} will be negative. The net solar flux $(1-A)F_{solar}^{\downarrow}$ solar is of course no longer negligible.

Insolation: The radiative fluxes during the spring and summer seasons are much stronger than during the winter. Therefore, the mass exchange during the sublimation phase is controlled by the local radiative balance. $F_{solar}^{\downarrow}$ is now the key parameter of this balance. It primarily depends upon the local incidence angle, which in turn depends upon the solar longitude Ls and the latitude (and locally upon the local slope). Because of the large eccentricity of the Martian orbit, the maximum flux $F_{solar}^{\downarrow}$ at the south pole at summer solstice is 1.5 times higher than at the north pole. The planetary albedo *A* is clearly a crucial parameter of the radiative balance. It is highly variable in space and time and its variations are not very well understood. The frost albedo issue is reviewed in the next subsection.

Atmospheric radiative effect: Both $(1-A)F_{solar}^{\downarrow}$ and $F_{IR}^{\uparrow}$ may be affected by the presence of dust or water clouds in the spring and summer atmosphere. Airborne dust has a non trivial impact on the sublimation rate at sunlit latitudes. On the one hand, it decreases the amount of solar radiation reaching the surface by scattering and absorbing at visible wavelengths. On the other hand, it increases the downward infrared fluxes because it raises the atmospheric emissivity and warms the atmosphere by absorbing the solar radiation. In equation 1.1, it raises $F_{IR}^{\uparrow}$, but it is likely to decrease the planetary albedo *A* if the surface albedo is high enough, as is expected on the polar caps. To first order, these

competing radiative effects cancel one another during the spring season, although dust should slightly reduce the total radiative flux at the surface and thus the sublimation rate during the cap recession (Davies, 1979; Lindner, 1990). However, Pollack et al. (1990) found that the net effect of enhanced dust loading may be a slight increase of the sublimation rate because it enhances the atmospheric heat transport into the polar cap regions. The impact of water ice clouds is also not simple. Lindner (1990) showed that clouds usually reduce the net radiation flux which strikes the surface except for low solar incidence angle, a common situation at polar latitudes. The cloud could then scatter the solar flux down to the surface and increase the surface illumination.

Atmospheric heat advection: The atmospheric heat advection *Adv* has been studied theoretically with atmospheric models which have shown that it should play a much smaller role during the cap recession than during the condensation phase (Pollack et al., 1990; Hourdin et al., 1995). In fact, this is due to the much stronger intensities of the radiative fluxes during the spring and summer seasons.

Subsurface heat conduction: During the sublimation phase, the surface CO_2 frost remains at a temperature similar to the fall and winter temperatures. Not much heat should be left stored in the ground. Thus, the subsurface heat conduction *Cond* is likely to remain positive and very small on average. (Paige and Ingersoll, 1985). However, it could be non negligible locally near the cap edge when contiguous regions are uncovered and warmed by the sun.

Energy balance of the residual south polar cap: During the year of Viking and Mariner 9 observations, CO_2 frost was stable at the south residual cap throughout the year, but was not stable at the north residual cap. This difference occurred in spite of the fact that both poles receive the same amount of annual insolation, and despite the higher elevation of the south residual polar cap compared to the northern cap, which should thus be more stable (the lower polar cap radiates more energy in the infrared be cause its pressure and thus its frost temperature is higher). Most theoretical models simulating the energy balance of the polar caps have been unable to preserve CO_2 ice at the south pole and still obtain agreement with other observations.

Paige and Ingersoll (1985) used the solar reflectance and infrared emission measurements obtained by the Viking IRTM to study the radiative balance of the residual polar cap areas. They calculated the annual radiative budgets and infer the annual CO_2 frost budgets. They confirmed the stability of the CO_2 frost near the south pole and showed that the north-south difference was due to very asymmetric behaviour during the spring sublimation phase. The CO_2 sublimation rates were then much smaller in the south than in the north, and this was due to the higher albedo of the south residual cap relative to the north cap. This difference in albedo, added to the difference in subsurface heat conduction - which is rather high on the residual north cap and close to zero on the south residual CO_2 cap where the temperature is constant all year long (Jakosky and Haberle, 1990) - explains why the north and south residual polar caps are so different.

1.3.3.2 Spectral albedo of CO2 ice

The albedo of the Martian polar caps is characterized by strong spatial and temporal variations. Getting quantitative measurements and understanding the process which control these variations is crucial for energy balance considerations and to explain the caps appearance. The radiative properties of pure CO_2 ice were reviewed by Warren (1986) and, more recently, by Hansen (1997a), and Hansen (1999). Warren et al. (1990) used a model originally developed for terrestrial snow (see paragraph 6.2.1.1) to study the theoretical behavior of the CO_2 frost albedo. Pure CO_2 frost was calculated to have a high albedo at visible wavelengths, strongly decreasing with grain size (e.g. ~ 0.8, 0.6 and 0.4 for grain radii of 0.1 mm, 0.5 mm and 2.0 mm). Dust contamination should lower the albedo whereas H_2O ice contamination should only increase it slightly.

Spacecraft or telescopic observations of the Martian frost albedo are made difficult by the presence of dust or clouds in the atmosphere. Even small optical depths of dust could significantly lower the planetary albedo over a bright surface (Davies, 1979). Several authors have published measurements of the polar caps reflectivity from telescopic observations (Dollfus, 1965; Lumme, 1976; Lumme and James 1984; James et al., 1994). Unfortunately, because of the very limited viewing geometries for the caps as seen from Earth, estimating a reliable albedo suitable for heat balance calculation (i.e. hemispherical albedo) is very difficult and model dependent. Lumme and James (1984) estimates for the south cap in 1971 gave 0.64 at 360 nm (uv filter) and about 0.79 at 620 nm (red). Observations of the spring north polar cap with the Hubble Space Telescope gave values of 0.12-0.15 at 230-330 nm (uv), 0.34 at 413 nm (violet), 0.47 at 502 nm (green), and 0.73 at 673 nm (red) (James et al., 1994). Similarly, Viking images were obtained through various filters and only included a limited range of viewing geometry. Photometric estimations for the bright portions of the seasonal polar cap led to albedoes of 0.55-0.6 at 590 nm (red) and 0.36-0.38 at 440 nm (violet) (James et al., 1979). These observations show that the Martian polar caps are reddish rather than white as would be expected for pure CO_2 or H_2O snow. This could be due to “red” dust contamination or maybe to the relative transparencies of the CO_2 frost layer so that the ground color is “viewed” through the frost (see section 1.4). James et al. (1979) found that the albedo of the residual south cap area was less dependent on wavelength (and usually higher than its surrounding).

The IRTM instrument aboard the Viking Orbiters made some calibrated, broadband (0.3 - 3 μm), solar reflectance measurements. The data obtained in the vicinity of both residual caps were studied in detail by Paige and Ingersoll (1985) and Paige (1985). In particular, they calculated the planetary albedo of these regions, and, using simple models, inferred the frost surface albedo. They found that it was approximately 25 percent lower in the north than in the south, and that it strongly varied through the summer, appearing to be nearly a linear function of insolation during this time. The difference between the south and north spring residual cap albedo is usually attributed to a difference in dust contamination, linked with the seasonal dust cycle (Paige and Ingersoll, 1985). However, it could be explained by Mars being closer to the sun during the southern spring and summer seasons.

The fact that the albedo could be an increasing function of insolation is not expected since it is the opposite of the relation for terrestrial frosts. In fact, the microphysical processes which control a CO_2 ice cap in vapor pressure equilibrium with the atmosphere are likely to be very different than on Earth. For instance, radiation incident on dust grains

imbedded in a CO_2 frost will heat up the grains because of their low albedo. The solid CO_2 supporting the grain will sublime and the grain will sink into the frost or float away in the sublimation gas flow (Paige, 1985; James et al., 1992). With such a process, the more insolation strikes the frost, the deeper the grains get, the brighter the surface becomes. Another specific process could be related to the fact that CO_2 ice is relatively "transparent" in the visible, more than in the thermal infrared (Warren et al., 1986). Thus, the sunlight could be absorbed below the cap surface, deeper than where the infrared emission is emitted ("greenhouse effect"). Because the frost must be isothermal, the net energy balance will favor sublimation at the depth where the insolation is absorbed and the condensation nearer the surface where the infrared radiation is emitted. A strong insolation could result in the growth of pristine, high albedo frost deposits over a bulk deposit which would actually experience net sublimation.

The seasonal south polar cap solar reflectance IRTM data were also discussed by Kieffer (1979) and are currently being reanalyzed by Ono and Paige (1995). Kieffer (1979) did not calculate hemispherical albedo but analyzed solar reflectances in term of Lambert albedo (reflectance normalized to that expected from an ideal diffuse white horizontal surface). In early spring, the Lambert albedo was found to decrease from ~ 0.5 near the cap edge to ~ 0.35 at -80° latitude, before raising again in the residual cap area. Here again, a possible explanation for this annular structure could be a coupling between albedo and insolation.

High-resolution calculation of CO_2 reflectance spectra will be presented throughout Chapter 7. By using different multiple scattering solutions for angular reflectance described in Section 6.2 we are able to compute synthetic spectra of CO_2 ice and study the effect of water ice and dust contamination, as well as of the lighting geometry and snowpack thickness, and to reproduce the observed spectra. The high spectral resolution of PFS (see Chapters 2 and 3) allow to resolve many of the narrow absorption lines of the solid carbon dioxide, which are very diagnostic of many of the CO_2 ice properties (see Chapter 4).

1.3.3.3 Spacecraft and telescopic observations

1.3.3.3.1 North polar cap

The spring north polar cap has not been observed in detail for several reasons. First, the north polar hood clouds usually shroud the high northern latitudes during the first part of the spring. Second, only limited synoptic imaging by spacecraft is available, since spacecraft orbits imposed a limited areal coverage for Viking Orbiter 2 and undesirably large emission angles for Orbiter 1. Third, terrestrial observations must be acquired during aphelic oppositions when Mars is relatively small in diameter.

Nevertheless, there have been many studies focusing on the shape of the cap during recession and on the latitude of the cap edge. These include spacecraft visual imaging data (James, 1979; James, 1982), infrared data (Christensen and Zurek, 1984) and telescopic data (see publications by Iwisaki et al., 1982; James et al., 1987; James et al., 1994). These observations indicate that during its recession, the north polar cap remains roughly circular and centered on the geographic pole. The cap edge usually "pauses"' during at least

60 Martian days at about 65° latitude during mid-spring (from roughly Ls = 20° to Ls = 50°). Interestingly enough, water ice clouds seem to be absent during the "standstill" but reappear when the recession resumes, suggesting that they are associated with water vapor released at the edge of the cap (James et al., 1987). By the beginning of the summer, the CO_2 north polar cap completely sublimes exposing an underlying water ice cap which acts as a source for atmospheric water vapor.

In section 7.4 we present the first comprehensive study of the north polar cap in mid-spring. Our results have been published in the scientific journal *Planetary and Space Science* (Giuranna *et al.*, 2007b); the paper is available in the Appendix of this book, Section A.5.

1.3.3.3.2 South polar cap

Since the south pole is tilted toward Earth during favorable oppositions, there are relatively high quality data from terrestrial observations for the subliming south polar cap. Moreover, the 1977 spring and summer south polar cap of Mars was monitored in detail by Viking Orbiter 2 (James et al., 1979; Thomas et al., 1979) and the 1972 summer cap by Mariner 9. An example is shown in Figure 1.5.

During the first part of the spring (until Ls ≅ 240°), the perimeter of the cap is roughly circular and centered on the pole. The cap seems to have an annular structure with a bright periphery surrounding a darker ring which itself encircles a very bright central area: the residual cap, which can almost be distinguished "through" the seasonal frost. The annular structure seems to persist as the cap recedes, suggesting that resurfacing is involved (see subsection 1.3.2 about CO_2 frost albedo). During the second part of the spring, the frost between 160° and 300° longitude rapidly sublimes, leading to a very asymmetric cap which, by southern summer solstice, results in a cap center displaced by 6.5° from the geographic pole.

After summer solstice, the cap keeps on shrinking slowly and by mid-summer remains a relatively small residual cap (Fig. 1.8).

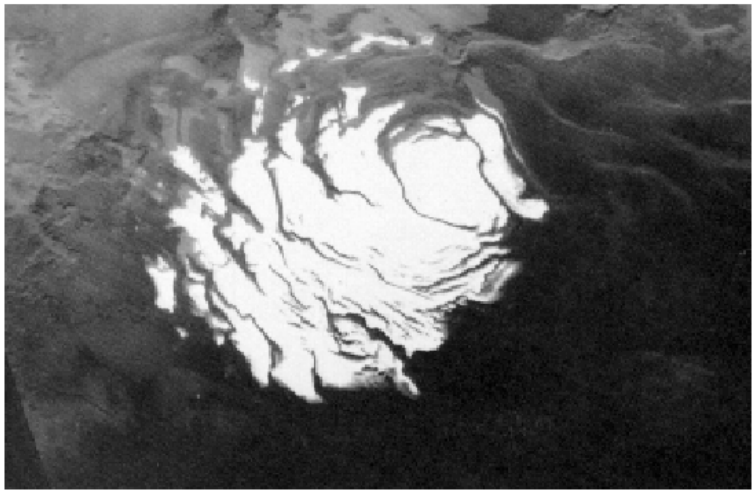

Fig. 1.8 The south residual cap observed by Viking (Ls = 341°). It is approximately 400 km accross. The frost outlier at the top of the picture survived the Viking year but not the year of Mariner 9. (James et al., 1979).

Then most of the changes are in detail rather than in the area covered by ice. Both Mariner 9 (Paige et al., 1990b) and Viking (Kieffer, 1979) thermal infrared observations showed that, at least in 1971 and 1977, carbon dioxide survived all year long on the south residual cap. This behavior is surprisingly different from what has been observed in the north where CO_2 completely sublimes by the beginning of summer. Such a difference cannot be explained straightforwardly by the orbital asymmetry or a topographic difference. It is a major Martian curiosity which is addressed in subsection 1.3.3.1.

In this thesis, the condensing CO_2 Martian south polar cap and the mechanisms of the CO_2 ice accumulation has been studied through the analysis of the PFS-MEX spectra acquired during the first two years of activity. Our work provides new insights in the explanation of the residual south polar cap asymmetry proposed by Colaprete et al. (2005). The results are presented in Section 7.3.

1.3.3.3.3 Near Infrared Observations

Telescopic and spacecraft near-infrared spectral observations have confirmed that the seasonal caps are mainly composed of CO_2. The Mariner 7 infrared spectrometer experiment first provided some spectroscopic evidence: Herr and Pimentel (1969) identified two diagnostic absorptions near 3.0 and 3.3 μm and cautiously concluded that a solid CO_2 composition “must be preferred". Later, Kieffer (1970b) pointed out that absorptions at 2.28 and 2.34 μm were characteristic of spin forbidden transitions in solid CO_2 but the features were not identified in the Mariner 7 data until 1974 (Pimentel et al., 1974). Meanwhile, using an Earth-based high-spectral resolution Fourier spectrometer, Larson and Fink (1972) confirmed the CO_2 identification based upon 11 absorption features including the 2.28 and 2.34 mm transitions and other features near 1.2, 1.5-1.65 and 2.05 μm (Figure 1.1). Water ice was also observed on or above (clouds) the north polar ice cap, although interpreting these observations appears not to be straightforward (Kieffer, 1970a; Clark and McCord, 1982; Jakosky, 1983; Bell and Crisp, 1993).

Unfortunately, besides the data obtained during the Mariner 7 flyby of Mars in 1969, no spacecraft data are available since neither Viking nor Mariner 9 carried a near infrared spectrometer and since Phobos 2 did not observe the high Martian latitudes. Mariner 7 provided 25 spectra of the early spring south polar cap (Ls = 200°) using wavelengths from 1.9 to 14.4 μm (Herr and Pimentel, 1969). This dataset was recently reanalyzed by Calvin (1990) and Calvin and Martin (1994). Using the accurate optical constants for solid CO_2 measured by Hansen (1992), Calvin and Martin (1994) modeled the spatial variability of CO_2 grain size and water ice abundance. They discussed in detail the 2.28 and 2.34 μm features and their implications for the surface physical properties. They estimated that there was very little dust and some water ice at the level of a few parts per thousand. Equivalent grain sizes in simulated ices were surprisingly large, on the order of millimeters to several centimeters. Spatial variations were observed. They are described in Figure 1.9.

Thanks to PFS, it is finally possible to acquire high-resolution spectra of the Martian polar caps in the Near Infrared (see, e.g., Figure 4.1).

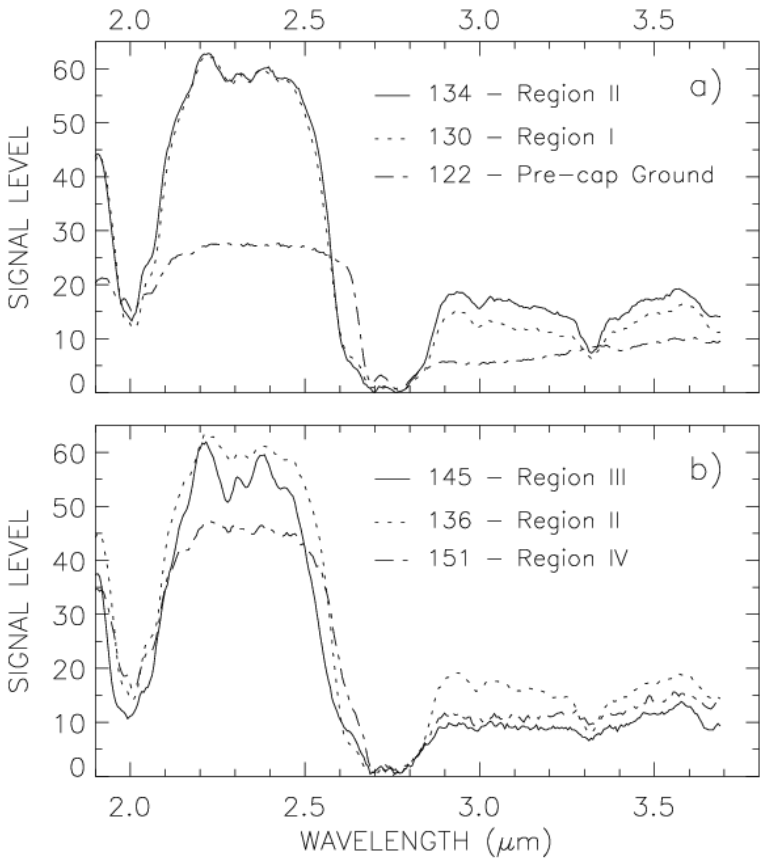

Fig. 1.9 Selected spring south polar cap spectra measured by Mariner 7 (Ls = 200°). Region I is at the cap edge, where there is enhanced water ice absorption beyond 3 μm, inferred to be caused by increased sublimation rates. Region II is the typical cap interior. Region III is an anomalous region discovered near South Crater. Its unique spectral characteristics could be caused by increased path length in the CO_2 ice but theoretical models are unable to accurately reproduce the spectrum. Region IV is an area of thinning frost coverage or transparent ice well in the interior of the seasonal cap (Combination of CO_2 and ground signatures). Figure from Calvin and Martin (1994).

1.3.4 Microphysical state of the CO2 frost

Both thermal infrared (Forget et al., 1995) and near infrared (Calvin and Martin, 1994) observations of the Martian polar caps suggest that the spectroscopic "grain sizes" of the spring CO_2 snow could be larger than several centimeters. The seasonal cap in spring may be more like glacier ice containing cracks and bubbles, rather than a snow pack with individual grains (Calvin and Martin, 1994). Such large textural scales have also been found for the N_2 ice deposits on Triton. Eluszkiewicz (1993) has examined the microphysical process involved in frost condensation and metamorphism. On Mars, like on Triton, the atmosphere condenses in the near absence of an inert gas and the frost temperature is nearly constant. Thus no "air bubbles" and no thermal cracking are expected. Over the winter, the Martian CO_2 snow could undergo seasonal densification and sintering into a "nonporous, polycrystalline" layer, provided freshly condensed grains are sufficiently small. Such a layer could be slightly transparent. That could explain why the southern residual cap can be distinguished when the seasonal frost is present.

As an important part of this thesis, we have determined the microphysical state and coexistence modes of the ices and dust composing the condensates of the residual south polar cap, and the seasonal north polar cap. The results are presented, respectively, in Sections 7.2 and 7.4. Our results have been published in the scientific journal *Planetary and Space Science* (Hansen *et al.*, 2005 and Giuranna *et al.*, 2007b, respectively). The paper are available in the Appendix of this book, Sections A.3 and A.5 respectively.

1.3.5 Interannual variability of the seasonal polar caps

The interannual variations in the observed seasonal polar caps could provide a measure of the degree of interannual variability within the Martian climate cycle. In particular, we have shown that the presence of dust and water ice is expected to affect the condensation and the sublimation phase of the caps through impact on the radiative properties of both the atmosphere and the cap surface, on the atmospheric circulation, and on the formation of CO_2 clouds and snow. Both the dust and the water cycle are thought to be highly variable from year to year on Mars. For instance, global dust storms such as the ones observed during the first Viking year do not occur every Martian year (Zurek and Martin, 1993) and in particular no dust storms were observed during the second and third Viking year.

South Polar Cap: James et al. (1987) reviewed the interannual variability of the Martian south polar cap recession for which data from many years are available. Several regressions, particularly the fast 1956 regression, were found to differ significantly from the mean. They explored the possibility of correlations with global dust storms and suggested that regressions associated with early spring storms may be slower than those that are not. However, summer global dust storms did not appear to have any systematic effect. The Mariner 9 and Viking missions permitted a detailed comparison of the summer phase of the south cap in 1972 and 1977 (James et al., 1979). In spite of the fact that the spring regression curves were very similar, the summer cap retreat observed by Viking was slower. The general behavior in 1977 was similar to that seen by Mariner 9, but delayed by several weeks. Several icy regions, including the cap outliers, survived the Viking year but totally sublimed in 1972.

North Polar Cap: In the northern hemisphere, less reliable data are available. Slight interannual differences were reported by Iwisaki et al. (1982) and Parker et al. (1983) but better data are probably needed to fully establish the existence and pattern of interannual fluctuations (James, 1979; James et al., 1994).

Seasonal pressure variation: In spite of the theoretical and observational evidence for some interannual variability in the seasonal polar caps, the seasonal pressure variations recorded by the Viking Landers over several Martian years (Fig. 1.2) were almost perfectly repeatable (Tillman, 1988; Paige and Wood, 1992). In particular, the pressure cycle, and thus the global CO_2 cap mass, was not significantly affected by the two global dust storms of the first Viking year. (The jump in pressure observed by VL2 during its first winter was caused by a dynamical effect related to the second Viking global dust storm; Hourdin et al., 1993). This puzzling repeatability suggests that dust and dust storms may not have a strong impact on the global polar energy balance, or, more likely that this impact was not very

different during these three years. Except for the fact that no global dust storm occurred during the second Martian year, the "background" airborne dust underwent a strong seasonal cycle comparable to the first year cycle (Colburn et al., 1989). Another - fascinating - explanation would be that the Martian CO_2 cycle is regulated by feedbacks which are still unknown.

1.3.6 Permanent CO_2 ice deposits

It has been shown that the residual south polar cap was covered by CO_2 ice at least when it was observed by spacecraft in 1972 and 1977 (Paige et al., 1990b; Kieffer, 1979).

The existence of large amount of permanent CO_2 ice on Mars would have great significance for the Martian climate: if CO_2 ice remains at the pole all year long, the mean annual atmospheric pressure is controlled through vapor-pressure equilibrium by the mean annual CO_2 ice temperature, which, in turn, mainly depends upon the radiative balance of the polar region (Leighton and Murray, 1966). Such permanent CO_2 deposit would thus buffer or regulate the atmospheric pressure in response to changes in orbital parameters, especially obliquity, since the average insolation at the pole is proportional to the sine of the obliquity (see review by Kieffer and Zent, 1992). Recent calculations of the Martian obliquity suggest that it varies chaotically, ranging from about 0° to 60° in about 10^7 years (Laskar and Robutels, 1993). In theory, at low obliquities, a lower annual polar insolation results in an increase in permanent frost at the pole and a decrease in atmospheric CO_2 (Ward et al., 1974). The system reaches a stable balance so that every year, the amount of CO_2 which condenses during the polar night is equal to the amount of CO_2 which sublimes during the sunlit seasons. Within this context, it is theoretically unlikely that both poles can keep a year round covering of CO_2 frost (Jakosky et al., 1993). That would require both polar caps to have just the right combinations of albedo, emissivity, radiation temperatures, etc. to perfectly balance each other. One cap will be favored at the expense of the other. For example, if albedo and emissivity are the same, CO_2 frost will move preferentially to the lower cap, with a time scale much shorter than the orbital oscillations (Jakosky et al., 1993). When the obliquity is high, the polar insolation can be too high to allow a limited cap + atmosphere CO_2 budget to keep both permanent CO_2 ice deposits at one pole and the corresponding high atmospheric pressure.

The current situation fits rather well within these theoretical considerations, which explains why there is a small permanent CO_2 ice cap at the south pole and not at the north pole. The fact that the south pole is currently favored is surprising at first glance because the south pole is higher than the north pole. This could be explained by the orbital eccentricity which affects the polar energy balance through seasonal asymmetries in insolation and airborne dust which in turn are thought to create the strong north-south polar albedo difference.

However, the capacity of a small south residual cap to actually buffer the Martian atmosphere depends on the amount of CO_2 currently stored in the south residual cap, which is unknown. It is a relatively small area and its thickness has not been estimated. A thickness of 1 to 100 m would correspond to 0.6 % to 60 % of the current atmospheric mass (Kieffer and Zent, 1992). This thickness could be variable from year to year. Comparison of 1972 (Mariner 9) and 1977 (Viking) images of the summer southern cap

shows that the residual cap grew during this period (James, 1979). Besides, there is a possibility that CO_2 ice does not always survive at the south pole during summer. In particular, Earth-based measurements made in 1969 showed a factor of 6 more water during late southern hemisphere summer that was seen by Viking. Jakosky and Barker (1984) suggested that the south cap lost its CO_2 ice coverage exposing an underlying water ice residual cap similar to the northern one (the presence of a water-ice cap underlying the CO_2 frost at the south pole is expected because the CO_2 ice acts as a cold trap for H_2O). However, alternative explanations exist. Rizk et al. (1995) computed that year-to-year variations in the amount of dust in the atmosphere could causes changes in the atmospheric dynamics and water vapor transport sufficient to explain the 1969 measurements.

Jakosky and Haberle (1990) modeled that the south cap could theoretically take two stable configurations at the current epoch: CO_2 frost can survive all year long, or sublime in early summer like in the northern hemisphere. The difference depends on the role of subsurface heat conduction: if the cap was exposed the previous year, conducted energy will cause less CO_2 frost to condense in winter, and the frost will disappear completely in summer; if the cap was covered the previous year, there will be no conducted energy, and it will stay covered again. Interannual variations affecting the local energy balance (see subsections 1.2.1 and 1.3.1) could cause the cap to jump from one stable state to the other (Jakosky and Haberle, 1990).

The fact that the current permanent CO_2 cap could be small, thin or even absent some years suggests that the current Martian system is precisely at the limit between the low obliquity and the high obliquity scenarios described above. Could this be fortuitous? Jakosky and Haberle's results suggest that the jump between the permanent cap state to the other can occur for a wide range of cap + atmosphere CO_2 budget; therefore the range of obliquity during which both states may be found could be quite large, and thus the current situation is not that exceptional. In spite of the Jakosky and Barker (1984) observations, the possibility that a large amount of CO_2 ice (a reservoir from an earlier epoch) is currently being uncovered at the south pole cannot be ruled out. Future observations, such as measurements by gamma ray and neutron spectrometers will provide indications of the thickness of the CO_2 frost. Radar experiments recently performed from Earth by Butler et al. (1995) found a unique, highly reflective feature with a polarization inversion associated with the residual south cap, and no features associated with the north residual cap. Although the radar observations cannot tell if one is composed of thick CO_2 or H_2O, they concluded that such a difference was probably due to fundamental differences in the structure and/or composition (amount of cracks, voids, dust contaminants).

Other permanent CO_2 ice reservoirs could exist on Mars and contribute to the CO_2 cycle on long timescales. First, a large amount of CO_2 ice may be adsorbed in the regolith of the planet (see review in Kieffer and Zent, 1992) . If so, such a reservoir could buffer the entire atmosphere plus cap system, and could explain why the current CO_2 inventory is so close to the limit between permanent and non permanent CO_2 ice caps. Second, Jakosky et al. (1995) have suggested that large amounts of CO_2 ice (or CO_2-H_2O clathrate hydrate) could be buried beneath the water ice cap at both poles. If true, it would mean that the Martian climate could fluctuate wildly with the obliquity cycle (Haberle 1995).

2 THE PFS EXPERIMENT

The scientific results presented in this work has been achieved mainly through the analysis of PFS data. This chapter presents the main characteristics of the Planetary Fourier Spectrometer (PFS) experiment. PFS is one of the instruments included in the scientific payload of Mars Express (MEX) mission to Mars. It was designed and manufactured in IFSI – CNR (now INAF) under the coordination of the principal investigator V. Formisano (Formisano et al., 1997 and 2005). The concept of the experiment is based on a previous instrument developed jointly by IFSI – CNR and IKI, flown on the lost mission Mars96. Very detailed information is available in the PFS technical documentation (Formisano and the PFS team, 2004).

2.1 General instrumental set-up

PFS is basically an interferometer. A complete description of this kind of instruments can be found in Hanel et al., 1992. Fig. 2.1 shows the optical design of the instrument.

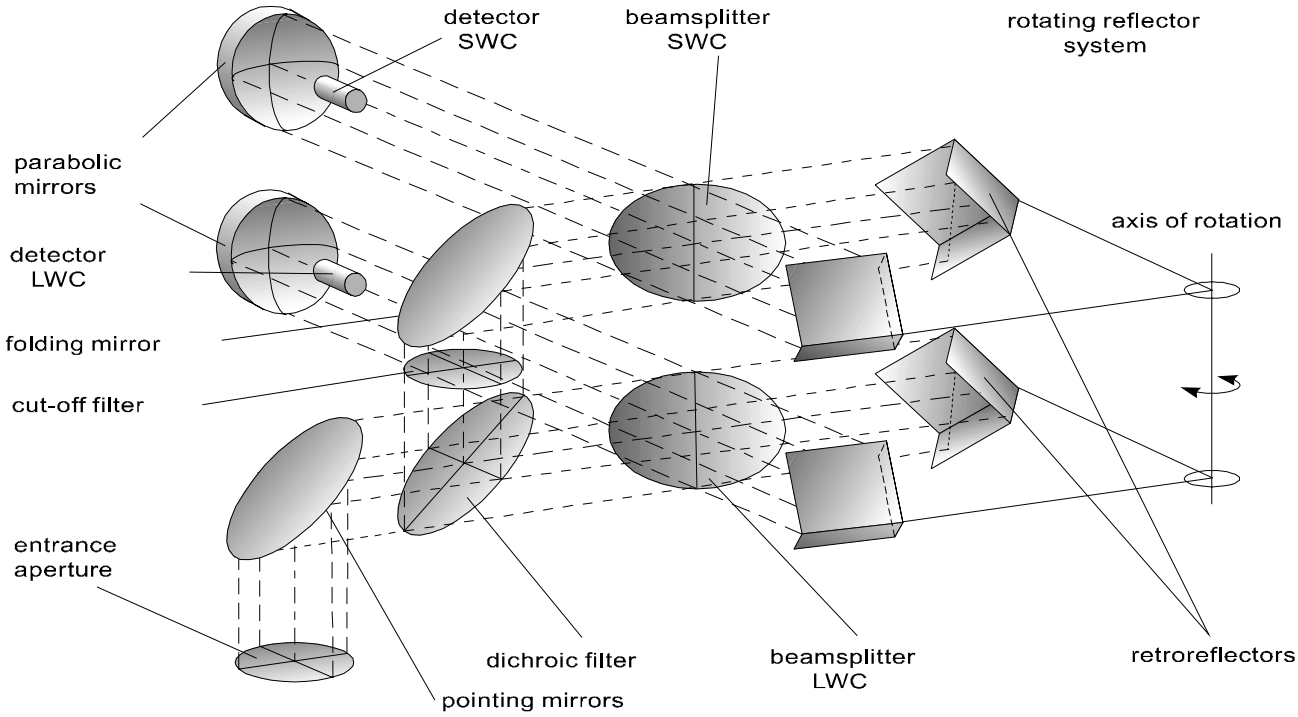

Fig. 2.1 Optical scheme of PFS instrument.

The incoming Martian radiation (with radiance $I_{\nu,Mars}$) is divided, depending on the wavenumber ν, in two main channels by a dichroic filter. These two channels are referred

hereon as long wavelength channel (LWC) and short wavelength channel (SWC). The radiation inside each channel is further divided by a beamsplitter in two beams and redirected toward a couple of retro-reflectors fixed at the ends of the arms of a rigid double pendulum. The rotation of the double pendulum around its axis determines a δ difference in the optical path of the two beams. This difference is two times the shift of each retro-reflector with respect to the beamsplitter. This design allows therefore a much more compact design compared to traditional interferometers (see, e.g., Hanel et al., 1972). The two beams interfere each other, producing at the detector a variable component of the signal given by:

$$i(\delta) = \int_0^\infty R(\nu)\left(I(\nu)_{\text{Mars}} - I(\nu)_{\text{instrument}}\right)e^{i(2\pi\delta\nu)}d\nu \tag{2.1}$$

where $I(\nu)_{\text{instrument}}$ is the thermal self-emission of the instrument and $R(\nu)$ a responsivity factor, that accounts for optical, detector and electronic efficiencies at each wavenumber. A constant term (not depending on δ) also exists, but it is subtracted from output signal by a capacitor in the read-out electronics. The term inside parenthesis in Eq. (2.1) is the net energy gain/loss experienced by the detector in an infinitesimal wavenumber interval, i.e.: the actual signal as seen by the instrument point. The function $i(\delta)$ is referred as interferogram: Eq. (2.1) demonstrates that its Fourier transform allows to recover $I(\nu)$ once $R(\nu)$ is known. In ideal conditions an interferogram is symmetric around $\delta = 0$, therefore its Fourier transform is real and equivalent to the uncalibrated spectrum $R(\nu)I(\nu)$, with a zero imaginary part. Real interferograms are not symmetric and must be symmetrized prior to Fourier transform, according procedures described, for example, by Forman et al., 1966.

Due to the limited number of points where the interferogram can be sampled, the basic theory of Fourier discrete transform demonstrates that the resulting spectrum is limited in its resolution as well as in its range. Namely, being $d\delta$ and $\Delta\delta$ the sampling step of the interferogram and the maximum optical difference sampled, it can be shown that the maximum spectral range covered $\nu_{\max}$ is given by

$$\nu_{\max} = \frac{1}{d\delta} \tag{2.2}$$

and the spectral resolution $d\nu$ is limited according:

$$d\nu \propto \frac{1}{\Delta\delta} \tag{2.3}$$

Defining the spectral resolution as the FWHM of the transfer function of each sampling point in the resulting spectrum, the proportionality constant of equation (2.3) varies according the apodization mask applied to the interferogram to reduce aliasing phenomena[1].

The sampling of the interferometer is carefully controlled in PFS. Two laser diodes (one per channel) emit monochromatic radiations that experience the same optical path of Martian radiation. Devoted detectors (not shown in Fig. 2.1) measure the intensity of the resulting sinusoidal interferogram, and command the sampling of scientific channels after a fixed number of zero-crossings in the reference one.

[1] Apodization consists in a numerical mask applied to measured interferogram prior to Fourier transform. Numerical filter leaves the interferogram unchanged in its central parts, while tends to nullify it at the boundaries. This procedure avoids very sharp spurious features in the resulting spectrum (Fourier components of a step function).

2.2 Resolution, transfer function and spectral range

Due to its compact design PFS allows the sampling of a very wide range of optical differences. This results in a sampling step of the spectrum equal to 1.0 cm^{-1} for both channels in nominal operative conditions. During the calibration campaign, measurements of the response function of the single sampling point in the spectrum were possible, confirming, for unapodized spectra, the expected sinc shape and a value of 1.3 cm^{-1} for spectral resolution. The measured transfer function, both with and without apodization, is shown in figure 2.2.

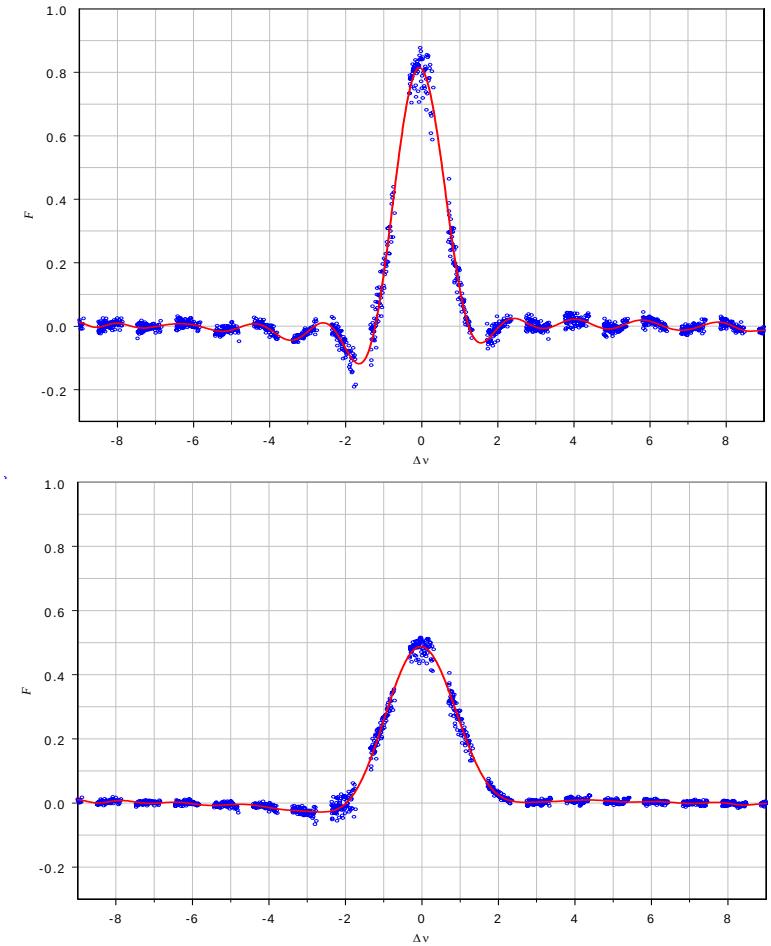

Fig. 2.2 Simulated (*red*) and measured (*blue*) monochromatic transfer function of PFS, without (*top*) and with (*bottom*) apodization (Hamming function).

In each channel the spectral range is limited by Eq. (2.2) as well as by the behavior of R_ν that in some spectral regions reduces the signal orders of magnitude below the noise. Calibration measurements allow to evaluate the responsivity of the instrument (see Chapter 3) and to fix the indicative spectral ranges of [250 ÷ 1750] cm^{-1} for LWC and [2000 ÷ 8200] cm^{-1} for SWC. The ranges of the two channels correspond approximately to spectral regions dominated by thermal emission and solar reflection respectively.

2.3 Field of view

PFS fields of view (FOV) for both channels were determined during the calibration campaign. The outputs of the instrument produced by a constant source were measured by

varying the direction of the incoming beam. The FWHM of the resulting functions allow to define unambiguously the fields of view. The LWC has a field of view of 2.77° degrees, while SWC has a smaller one, being only 1.57° wide. The two channels are not perfectly co-aligned, but are largely overlapping (figure 2.3).

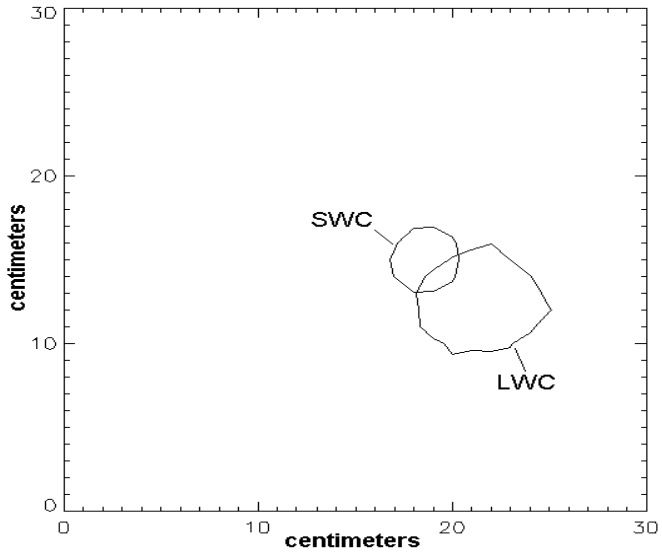

Fig. 2.3 FWHM for both PFS channels: 1.57° for the SWC, 2.77° for the LWC. The two channels overlap only partially, the distance between the two centers being ~ 1.8°.

These FOV values would correspond to a size of the footprints on the Martian surface of 7.1 km and 12.6 km at the pericenter (260 km). PFS can not compensate for the motion of the spacecraft during data acquisition. Considering that each measure will take about 6 seconds, the resulting smearing of the image will produce elongated footprints of 7.1 x 22.5 km and 12.6 x 27.5 km at the pericenter.

PFS will acquire at Mars almost latitudinal tracks of spot observations. Footprints of different measurements will not overlap at the pericenter, due to the time spacing of 10 sec between the beginning of consecutive measurements. Therefore, it is not possible in these conditions to reconstruct, for instance, the surface albedo at sub-pixel resolution. In theory, this would be possible for measurements acquired at higher altitudes. In the context of this work, it is important to stress that for our analysis we will NOT assume that the surface physical conditions inside a footprints are homogeneous. Spatial mixtures of ices and uncovered soil will be kept into account and reproduces by the models. On the other hand, considering the albedo features as tracers of surface characteristic, MOC images demonstrated a variability on tenth meter scale, beyond the possibility of any remote sensing spectrometer. Therefore, it is important to remember that the retrieved quantities, even by single measurements, represent actually only an average situation inside the footprint. On the contrary, the atmospheric state is expected to vary on a greater scale than footprints, an exception is made for pressure variations related to topography.

2.4 Effects of the space environment on PFS measures

In order to minimize the number of corrupted measures and the systematic errors, the PFS design takes into account expected environmental conditions in orbit around Mars. PFS data may nevertheless be influenced by several aspects of space environment.

2.4.1 Thermal conditions

The thermal environment has a remarkable influence on PFS measurements, due to the thermal contribution by instrument parts to the effective signal measured by detectors (Eq. 2.1). This aspect will be described in the context of calibration procedure on chapter 3. From a more general point of view, PFS has four main thermal requirements. They are fulfilled mainly with a cold bias design of the instrument (in different degrees, considering different parts) and active control by electrical heaters.

1. Short Wavelength Sensor: the requirement for the SWC detector is to have a working temperature inside the range 200÷220 K. This goal is achieved by means of a passive radiator, connected to the sensor by means of an aluminum cold finger. The sensor is mounted on a three legged pure aluminum structure, connected to the cold finger by a copper braid strap and mechanically fixed to the optical bench by a thermally insulating structure made in Vespel®, having a thermal resistance higher than 500 K/W. The aluminum cold finger and the mounting thermal resistance were devised so that the Mars radiative peak power on the radiator expected at perihelion was delayed on the sensor of about 30 minutes, to allow a complete one hour session to be performed before the transient. The cold finger is MLI insulated and all the fixation structures are made in Vespel®. An electrical heater is implanted behind the sensor for temperature stabilization during the measurement session. The radiative flux on the sensor holding structure is minimized by polishing the metallic surfaces.
2. Long Wavelength Sensor: the requirements for the long wavelength sensor are less stringent for the working temperature, about 300 K, but challenging for the stability, <0.01 K/h. The sensor is mounted on an insulating Stainless Steel structure and the temperature is controlled by an electrical heater placed at its back, fed by an electronic circuit.
3. Lasers Diode: a wrong operative temperature of the diode lasers along with its fluctuations in time may cause degradation of the spectral resolution of the interferometer. The wavelength of emitted laser diode radiation, used to sample the interferogram, is a discontinuous function of temperature. Therefore a tight thermal control of the reference channel is absolutely mandatory for reliable results. The degradation is a function of power, temperature and manufacturing of the device. In PFS the two diode lasers are thermally controlled within 0.01 K. The temperature itself can be set in a wide range between 275 K up to 315 K. Dependence of resolution on laser diode temperature would imply the explicit computation of wavenumber grid for every single PFS measure (see chapter 3). Measurements acquired at anomalous laser diode temperatures (i.e.: close to discontinuity points in $\lambda_{emiss} = f(T_{laser})$ function) show spikes in the interferograms, almost randomly distributed in the optical path difference (δ) space. These spikes determine periodic deformations on the resulting spectrum, with a wavelength (in the physical space of wavenumbers!) given by

(2.4) $$\lambda_{def} = (2\pi\delta_{spike})^{-1}$$

as expected for the Fourier transform of a Dirac function.

4. Optical bench temperature control. The thermal requirement is mainly in the uniformity of the temperature; differences of the order of 2 K between the average temperatures of the brackets of the pendulum lead to a reduction of the signal-to-noise ratio (SNR) of 1%. The countermeasures implemented to avoid the critical gradients are mainly the thermal insulation from the surrounding. The interferometer module is covered with an MLI insulator and fastened to the interface plate with low conductivity bolts to reduce the influence of temperature fluctuation in the parts facing its sides i.e. the electronics box, and the external box.

In the interferometer unit there is, during operation, a dissipation of about 5 W of electrical power, mainly due to the motors of the pendulum and to the sensor' proximity electronics. The electronics box has a power consumption of about 10 W while operating. The whole optical bench is thermally insulated from the spacecraft because of the low thermal conductance of the dampers and of the MLI covering all the external surfaces. The electrical power dissipated inside the module is removed by the radiator of the SWC detector because of the heat leakage through the mountings and the radiative fluxes.

An extensive thermal analysis has been carried on using ESATAN suite (Saggin, 2001), taking into account orbital parameters, expected Sun's flux at the Martian orbit and the albedo of the planet. The total heat flux in the design configuration is about 6 W. In case the of a Martian orbit of 7.6 h period the removal of the 15 watts dissipated during the two hours of operation goes on in the following 5.6 h of sleeping mode. The resulting temperature profile for the interferometer bench shows a peak of temperature during data acquisition (with an increase of about 10 K) and a cooling down phase in the rest of the orbit. Thermal analysis demonstrated further that, during operations, control requirements on detectors and laser diodes remain satisfied. The overall thermal control design demonstrated to be effective and able to achieve the expected temperature values during thermovacuum tests of integrated MEX satellite, held in ASTRIUM facilities in autumn 2002. Preliminary analysis of data acquired during cruise phase further confirm the expected thermal behavior of the instrument.

2.4.2 Radiative conditions

Radiation effects can be quantified as radiation deposit dose. The cumulative effects of radiation can degrade the performances of the payload and possibly produce permanent damage to electronic parts. To compute the radiation deposit dose expected for PFS components, several aspects must be considered:

1. A transfer to Mars suppose crossing the Van Allen radiation belts. The Soyuz-Fregat launcher placed the S/C on the escape orbit to Mars so that the S/C crossed the radiation belts only once. The worst case radiation dose is received when crossing the South Atlantic Anomaly (SAA). The standard AE8MAX-AP8MAC trapped radiation environment models were used to assess the radiation dose level received by the S/C during this mission phase.
2. During the cruise phase (outside the Earth magnetosphere), the whole S/C is subjected to solar flares and Galactic Cosmic Rays (GCR). Solar flares are composed of high energy protons and heavy ions. A flare can last from a few hours to a few days. The computation of solar flares energy spectrum for the 4.5-years Mars mission is performed with the Feynman model.
3. Galactic Cosmic Rays are a continuous flux of high energy particles (heavy ions). The GCR spectrum can be computed for the Mars Express mission using standard NASA model (COSMIN, COSMAX models). The GCR energy spectrum is not expected to be at its maximum during the Mars Express lifetime as a maximum solar activity corresponds to a minimum GCR activity.
4. The radiation environment during scientific phase is not severe. The charged particle radiation environment of Mars is not expected to exceed the weak charged particle environment encountered during the interplanetary transfer.

Once these aspects are taken into account, it is possible to calculate the integrated radiation dose during a 4.5 year mission as a function of different thickness of surrounding shielding aluminum layers (Fig. 2.4). PFS location in the body of MEX bus can not be described extensively here. It is worth remembering that:

- The interferometer unit is protected by a minimum thickness of 10 mm of aluminum, represented by the walls of the spacecraft, the case of the optical bench, bodies of other instruments and MLI covers.
- PFS autonomous pointing system (scanner) is the most exposed part of the instrument. Electronic components of the scanner are protected by a minimum thickness of 2 mm of aluminum, while its pointing mirror is the only part of the instrument exposed directly to space during measurements.

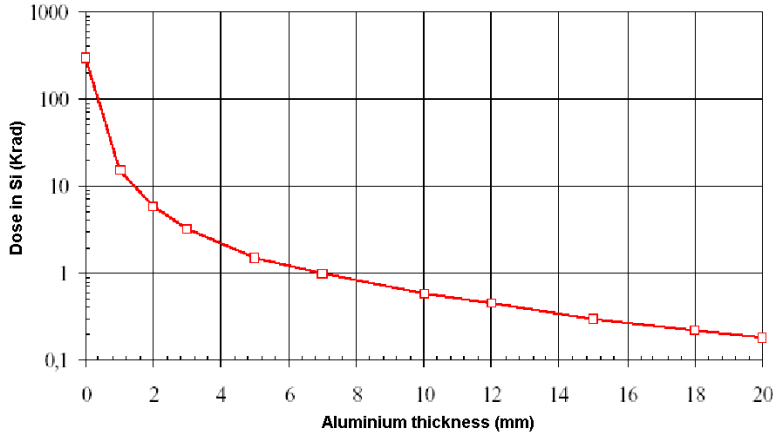

Fig. 2.4 Integrated radiation dose expected for MEX components, for different thickness of surrounding aluminum shielding. Integration time is equal to 4.5 years, i.e.: the length of nominal + extended mission (1 krad = 10 joule of energy per kilogram of mass). From Mars Express interface design document.

Radiation impinging on electronic circuits/detectors can produce, in theory, an increase of the background noise. Nevertheless, every electronic component in PFS, including detectors, are fully qualified to maintain their nominal properties up to 10 Krad. We may conclude therefore that integrated radiation effect shall have negligible impact on the behavior of the electrical components of the instrument.
The effect of radiation on the optics can be twofold:

1. A decrease of the reflectivity of gold-coated mirrors. This phenomenon may become relevant for the scanner mirror, that is consequently closed during inoperative phases. Due to the effective shielding by surrounding aluminum structures, corner cubes, parabolic and folding mirrors are less affected by this degradation. This effect has been reported for UV and visible range by Herzing et al. (1993). Their results however refer to Earth orbit environment, where atomic oxygen represents the main weathering agent.
2. A decrease of optical transmissivity of refractive elements. An extensive study of space weather effects on IR optics was presented by Hawkins (1991) in the context of LDEF mission. Even if material exposed directly to space shows substantial alterations, it has been demonstrated that their optical properties remain almost unchanged when multi-layer optical coatings are used. The shielding of refractive elements by PFS and satellite structural elements shall ensure a much more effective protection against radiation and, consequently, constant optical properties in time.

In theory, both phenomena would lead to a decrease in the responsivity function $R(\nu)$ and, consequently to a worsening of NER, detectable in its magnitude during calibration activity. However none of the previous missions to Mars reported this source of degradation (see, for example, Hanel et al., 1972, Christensen et al., 2001).

2.4.3 Meteoroids

During its journey to Mars, the Mars Express S/C encountered two different sources of dust and meteoroids: the particles coming from the asteroid belt and the particles from the comets. The former type distinguishes isotropic population of meteoroids and localized particles streams along well defined interplanetary orbits. The meteoroids fluence spectrum applicable for all instruments is given in figure 2.5.

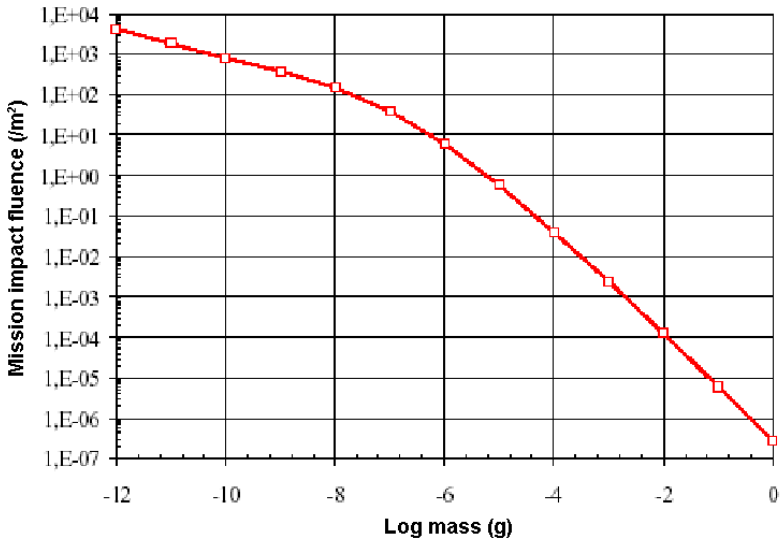

Fig. 2.5 Expected number of meteoroid impact per m² on MEX, for the whole duration of nominal + extended mission. From Mars Express interface design document.

Dust from the Martian surface should have a negligible effect. No experimental evidence exists to confirm the presence of aerosols at the expected pericenter height (260 km) and theoretical models foresee a rapid cutoff of particles concentration above 80 km even in the dustiest periods.

The mean impact velocity is about 17 km/s, and the mean particle mass density is about 0.5 g/cm³ for comet particles and about 3.5 g/cm³ for asteroid ones.

From PFS point of view, meteoroids should not represent a major issue. Scanner mirror is the only exposed part of PFS. Impact of energetic bodies at its surface may produce a reduction in reflectivity, and, for very severe events, the breaking of the optical element. The scanner mirror has an effective section of 0.02 m². Considering typical operative conditions of 2 hours over a 7.6 h periods, a further multiplicative factor of 0.005 shall be applied to values reported in y axis of figure 2.5 to get the effective impact statistic. Fluence greater than 1 is achieved only for particles lighter than 10^{-9} g, with negligible energy release. Cumulative abrasive effects on gold coating are hard to evaluate, due to lack of information on its mechanical properties. Once again, this phenomenon would induce a decrease in the responsivity function $R(\nu)$ and a related increase of NER, but no similar phenomenon has been previously reported.

2.4.4 Vibrations

Scientific payloads of Mars Express are subject to mechanical vibrations even in orbit around Mars. From this point of view, the most severe conditions are expected during orbital maneuvers, when the main engine of the S/C is used. During these periods, payload

scientific measurements are not allowed and instruments are kept in adequate safe modes. Operations of payload are also inhibited during main pointing motions which are scheduled every orbit, taking into account also adequate tranquilization times.
Mechanical disturbances can be classified in two main classes:

- Low frequency disturbances (<10 Hz), generated by the attitude control system (thrusters, not active during scientific observations).
- Microvibrations at higher frequency (>10 Hz), mainly due to the reaction wheels, and possibly to other instruments.

Both effects are expected to produce accelerations on PFS lower than 0.01 m/sec^2. PFS, as every interferometer, is very sensitive to mechanical vibrations, that determine irregularities in the motion of the double pendulum. In order to minimize these irregularities PFS optical module is fixed to the main S/C body by four dampers based on silicon rubber elements. Another potential issue is represented by the mass of corner cubes, that carry the mass center of the double pendulum far from rotation axes. The sensitivity of the instrument to acceleration transversal to the axle has been reduced by adding a balancing mass. The resulting compensation of static momentum is however limited to 50%, due to mass saving reasons.

The effects of vibrations on PFS data has been studied extensively on PFS flight model prior to launch (Comolli and Saggin, 2005; Saggin *et al.*, 2007). This work demonstrated that a periodic disturbance on the instrument produces a narrow peak in the (uncalibrated) spectrum, placed at a wavenumber directly proportional to the frequency of vibration. The main peak is also surrounded by a series of minor satellite peaks, uniformly spaced in wavenumber.
Actual effects of the external mechanical vibrations on PFS spectra have been studied and reported in Giuranna *et al.*, 2005b (see Appendix A.2). They are very similar to those predicted by Saggin *et al.*, 2007. An external mechanical vibration present on the MEX spacecraft is responsible of a non-uniform motion of the double-pendulum: time intervals between contiguous zero-crossings of the reference laser diode interferogram should be close to 250 μs for the nominal speed of the pendulum; tests performed in space always showed strong modulations around this value. The two PFS channels has a band-pass filter, whose actual range is related to the speed of the pendulum and the sampling frequency: for nominal speed, filter's frequencies are 50÷500 Hz for the LWC and 500÷2000 Hz for the SWC. The frequencies of the mechanical disturbances are some within these bands and some outside them. The effect of all the frequencies of the mechanical vibrations in the spectra may thus be seen either directly or by aliasing. Thanks to the special optical and mechanical design of the PFS, the effect of such vibrations is only to induce a fluctuation in the integration time of the measured signal which, in turn, causes an increase of the instrumental noise in special narrow bands.

As an example, in Figure 2.6 are shown the average and the standard deviation (sigma) of a set of LWC measurements acquired during the Near Earth Verification tests looking at deep space. Sigma has values between 0.06 and 0.08 DN almost everywhere. Two peaks go up to 0.4 DN (a factor 5 higher), while a smaller peak is observed going up to 0.1 DN. These peaks are at 1660 and 1880 cm^{-1}; the small peak is at 400 cm^{-1}; another peak should be present at 2180 cm^{-1}, but it's out of the LW range. This can be explained as follows: the mechanical vibrations have three fundamental frequencies, ν_1=10÷20 Hz, ν_2=105÷110 Hz, and ν_3=595÷600 Hz, modulating each other (satellites); each peak is generated by a well defined vibration and it's position in the spectrum is equivalent in frequency to the one of the mechanical vibration. Referring to figure 2.6, the first two peaks are actually aliasing from 595 Hz (ν_3) and 545 Hz respectively, the latter being a satellite of ν_3 caused by ν_2. The third peak is generated directly by the 545 Hz satellite. The small peak at 400 cm^{-1} corresponds to ν_2. The same peaks are present when looking at the internal blackbody or at

the calibration lamp with the LW channel. The effects of the external vibrations on the SWC are essentially the same as for the LWC described above, with the only difference that the positions of the peaks are different.

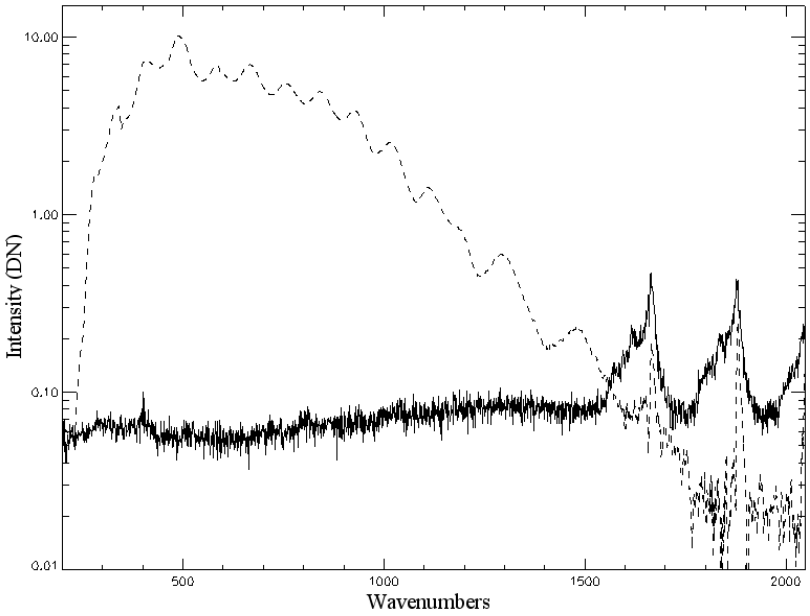

Fig. 2.6 Deep-space observation. Average uncalibrated spectrum (dashed) and sigma (line) in the LW channel (figure from Giuranna *et al.*, 2005b; see Appendix A.2).

We can evaluate where a mechanical vibration line will be directly in the IR spectra in the following way:

$$N_{dist} = f_{dist} \cdot \frac{N_{points}}{f_{samp}} \tag{2.5}$$

where f_{dist} is the frequency of the mechanical disturbance in Hertz, f_{samp} is the mean sampling frequency in Hertz, N_{points} is the number of points in the interferograms ($N_{SWC}=2^{14}$, $N_{LWC}=2^{12}$), N_{dist} is the position of the disturbance in the raw Fast Fourier Transform (FFT) of the interferogram.

It has been found that, by changing the speed of the pendulum, therefore changing band-pass frequencies range, it is possible to "move" the vibration disturbances from a portion of the spectrum to another, leaving the rest clean and uncontaminated. In fact, the position of these peaks is changing with the speed of the double pendulum: they seems to enter from right side and move toward the center of the spectral range when the speed increases; moreover, the actual intensity of the disturbances is increasing with increasing speed. The explanation is that, at low speeds, the vibration frequencies may be out of the frequency range of the channel and the disturbances present in the channel cause only a small jitter of the optical path difference increment. As a result, it is possible to repeat measurements with different speeds, in order to cover the whole LWC spectral range with a good SNR (i.e. without disturbances).

2.4.5 Contamination of the pointing-mirror

Generally speaking, several parts of the S/C may experience release of volatile molecules during the mission, due to the extreme thermal and radiative conditions encountered. This

contamination is kept low by adopting for the manufacturing adequate space qualified components. For external surfaces of MEX this value is estimated to be lower than 2 10^{-7} g/cm². PFS optical module is not affected by this contamination, being closed in a gas-tight box. Surfaces exposed include the pointing mirror, the dichroic filter and the cutoff filter of SWC. Deposition on these surfaces shall anyway be very limited because during the inoperative part of the orbit (5.6 hours), the pointing mirror is closed toward the dichroic filter, acting as a cover.

Nevertheless, it has been found that a spurious spectral feature, extending roughly from 2800 to 3000 cm^{-1}, is always present in the SWC spectra (Fig. 2.7). This feature was absent in the laboratory measurements. We have been able to trace all the experiment activity until the Launch preparation activity in Baikonour. Still in Baikonour we had spectra of the Internal Calibration Lamp without this structure, so it must have been generated during the launching itself, or immediately after in space. The contamination is found to be a hydrocarbon (or mixture); that is, the PFS pointing mirror has been contaminated by the degassing oil of the ball-bearings of the pointing mirror itself. Thus, in the 2800÷3000 cm^{-1} spectral range, the SWC spectra show the features of the stretch transitions of the CH_2 and CH_3 groups. The general shape of these bands has been verified to be essentially constant and can be corrected when generating the calibrated spectra.

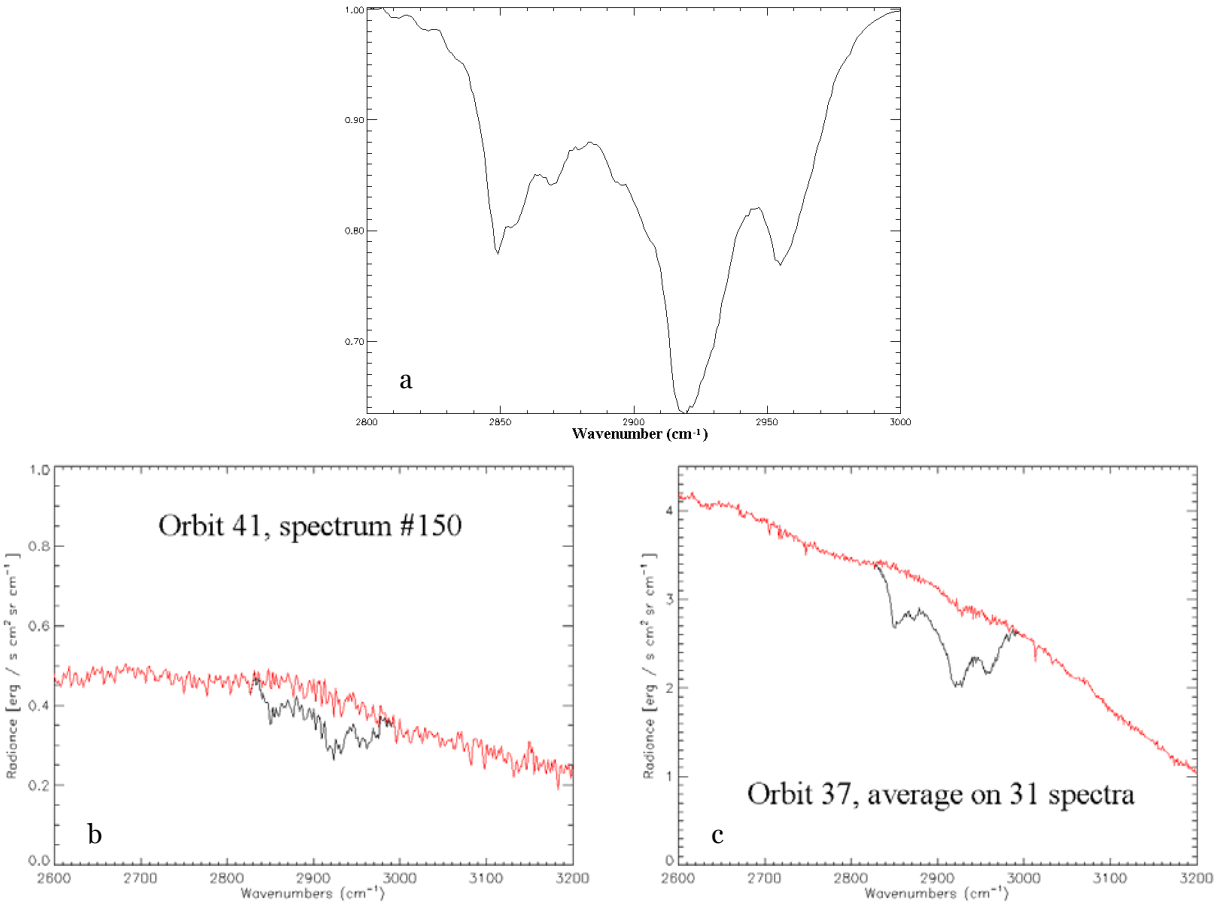

Fig. 2.7 *a*. Details of the contamination bands. *b*. Example of a single-spectrum decontamination. c. The procedure to remove the pollution is applied to an average of 31 spectra.

3 PFS SPECTRAL AND RADIOMETRIC CALIBRATION

The work reported in this thesis deals with calibrated radiances. Since the author of this thesis is also the official responsible for the PFS calibrations, and since the PFS spectra of the polar regions may have unique instrumental effects (e.g., phase inversions, see subsection 3.3.1), the calibration, the filtering of measurements on quality basis, and the removal of instrumental effects of whatever origin come not only before, but often *during* our work, as a part of it.

The calibration of a space radiometric instruments is a very complex task. Even in an accurately controlled laboratory situation, issues may arise from:

1. The lack of reliable sources: reference certified sources available on the market are very limited, especially in the thermal infrared. When available, little information is actually provided about their properties as a function of wavenumber and relative errors. Production of custom sources may often exceed money and manpower budgets.
2. Thermal environment: instruments are designed to achieve optimal performances at the thermal conditions expected in space. These conditions may be very difficult to reproduce in laboratories. Moreover, degradation of thermal control subsystem may compromise the performance and reliability of the instrument in several and often unexpected ways.
3. Unexpected behavior of instrument's components (e.g.: deviation from linearity).
4. Other disturbances from laboratory environment (namely, electro-magnetic perturbations and gases in the atmosphere).

The PFS flight unit was calibrated in IFSI facilities prior to launch. Each of the potential problems mentioned above had to be faced during this campaign. The main purposes of Earth calibrations were:

1. a preliminary assessment of instrument performance, to be used in preparatory analysis works such as this one,
2. modeling of instrument behavior, to produce suitable calibration software for scientific measurements at Mars,
3. full characterization of reference internal sources.

Namely, PFS hosts in its scanner two reference sources: a blackbody for calibration of LWC and long wavelength part of SWC and a filament lamp for the calibration of the remaining part of SWC. These two sources should allow a reliable space calibration of the instrument, able also to account for degradation of performances with time.

A detailed report of laboratory calibration campaign, as well as a description of earlier calibration procedures in space for the SWC and the LWC, can be found in Giuranna *et al.*, 2005a and 2005b, respectively, and are available in the Appendix A.1 and A.2 of this work. Nevertheless, the calibration process is in continual evolution and update, as new instrumental effects can be detected or solved, better description of the instrument achieved, thermal and statistical analysis performed, and so on. In this chapter we will

describe the latest calibration procedures adopted “at Mars” for the two PFS spectral Channels.

3.1 Basic concepts

3.1.1 Digital Numbers

Early statistical models in remote sensing often employed *digital numbers* (DNs) to estimate surface characteristic variables directly. DNs are what we get after purchasing data from the data providers. But DNs are the scaled integers from *quantization,* which is not a physical quantity. Although it might be desirable to use nonlinear quantization for low-reflectance cases such as oceanography, most quantization systems in remote sensing are linear, typically 6-12 bits. The DN can be any integer in the range

(3a) $\quad DN \in [1, 2^Q]$

where Q is an integer representing the bits. For example, an 8-bit ($Q = 8$ and $2^8 = 256$) linear quantization system equally divides the dynamic range of response of the sensor into 255 steps, from 1 to 256. The same response of the sensor will produce totally different DNs if a 10- or 12-bit quantization system is used. It is obvious that a larger Q leads to a higher radiometric precision.

3.1.2 Radiance

We now realize that DNs should be converted to physical quantities for estimating surface variables such as *radiance* (sometimes called *intensity* or *brightness),* which is defined as the amount of power at position $\vec{s}$ crossing unit area perpendicular to the direction of propagation Θ, traveling into unit solid angle about Θ, and will be denoted by $I(\vec{s},\Theta)$. The solid angle is explained in subsection 3.1.3. The spectral (monochromatic) radiance (or *specific intensity*) is the radiance per unit wavelength or, as in the case of a Fourier spectrometer, per unit *wavenumber* υ, which is the reciprocal of the wavelength ($1/\lambda$). Traditionally, wavenumber is expressed in inverse centimeters (cm^{-1}), which is numerically equivalent to $10^4/\lambda$, where λ is in μm (1 cm = 10^4 μm). For example, the wavelength at 10 μm has a wavenumber of 1000 cm^{-1}. To convert radiance in (W cm^{-2} sr^{-1})/cm^{-1} to (W cm^{-2} sr^{-1})/ μm, one must multiply by $\upsilon^2/10^4$.
The procedure that determines the conversion coefficients is called *calibration* and the instrumental function which permits the conversion DNs -> radiance is called *responsivity*. The calibration procedures for the PFS instrument will be descripted in the next sessions.

3.1.3 Solid angle

The directional dependence of radiance is taken into account by employing the *solid angle* (Ω), which is an extension of two-dimensional angle measurement. Understanding the angular dependence is very important since most instruments are targeting a planet in a specific direction. The solid angle Ω is defined as the ratio of the area A of a spherical surface (with a given radius r) intercepted by a cone (with the vertex placed at the center of the sphere) to the square of the radius

(3b) $$\Omega = \frac{A}{r^2}$$

For a sphere whose surface area is $4\pi r^2$, its solid angle is 4π sr (steradians). Thus, the solid angle of the upper or lower hemisphere is 2π sr.
A solid angle is often represented by the zenith and azimuth angles in polar coordinates. If θ represents the zenith angle (the angle measured from the vertical to a surface), and φ represents the azimuth angle (fig. 3.1), then a differential element of solid angle is mathematically given by

(3c) $$d\Omega = \frac{dA}{r^2} = \frac{(r \cdot d\theta)(r \cdot \sin\theta \cdot d\varphi)}{r^2} = \sin\theta \cdot d\theta \cdot d\varphi = d\mu \cdot d\varphi$$

where $\mu = \cos\theta$. Note that the zenith angle θ ranges from 0 to 180°. In the literature, the range of 0-90° (i.e. $0 \le \mu \le 1$) usually represents the up-welling hemisphere and 90-180° (i.e. $-1 \le \mu \le 0$) the downward hemisphere, which will be used throughout this thesis.
The azimuth angle φ ranges from 0 to 360°, that is $0 \le \varphi \le 2\pi$.

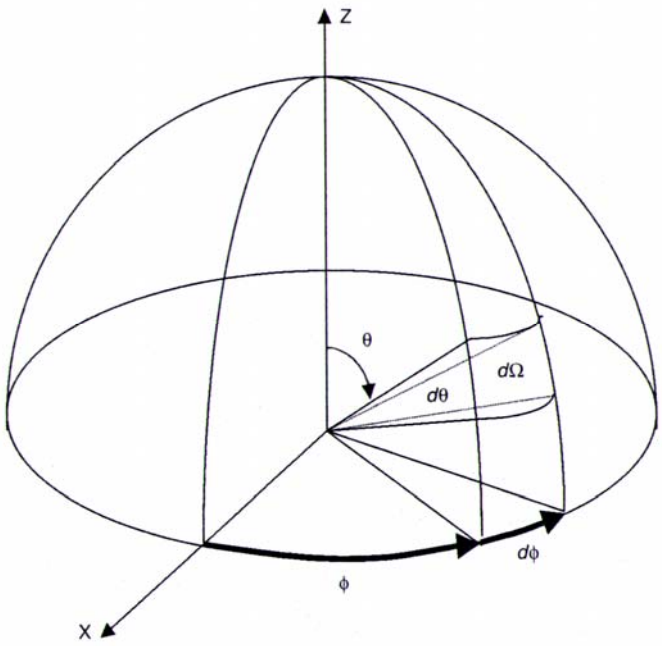

Fig. 3.1 Illustration of the zenith angle (θ), azimuth angle (φ), and solid angle(Ω).

3.1.4 Irradiance

By definition, *irradiance* (J) is the integration of radiance (I) over the entire solid angle of a hemisphere consisting of the zenith angle θ and the azimuth angle φ:

(3d) $$J = \int_0^{2\pi} \int_0^{\pi/2} I(\theta,\varphi)\cos\theta \cdot \sin\theta \cdot d\theta \cdot d\varphi = \int_0^{2\pi} \int_0^{1} I(\mu,\varphi)\mu \cdot d\mu \cdot d\varphi$$

Note the difference between irradiance J, which refers to power per unit area of a collimated beam, and radiance I, which is the uncollimated power per unit area per unit solid angle.

If radiance is independent of the direction (isotropic), equation 3d becomes $J = \pi I$. The irradiance is often called *flux density* or simply *flux* in the remote sensing literature.

3.2 LWC

The LW Channel detector is a pyroelectric sensor ($LiTaO_3$, with a 15μm gold film); it is sensitive to the temperature difference between the emitting sources (including the emission of the optical elements inside the instrument) and its own temperature. The measured signal is thus sensitive to the thermal conditions of the ensemble "instrument + detector", in particular to the temperature of the detector and its variations. The PFS has the ability to control and stabilize the LW Channel detector temperature with an accuracy of 0.01 K. In space, the detector temperature is fixed and usually stable at 286.950 ± 0.005 K, allowing measurements in controlled conditions. Exceptions occasionally occur, especially in some critical conditions where the thermal balance varies heavily:

- entering/exiting the ice-covered polar regions;
- going from day-side to night-side and vice versa;
- during limb measurements;
- entering/exiting the planet.

The most important quantity to be considered is the instrumental thermal emission. While in laboratory, it has been studied and modeled in several ways (see Giuranna et al., 2005a). In space, the best way to get the instrumental thermal emission is looking at the deep space. It has been reported (see Giuranna *et al.*, 2005a; Appendix A.1) that the responsivity when the instrument is looking at the deep space (i.e. no incoming radiation is present) must be considered different from the responsivity when it is looking at some emitting source (e.g. Mars). In the most general case, the measured power spectrum can be written as follows:

(3.1) $$S(\nu) = \left| R(\nu) I(\nu) - R_o(\nu) I_o(\nu) \right|$$

where $S(\nu)$ is the power spectrum as a function of wavenumber ν, $R(\nu)$ is the instrumental responsivity for the incoming radiation $I(\nu)$ (e.g. the radiation coming from Mars), and $R_o(\nu)$ is the responsivity for the instrumental thermal emission $I_o(\nu)$.
When looking at the Deep Space, $I(\nu) = 0$ (for all practical purposes), so that:

(3.2) $$S_{DS}(\nu) = R_o(\nu) I_o(\nu)$$

The deep space signal is the highest signal that PFS can measure (the temperature difference between the source and the detector is maximum), so we can remove the ambiguities of sign and write:

(3.3) $$S(\nu) = R_o(\nu) I_o(\nu) - R(\nu) I(\nu) = S_{DS}(\nu) - R(\nu) I(\nu)$$

where eq. (3.2) has been used in the last step.

The responsivity can be easily computed by inverting eq. 3.3, using the spectra of the internal blackbody (S_{IntBB}) and of the deep space measured at the beginning and at the end of each session of measurements on Mars:

(3.4) $$R(\nu) = \frac{S_{DS}(\nu) - S_{IntBB}(\nu)}{I_{IntBB}(\nu)}, \quad I_{IntBB}(\nu) = 0.99 \cdot BB(\nu, T_{IntBB})$$

Now, both $S_{DS}(\nu)$ and $I_{IntBB}(\nu)$ are known, since the internal blackbody has been full characterized by both laboratory and space measurements. Essentially, it behaves as a blackbody at known temperature (given by the PFS housekeeping information) with an emissivity of 0.99 (see Giuranna *et al.*, 2005a, Appendix A.1). $BB(\nu, T_{IntBB})$ is the Planck function at the temperature T_{IntBB} of the internal Black-Body.
Once we have the responsivity, the calibrated spectrum is given by:

(3.5) $$I_{Mars}(\nu) = \frac{S_{DS}(\nu) - S_{Mars}(\nu)}{R(\nu)}$$

where $I_{Mars}(\nu)$ is the calibrated radiance coming from Mars and $S_{Mars}(\nu)$ the uncalibrated power spectrum of Mars.

As said, the measured signal is sensitive to the detector temperature, and the same is true for the deep space measured spectrum S_{DS}. The best way to operate would be to acquire a DS spectrum (or, better, a set of DS spectra to be averaged in order to achieve a better SNR) before ANY Martian measurement. For practical reasons, this is not possible and we only have two sets of calibration measurements per orbit, one at the beginning and one at the end of the session, each one consisting of ten measurements of the Internal Black Body, ten of Deep Space and ten of the Internal Lamp, for a total of 30 + 30 measurements. Unfortunately, in some critical conditions (described above), the detector temperature may not be stable during a whole orbit. In these cases, the acquired S_{DS} may not be representative of the actual PFS thermal conditions and thus the calibrated spectrum obtained by eq. 3.5 may show some artefacts (i.e. the spectral features of the optical elements) and/or have zero-level radiance problems.

It has been empirically found that the 2nd Deep Space and Internal Blackbody measurements (needed to compute the responsivity and the instrumental emission) give better results (i.e. a better radiometric calibration). This is likely due to the fact that the first set of measurements occur when PFS is still, from a thermal point of view, in a stabilization process (laser diode temperature, detector temperature, Interferometer Block temperatures etc.). As an example, we show on figure 3.2 the temperatures of the detector during a huge set of deep space measurements performed during the first two year of PFS activity. As can be seen by the large range of temperatures through which the data relative to the first sessions are displaced (red and orange "plus" signs), the first set of measurements occur when the detector temperature is not yet properly stabilized.
For this reason, a second version of the calibration procedure make use only of the second set of calibration measurements to compute the responsivity and the instrumental emission for each orbit.

Naturally, this procedure has the inconvenient that, if for some reason (i.e. spiked interferograms, data losses etc.) this second set of internal black-body and Deep Space measurements is not available for a particular orbit, this orbit cannot be calibrated and is skipped by the automated calibration program. In addition, even using exclusively the second set of calibration measurements, strange slopes and artefacts may still be observed in the calibrated spectra. In principle, a solution to these "2nd order" problems (in fact, they occur only in a very limited number of spectra) may be found after a comprehensive study of the thermal behavior of the instrument. This has been possible only when a massive amount of data has been collected, namely after the firsts two years of PSF activity.

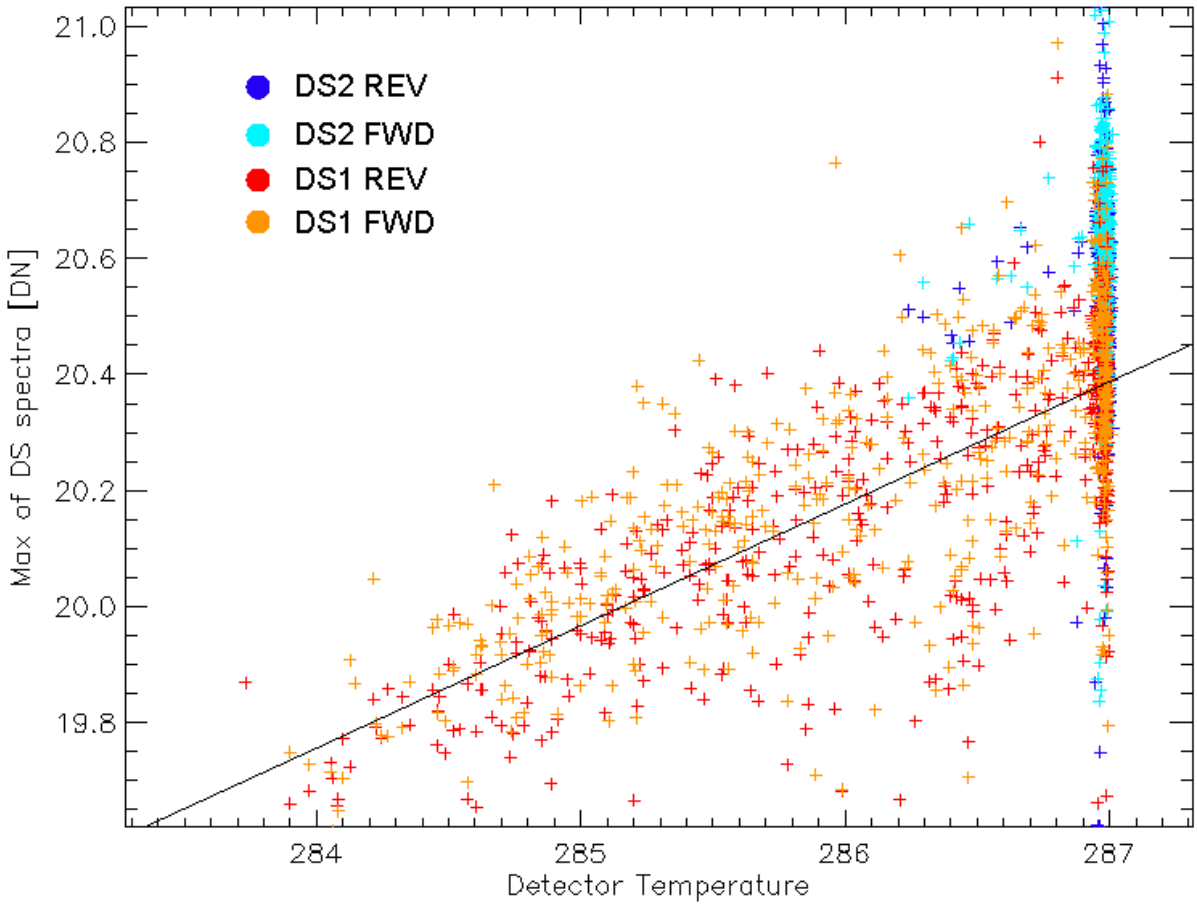

Fig. 3.2 Maximum of deep space spectrum (at ~ 490 cm^{-1}) versus detector temperature. Indexes 1 and 2 refer to the calibration measurements performed at the beginning and at the end of a session, respectively. "Rev" and "Fwd" labels indicate the spectra acquired in the "reverse" and "forward" double-pendulum motion directions (see Giuranna et al., 2005b for details). The black line is the linear best-fit of the data. It allows an estimate of the thermal emission of the instrument also for non-regime thermal conditions. The large spread of the points even for a fixed temperature of the detector is due to the external mechanical vibrations of the spacecraft.

3.2.1 Thermal and statistical analysis

As anticipated above, a comprehensive study of the thermal behavior of the instrument has been possible only after the firsts two years of PSF activity, when a massive amount of data has been collected. For this purpose (and for statistical analysis, stability studies etc.), a set of more than sixty-thousand spectra of deep space and internal black-body has been collected, while monitoring the temperatures of the detector, the internal blackbody and inside the Interferometer Block.

What one expects, is an increase of the measured signal as the temperature of the detector increases (both the deep space and the internal black-body are sources "colder" then the detector; thus increasing the detector temperature, the ΔT increases and consequently the signal). No variation of the signal is expected when both the detector temperature and the source are stable. Figure 3.1 clearly shows that this dependence on the detector temperature is linear. Thus, a linear best-fit of the data allows an estimate of the thermal emission of the instrument also for non-regime thermal conditions. It is also clear from figure 3.2 that variations of the measured signal, of the same order of magnitude of those due to the detector temperature changes (i.e. around 5 - 7 % of the signal), are always

present in the measurements even for thermal regime conditions, that is when the detector temperature is stable at ~ 286.95 K. This is an additional effect of the mechanical vibrations of the S/C, described in subsection 2.4.4.

The main "predictable" results of this analysis have been:

1) as already found in laboratory, the instrumental thermal emission is mainly controlled by the detector temperature;
2) as a consequence of the previous point, the measured signal depends on the detector temperature;
3) this dependence on the detector temperature is linear so that, knowing the detector temperature, we have the instrumental thermal emission by interpolation.

This study has also lead to some other interesting results:

a) the mechanical vibrations affect also the LW channel spectra;
b) they cause systematic statistical errors in the measured signal of the same order of magnitude of the variations due to the detector temperature changes. In other words, even for thermal regime conditions (i.e. with the detector temperature well stable at ~ 286.95 K), observing the same source (i.e. looking at the deep space) we see variations of ~ 5 - 7 % of the signal (see figure 3.2);
c) very important, these systematic statistical errors have a ZERO MEAN VALUE: averaging independent sets of Deep-Space spectra (at a given detector temperature) we get identical curves, providing *the data are separated for the two double-pendulum motion directions*. The same is true for the responsivity curves computed from the Deep-Space and the internal Black-Body measurements;
d) more than 95% of the Martian data and 99% of the Deep-Space and internal Black-Body measurements performed at the end of the various sessions are acquired with the detector temperature stable around ~286.95 K (see figure 3.2).

As a consequence of the above results we have that:

- averaging all the DS measurements we obtain a very accurate estimate of the thermal emission of the instrument at thermal regime condition (i.e. for more than 95% of the data): first, the systematic errors in the single spectra due to the external vibrations are eliminated by the averaging (see point *c*); second, by averaging more than thirty-thousand spectra we get a very high SNR. The same can be done with the responsivity curves. These averages can be used in equation 3.5, leading to a much more accurate radiometric calibration. Thus, by denoting $\overline{S_{DS}(\nu)}$ and $\overline{R(\nu)}$ the average of the Deep-Space measurements (i.e. the thermal emission of the instrument) and of the responsivity curves, we can write:

$$I_{Mars}(\nu) = \frac{\overline{S_{DS}^{F,R}(\nu)} - S_{Mars}^{F,R}(\nu)}{\overline{R^{F,R}(\nu)}} \quad , \tag{3.5a}$$

where the indexes *F* and *R* specify the *Forward* and the *Reverse* direction of the double-pendulum, respectively. $\overline{R(\nu)}$ is the average of the responsivities obtained by each single measurement of the Internal Black-Body by means of eq. 3.4 where, however, $S_{DS}(\nu)$ has been replaced by $\overline{S_{DS}(\nu)}$.

Figure 3.3 shows the thermal emission and the responsivity of the instrument at thermal regime condition, for both the Forward and the Reverse directions.

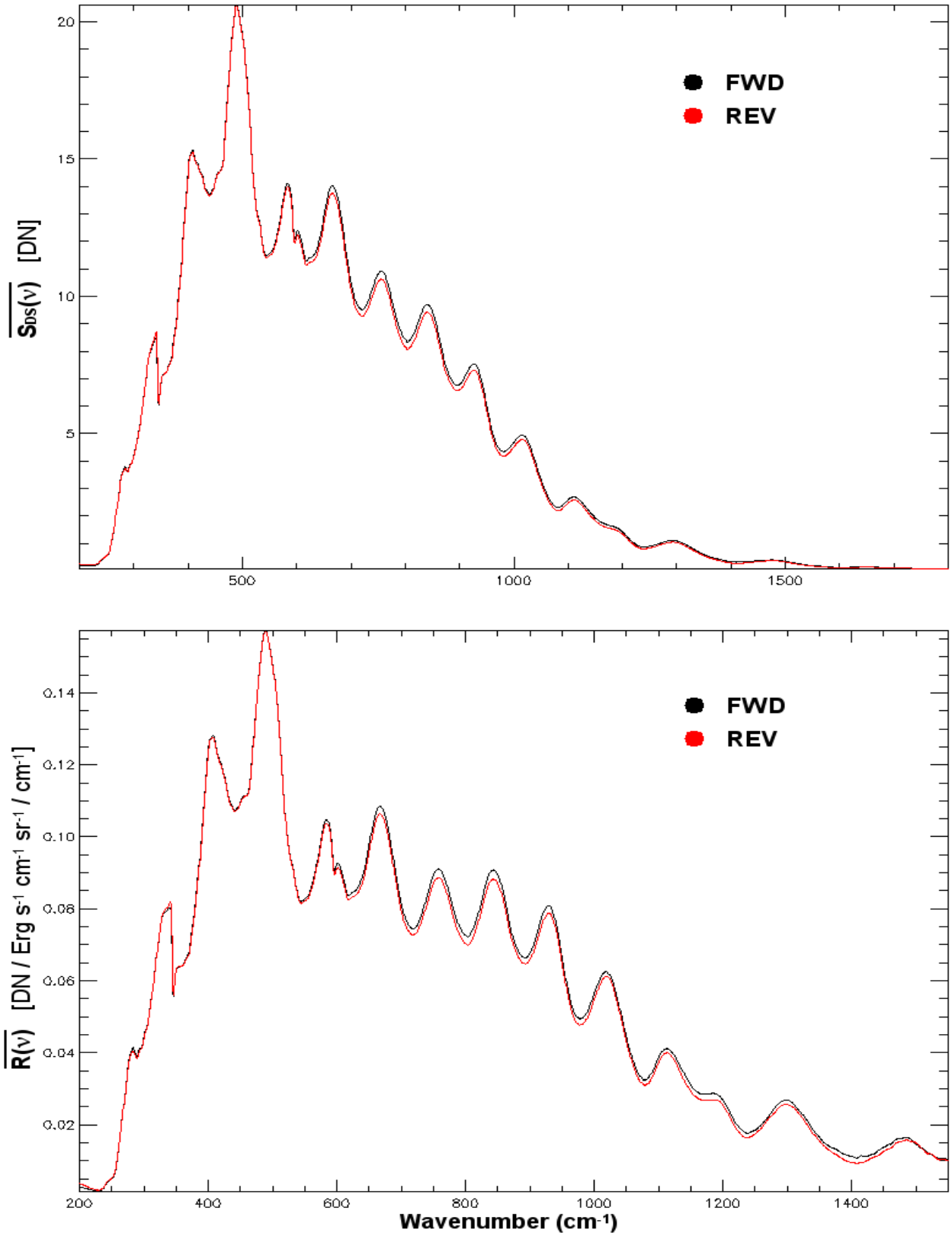

Fig. 3.3 Thermal emission (*Top*) and responsivity (*Bottom*) of the PFS Long Wavelength Channel at thermal regime condition.

- Thanks to point 3), it is possible to have a very accurate estimate of the thermal emission of the instrument also for non-regime conditions: by repeating the same study as in figure 3.1 for each wavenumber, we can interpolate the Deep-Space spectrum for any given temperature of the detector (essentially, we have a linear best-fit for each wavenumber), thus improving the radiometric calibration for non-regime conditions.

- The artefacts (spurious slopes, spectral features of the optical elements etc...) sometimes present in the LWC spectra, will be reduced by the interpolation of the thermal emission of the instrument for non-regime thermal conditions, but they will still be present, for they are not only due to changes in the thermal conditions of the instrument, but also to the external mechanical vibrations, and the two effects are of the same order of magnitude. However, they can still be eliminated after the calibrations, by averaging several Martian spectra, but in this case one has to be careful to average homogeneous data.

- Last but not least, we don't need to use the calibration measurements of each session to have the instrumental thermal emission and the responsivity: $\overline{S_{DS}(\nu)}$ and $\overline{R(\nu)}$ are known *a priori*, being either the pre-computed curves shown in figure 3.3, which are valid at thermal regime condition (i.e. when the detector temperature is stabilized at ~ 286.95 K), or interpolated for the actual temperature of the detector (this last case occurs for less than 5% of the data). Consequently, there is no reason to skip an orbit if the calibration measurements are missing, as in the previous calibration procedure (see section 3.1), and all the orbits can now be calibrated.

Practically, the Martian spectra are divided in two sets, one for each direction of the double-pendulum, and calibrated separately by means of eq. 3.5a, using the instrumental thermal emissivity and the responsivity curves shown in figure 3.3.

3.3 SWC

The procedure for the radiometric calibration of the thermal part of the Short Wavelength Channel is essentially the same as that for the LWC and can be formalized by an expression formally identical to equation (3.5a). The calibration of the near-infrared range of the SWC has been discussed in detail by Giuranna *et al.*, 2005b (see Appendix A.2).

The SWC is affected by several instrumental effects, namely

- Spikes in the spectra
- Phase inversions
- Modulations in the spectra
- Ghosts

As described in Section 2.1, the motion of the double pendulum and the sampling of the interferogram is controlled by a laser diode, one per each spectral channel. The spikes in the spectra are actually direct observations of the light of the laser diode that reaches the detector, probably as a consequence of internal diffusion by the optical elements. The number and the positions of these spikes depend on the external mechanical vibrations. A detailed description of this effect has been reported by Giuranna *et al.* 2005b (Appendix A.2). Starting from orbit #634, the SW laser diode has been switched off (both channels are controlled by the LWC laser diode) and the spikes are no longer present in the spectra. The modulation around 5000 cm^{-1} is still not well understood. At the beginning, it was attributed to the vibrations of the spacecraft, but the actual idea is that it may be caused by some sort of straylight, due to reflection of off-axis radiation on the cube corners. “Ghosts”

are mainly seen in the spectra as repetitions of the 4.3-μm CO_2 absorption band (1-3 % of the original depths), and appear both in emission and in absorption, with almost a random phase. This are due to different effects, mainly a non-constant optical path difference among consecutive sampling points of the interferogram. These effects have been studied in some detail by Bortolino et al., 2007.

The phase inversion is a very tricky problem. Phase inversions may occur wherever in the thermal part of the SW Channel (i.e. up to 2700 cm^{-1}), whenever the thermal balance changes its sign, at a particular wavenumber (i.e. along an absorption line/band). A possible solution to this problem has been developed and applied by the author of this thesis and it is currently providing good result. A brief description of this procedure and the results it is currently providing is given in the next subsection. Further details will be discussed in a forthcoming paper.

3.3.1 APIC: Automated Phase Inversion Correction

A special procedure has been developed to solve the phase inversion problems that occur in the thermal part of the SWC spectra. This procedure is called APIC (Automated Phase Inversion Correction) and it is currently on its version V8 (APIC_8).

During the calibration process, before computing the FFT, the interferograms are symmetrized. The symmetric interferogram, spectrum and phase function are computed using the phase error correction function constructed by modified Forman algorithm (Forman *et al.*, 1966). One of the input parameters for the symmetrisation process is the "wing-size", i.e. the number of points at both sides of the central peak of the interferogram that will be used for the phase error correction. The results strongly depend on this parameter. Unfortunately, it is not possible to use a fixed value of this parameter for all the interferograms and, most of the times, more than one value is needed even for a single interferogram. An extensive analysis has revealed that, when the motion of the double pendulum is controlled by the SW laser diode, it is always possible to find a couple (or, in the worst cases, a triplet) of values for the "wing-size" parameter in order to generate two (three in the worst cases) symmetrized spectra which, each one in different spectral range, are inversion-free, so that all together cover the whole spectral range without phase inversions. The program cycles the values for the wing-size parameter and finds the couple (or triplet) of values described above by studying and comparing the original phase function with the symmetrized phase functions: when no phase inversions are detected in the phase functions over the entire spectral range for a given combination of values (again, each phase function is inversion-free in a limited spectral range, all together covering the whole spectral range) the cycle stops. The program actually computes a number of symmetrized spectra which is twice the number of used values for the wing-size (so 4 or 6 spectra in total), by adding AND subtracting the instrumental emission (see Eq. 3.5a). Then the program automatically joins together the spectra free of inversions in order to have a single final phase-corrected spectrum in the entire spectral range.

Which parts of these spectra are needed to "reconstruct" the corrected spectrum is automatically chosen by the APIC_8 procedure, by a linear correlation with a pre-computed Martian synthetic spectrum. The "joining points" are individuated by the positions of the phase inversions in the original phase function and by a set of subroutines based on empirical and a-priori information on the PFS Martian spectra. A set of subroutines have also been implemented in the procedure to detect special cases, such as polar spectra, night-side spectra and others.

In some cases it is not possible to find optimal joining points. This happens only in very few cases and in particular observation conditions, especially with very low signals (such as night spectra, polar spectra, limb spectra etc.). The procedure detects such failures

and the “SWC QUALITY” flag is set to “1” (this is one of the many parameters contained in the header of the calibrated data, which warns the user that some issue occurred during the calibration process). Examples of APIC_8 reconstructed spectra and failures are given in the next figures.

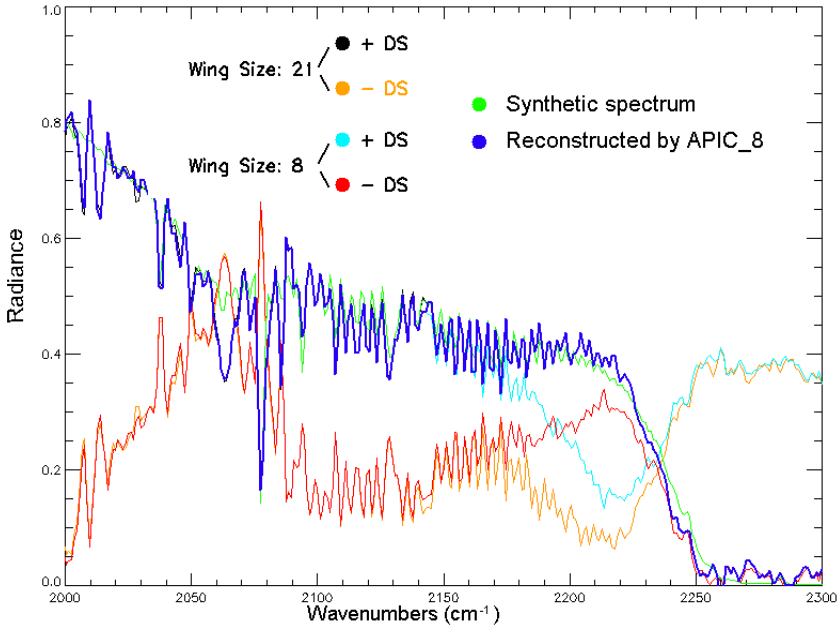

Fig. 3.4 Example of APIC_8 reconstructed spectrum. In this simple case, cyan curve is chosen by the procedure up to ~2150 cm^{-1} (joining point) and then joined with the black curve.

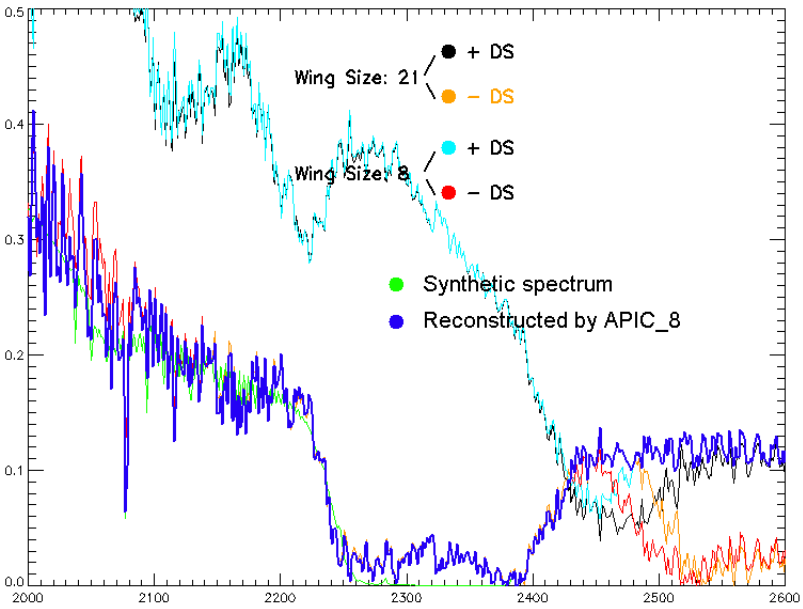

Fig. 3.5 Example of APIC_8 reconstructed spectrum. In this complicated case, orange curve is chosen by the procedure up to ~2150 cm^{-1} (1st joining point) and then joined with the red curve up to ~2430 cm^{-1} (2nd joining point) where the orange curve is selected and joined with the cyan curve at ~ 2490 cm^{-1} (3rd joining point). Three different curves have thus be used by the APIC_8 procedure to reconstruct the final spectrum (blue curve).

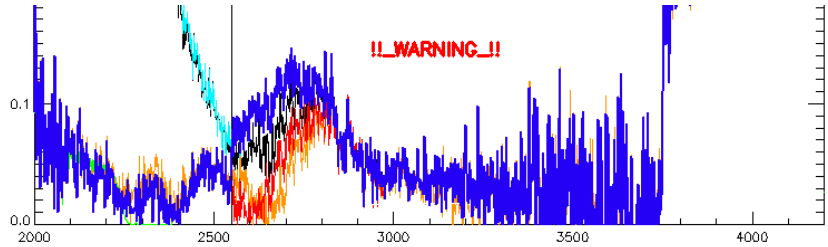

Fig. 3.6 Bad joining point (black vertical line). It has not been possible to find an optimal joining point. The procedure still select the “best possible” point and sets the “SWC QUALITY” flag value to 1. Note the very low signal in the thermal part (a spectrum of water ice in this example).

4 REMOTE SENSING SPECTROSCOPY FOR THE POLAR REGIONS OF MARS

The goal of this thesis is mainly to fill the lack of information about the composition of the Martian polar caps and the processes that occur during their seasonal cycles, as well as to answer, or at least address, some of the many outstanding polar questions that are still pending. In this chapter we will discuss on how this can be possible by using the thermal and Near Infrared measurements of the Planetary Fourier Spectrometer, which has been described in chapters 2 and 3. First, we will briefly discuss the potentiality of the remote sensing spectroscopy for the polar regions of Mars. We will then analyze the general instrumental requirements (section 4.1) and the limitations of the previous missions and existing datasets (subsections 4.2.1 and 4.2.2). Finally, we will examine the most diagnostic spectral regions from visible through thermal infrared for polar studies and, thus, the unique capabilities of PFS with respect to the previous missions (subsection 4.2.3).

Orbital spectral measurements of the volatile (CO_2, H_2O) polar caps of Mars can potentially answer many questions about the current climate, and the inventory and transport of volatiles and dust. These, in turn, can address questions related to past and future climates and the ultimate reservoir sizes for volatiles. The observations in the polar night require thermal infrared or active instruments (that provide their own illumination). However, the most diagnostic bands for both CO_2 and H_2O occur in the solar reflected wavelengths < 5 μm and are easiest to measure after spring sunrise.

As discussed in chapter 1, a significant fraction of the ~6 mbar CO_2 atmosphere of Mars condenses onto the winter polar regions each year. This process brings into and releases from the polar latitudes significant, but largely unknown amounts of dust and water ice. If the net balance of these materials is positive, they can accumulate in perennial water ice and dust polar caps such as are observed in the summer north pole (Kieffer et al., 1976). Using summer surface temperatures, however, it has been determined that the exposed south residual cap appears to remain covered by CO_2 (Paige et al., 1990b; Kieffer, 1979). In addition to net accumulation, the dust and water ice added to the seasonal CO_2 cap have potentially large effects on the net radiative balance during condensation and sublimation (Wood and Paige, 1992), and hence on interannual atmospheric pressure variations and on the net accumulation of CO_2 such that it can last throughout the summer.

Orbital spectra of the polar caps can potentially measure the concentration of dust and water ice in the optical surface and constrain the dust and water ice fluxes and determine the radiative energy balance. A determination of the dust concentration in the summer north cap could provide a highly valuable constraint on the important water-to-dust ratio (Fanale et al., 1992) and therefore the water reservoir capacity of the perennial cap (Zuber et al., 1998). Estimates of the typical surface deposit grain sizes can also be made; they should be strongly related to measurable properties of the surface such as the thermal inertia.

4.1 Instrumental requirements

Thermal: Thermal radiation from the winter poles is more or less restricted to wavelengths longer than 10 μm, depending on instrument signal-to-noise ratio (SNR). Although significant radiation continues to > 200 μm, it is unclear whether any significant information can be extracted from $\lambda > 50–60$ μm (see, however, Johnson and Atreya, 1996). Although dust and CO_2 ice have strong spectral contrast in this region, the emissivity of surface water ice typically varies by less than 5%, except for the smallest grain sizes. It is thus very difficult to accurately analyze water ice grain sizes or dust mixing ratios using only thermal spectra, even if the temperatures are warm enough to have reasonable SNRs up to ~ 7 μm. For the purposes of studying the surface properties, spectral resolving powers ($R = \lambda/\Delta\lambda$) ≤ 100 are more than adequate, but the optimal separation of atmospheric gas and aerosol signals from a top-of-atmosphere spectrum may well require higher values.

Solar reflected: In the visible and near-infrared wavelengths, all the polar materials have significant and contrasting optical properties, so remote sensing of both mixing ratios and microphysical state is very feasible. For $0.3 < \lambda < 1$ μm, both ices are bright and white, while dust is dark and red. In the infrared both ices have strong bands whose shape is strongly dependent on particle size while dust is mostly featureless, except for a possible 2.7-μm hydroxyl absorption. Except for the finest grain sizes, water ice is very dark above 3 μm, but there is a well characterized variation of the 1÷2.5 μm spectrum of water ice with temperature (Grundy and Schmitt, 1998). This can provide information independent of thermal measurements if the spectrum is well resolved and the grain size is < 1 cm. Resolving power requirements can be quite stringent in this region. $R \approx 100$ is adequate for visible measurements, while $R \approx 300$ is needed to resolve water ice features in the infrared, and $R \approx 5000$ may be needed to fully resolve the features of CO_2 ice (Hansen, 1997a, 1997b) and separate them from nearby CO_2 atmospheric bands.

4.2 Examination of the most diagnostic spectral regions for polar studies

Many outstanding polar questions can be examined using data returned by spacecraft instruments that record either multiband measurements or spectra from visible or infrared wavelengths. Here, we discuss which spectral regions provide the most diagnostic information to address the following polar questions:

10. seasonal and perennial ice cap composition;
11. ice grain sizes and/or layer thicknesses;
12. fractional coverage of the ground by ice, and mixtures of ices with dust or soil;
13. radiative balance;
14. non-ice surface composition;
15. presence and composition of clouds;
16. mechanisms of CO_2 ice accumulation;
17. thermal field, thermal winds and circulation in the polar atmosphere.

To make the discussion more manageable, we divide the spectral ranges into four convenient groups: visible only; near-infrared (NIR) (~ 1÷5 μm); thermal infrared (~ 5÷50 μm); and near through thermal infrared (~ 1÷50 μm).

4.2.1 Existing data sets

Table 4.1 summarizes instruments that have returned spectral data from Mars. NIR spectra returned by the 1969 Mariner Infrared Spectrometer (IRS) have been used to examine the composition of the southern polar cap (Calvin and Martin, 1994), and the 1969 Mariner Infrared Radiometer (IRR) measured the cap temperature (Neugebauer et al., 1971). Spectra returned by the 1971 Mariner Mars Infrared Interferometer Spectrometer (IRIS) have been used to model the south residual cap in the summer (Paige et al., 1990), and Forget *et al.* (1995) presented a few late winter spectra of the north polar seasonal cap. Data from the two 1976 Viking Infrared Thermal Mappers (IRTM) have been extensively used for radiative balance studies in the polar night (Forget et al., 1995; Paige and Ingersoll, 1985) and other polar process studies (Kieffer, 1990; Christensen and Zurek, 1984). Spectra from the Mars Global Surveyor Thermal Emission Spectrometer (TES) have been largely used to study both Martian polar caps (Christensen et al., 1998; Kieffer *et al.*, 2001; Kieffer and Titus, 2001; Titus et al., 2001). Both IRTM and TES have broadband (~ 0.3÷3 μm) solar reflectance channels which can be used for radiative balance studies, but only spectra are useful for understanding the cause of broadband albedo variations.

Table 4.1 Comparison of Mars spectral instruments

	1969 IRS	1969 IRR	1971 IRR	1971 IRIS	1976 IRTM	1997 TES	2001 THEMIS
wavelength range, μm; or ch. band centers	1.8-14.4	10;20	10;20	5-50	7;9;11;15;20	6.5-50	6.5-14
spectral resolution	[B]10 cm^{-1} (1%)	370; 156 cm^{-1}	370; 156 cm^{-1}	2.4 cm^{-1} (.24%)[B]	140-1400cm^{-1}	5 or 10 cm^{-1} (.5 or 1%)[B]	
spatial resolution (km)	130-500	>50km	15-1000km	125-1000	30-40	3	
rms SNR: 2.2μm	~190			—	—	—	
rms SNR: 10μm, 270K	~600			~110	~200	~400	
measurements[A]	1340	2	2	1500	5	286 or 143	10

[A]Number of measurements per spectrum, or number of channels. [B]At 10 μm. *SNR*: signal to noise ratio; *ch*: channels.

Thermal: The substantial data sets are

(1) the Mariner 7 Infrared Spectrometer (IRS), measuring the radiation in the 4÷14.3 μm spectral range, with a resolving power R≈100;
(2) the Mariner 9 high-resolution infrared interferometer (IRIS), measuring the radiation in the 5÷50 μm, with a resolving power R~500;
(3) the Viking Orbiter 1 and 2 Infrared Thermal Mapper (IRTM) with four infrared surface-sensing broad-band channels covering the 6÷25+ μm spectral range;
(4) the thermal emission spectrometer (TES) on Mars Global Surveyor (MGS), observing a similar spectral range (6.5÷50 μm) as the Mariner 9 IRIS, but with a much greater spatial resolution and improved SNR, at the expense of reduced spectral resolution (by a factor of 3–6);

(5) the Thermal Emission Imaging System (THEMIS) on board the Mars Odyssey spacecraft, combining a 5-wavelength visual imaging system with a 9-wavelength infrared imaging system.

Mariner 7 was a flyby, and IRS provides only a handful of spectra of the south seasonal polar cap in the spring, but these are among the highest SNR measurements available, especially in the wavelengths 6÷8 μm. The IRIS was intended for atmospheric studies and had a large field of view and low SNR; its observations of the polar regions are limited and rarely discussed. The IRTM instruments provide infrared coverage at generally high spatial resolution over large parts of two Martian years, but the information available from the broad-band sensors is limited for several reasons. Only two of the surface channels are usable during polar night, making it, for example, impossible to distinguish between variations in grain size and variations in dust content of CO_2 frosts (Forget et al., 1995). TES has already revealed new properties of the polar caps (see also Hansen, 1999). The broad spectral features in the thermal infrared allow for less precise analysis than is possible using the finer bands in the near infrared, but the capabilities are still vary much improved over IRTM. PMIRR is designed for atmospheric studies, but observations of the surface are planned with broadband sensors similar to IRTM. However, PMIRR has two channels with $\lambda > 30$ μm and will is in a low orbit; it could outperform IRTM in polar studies (given sufficient SNR). THEMIS has several narrow filters in the 6.5 to 14.5 μm region intended for mineralogical studies and is not well suited for polar observations where this region is more or less dominated by dust.

Solar reflected: Broad band measurements by cameras on Mariners 6, 7, and 9 and the Viking Orbiters, and the solar channel on Viking IRTM provide very limited information in the visible and near-infrared (for IRTM) range. Only the Viking cameras give us any significant narrow-band color observations, but very few polar observations were made using color filters. The infrared imaging spectrometer on the Phobos spacecraft only observed the equatorial region, but the short wave channel of the Mariner 6/7 IRS took 1.9÷6 μm spectra (R≈100) of Mars during two flybys. The Mariner 7 spectra of the spring polar cap (see Subparagraph 1.3.3.3.3 and figure 1.9) are unique and valuable (Calvin and Martin, 1994). Mars Orbiter Camera (MOC) on MGS has a two-color wide-angle camera and a monochromatic narrow-angle camera, and may only be useful for determining the distribution of bright and dark regions on the poles. The color imager (MARCI) on MCO has a wide-angle, five-color camera, mainly for atmospheric observations and a narrow-angle, 10-color camera designed for color surface imaging.

4.2.2 Limitations of previous data sets

Each of the spectral data sets returned thus far has significant limitations. Multi-channel radiometers such as IRR, IRTM, and THEMIS (Mars Surveyor 2001) cannot directly provide spectral signatures that can strongly constrain the composition of the surface or ice. For example, it is impossible to use broad-channel infrared data like that of the IRTM to distinguish variations of CO_2 particle size from dust or ice contamination. Instruments that return spectra have the potential to provide much more information. However, IRS returned spectra with very limited spatial and temporal coverage, and low spatial resolution. IRIS had a low signal to noise ratio, and also low spatial resolution. Both IRIS and TES spectra cover only the thermal infrared, and so do not measure the spectral region that is most useful for determining the composition of the surface and ice (see next subsection).

4.2.3 Information from different spectral regions

4.2.3.1 Visible (VIS)

Visible wavelength spectra can provide some constraints on the surface composition, but because ices are very transparent in this region, minerals and other opaque materials tend to dominate the reflectance. For thermal balance, VIS is only a part of the reflected energy. A significant portion of reflected or absorbed solar energy occurs in the 1÷2.5 μm region, where the properties of the ices can dominate those of minerals.

4.2.3.2 Near Infrared (1 to 5 μm)

Except during the polar night, this is the most important spectral region for determining composition and grain sizes. Both water ice and CO_2 ice have rich spectral structure in this region that is diagnostic of their abundance and grain size. Strong spectral features in this region also make this an important region to use in the analysis of energy balance. For example, the absorption of water ice varies over about 6 orders of magnitude from 1 to 3 μm. Spectral resolutions as high as ~1 cm^{-1} are needed to resolve many of the narrow CO_2 lines (Hansen, 1997a, 1997b). Paige et al., 1995, used IRTM solar and thermal data to show that the autumn seasonal cap is dark and cold, while the spring seasonal cap is bright and cold, and proposed a solid, transparent layer of ice to explain the autumn results. A transparent CO_2 coating will appear strongly in the NIR due to both weak and strong absorptions that would be diagnostic of the layer thickness.

Grain sizes speak to history and age of the deposits. To the extent that age controls the average grain size by processes of sintering, any spectral data which are sensitive to ice grain size are valuable, and the greatest sensitivity is in the NIR. The regions most sensitive for water ice are 1÷3 (5) μm and for CO_2 ice 1÷5 (7) μm. Grain sizes are hard to determine from VIS since even small amounts of highly absorptive materials dominate this region, and thermal infrared measurements are also much less diagnostic.

In Figure 4.1a we show a typical PFS measurement of the Martian polar ices in the Near Infrared. In this small portion of the SWC spectral range, the CO_2 ice has many narrow absorption lines that are very diagnostic of its grain size. Thanks to the high spectral resolution of PFS, these absorptions are well resolved in the spectrum. The effect of different grain sizes on CO_2 ice spectral reflectance is shown in Figure 4.1b.

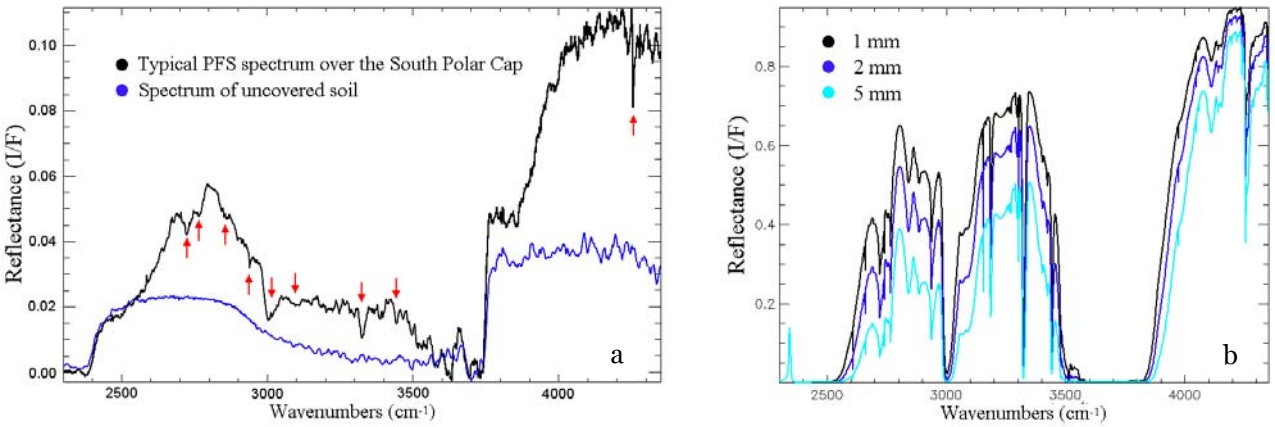

Fig. 4.1 *a*. The PFS spectra of the Martian polar caps show the distinctive features of CO2 ice, including a number of small absorption bands at 2720, 2770, 2850, 2940, 3000, 3320 and 3440 cm-1 (red arrows). *b*. Spectral albedo of pure CO2 snow calculated for different grain sizes.

4.2.3.3 Thermal infrared (5 to 50 μm)

In the thermal infrared, water ice is hard to identify unless the effective grain size is < 100 μm. Minerals such as dust tend to be almost featureless in the thermal infrared as well, unless the grain size is very small. This region, however, is the only one useful when observing in the polar night, mainly from 20 to 50 μm, where there is easily measurable flux from the polar regions, and where both CO_2 and water ice (of sufficiently small grain size) can have low emissivity (Warren et al., 1990). For quantitative determinations it is important to have a high enough signal-to-noise ratio to get good measurements in the 8÷12 μm range, and spectral resolution ≤ 10 cm^{-1}.

The radiance observed at Mars in the thermal infrared depends on several parameters of the atmosphere and surface of Mars as described by the radiative transfer theory. Namely, they are: the surface temperature, the column density of dust and water ice aerosols in the atmosphere, the surface pressure, column density of water vapors and carbon monoxide, and the air temperatures as a function of altitude. All these parameters provide useful information for polar studies. For example, the measured surface temperatures can reveal the presence of CO_2 ice at the surface, as discussed in Section 7.1; the column density of suspended aerosols could reveal the presence of clouds (ice and dust) and has great importance in the atmospheric radiative budget, also affecting the H_20 and CO_2 condensation rates; the surface pressure determinates the condensation temperature of carbon dioxide, while the vertical temperature profiles allow us to study the thermal field, the thermal winds, and thus the atmospheric circulation in the polar region, as well as the complex dynamical processes that occur in the atmosphere and particularly in the polar nights (e.g., the polar warming and large-scale thermal waves).

4.2.3.4 NIR + thermal coverage

Coverage of both the near and thermal infrared can significantly improve the determination of the percent coverage of the ground by ice. For example, when making the determination from the thermal region alone, mixed surface temperatures combined with non-unit emissivity introduce uncertainty into the result. Incorporating information from the NIR should make modeling much more accurate. CO_2 ice clouds may be measurable at 15 μm using limb scans, if the clouds are high enough to see them through the atmospheric 15-μm band. During daylight limb scans, the 4.3-μm reflection spike provides a unique signature of CO_2 clouds. The optical depths are probably too small to see them other than on the limb, except for thick clouds in the winter night, which tend to be indistinguishable from surface snow in the thermal infrared (Forget et al., 1995).

The information available from each of the different spectral region here examined are summarized in table 4.2.

The Planetary Fourier Spectrometer has the unique, unprecedented capability of measure both the thermal and the Near Infrared radiation with a high spectral resolution (see Chapters 2 and 3). A synergistic study with high spatial resolution color imaging and both near and thermal infrared spectra with suitable spatial and spectral resolutions is most desirable for addressing Mars polar questions, and has been finally possible thanks to the *Mars Express* ESA mission.

Table 4.2 Information from each spectral region

spectral region	Compositional information	Mixture information: CO_2+water ice+dust	Ice history and age (from grain size)	% coverage of ground by ice	CO_2 clouds (limb scans)	Energy balance
VIS	can provide some constraints on dark materials	can quantify and identify dark materials (dust, etc.)	Very large water grains detectable in silicon NIR (< 1.1 μm)	vs. soil; water and CO_2 not distinct	cannot tell water from CO_2 ice	some
NIR	most important region except during polar night	most important region except during polar night	most important region except during polar night	good	4.3mm spike (day only)	important
thermal	weak but possible; most materials very dark	weak but possible; most materials very dark (~blackbody)	for finest grain sizes	good (under solar heating)	15μm band (but atm complications	some
NIR + thermal	thermal constrains NIR information	thermal constrains NIR information	good	best	high probability of identification	good

5 RADIATIVE TRANSFER MODELING

The atmosphere of a planet modulates any surface signals twice. It affects the distribution of incoming solar radiation at the surface that is related to the surface reflectance responses. The solar radiation reflected by the surface is further scattered and absorbed by the atmosphere before reaching the sensor. Since the sensors are located at the top (as in our case) or the middle of the atmosphere, the radiance received by a detector contains information of both the atmosphere and land surface. The main theme of this thesis is the estimation of atmospheric, snow and surface variables from remote sensing observations in the Martian polar regions. Computation, and occasionally removal, of atmospheric effects is a necessary step.

Radiative transfer theory has been recognized as the principal modeling method that accounts for the solar radiation in the atmosphere. It is also widely used for surface modeling (e.g., snow, and soil) as discussed in the next Chapter. This chapter introduces shortwave radiative transfer models and their solutions. In our work we are primarily concerned with the scalar approximation of the full vector description of the theory, and thus polarization is not discussed. Readers who are interested in vector radiative transfer theory should consult related books (e.g., Fung 1994). The introduction of radiative transfer theory in this chapter will be fundamental to understanding subsequent chapters since some of the important concepts are not repeated.

After radiative transfer formulation and its linkage with optical properties of a medium are introduced, both numerical and approximate solutions to radiative transfer equations are discussed. Section 5.2 defines the radiative transfer equation in the solar spectrum. The general form of the equation of radiative transfer will be first derived, and then the case of a horizontally stratified medium will be considered. Subsections 5.2.x link the quantities in radiative transfer equations with the properties of a medium. The algorithms for calculating the optical properties of a single particle are introduced. Special attention has been given to the computation of the phase function. The particle size distribution functions and the refractive indices are presented; the distribution function and corresponding parameters adopted so far for Martian aerosols will be reviewed in the next chapter. Section 5.3 describes the numerical and approximate solutions to the radiative transfer equation that have been used in our work, namely two-stream approximations, and the method of discrete ordinates. Some typical radiative transfer solvers (computer software packages) in the public domain are also summarized.

5.1 Basic definitions

In our work we will estimate the properties of a medium (the Martian polar caps) from the way it scatters or emits electromagnetic radiation from its upper surface. There are many ways to define the fraction of incident light scattered by a material, depending on the geometry, so that the terms must be appropriately qualified to be unambiguous (subsection 5.1.3).

In addition, before discussing the radiative transfer equation and how to solve it, it is necessary to introduce some geometry and notations (subsection 5.1.1) and a series of definitions of the optical properties of a medium (subsection 5.1.2). The interaction processes of a medium with the radiation that are associated with the radiative transfer equation will be discussed in the next session.

5.1.1 Scattering, phase, incidence and emission angles

Consider the radiance scattered by a particle into some direction of interest that makes an angle θ with the direction of propagation of the incident irradiance; θ is the *scattering angle*, and the plane containing the incident and scattered propagation vectors of interest is the *scattering plane*.
The complement of the scattering angle is called the *phase angle*, $g = \pi - \theta$. The phase angle is the angle between the source and the detector of radiation as measured from the center of the particle. In the literature of scattering by a single particle, the scattering angle θ is usually used. However, in discussions of diffuse scattering by particulate media, including remote-sensing applications, the phase angle g is often more convenient.
The *emission angle e* is the angular position of the detector of radiation (i.e. the observer) measured from the vertical to a surface.
The *incidence angle i* is the angle of the incoming radiation measured from the vertical to a surface; if the radiation source is the Sun, then it coincides with the solar zenith angle.
The azimuth, phase, incidence and emission angles are shown in figure 5.1.

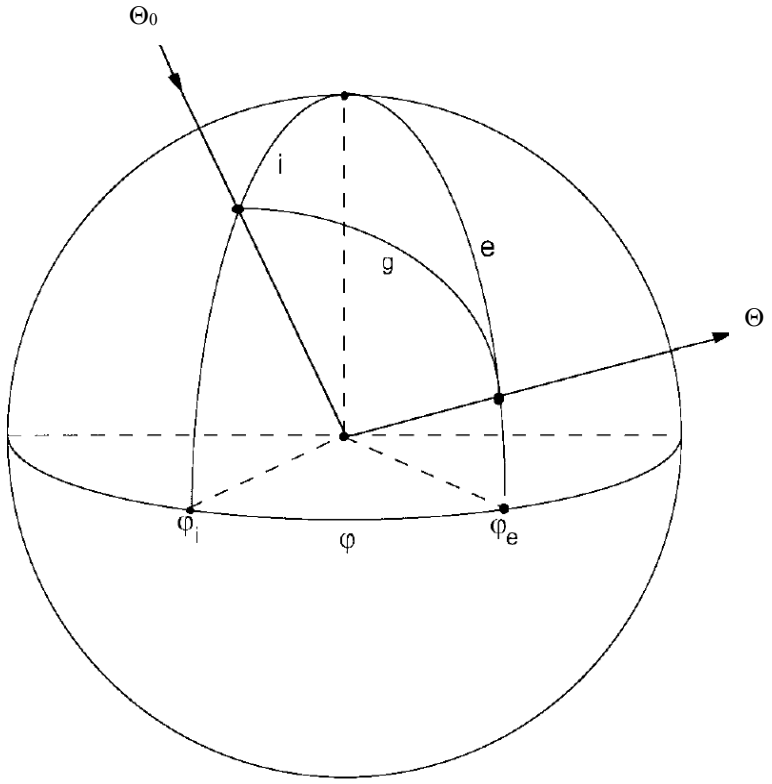

Fig. 5.1 Diagram of angles defined in subsection 5.1.1. φ is the azimuth angle defined in subsection 3.1.3.

They are related by the relation $\cos g = \cos i \cdot \cos e + \sin i \cdot \sin e \cdot \cos \varphi$.

A commonly used notation, which will be followed in this thesis, is to let

(5.a) $\mu = \cos e \quad ; \quad \mu_0 = \cos i$

In general, three angles are needed to specify the geometry. The angles usually used in remote sensing applications are *i*, *e*, and φ. However, most planetary applications specify *i*, *e*, and *g*, the reason being that in a spacecraft acquisition of a planet, *g* is very nearly constant over the entire image. Occasionally, the scattering angle θ may be used instead of *g*.

5.1.2 Optical properties of a medium

5.1.2.1 Cross sections

Let the total amount of power of the incident irradiance *J* that is affected by a particle be P_E. Then the *extinction cross section* is

(5.b) $\sigma_E = P_E / J$

A certain portion *Ps* of P_E is scattered into all directions, and the remainder P_A is absorbed by the particle. The *scattering cross section* is

(5.c) $\sigma_S = P_S / J$

And the *absorption cross section* is

(5.d) $\sigma_A = P_A / J$

The cross sections have the units of area. Because $P_E = P_S + P_A$, the cross sections are not independent, but related by $\sigma_E = \sigma_S + \sigma_A$.

5.1.2.2 Efficiencies

The ratios of the cross sections to the geometrical cross-sectional area of the particle $\sigma = \pi a^2$, where *a* is the particle radius, are the corresponding efficiencies. Thus, the *extinction*, *scattering* and *absorption efficiencies* are, respectively,

(5.e) $Q_E = \sigma_E/\sigma \quad ; \quad Q_S = \sigma_S/\sigma \quad ; \quad Q_A = \sigma_A/\sigma$

5.1.2.3 Particle single scattering albedo

The ratio of the total amount of power scattered to the total power removed from the wave is the *particle single-scattering albedo*, ω.
From the definitions of the cross sections and efficiencies,

(5.f) $\omega = P_S/P_E = \sigma_S/\sigma_E = Q_S/Q_E$

5.1.2.4 Particle phase function

Suppose the power described by irradiance $J(\vec{s},\Theta_o)$ traveling into a direction Θ_o is scattered by a particle at a position $\vec{s}$ into a radiance pattern $I(\vec{s},\Theta)$. The *particle phase function* $p(g)$ describes the angular pattern into which the power $Ps = J\sigma Qs$ is scattered. Let $(dPs/d\Theta)(\Theta_o,\Theta)$ be the power scattered by the particle from direction Θ_o into unit solid angle centered about direction Θ, and let g be the phase angle between Θ_o and Θ (figure 5.1). Then $p(g)$ is defined by

(5.g) $$\frac{dP_S}{d\Theta}(\Theta_o,\Theta) = J(\Theta_o)\sigma Q_S \frac{p(g)}{4\pi}$$

The particle phase function may be described equivalently by $p(\theta)$.
Because the area perpendicular to the incident radiation affected by the particle is σ_E, the scattered radiance (or power pr unit area scattered into unit solid angle) is

(5.h) $$I(\Theta) = J(\Theta_o)\frac{\sigma_S p(g)}{\sigma_E 4\pi} = J\omega\frac{P(g)}{4\pi}$$

If the particle scatters isotropically, $p(g) = 1$.
Because the total power scattered in all directions must be equal Ps, there is a normalization condition on $p(g)$ such that

(5.i) $$\int_{4\pi} p(g)d\Theta = 4\pi$$

5.1.2.5 Asymmetry factor

The particle angular-scattering function may be characterized by various parameters, usually referred as asymmetry factors. One such parameter is the *cosine asymmetry factor* ξ (also called *asymmetry parameter*), which is the average value of the cosine of the scattering angle $\theta = \pi - g$:

(5.j) $$\xi = \langle\cos\theta\rangle = \frac{\int_{4\pi}\cos\theta p(\theta)d\Theta}{\int_{4\pi} p(\theta)d\Theta} = \frac{1}{2}\int_0^{\pi}\cos\theta p(\theta)\sin\theta d\theta = -\langle\cos g\rangle$$

5.1.3 Reflectances and Albedos

There are many kinds of reflectance, depending on the geometry. In modern usage the word is preceded by two adjectives, the first describing the degree of collimation of the source, and the second that of the detector. The usual adjectives are *directional, conical,* or *hemispherical.* For example, the directional-hemispherical reflectance is the total fraction of light scattered into the upward hemisphere by a surface illuminated from above by a highly collimated source. If the two adjectives are identical, the prefix *bi-* is used. Thus, the bidirectional reflectance is the same as the directional-directional reflectance. In reality, all

measured reflectances are biconical, because neither perfect collimation nor perfect diffuseness can be achieved in practice. However, many situations in nature approach the ideal sufficiently that the other quantities are useful approximations.
We now define the various reflectances and the symbols that will be used to represent them in this thesis.

The *bidirectional reflectance* of a medium (BDR) is a fundamental optical property. It characterizes the energy scattered into the hemisphere above a surface as a result of incident radiation. It is defined as the ratio of the radiance scattered by a surface into a given direction to the incident irradiance:

(5.k) $r(i,e,g) = r(\vec{s},\Theta_0,\Theta) = I(\vec{s},\Theta)/J(\vec{s},\Theta_0)$

The units of the BDR are inverse solid angle (sr^{-1}).

An empirical expressions that is widely used because of its mathematical simplicity is known as *Lambert's law*, and is the simplest and one of the most useful analytic bidirectional-reflectance functions. Although no natural surface obeys Lambert's law exactly, many surfaces, especially those covered by bright, flat paints, approximate the scattering behavior described by this expression.
Lambert's law is based on the empirical observation that the brightnesses of many surfaces are nearly independent of the emission angle e and the azimuth angle φ, and on the fact that the brightness of any surface must be proportional to cos i. Because light scattering is a linear process, the scattered radiance $I(i,e,\varphi) = Jr(i,e,\varphi)$ must be proportional to the incident irradiance per unit surface area $J\mu_0$. The bidirectional reflectance of a surface that obeys Lambert's law is defined to be

(5.l) $r_L(i,e,\varphi) = K_L \cos i$

where K_L is a constant.
The total power scattered by unit area of a Lambert surface into all directions of the upper hemisphere is

$$P_L = \int_{2\pi} I(i,e,\varphi)\mu \cdot d\Omega = \int_{e=0}^{\pi/2}\int_{\varphi=0}^{2\pi} JK_L \cos i \cos e \sin e \cdot de \cdot d\varphi = \pi J K_L \mu_0$$

Because the incident power per unit area is $J\mu_0$, the fraction of the incident irradiance scattered by unit area of the surface back into the upper hemisphere is the *Lambert albedo* $A_L = P_L/J\mu_0 = K_L\pi$, so that $K_L = A_L/\pi$. Thus, Lambert's law is

(5.m) $$I(i,e,\varphi) = \frac{J}{\pi} A_L \mu_0$$

And the *Lambert reflectance* is

(5.n) $$r_L(i,e,\varphi) = \frac{1}{\pi} A_L \mu_0$$

If $A_L = 1$, the surface is a *perfectly diffuse surface*.
Lambert's law is widely used as a mathematically convenient expression for the bidirectional reflectance when modeling diffuse scattering. In fact, it does provide a

reasonably good description of the reflectances of high-albedo surfaces, like snow, but the approximation is poor for dark surfaces, such as soils.
More in general, the *directional hemispherical reflectance* (also called *local* or *planar albedo*) is defined as $A = P/J\mu_o$, where P is total power scattered by unit area of a surface into all directions of the upper hemisphere.

The *bidirectional reflectance distribution function* (BRDF) is the ratio of the radiance scattered by a surface into a given direction to the collimated power incident on a unit area of the surface. The incident radiant power per unit area of surface is $J\mu_o$ and the scattered radiance is $J \cdot r(i,e,g)$. Thus,

(5.o) $$\mathrm{BRDF}(i,e,g) = r(i,e,g)/\mu_o$$

The *reflectance factor*, denoted by REFF, of a surface is defined as the ratio of the reflectance of the surface to that of a perfectly diffuse surface under the same conditions of illumination and measurement.
Because the bidirectional reflectance of a perfect Lambert surface is $r_L=\mu_o/\pi$, the reflectance factor of a surface with bidirectional reflectance $r(i,e,g)$ is

(5.p) $$\mathrm{REFF}(i,e,g) = \pi r(i,e,g)/\mu_o$$

The *radiance factor*, denoted by RADF (and usually denoted by I/F), is similar to the reflectance factor, except that it is defined as the ratio of the bidirectional reflectance of a surface to that of a perfectly diffuse surface illuminated at i=0, rather than at the same angle of illumination as the sample. The radiance factor is given by

(5.q) $$I/F = \mathrm{RADF}(i,e,g) = \pi r(i,e,g)$$

5.2 Radiative Transfer Equation

The formalism that is commonly used to calculate how the intensity of an electromagnetic wave is changed by the processes of emission, absorption, and scattering as the wave propagates through a complex medium is a form of the transport equation known as the *equation of radiative transfer*. The fundamental assumption of this formalism is that the inhomogeneities of the medium emit and scatter the radiation independently of each other and incoherently.

The derivation of the equation of radiative transfer is as follows: consider a radiance field $I(s,\Theta)$, which describes the intensity of electromagnetic radiation at a point s, propagating into a direction Θ, that has been emitted or scattered at least once within a particulate medium. Suppose s lies on the base of a right cylinder of area dA, length ds, and volume $dsdA$, where ds points in the direction of Θ. Then the radiant power at s passing through the base contained in a cone of solid angle $d\Theta$ about Θ is $I(s,\Theta)dAd\Theta$.

Similarly, the power emerging from the top of the cylindrical volume into $d\Theta$ is $I(s+ds,\Theta)dAd\Theta = \left[I(s,\Theta) + \frac{\partial I(s,\Theta)}{\partial s} ds \right] dAd\Theta$.
The difference between the power emerging from the top and that entering at the bottom is $(\partial I / \partial s)dsdAd\Theta$.

The change in radiant power is due to various processes occurring in the cylinder that add or subtract energy from the beam: absorption, scattering, and emission. Those effects

of absorption and scattering that subtract energy from the radiance are usually lumped together into a single process called *extinction*. Each of these processes will now be considered.

Extinction. The volume extinction coefficient $E(s,\Theta)$ of the medium is defined such that the decrease in power ΔP_E due to extinction as the beam propagates through the volume element is

(5.1) $$\Delta P_E = -E(s,\Theta)\, I(s,\Theta)\, dsdAd\Theta$$

If extinction were the only process acting on the intensity, then

$$\Delta P_E = (\partial I / \partial s)dsdAd\Theta = dIdAd\Theta \quad \Rightarrow \quad dI/I = -Eds$$

which may be integrated to

(5.2) $$I(s) = I(0)\exp\left[-\int_0^s E(s')ds'\right]$$

The volume extinction coefficient may be separated into the volume absorption coefficient $K(s,\Theta)$ and the volume scattering coefficient $S(s,\Theta)$, so that $E(s,\Theta) = K(s,\Theta) + S(s,\Theta)$.

Scattering. Scattering increases as well as decreases the power in the beam, because light of intensity $I(s,\Theta')$ propagating through the volume element $dsdA$ in a direction Θ' can be scattered into the direction Θ. The volume angular scattering coefficient $G(s,\Theta',\Theta)$ of the medium is defined such that the power dP_S passing through $dsdA$ into a cone of solid angle $d\Theta'$ about direction Θ' that is scattered into a cone $d\Theta$ about direction Θ is

$$dP_S = \frac{1}{4\pi} G(s,\Theta',\Theta) I(s,\Theta') \cdot ds \cdot dA \cdot d\Theta' \cdot d\Theta$$

To find the total amount of power ΔP_S scattered into the beam, the contribution of intensities traveling through the volume in all directions Θ' must be added together, so that $\Delta P_S = \int_{4\pi} dP_S d\Theta' = dsdAd\Theta \frac{1}{4\pi} \int_{4\pi} I(s,\Theta')G(s,\Theta',\Theta)d\Theta'$.

The integral of $G/4\pi$ over all directions is the volume scattering coefficient,

(5.3a) $$S(s,\Theta) = \frac{1}{4\pi} \int_{4\pi} G(s,\Theta',\Theta)d\Theta'$$

For an ensemble of randomly oriented particles, G depends only on the scattering angle θ between Θ' and Θ, rather than on the two directions separately. In that case, S is independent of Θ, and $d\Theta' = 2\pi \sin\theta d\theta$, so that

(5.3b) $$S(s) = \frac{1}{2}\int_0^\pi G(s,\theta')\sin\theta' d\theta'$$

Emission. Let the volume emission coefficient $F(s,\Theta)$ be the power emitted per unit volume by the element at position s into unit solid angle about direction Θ. Then $F(s,\Theta)$ is defined so that the contribution of the emitted radiation to the change in power is

(5.4) $$\Delta P_F = F(s,\Theta)\,ds\,dA\,d\Theta$$

In general, there are at least four processes that may contribute to the volume emission: single scattering, thermal emission, fluorescence and luminescence, and stimulated emission. Fluorescence and luminescence will not be considered further in this work. Stimulated emission is important in gaseous media that are not in thermodynamic equilibrium, but usually not in particulate media. Hence, only single scattering and thermal emission are usually considered; their volume coefficients will be denoted by $F_S(s,\Theta)$ and $F_T(s,\Theta)$, respectively. Then $F(s,\Theta) = F_S(s,\Theta) + F_T(s,\Theta)$.

Since we are interested on the shortwave range, the thermal radiation $F_T(s,\Theta)$ will be neglected and only the single scattering will be discussed. In a large number of problems the medium is illuminated by highly collimated radiation incident on the top surface from a source that may be considered to be effectively at an infinite distance above the medium in a direction Θ_o making an angle i from the zenith. Let J be the irradiance at the upper surface of the medium from such a source. Then at any altitude below the surface of the medium the irradiance that has not been extinguished is, according to equation 5.2a, $J\delta(\Theta-\Theta_o)\exp[-\int_S^\infty E(s',\Theta)ds']$, where δ is the delta function. The irradiance that is scattered by the medium may be considered to be a source of diffuse radiance that contributes an amount

(5.5) $$\begin{aligned} F_S(s,\Theta) &= \int_{4\pi} J\delta(\Theta'-\Theta_o)\exp\left[-\int_S^\infty E(s')ds'\right]G(s,\Theta',\Theta)d\Theta' \\ &= JG(s,\Theta_o,\Theta)\exp\left[-\int_S^\infty E(s')ds'\right] \end{aligned}$$

to the volume emission coefficient.

Equating the sum of all the contributions ($\Delta P_S+\Delta P_E+\Delta P_F$) to $(\partial I/\partial s)\,ds\,dA\,d\Theta$ and dividing by $ds\,dA\,d\Theta$ gives

(5.6) $$\frac{\partial I(s,\Theta)}{\partial s} = -E(s,\Theta)I(s,\Theta) + \frac{1}{4\pi}\int_{4\pi} I(s,\Theta')G(s,\Theta',\Theta)d\Theta' + F_S(s,\Theta)$$

Equation 5.6 is the general form of the equation of radiative transfer. The first term on the right side represents the loss (attenuation) of radiance in the direction Θ due to both absorption and scattering, while the second term indicates the gain of radiance due to scattering from all other directions Θ' into the direction Θ.

In most applications the medium is horizontally stratified. Let the positive z axis point in the vertical direction, and let ds make an angle e (viewing zenith angle or emission angle, defined in figure 5.1) with dz, so that $ds = dz/\cos e$. Making this substitution and dividing through by $E(z)$ gives

(5.7) $$\frac{\cos e}{E(z)}\frac{\partial I(z,\Theta)}{\partial z} = -I(z,\Theta) + \frac{S(z)}{E(z)}\frac{1}{4\pi}\int_{4\pi} I(z,\Theta')\frac{G(z,\Theta',\Theta)}{S(z)}d\Theta' + \frac{F_S(z,\Theta)}{E(z)}$$

Let τ be the *optical depth*,

(5.8a) $$\tau = \int_s^\infty E(s')ds' / \cos e = \int_z^\infty E(z')dz'$$

so that

(5.8b) $$d\tau = -E(s)ds/\cos e = -E(z)dz$$

Radiance emitted vertically upward at altitude z within the scattering medium is reduced by a factor $e^{-\tau}$ by extinction as it propagates to the top of the medium. Conversely, light incident vertically on the top of the medium will be reduced in intensity by the same factor $e^{-\tau}$ as it penetrates to the altitude corresponding to τ.

Let $\omega(z)$ be the volume *single-scattering albedo*, $\omega(z) = S(z)/E(z)$, and let $p(z,\Theta',\Theta)$ be the *volume phase function*, $p(z,\Theta',\Theta) = G(z,\Theta',\Theta)/S(z)$. Then the equation of radiative transfer may be written

(5.10) $$\boxed{\mu \frac{\partial I(\tau,\Theta)}{\partial \tau} = I(\tau,\Theta) - \frac{\omega(\tau)}{4\pi} \int_{4\pi} I(\tau,\Theta') p(\tau,\Theta',\Theta) d\Theta' - J \frac{\omega(\tau)}{4\pi} p(\tau,\Theta_o,\Theta) e^{-\tau/\mu_o}}$$

where $\mu = \cos e$ and $\mu_o = \cos i$.
The radiance distribution of the atmosphere depends on both optical properties and surface reflectivity. Atmospheric properties determine the key parameters in the radiative transfer equation, such as the volume extinction coefficient, single-scattering albedo and phase function.
The surface influence is taken into account through the lower boundary condition.

In fact, the radiative transfer equation cannot be solved unless the boundary conditions are specified. For the 1D atmosphere, two boundary conditions are needed. At the top pf the atmosphere

(5.11) $$I(0,\Theta) = J\,\delta(\Theta - \Theta_o)$$

where δ is the Dirac delta function, indicating that the incoming radiation is from only one single direction Θ_o , at the specific incidence and azimuth angle (i, φ_o).

The lower boundary condition at the surface is

(5.12) $$I(\tau_t,\Theta) = \frac{1}{\pi} \int_{2\pi} r(\Theta',\Theta) I(\tau_t,\Theta') d\Theta' + J e^{-\tau_t/\mu_o} r(\Theta_o,\Theta)$$

where r is the bidirectional reflectance discussed in subsection 5.1.3. The first term of the right side of Eq. 5.12 corresponds to the diffuse sky radiance and the second term, the reflected direct solar radiation.

Before discussing how to solve the radiative transfer equation, it is necessary to know how to get the optical properties of the medium that are associated with the radiative transfer equation. The optical properties of a medium (see subsection 5.1.2) are determined by the particles that compose the medium and their properties. For spherical particles, their scattering behaviour only depends on the *refractive index* (also referred as *optical constants*; see subsection 5.2.5) and the *size parameter* defined as

(5.13) $$\chi = \frac{2\pi r}{\lambda}$$

where r is the radius of the sphere.
If the molecular particles of a medium are far smaller that the wavelength ($\chi << 1$), its scattering pattern can be calculated by the Rayleigh scattering law. When $\chi >> 1$, the scattering properties of a particle can be understood in terms of geometric optics. In all the other cases, the scattering by a perfect, uniform sphere is described by the *Mie theory*.

5.2.1 Mie scattering

The simplest case of single-particle scattering is that of a plane electromagnetic wave scattered by a uniform spherical particle. This problem was solved by Gustav Mie, and the result has come to be known as Mie theory. Frequently in the remote-sensing literature the term *Mie theory* or *Mie scattering* is used to refer to scattering by a particle large compared with the wavelength and of any shape. However, this is an incorrect and corrupt usage of the term, which refers *only* to scattering by an *isolated spherical* particle of *any* size.

Mie theory is treated in greater or lesser detail in a number of books, including the work of Born and Wolf (1980), Stratton (1941), and Van de Hulst (1957). The most readable, especially for the novice, are the books by Bohren and Huffman (1983) and Kerker (1969). The solution to the Mie problem is lengthy and complicated, and its details are outside of the scope of this thesis.

Many numerical codes for calculating the Mie quantities are available in the public domain. One of the best Mie code available, which has been used to computes all the single-scattering quantities needed in our work, is the FORTRAN MIEV0.f (W. J. Wiscombe, 1980 and 1996). For solving the atmospheric radiative transfer equation, we need only the phase function $P(g)$ and the single-scattering albedo ω (see paragraphs 5.1.2.3 and 5.1.2.4), which are the outputs of the MIEV0.f code. These quantities are needed to solve any multiple-scattering problem, regardless of the used theory or approximation, and their computation is thus very important for our work. To help understand and use the inputs and outputs of this Mie code, the resulting formulas are given below.

The exact expression for the element of the amplitude scattering matrix (2x2) for isotropic spherical particles illuminated by a linearly polarized plane electromagnetic wave are (Van de Hulst, 1981)

(5.14) $$S_{11}(\theta) = \sum_{n=1}^{\infty} \frac{2n+1}{n(n+1)} \{a_n \tau_n(\cos\theta) + b_n \pi_n(\cos\theta)\}$$

(5.15) $$S_{22}(\theta) = \sum_{n=1}^{\infty} \frac{2n+1}{n(n+1)} \{a_n \pi_n(\cos\theta) + b_n \tau_n(\cos\theta)\}$$

(5.16) $$S_{12}(\theta) = S_{21}(\theta) = 0$$

where

(5.17) $$a_n = \frac{\psi'_n(m\chi)\psi_n(\chi) - m\psi_n(m\chi)\psi'_n(\chi)}{\psi'_n(m\chi)\xi_n(\chi) - m\psi_n(m\chi)\xi'_n(\chi)}$$

(5.18) $$b_n = \frac{m\psi_n'(m\chi)\psi_n(\chi) - \psi_n(m\chi)\psi_n'(\chi)}{m\psi_n'(m\chi)\xi_n(\chi) - \psi_n(m\chi)\xi_n'(\chi)}$$

where $m = m_{re} - i\, m_{im}$ is the relative refractive index of the spherical particle with radius r (see Section 6.1), χ is the size parameter defined by Eq. 5.13,

(5.19) $$\psi_n(\chi) = \sqrt{\pi\chi 2} J_{n+1/2}(\chi)$$

(5.20) $$\xi_n(\chi) = \sqrt{\pi\chi/2} H_{n+1/2}(\chi)$$

The derivatives of these functions are denoted by primes. $J_{n+1/2}$ and $H_{n+1/2}$ are the Bessel and Hankel function, respectively. The angular functions are determined by the following formulas

(5.21) $$\pi_n(\cos\theta) = \frac{P_n^1(\cos\theta)}{\sin\theta}$$

(5.22) $$\tau_n(\cos\theta) = \frac{dP_n^1(\cos\theta)}{d\theta}$$

where θ is the scattering angle and $P_n^1(\cos\theta)$ is the first of the associated Legendre polynomials. Their most straightforward definition is in terms of derivatives of ordinary Legendre polynomials $P_n(\cos\theta)$

(5.23) $$P_n^k(x) = (-1)^k (1-x^2)^{k/2} \frac{d^k}{dk^k} P_n(x) \quad ; \quad P_n(x) = \frac{1}{2^n n!} \frac{d^n}{dx^n}\left[(x^2-1)^n\right]$$

The MIEV0.f FORTRAN code by W. J. Wiscombe (1980, and 1996) computes the following quantities:

Extinction efficiency:

(5.24) $$Q_E = \frac{2}{\chi^2} \sum_{n=1}^{\infty} (2n+1)\,\mathrm{Re}(a_n + b_n)$$

Scattering efficiency:

(5.25) $$Q_S = \frac{2}{\chi^2} \sum_{n=1}^{\infty} (2n+1)\left[|a_n|^2 + |b_n|^2\right]$$

Phase function:

(5.26) $$P(\theta) = \frac{2\left(|S_{11}|^2 + |S_{22}|^2\right)}{k^2 r^2 Q_S}$$

where $k = 2\pi/\lambda$.

Very often, the Legendre expansion coefficients of the phase function are also needed to solve the multiple scattering part of the Radiative Transfer (see paragraphs 5.3.2.1 and

6.2.1.2 for examples). It is thus convenient to represent $P(\theta)$ as a series of Legendre polynomials $P_n(\cos\theta)$:

$$P(\theta) = \sum_{n=0}^{\infty} (2n+1) c_n P_n(\cos\theta) \tag{5.27}$$

The normalization condition remains the same (Eq. 5.i).
The n-th expansion coefficient is given by

$$c_n = \frac{1}{2} \int_{-1}^{1} P_n(\cos\theta) P(\theta) d\cos\theta \tag{5.28}$$

and may also be outputted by the Mie code. c_1 is the *asymmetry factor* ξ defined in Eq. 5.j and represents the degree of asymmetry of the angular scattering; ξ = 0 represents isotropic scattering; ξ = − 1 represents complete backscattering; and ξ = 1 complete forward scattering. Further details on the Legendre polynomial expansion of the phase function will be discussed in subsection 5.2.4.

For particles with a size distribution $f(r)$, we can calculate the extinction and scattering coefficients σ_E, σ_S, phase function $P(\theta)$, single scattering albedo ω, and the asymmetry parameter ξ:

$$\sigma_E = N \int_0^{\infty} \pi r^2 Q_E f(r) dr \tag{5.29}$$

$$\sigma_S = N \int_0^{\infty} \pi r^2 Q_S f(r) dr \tag{5.30}$$

$$P(\theta) = \frac{2\pi N \int_0^{\infty} \left(|S_{11}|^2 + |S_{22}|^2 \right) f(r) dr}{k^2 \sigma_S} \tag{5.31}$$

$$g = \frac{\int_0^{\infty} r^2 Q_S g(r) f(r) dr}{\int_0^{\infty} r^2 Q_S f(r) dr} \tag{5.32}$$

$$\omega = \frac{\sigma_S}{\sigma_E} \tag{5.33}$$

where N is the total number of particles per unit volume given by

$$N = \int_{r_1}^{r_2} f(r) dr \tag{5.34}$$

We just discussed the scattering behaviour of a large particle and a group of particles using Mie theory. For a group of particles, we need to specify the particle size distribution function $f(r)$, which is the subject of the following subsection.

5.2.2 Particle Size Distributions

5.2.2.1 Moments of a Distribution

When a set of values has a sufficiently strong central tendency, that is, a tendency to cluster around some particular value, then it may be useful to characterize the set by a few numbers that are related to its *moments*, the sums of integer powers of the values.
Best known is the *mean* of the values $x_1, \ldots, x_N$,

$$\bar{x} = \frac{1}{N}\sum_{j=1}^{N} x_j \tag{5.35}$$

which estimates the value around which central clustering occurs. Note the use of an overbar to denote the mean; angle brackets are an equally common notation, e.g., $\langle x \rangle$. You should be aware that the mean is not the only available estimator of this quantity, nor is it necessarily the best one. For values drawn from a probability distribution with very broad "tails", the mean may converge poorly, or not at all, as the number of sampled points is increased. It may be then convenient to use an alternative estimator: the *mode*. The mode of a probability distribution function $p(x)$ is the value of x where it takes on a maximum value. The mode is useful primarily when there is a single, sharp maximum, in which case it estimates the central value. Occasionally, a distribution will be *bimodal*, with two relative maxima; then one may wish to know the two modes individually. Note that, in such cases, the mean is not very useful, since they it gives only a "compromise" value between the two peaks.

Having characterized a distribution's central value, one conventionally next characterizes its "width" or "variability" around that value. Here again, more than one measure is available. Most common is the *variance*,

$$\mathrm{Var}\,(x_1 \ldots x_N) = \frac{1}{N-1}\sum_{j=1}^{N}(x_j - \bar{x})^2 \tag{5.36}$$

or its square root, the *standard deviation*,

$$\sigma(x_1 \ldots x_N) = \sqrt{\mathrm{Var}\,(x_1 \ldots x_N)} \tag{5.37}$$

Equation 5.36 estimates the mean squared deviation of x from its mean value. As the mean depends on the first moment of the data, so do the variance and standard deviation depend on the second moment.

The *skewness* or *third moment* characterizes the degree of asymmetry of a distribution around its mean. While the mean and standard deviation are *dimensional* quantities, that is, have the same units as the measured quantities x_j, the skewness is conventionally defined in such a way as to make it *nondimensional*. It is a pure number that characterizes only the shape of the distribution. The usual definition is

$$\mathrm{Skew}(x_1 \ldots x_N) = \frac{1}{N}\sum_{j=1}^{N}\left[\frac{x_j - \bar{x}}{\sigma}\right]^3 \tag{5.38}$$

where $\sigma = \sigma(x_1 \ldots x_N)$ is the distribution's standard deviation defined above. A positive value of skewness signifies a distribution with an asymmetric tail extending out towards more

positive x; a negative value signifies a distribution whose tail extends out towards more negative x (see Figure 5.2).

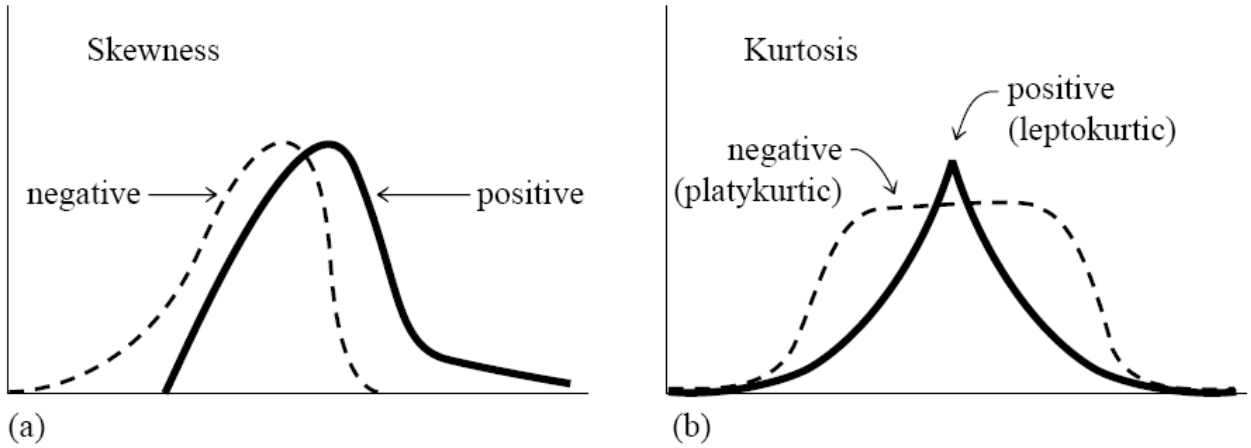

Figure 5.2. Distributions whose third and fourth moments are significantly different from a normal (Gaussian) distribution. (a) Skewness or third moment. (b) Kurtosis or fourth moment.

The *kurtosis* or *fourth moment* is also a nondimensional quantity. It measures the relative (to a normal distribution) peakedness or flatness of a distribution. A distribution with positive kurtosis is termed *leptokurtic*; a distribution with negative kurtosis is termed *platykurtic*; an in-between distribution is termed *mesokurtic* (see Figure 5.2). The conventional definition of the kurtosis is

$$\text{Kurt}(x_1 \ldots x_N) = \left\{ \frac{1}{N} \sum_{j=1}^{N} \left[\frac{x_j - \bar{x}}{\sigma} \right]^4 \right\} - 3 \tag{5.39}$$

where the – 3 term makes the value zero for a normal distribution.

5.2.2.2 Typical size distributions

In general, aerosol particle sizes (or snow grain radii) are not identical (monodisperse distribution). Their radii can be represented by many different functions, such as the power-law function, the modified gamma distribution function, and the lognormal distribution function. Letting $n(r)dr$ be the number of particles per unit volume in the size range r to $r + dr$, this distribution can be expressed as follows:

- The *power-law* (Junge) distribution:

$$n(r) = \begin{cases} Cr^{-\alpha} & r_1 \le r \le r_2 \\ 0 & \text{otherwise} \end{cases} \tag{5.40}$$

where α is a parameter between 2.5 and 5.0 for the natural aerosols.

- The *modified power-law* distribution:

(5.41) $$n(r) = \begin{cases} C \cdot \left(\dfrac{r}{r_1} \right)^{\alpha} & r_1 \le r \le r_2 \\ 0 & \text{otherwise} \end{cases}$$

- The *gamma* distribution (Hansen and Travis, 1974):

(5.42) $$n(r) = Cr^{(1-3b)/b} e^{-r/ab}$$

where a and b are parameters.

- The *modified gamma* distribution (Deirmidjian, 1964):

(5.43) $$n(r) = Cr^{\alpha} \exp\left[-\frac{\alpha}{\gamma} \left(\frac{r}{r_m} \right)^{\gamma} \right]$$

where r_m is the mode radius.

- The *lognormal* distribution:

(5.44) $$n(r) = Cr^{-1} \exp\left[\frac{-(\ln r / r_g)^2}{2\sigma_g^2} \right]$$

where r_g is the logarithmic mode radius of the distribution and σ_g is the standard deviation of the logarithms.

In the above equations, the constant C for each size distribution is chosen such that the size distribution satisfies the standard normalization

(5.45) $$\int_{r_{\min}}^{r_{\max}} n(r) dr = 1$$

Mathematically, particle radii in the modified gamma, lognormal, and gamma distributions may extend to infinity. However, a finite $r_{\max}$ must be chosen in actual computer calculations.

Often it is advantageous to express the size parameters of the different distributions in terms of two common parameters. This is useful for inter-comparisons between size distributions as well as in their retrieval. Such parameters are (Hansen and Travis, 1974) the area-weighted mean, or *effective radius* r_{eff}

(5.46) $$r_{eff} = \frac{\int_{r_1}^{r_2} \pi r^2 n(r) r dr}{\int_{r_1}^{r_2} \pi r^2 n(r) dr}$$

and the *effective variance* v_{eff}

$$v_{eff} = \frac{\int_{r_1}^{r_2} (r - r_{eff})^2 \pi r^2 n(r) r dr}{r_{eff}^2 \int_{r_1}^{r_2} \pi r^2 n(r) dr} \tag{5.47}$$

As we will see in the following paragraph, Martian aerosol particles have been characterized by various authors by the lognormal and the modified gamma distributions. It is thus useful to explicit the relation between r_{eff} , v_{eff} , and the parameters of the above distributions:

- The *gamma* distribution (Eq. 5.42) is often referred as the *standard distribution*, because it has the simple properties

$$\begin{aligned} a &= r_{eff} \\ b &= v_{eff} \end{aligned} \tag{5.48}$$

as may be verified by substitution into Eq. 5.46 and 5.47 with $r_1 = 0$ and $r_2 = \infty$.

- For the *lognormal* distribution (Eq. 5.44) we have

$$\begin{aligned} r_{eff} &= r_g e^{2.5\sigma_g^2} \\ v_{eff} &= e^{\sigma_g^2} - 1 \end{aligned} \tag{5.49}$$

- The effective radius for *modified gamma* distribution (Eq. 5.43) can be expressed in terms of the parameters of the distribution and the Gamma function Γ, as follows:

$$r_{eff} = \frac{1}{k} \cdot \frac{\Gamma\left(\frac{\alpha+4}{\gamma}\right)}{\Gamma\left(\frac{\alpha+3}{\gamma}\right)} \quad , \quad \text{where } k = \left(\frac{\alpha}{\gamma}\right)^{1/\gamma} \cdot \frac{1}{r_m} \tag{5.50}$$

Size distributions of Martian aerosols will be discussed in subsection 6.1.4; they represents a key parameter for the computation of the single scattering quantities of the Martian polar cap constituents, by means of Equations 5.29–5.33.

5.2.3 Nonspherical particles

Mie theory has found extensive applications since spherically shaped particles are frequent in nature. Atmospheric aerosols, however, may have nonspherical form for which Mie theory is not valid. There are two common approaches to calculating their scattering properties.

1. The first approach is to treat a nonspherical particle as a sphere with an equivalent diameter. Thus, Mie theory still can be used. Different methods have been used to determine the equivalent diameter, for example
   Volume diameter — the spherical volume V equals that of the nonspherical particle, $d = \sqrt[3]{6V/\pi}$.
   Surface diameter — the spherical surface area A equals that of the nonspherical particle, $d = \sqrt{A/\pi}$.
   Surface volume diameter — the sphere has the same ratio of external surface area A to the volume V as the spherical particle, $d = 6V/A$.
   This approach is easy to calculate but is only approximate.

2. The other approach is to develop more rigorous computational methods. For small particles, the T-matrix algorithm (Mishchenko 1993) is a good choice. For large particles, such as ice crystals, ray tracing methods are better (Takano and Liou 1989a, 1989b, 1995).

5.2.4 The Phase Function

As mentioned above, the Mie code outputs the single scattering albedo and phase function required by the radiative transfer calculations. The phase function is often expanded by the Legendre polynomials (Eq. 5.27). The expansion of the phase function in Legendre polynomials has the advantage that in slab geometry the intensity can be represented by a Fourier cosine series, and each expansion coefficient (i.e. intensity component) in the series satisfies an azimuthally independent, integro-differential radiative transfer equation. There is one equation associated with each cosine term, and these equations are uncoupled and mathematically identical. Thus, we can solve each of these equations with the same mathematical scheme (see paragraph 5.3.2.1).

For very small particles (i.e. size parameter much smaller than 1), the scattering phase function can be accurately determined from just a few Legendre polynomial expansion terms. For moderately larger particles, such as cloud droplets, the scattering phase function is strongly forward peaked. The Legendre polynomial series converges very slowly as the number of terms increases because of the δ-function-like forward peak feature.

The Delta-M method (W. J. Wiscombe, 1977), which takes advantage of the fact that the higher-order Legendre polynomial expansion terms contribute primarily to the δ-function-like forward peak (J. F. Potter, 1970), is a very efficient technique of removing the strong forward-scattering peak and reducing the error resulting from use of a limited number of Legendre polynomial expansion terms (so-called “streams”). The Delta-M method conserves most moments of a phase function and it provides accurate fluxes for optically thick media. But the Delta-M method can cause problems for radiance computations if there are not enough terms in the expansion. The ice phase function (Takano and Liou, 1992) has a sharp forward peak, a 23° halo and a 180° backscattering peak; thousand of Legendre expansion terms are required to reproduce the δ-function-like forward peak, and hundreds of terms are required to avoid negative phase function values for large scattering angles as well as for angles around 23°. For optically thin media (optical depth less than 1), use of the exact phase function for single scattering and a few moments of the phase function for multiple scattering calculation gives good accuracy for the radiance fields (Nakajima and Tanaka, 1988). However, for optically thicker media (such as the semi-infinite layers of the Martian polar caps), this correction may not be self-consistent.

With a limited number of polynomial terms, there are significant differences between a phase function and its Legendre polynomial expansion at large scattering angles, *which are important to satellite observations*. Since the CPU-time for computing the expansion coefficients (Eq. 5.28) is large, and for multiply scattered radiances with the discrete ordinate method (see paragraph 5.3.2.1) is proportional to the third power of the number of streams, accurate radiance computation is difficult to achieve because of the computational burden. To use a practical number of expansion terms, which means less CPU time, the truncation of the forward peak is required.

In the next paragraph we will compare the two available truncation schemes, namely the Delta-M and the δ-fit (Hu et al., 2000), which is an extension and an enhancement of the Delta-M scheme and provides the expansion coefficients through a weighted least-squares fitting procedure.

5.2.4.1 Improved Legendre polynomial approximation of the phase function: Delta-M and δ-Fit truncation schemes

A δ-function with an integration value f requires an infinite number of Legendre polynomial expansion terms and all expansion coefficients have the value f. To remove a δ-function-like forward peak, the Delta-M method replaces c_n of Equation 5.27 by $(c_n\text{-}f)/(1\text{-}f)$,

$$P_{\delta_M}(\theta) = \sum_{n=0}^{2N-1}(2n+1)\frac{(c_n - f)}{(1-f)}P_n(\cos\theta) \quad , \quad f = c_{2N} \tag{5.51}$$

For a given number of terms N, with this simple substitution, we may achieve significant improvements in the polynomial approximation of the phase function. Although both the standard Legendre polynomial expansion method (i.e. computing the first $2N$ - 1 expansion coefficients c_n of Equation 5.27) and the Delta-M method reproduce the exact phase function only when a sufficient number of terms is provided (that is when, for a given wavelength, the last coefficient of the expansion is $< 10^{-7}$), the Delta-M method gives in general much better approximations. For example, to reproduce the exact phase function of a 10 μm water ice particle in the whole spectral range [0.35–5.1] μm (i.e. the PFS spectral range, extended up to the visible), 512 streams are needed (Figure 5.3).

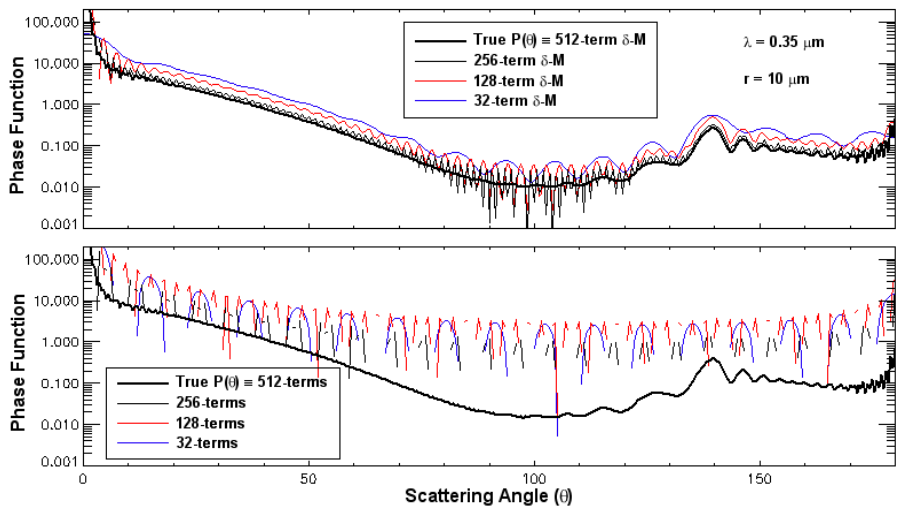

Figure 5.3. Phase function of a 10 μm water ice particle at λ = 0.35 μm, for different number of terms in the Legendre polynomial expansion. *Top*: Delta-M truncation scheme adopted. *Bottom*: standard expansion. Note the vertical log-scale.

If we use 256 and 128 streams, the expanded functions coincide with the exact function only in the reduced intervals [0.55–5.1] and [1.2–5.1] μm, respectively (the larger the size parameter, the higher the number of streams needed). Nevertheless, in both cases, the Delta-M method gives "acceptable" approximations of the phase function in the whole [0.35–5.1] μm spectral range. On the contrary, the standard expansion returns non-sense, unacceptable, positive-negative oscillatory functions. If in the above example we use 32 streams, the condition $c_n < 10^{-7}$ is unsatisfied in the entire spectral range considered. Once again, Delta-M method results may be considered as acceptable, while the standard expansion functions must be discarded.

If we consider larger particles (> 100 μm) or, equivalently, larger size parameters, the situation get worse. Thousands of streams are needed and, for a limited number of terms N, the phase function computed from Equation 5.51 can be very different from the actual phase function. For any given number of terms N, Equation 5.51 is not the best Legendre polynomial fitting of the phase function.

Hu et al., 2000, developed a robust technique which performs a least-square fitting to generate coefficients x_n of the Legendre polynomial expansion that minimize the relative difference ε between the approximate phase function $P'(\theta_i)$ and the actual phase function $P_{ac}(\theta_i)$:

$$\varepsilon = \sum_i w_i \left(\frac{P'(\theta_i)}{P_{ac}(\theta_i)} - 1 \right)^2 \tag{5.52}$$

$$P'(\theta_i) = \sum_{n=0}^{N_{str}} x_n p_n(\cos\theta_i) \tag{5.53}$$

were θ_i is the scattering angle, w_i is the weight for each scattering angle, $p_n(\cos\theta_i)$ is the nth-order Legendre polynomial, and N_{str} is the number of streams needed in order to achieve a desired accuracy.

With the δ-Fit the expansion coefficients x_n are computed by solving the least-squares fitting problem $\partial\varepsilon / \partial x_k = 0$ (k = 0, N_{str}):

$$\sum_{i=0} \frac{p_k(\cos\theta_i)}{P_{ac}(\theta_i)} w_i \left(\sum_{n=0}^{N_{str}} \frac{x_n p_n(\cos\theta_i)}{P_{ac}(\theta_i)} - 1 \right) = 0 \tag{5.54}$$

If the weights for the forward-scattering angles (e.g. $\theta < 3°$) are set to zero, x_0 will not vanish because the forward peak is automatically truncated (δ-function at 0° scattering angle) with truncation factor $f = 1 - x_0$. The normalized phase function $P_{\delta-Fit}(\theta)$ is

$$P_{\delta-Fit}(\theta_i) = \frac{1}{1-f} P'(\theta_i) \tag{5.55}$$

The advantages of the above method are:

- better estimation of phase function at large scattering angles with small phase function values;
- easy removal of the forward peak by selecting small weights for scattering angles close to zero;
- ability to keep the lowest several moments if needed.

The results can then be compared with the true phase function as well as the Delta-M method (Figure 5.4).

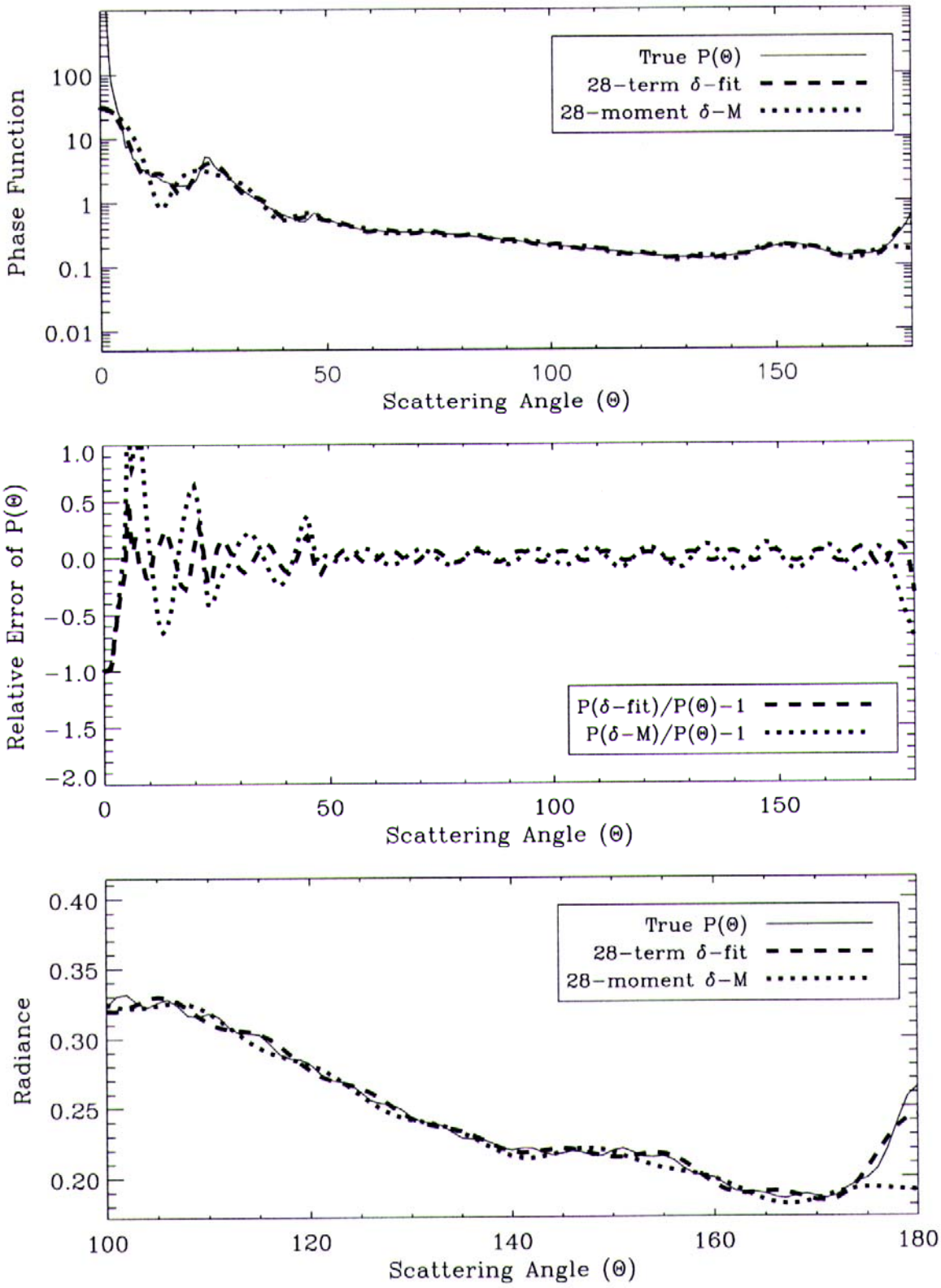

Figure 5.4. Ice cloud phase function (for λ = 0.55 μm, r = 10 μm) (*top*), differences among them (*middle*) and radiances (*bottom*): original phase function (*solid*), δ-Fit 28 term Legendre polynomial fits (*dash*), and Delta-M 28-moments of Legendre polynomial expansion (*dot*). (from Hu et al., 2000).

The actual procedure to fit the phase function is:

- interpolate the actual phase function $P_{ac}(\theta)$ to 361 scattering angles θ_i with half-degree equal intervals;
- select a forward peak removal angle θ_c. for $\theta_i < \theta_c$, $w_i = 0$;
- select an initial number of streams, N_{str}, and compute all required Legendre polynomials $p_n(\cos\theta_i)$ for $n \le N_{str}$;
- solve the linear equations $\partial\varepsilon / \partial x_k = 0$ to derive the coefficients x_n with the singular-value decomposition method;
- if ε is larger than expected, increase N_{str} and repeat the above procedures until ε is small enough;
- determine the scaling factor $f = 1 - x_0$ and renormalize the phase function (i.e. divide all x_n by x_0);
- adjust the single scattering albedo ω : $\omega' = (1 - f)\,\omega\,(1 - \omega f)^{-1}$ to subtract the removed forward δ-peak from the scattering cross section.

As Hu et al., 2000, pointed out, since the scattering phase function changes from 0.001 to ∞, it is crucial to treat the interpolation and integration properly. The 180° scattering angles are divided into 18 angular intervals and for each interval the use of 20 Lobatto quadrature points and weights for the integration is suggested. A four-point Lagrange interpolation scheme is suitable to take the curvature into account.

5.3 Solving Radiative Transfer Equation

Few readers need to write the codes to solve the radiative transfer equation for general applications since many radiative transfer solvers are available in the public domain (see subsection 5.3.4). Nevertheless, it is important to understand some of the basic principles.

5.3.1 Radiation Field decomposition

The standard practice now is to divide the total radiance into direct and diffuse components ($I = I_I + I_D$). The direct component (i.e., direct sunlight without scattering) in the downward direction is calculated from Beer's law:

(5.56) $$I_I(\tau,\Theta) = J\delta(\Theta - \Theta_o)e^{-\tau/\mu_o}$$

If we account for the upwelling reflected component into the diffuse component, the upwelling direct component is zero.

The radiative transfer equation for diffuse radiance $I_D(\tau, \Theta)$ can be written based on Eq. 5.10 as

(5.57) $$\mu\frac{\partial I_D(\tau,\Theta)}{\partial\tau} = I_D(\tau,\Theta) - \frac{\omega(\tau)}{4\pi}\int_{4\pi} I_D(\tau,\Theta')\,p(\tau,\Theta',\Theta)\,d\Theta' - J\frac{\omega(\tau)}{4\pi}\,p(\tau,\Theta_o,\Theta)e^{-\tau/\mu_o}$$

where the incoming radiation at the top of the atmosphere is zero

(5.58) $$I_D(0, \Theta) = 0$$

and the lower boundary condition is given by Eq. 5.12, by substituting $I(\tau, \Theta)$ with $I_D(\tau, \Theta)$. In the following paragraphs, we will drop the subscript D in the notation and discuss only the diffuse radiation.

Given the optical properties of the medium and their boundary conditions, the next key step is to solve the radiative transfer equation. There are roughly two types of algorithms, approximate solutions, and numerical solutions. Approximate solutions, such as two streams approximations (Meador and Weaver, 1980; Kaufman and Joseph, 1982; Liang and Strahler, 1994a) and four-stream approximations (liou, 1974; Liang and Strahler, 1994b), widely used in earlier radiative transfer calculations, are still used in GCM (Global Circulation Model) and other applications. With the rapid development of computer technology, more people tend to use numerical algorithms, which are computationally expensive but more accurate. In our work, we often have to compute thousand of synthetic spectra in order to best-fit the observations, and the use of numerical algorithms is unfeasible.

5.3.2 Numerical solutions

There are many different methods available to calculate the diffuse radiation field (e.g. Lenoble, 1985). The most known for the radiative transfer problem of an one-dimensional atmosphere are: method of successive orders of scattering and method of discrete ordinates. We will now briefly describe the method of discrete ordinates, which has been used in our work to validate the approximate-solution model we developed for the bidirectional reflectance (see paragraph 6.2.1.2).

5.3.2.1 Method of Discrete Ordinates

The idea of discrete ordinates is to replace the integrals in the radiative transfer equation with *Gauss quadrature* sums and thus transform the pair of coupled integral-differential equations into a system of coupled differential equations that are finally converted into a high-dimensional linear algebra system.

Gaussian quadrature points x_k have the property that

$$\int_a^b f(x)w(x)dx \approx \sum_{i=1}^{N} A_k f(x_k) \tag{5.59}$$

is *exact* if $f(x)$ is any polynomial of degree $\leq 2N - 1$. The values of the x_k are determined by the form of the weighting function $w(x)$ and the interval boundaries (a, b). In fact, the x_k are the roots of the orthogonal polynomial with weighting function $w(x)$ over the interval (a, b). For example, in radiative transfer calculations,

$$\int_{-1}^{1} I(\tau,\mu)d\mu \approx \sum_{i=1}^{N} w_i I(\tau,\mu_i) \tag{5.60}$$

where w_i is a quadrature weight and μ_i is the discrete ordinate. The low-order quadrature and weight are given in Table 5.1. For high-order quadrature and weights, some programs are available for easy calculation (e.g. Press et al., 1989)

Table 5.1 Low-Order Gaussian Quadrature Discrete Ordinates and Weights

M	i	μ_i	w_i
1	1	0.57735	1.00000
2	1	0.33998	0.65215
	2	0.86112	0.34785
3	1	0.23862	0.46791
	2	0.66121	0.36076
	3	0.93247	0.17132
4	1	0.18343	0.36268
	2	0.52553	0.31371
	3	0.79667	0.22238
	4	0.96029	0.10123
5	1	0.14887	0.29552
	2	0.43340	0.26927
	3	0.67941	0.21909
	4	0.86506	0.14945
	5	0.97391	0.06667
6	1	0.12523	0.24915
	2	0.36783	0.23349
	3	0.58732	0.20317
	4	0.76990	0.16008
	5	0.90412	0.10694
	6	0.98156	0.04718

Let us start from the elimination of dependence of the azimuth angle φ.

Radiance $I(\tau, \Theta) = I_D(\tau, \mu, \varphi)$ has three arguments. The typical approach is to expand radiance into the Fourier cosine series first:

$$I(\tau,\mu,\varphi) = \sum_{m=0}^{2N-1} I^m(\tau,\mu)\cos m(\varphi-\varphi_0) \tag{5.61}$$

The original radiative transfer equation 5.57 is replaced by $2N$ independent equations (one for each Fourier component), and the equation for each of the Fourier components is

$$\mu\frac{\partial I^m(\tau,\mu)}{\partial\tau} = I^m(\tau,\mu) - \frac{\omega(\tau)}{2}\int_{-1}^{1} I^m(\tau,\mu)p^m(\tau,\mu_i,\mu)d\mu_i - Jk_m\frac{\omega(\tau)}{4\pi}p^m(\tau,-\mu_o,\mu)e^{-\tau/\mu_o} \tag{5.62}$$

where $k_m = 1$ for $m = 0$ and $k_m = 2$ for $m \neq 0$, and the phase function is also expanded into Fourier series:

$$p(\tau,\mu,\varphi,\mu_i,\varphi_i) = \sum_{m=0}^{2N-1} p^m(\tau,\mu,\mu_i)\cos m(\varphi-\varphi_0) \tag{5.63}$$

The Fourier component of the phase function therefore is

$$p^m(\tau,\mu,\mu_i) = k_m\sum_{l=m}^{2N-1}(2l+1)\chi_l(\tau)\Lambda_l^m(\mu)\Lambda_l^m(\mu_i) \tag{5.64}$$

where $\chi_l(\tau)$ are the coefficient. The *normalized associated Legendre polynomial* is related to the associated Legendre polynomial $P_l^m(\mu)$ (Eq. 5.23) in the following way:

(5.65) $$\Lambda_l^m(\mu) = \sqrt{\frac{(l-m)!}{(l+m)!}} P_l^m(\mu)$$

After eliminating the dependence of the azimuth angle, the second step is to convert the continuous differential equation into a form suitable for numerical calculation by computer. If the integrals are replaced by quadratures, Eq. 5.62 becomes

(5.66) $$\mu \frac{\partial I^m(\tau, \mu_i)}{\partial \tau} = I^m(\tau, \mu_i) - \sum_{j=-N}^{N} w_j I^m(\tau, \mu_i) D^m(\tau, \mu_j, \mu_i) - Q^m(\tau, \mu_i)$$

where μ_i and w_i are quadrature points and weights and

(5.67) $$D^m(\tau, \mu_j, \mu_i) = \frac{\omega(\tau)}{2} \sum_{l=m}^{2N-1} (2l+1) \chi_l(\tau) \Lambda_l^m(\mu) \Lambda_l^m(\mu_i)$$

(5.68) $$Q^m(\tau, \mu_i) = Jk_m \frac{\omega(\tau)}{4\pi} e^{-\tau/\mu_o} \sum_{l=0}^{2N-1} (-1)^{l+m} (2l+1) \chi_l(\tau) \Lambda_l^m(\mu_0) \Lambda_l^m(\mu_i)$$

Since the single scattering albedo and the phase function are the function of τ in a vertically inhomogeneous atmosphere, Eq. 5.66 constitutes a system of $2N$ coupled differential equations with variable parameters for which analytic solutions do not exist. A common practice is to divide the atmosphere into L homogeneous layers in which the single scattering albedo and the phase function can be approximated as the same (see Fig. 5.5).

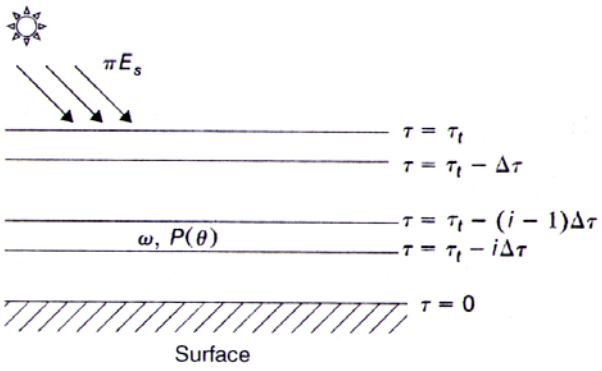

Figure 5.5. Atmospheric stratification for numerical calculation of radiative transfer. Each layer has different single scattering albedos (ω) and aerosol phase functions $P(\theta)$.

It is actually in the process of converting the continuous variable τ into a discrete format. For any layer in this figure, we can write Eq. 5.66 in matrix form as

(5.69) $$\begin{bmatrix} \frac{d\mathbf{I}^+}{d\tau} \\ \frac{d\mathbf{I}^-}{d\tau} \end{bmatrix} = \begin{bmatrix} -\alpha & -\beta \\ \beta & \alpha \end{bmatrix} \begin{bmatrix} \mathbf{I}^+ \\ \mathbf{I}^- \end{bmatrix} + \begin{bmatrix} \tilde{\mathbf{Q}}^+ \\ \tilde{\mathbf{Q}}^- \end{bmatrix}$$

where

$$
\begin{aligned}
&\mathbf{I}^{\pm} = \left\{ I^m(\tau, \pm\mu_i) \right\} && i = 1,\ldots,N \\
&\widetilde{\mathbf{Q}}^{\pm} = \mathbf{M}^{-1}\mathbf{Q}^{\pm} && \\
&\mathbf{Q}^{\pm} = \left\{ Q^m(\tau, \pm\mu_i) \right\} && i = 1,\ldots,N \\
&\mathbf{M} = \left\{ \mu_i \delta_{ij} \right\} && i, j = 1,\ldots,N \\
&\alpha = \mathbf{M}^{-1}\left(\mathbf{D}^{+}\mathbf{W} - \mathbf{1}\right) && \\
&\beta = \mathbf{M}^{-1}\mathbf{D}^{-}\mathbf{W} && \\
&\mathbf{W} = \left\{ w_i \delta_{ij} \right\} && i, j = 1,\ldots,N \\
&\mathbf{D}^{+} = \left\{ D^m(\mu_i, \mu_j) \right\} = \left\{ D^m(-\mu_i, -\mu_j) \right\} && i, j = 1,\ldots,N \\
&\mathbf{D}^{-} = \left\{ D^m(-\mu_i, \mu_j) \right\} = \left\{ D^m(\mu_i, -\mu_j) \right\} && i, j = 1,\ldots,N \\
&\mathbf{1} = \left\{ \delta_{ij} \right\} && i, j = 1,\ldots,N
\end{aligned}
\tag{5.70}
$$

Equation 5.69 is a system of $2N$-coupled ordinary differential equations with constant coefficients. Since they are linear, they can be solved using well-known methods of linear algebra. The first step is to seek the solution to the homogeneous version (i.e., $\widetilde{\mathbf{Q}} = 0$ of the equation system that is a standard algebraic eigenvalue problem of order $2N \times 2N$ determining the eigenvalues and eigenvectors). The second step is to obtain the particular solution with the source function. The general solution is the sum of the homogeneous solutions and the particular solutions. In a multilayered atmosphere, an integration is needed layer by layer to obtain the expressions for both upwelling and downward radiance at arbitrary τ and μ. The sum of all Fourier components through Eq. 5.61 gives the final solution. The details are omitted here, but interested readers should read the original papers and textbooks (e.g., Liou, 1980; Stamnes et al., 1988; Thomas and Stamnes, 1999). The discrete ordinate method has been implemented numerically into a FORTRAN code called DISORT (discrete ordinate radiative transfer) (Stamnes et al., 1988), which has been used in our work mainly to validate the approximate-solution model we developed for the bidirectional reflectance (see paragraph 6.2.1.2).

As Stamnes et al. (1988) summarized, this approach has many important features, some of which are:

- It is unconditionally stable for an arbitrarily large number of quadrature angles (streams) and arbitrarily large optical depths.
- It allows for an arbitrary bidirectional reflectivity at the lower boundary.
- It offers rapid computation of albedo and transmissivity when thermal sources are absent.
- Unlike the popular doubling method, computing time for individual layers is independent of optical thickness.

5.3.3 Approximate solutions: Two-Stream Algorithms

Although numerical radiative transfer solvers are widely available, some approximate methods are still used, primarily for calculating radiant flux (irradiance) or directional-hemispherical reflectance (albedo). In general, they cannot describe the radiance angular distribution accurately because of the nature of approximation.

For Eq. 5.66, if $N = 1$, we have a two-stream solution although it is seldom accurate and some special modifications are needed. If $N = 2$, we can obtain the four-stream solution that can be derived analytically (Liou, 1974; Liang and Strahler, 1994b). If the optical depth

is very large, such as in the semi-infinite particulate layers used in our models of the polar caps, the asymptotic fitting algorithm may be very suitable (King and Harshvardhan 1986). We will briefly discuss various two-stream algorithms as follows.

Meador and Weaver (1980) presented all existing two-stream approximations in identical forms of coupled differential equations for the integrated radiance over hemispheres and a set of common solutions for all approximations. We will first closely follow their notion for deriving the integrated radiance and then present different methods for calculating the angle-dependent radiance.

We will consider only the diffuse radiance here. The standard radiative transfer equation has been presented in Eq. 5.57. For the azimuthally integrate radiance $I(\tau,\mu)=\int_0^{2\pi} I(\tau,\mu,\varphi)d\varphi$, the radiative transfer equation, after the azimuthal integration, becomes

$$\mu\frac{\partial I(\tau,\mu)}{\partial\tau}=I_D(\tau,\mu)-\frac{\omega}{2}\int_{-1}^{1}p(\mu,\mu')I(\tau,\mu')d\mu'-J\frac{\omega(\tau)}{4\pi}p(\mu,-\mu_o)e^{-\tau/\mu_o} \tag{5.71}$$

where

$$p(\mu,\mu')=\sum_{n=0}^{\infty}(2n+1)g_nP_n(\mu)P_n(\mu') \quad , \quad g_n=\frac{1}{2}\int_{-1}^{1}P_n(\mu)p(\mu,1)d\mu \tag{5.72}$$

and $P_n(\mu)$ is the Legendre polynomial function of order *n*.

If we further integrate the azimuth-independent radiance $I^{\pm}(\tau)=\int_0^1 I(\tau,\pm\mu)\mu d\mu$ and integrate Eq. 5.71 in a similar way, we can obtain the following pair of equations

$$\frac{dI^+}{d\tau}=\int_0^1 I(\tau,\mu)d\mu-\frac{\omega}{2}\int_0^1\int_{-1}^1 p(\mu,\mu')I(\tau,\mu')d\mu'd\mu-J\omega\beta_0e^{-\tau/\mu_o} \tag{5.73}$$

and

$$\frac{dI^-}{d\tau}=-\int_0^1 I(\tau,-\mu)d\mu-\frac{\omega}{2}\int_0^1\int_{-1}^1 p(\mu,-\mu')I(\tau,\mu')d\mu'd\mu+J\omega(1-\beta_0)e^{-\tau/\mu_o} \tag{5.74}$$

where

$$\beta_i=\frac{1}{2}\int_0^1 p(\mu_i,-\mu')d\mu'=1-\frac{1}{2}\int_0^1 p(\mu_i,\mu')d\mu' \tag{5.75}$$

Different approaches have been proposed to simplify these two equations, which lead to different two-stream approximations, but all of them can be presented in a unified expression:

$$\frac{dI^+}{d\tau}=\gamma_1I^+-\gamma_2I^--\gamma_3J\varpi e^{-\tau/\mu_o} \tag{5.76}$$

(5.77) $$\frac{dI^-}{d\tau} = \gamma_2 I^+ - \gamma_1 I^- + \gamma_4 J \varpi e^{-\tau/\mu_0}$$

where γ_i are listed in Table 5.2 corresponding to different two-stream approximations, and $\gamma_3 + \gamma_4 = 1$.

Table 5.2 Parameters in Two-Stream formulas

Algorithm	γ_1	γ_2	γ_3
Eddington	$\frac{1}{4}\{7 - \omega(4 + 3g)\}$	$-\frac{1}{4}\{7 - \omega(4 - 3g)\}$	$\frac{1}{4}(2 - 3g\,\mu_0)$
Modified Eddington	$\frac{1}{4}\{7 - \omega(4 + 3g)\}$	$-\frac{1}{4}\{7 - \omega(4 - 3g)\}$	β_0
Quadrature	$\sqrt{3}/2\{2 - \omega(1 + g)\}$	$\sqrt{3}/2\{2 - \omega(1 + g)\}$	$\frac{1}{4}(2 - 3g\,\mu_0)$
Modified quadrature	$\sqrt{3}\{1 - \omega(1 - \beta_1)\}$	$\sqrt{3}\,\omega\beta_1$	β_0
Hemispheric constant	$2\{1 - \omega(1 - \beta_1)\}$	$2\,\omega\beta_1$	β_0
Delta function	$\sqrt{3}\{1 - \omega(1 - \beta_1)\}$	$\omega\beta_1$	β_0
Hybrid method	$\frac{t_1 = 7 - 3g^2 - \omega(4 + 3g)}{4[1 - g^2(1 - \mu_0)]}$	$-\frac{t_2 = 1 - g^2 - \omega(4 - 3g)}{4[1 - g^2(1 - \mu_0)]}$	β_0

Source: Meador and Weaver (1980).

*β_1 corresponds to $\mu_1 = 3^{-1/2}$

As discussed in subsection 5.2.4, for most particles the calculated phase function may have a very sharp peak in the forward direction (see Fig. 5.4) and usually requires hundreds of terms in a Legendre polynomial expansion. A scaling approximation is a procedure that assumes that photons scattered within the peak are not scattered at all, and thus the accuracy is not significantly reduced if we scale the single scattering albedo and optical depth as follows:

(5.78) $$\tilde{\omega} = \frac{(1 - f)\omega}{1 - \omega f}$$

(5.79) $$\tilde{\tau} = (1 - \omega f)$$

where f is the fraction of the phase function within the forward peak. The value of f may be determined in various ways (e.g the Delta-M method, which has been discussed in paragraph 5.2.4.1), but $f = \xi$ is often used where ξ is the asymmetry factor The approximation with such a scaling is usually called a δ-approximation.

We will use the results presented here in the next chapter (subsection 6.2.1.1) to discuss a possible multiple scattering approximate solution for angular reflectance from snow (both H_2O and CO_2), as derived by Wiscombe and Warren, 1980a, 1980b, and 1990.

5.3.4 Available software packages

We have just discussed the general principles of one numerical method and one approximate method for solving radiative transfer equations. Under most circumstances,

we do not need to code these algorithms as a user since many radiative transfer solvers (software packages) are available in the public domain. Table 5.3 lists some of the them. Although the www or ftp addresses are given, keep in mind that they may be changed from time to time. No attempt was made to conduct the detailed analysis and comparison of these codes, although some general comments are provided in the table.

Table 5.3 Typical Radiative Transfer Solvers

Name	Author	Type	Description
STREAMER	Key (1998)	Discrete ordinate (atmosphere)	STREAMER is a radiative transfer model that can be used for computing either radiances (intensities) or irradiances (fluxes) for a wide variety of atmospheric and surface conditions (available from http://stratus.ssec.wisc.edu/ streamer/streamer.html)
HYDROLIGHT	Mobley(1994)	Invariant embedding (ocean)	HYDROLIGHT is a radiative transfer numerical model that computes radiance distributions and derived quantities for natural water bodies, it is based on the invariant imbedding numerical algorithm (available from http://www.sequoiasci.com/publications2.asp?a_id=9)
DISORT	Stamnes et al. (1988)	Discrete ordinate	DISORT is one of the most heavily tested radiative transfer code available for A/-stream plane-parallel atmospheric cases (available from fttp://climate.gsfc.nasa.gov/pub/wiscombe/Dis_Ord)
SBDART	Ricchiazzi et al. (1998)	Revised DISORT	SBDART (Santa Barbara DISORT atmospheric radiative transfer) is a FOR-TRAN computer code designed for the analysis of a wide variety of radiative transfer problems encountered in satellite remote sensing and atmospheric energy budget studies (available from http://www.icess.ucsb.edu/esrg/paulsdir/)
Clirad_sw, clirad_lw	Chou (1990)	Two-stream	Radiative transfer code used in global circulation models and mesoscale models (developed at NASA Goddard; (available from http://climate.gsfc.nasa.gov/~chou/clirad.sw/ or http://climate.gsfc.nasa.gov/~chou/clirad.lw/)
FEMRAD	Kisselev et al. (1994)	Finite element	FEMRAD is a FORTRAN code based on the finite element method (FEM) for the solution of the radiative transfer equation (available from http://atol.ucsd.edu/~)
SHDOM	Evans(1998)	Discrete ordinate	This program computes unpolarized monochromatic or spectral band radiative transfer in a one-, two-, or three-dimensional medium for either collimated solar and/or thermal emission sources of radiation (available from http://nit.colorado.edu/~evans/shdom.html)
PolRadTran	Evans and Stephens (1991)	Discrete ordinate	PolRadTran is a plane-parallel fully polarized atmospheric radiative transfer model (available from http://nit.colorado.edu/~evans/polrad.html)
mc-layer	Macke (1999)	Monte Carlo	Monte Carlo radiative transfer code for multiple scattering in vertically inhomoge-neous atmospheres (available from http://www.ifm.unikiel.de/me/research/Projekte/RemSens/SourceCodes/ source.html)
MCML	Wang and Jacques (1995)	Monte Carlo	MCML is a steady-state Monte Carlo simulation program for multilayered turbid media with an infinitely narrow photon beam as the light source; each layer has its own optical properties of absorption, scattering, anisotropy, and refractive index (available from http://ee.ogi.edu/omlc/science/software/mc/index.htm)
DOM VDOM	Haferman (1993)	Discrete ordinate	Three-dimensional (3D) discrete ordinates method (available from ftp://iihr.uiowa.edu/pub/hml/haferman)
libRadtran	Kylling and Mayer		libRadtran is a collection of C and FORTRAN functions and programs for calculation of solar and thermal radiation in Earth's atmosphere (available from http://www.1ibradtran.org)
MODTRAN	Anderson et al. (2001)	Discrete ordinate	This is the one of the most widely used radiative transfer simulation codes for remote sensing and other applications; UNIX version: http://www.vsbm.plh.af.mil/soft/modtran4.html PC version: www.ontar.com Parallel machine: www.hpc.jpl.nasa.gov/PEP/wangp/ParaModtra
6S	Vermote et al. (1997)	Successive orders of scattering	6S (second simulation of satellite signals in the solar spectrum) has been widely used in optical remote sensing; many sensor spectral response functions are incorporated; covers wavelength 0.4-2.5 μm. (available at ftp://loaser.univ-lillel.fr/ or ftp://kratmos.gsfc.nasa.gov/6S/)

6 MODELING THE SPECTRAL PROPERTIES OF ICES

Soil and snow play very important interactive roles in the surface radiation budget because of their high albedo values. There are important similarities between modeling the bidirectional reflectances of soils and snow. These similarities include the fact that they are both characterizations of dense particulate media that can be models as spheroids, surface roughness on the order of millimeters to centimeters, and anisotropic diffuse and direct solar illumination irradiance. This chapter introduces their reflectance models together, including mainly radiative transfer models.

Section 6.1 introduces the basic concepts of the single-scattering properties of a single particle. To calculate multiple scattering of radiation by snow and soil, one must begin with knowledge of the single particle properties that govern the ensemble properties of the bulk medium. For both snow and soil, the individual particles are often characterized as simple spheres but may also be represented as other geometric shapes (cylinders, hexagonal plates) or as irregularly shaped particles. In this section, individual particle characterizations and single scattering properties for H_20 and CO_2 snow, and Martian dust particles are examined.

Section 6.2 discusses commonly used methods for calculating multiple scattering from snow and soil. These methods fall into two categories: approximate and numerical solutions to the equation of radiative transfer. They have been optimized for the purposes of these thesis, and extensively used as a fundamental tool in our work as described in the next Chapter.

6.1 Single scattering properties of ices and dust

As introduced in Section 5.2, the single particle scattering and absorbing quantities that are required for calculation of multiple scattering are, regardless of the used theory, algorithm or approximation, (1) the single scattering albedo, ω, which represents the probability that light incident on a particle will be scattered; and (2) the particle scattering phase function $p(\theta)$, where θ is the scattering angle, which describes the angular distribution of the photons scattered by a single particle.

If snow and dust particles can be assumed to behave as spheres and the size distribution and refractive indices of components comprising the particulate media are known, then Mie theory (van de Hulst 1980, Bohren and Huffman 1983) can provide the optical parameters of individual particles. Subsection 5.1.1 has discussed this topic. For axially symmetric nonspherical particles with size parameters less than about 130, Mishchenko (1991, 1993) has developed the T-matrix approach to compute the optical parameters. For nonspherical particles that are large relative to the wavelength, the geometric optics method can be used to compute the single scattering albedo and asymmetry parameter. This topic has been discussed in Section 5.2.3.

The single-scattering calculation at a particular wavelength λ requires as input

(3) the *size parameter* $x = 2\pi r/\lambda$, i.e. the ratio of the particle's circumference to the wavelength;

(4) the *complex index of refraction* m at that wavelength; $m = m_{re} - i m_{im}$, where m_{re} is the ordinary refractive index which determines the phase speed and m_{im} is related to the linear absorption coefficient as $K_{abs} = 4\pi m_{im}/\lambda$.

m_{re} and m_{im} are together called the *optical constants*.

In our work, the single-scattering calculation follows the "exact" Mie theory, using the algorithm of Wiscombe, 1980 and 1996, described in subsection 5.2.1 or (for $x > 2000$) the asymptotic formulae of Nussenzveig and Wiscombe, 1980.

6.1.1 Optical constants of CO_2 ice

Laboratory measurements of the absorption spectrum of pure solid CO2 were reviewed by Warren, 1986, who also compiled a set of values for radiation modeling. However, there are considerable uncertainties in that compilation, in nearly all spectral regions except the strong absorption bands at 4-μm and 15-μm wavelength.

At that date, the near-infrared region, 1.0-2.5 μm, was never been measured. The visible and near-visible, 0.3-1.0 μm, were measured by Egan and Spagnolo, 1969, but they used unpurified commercial dry ice, and it is difficult to rule out the presence of trace amounts of an absorptive impurity. Spectral transmittance for the infrared region, 2.5-25 μm, was measured by Ditteon and Kieffer, 1979, but their crystals were poorly formed and probably scattered as much light as they absorbed. The amount of scattering has been estimated (Ditteon and Kieffer, 1979; Warren, 1986), but it is quite uncertain, so the optical constants in this spectral region are correspondingly uncertain. Finally, the spectrum was never been measured beyond 25-μm wavelength.

The optical constants of solid carbon dioxide are needed to accurately reproduce the measured spectra and to calculate the energy balance of the seasonal polar caps of Mars, which are composed primarily of CO_2 ice (see Chapter 1). Since only a few measurements of uncertain accuracy were made in the broad wavelength regions of weak absorption between the isolated narrow infrared absorption bands of solid CO_2, a laboratory experiment was undertaken to improve on and extend the wavelength range of the previous data by measuring transmission through thick samples of high quality to determine the spectral absorption coefficient K_{abs} in infrared wavelength regions of low absorption from ultraviolet to far-infrared (i.e. between 0.17 and 333 μm) (G. B. Hansen, 1997a, 1997b, 2005). A technique was developed to grow clear, thick CO_2 ice samples from the gas at a temperature of 150 K (i.e. the CO_2 condensation temperature on Mars), with optical path lengths between 1.6 and 107.5 mm. The extremely fine spectral structure of this material was measured using resolutions finer than 0.5 cm^{-1}.

Absorption coefficients obtained from these new measurements are an order of magnitude or more lower than earlier estimates in the transparent wavelength regions between the strong infrared bands. Also, many weak bands between 1.2 and 5.2 μm (which is essentially the spectral range of the PFS SWC; see Section 2.2)), which were only poorly defined previously, have been more accurately measured.

The optical constants of CO_2 derived from these measurements have been used in our work (G. B. Hansen, 1997a, 1997b, 2005; G. B. Hansen, personal communication). They are shown on Figure 6.1 for the spectral region of our interest.

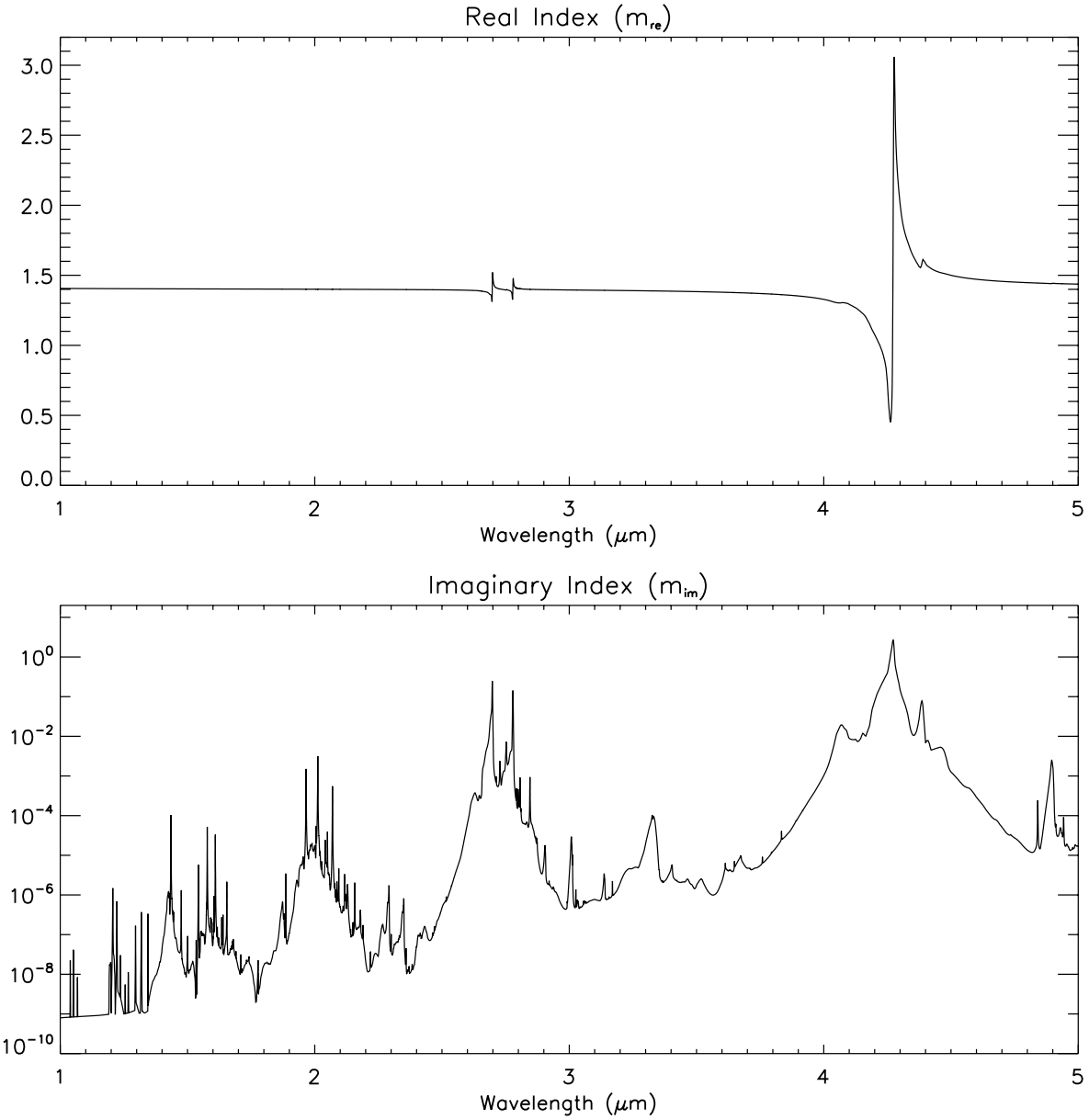

Figure 6.1. CO_2 ice refractive indexes used in our work (Hansen 2005, personal communication)

6.1.2 Optical constants of H_2O ice

The laboratory measurements of the absorption spectrum of water ice were reviewed by Warren, 1984. The work was aimed at the Earth science community, and hence concentrated on measurements made within 30–40 degrees of the freezing point. He made a major adjustment to the 45-μm band due to the lack of any measurements of this region at warmer temperatures. The numbers in this review are only applicable to temperatures near 250 K. It was noted by Warren that the optical properties were quite different at lower temperatures even at wavelengths outside the very sensitive 45-μm lattice absorption. For ice at the temperatures expected in the Martian polar cap mixtures (i.e. 150 K), one must consult other literature. Although several measurements are available of the optical constants of hexagonal ice for T > 50 K, most of these measurements are of thin films, limited to about 100 μm thickness, and thus unable to accurately measure the more transparent region below 2.5 μm.

A new set of thick-film measurements which provide temperature-dependent absorption coefficients of water ice from 20 to 270 K has been completed by Grundy and Schmitt, 1998. The data presented in that paper by are the result of fitting the absorption coefficient spectrum with a set of 17 Gaussian functions. The Gaussian functions were chosen such that the same set, with frequencies, widths, and intensities smoothly varying with temperature, were able to fit the absorption coefficient spectrum at all the temperatures considered (20–270 K). The fitted parameters corresponding to the Gaussian functions were then used to parameterize the temperature-dependent water ice absorption coefficient spectrum. The results of Grundy and Schmitt, 1998, cover only a limited range of the near infrared, from 1 to 2.5 μm. A review of the available measurements come from Rajaram *et al.*, 2001. They also provided new results in the 1.4–2.5 μm spectral range for temperatures between 166 and 196 K. Beyond 2.5 μm, the data are more sparse and for temperatures ≥ 166 K. Table 6.1 summarizes the various experimental measurements of the optical constants and absorption coefficients of water ice availablein the near infrared.

Table 6.1 Summary of experimental measurements of the optical constants of water ice in the Near Infrared

Author	Temperature (K)	Sample Thickness	Sample preparation	Optical Constant Determined
Rajaram *et al.*, 2001	166	16 films, ~255–956 μm	Condensing water vapour on a cold silicon surface	Real and imaginary index with an iterative Kramers–Kronig analysis
	176	14 films, ~267–1055 μm		
	186	19 films, ~247–1164 μm		
	196	18 films, ~264–1135 μm		
Grundy and Schmitt, 1998	20-270	10 μm – 1 cm	Monocrystalline samples prepared in closed cells	Absorption coefficient
Gosse *et al.*, 1995	251	2 films < 1 and 309 μm	Wedged cell arrangement placed inside a cryostat	Imaginary index, from $K_{abs} = 4\pi m_{im}/\lambda$
Toon *et al.*, 1994	166	0–30 μm	Condensing water vapour on a cold silicon surface	Real and imaginary index using an iterative Kramers–Kronig analysis
Kou *et al.*, 1993	248	116–269 μm	Drop of water placed between windows in a temperature-controlled cryostat	Imaginary index, from $K_{abs} = 4\pi m_{im}/\lambda$
Ockman, 1958	247	358 μm	Single crystal grown in glass cell	Absorption coefficient

As can be seen from table 6.1, the only measurements available at 150 K are those of Grundy and Schmitt, 1998. In principle, one can use such optical constants up to 2.5 μm, and above 2.5 μm, where the dependence on the temperature is much less important, those of Warren, 1984. However, we have found that the results of Grundy and Schmitt, 1998, in the 1–1.5 μm are whether too noisy or not enough accurate (absorption coefficients goes negative!) to be used in our work, especially in the 1.085-μm absorption band, which is the most sensitive to temperature variations (see Figure 6.2).

A set of recommended values of H_2O ice optical constants for radiation modeling, for a wide spectral interval including visible, thermal and near infrared, and for temperatures of 130–150 K appropriate to the Martian polar cap mixtures (and to the large and medium satellites of Jupiter, Saturn, and the rings of Saturn, which they were compiled for) was compiled by Hansen et. al, 1997c. These are the optical constants of water ice used in our work, and are shown on Figure 6.2 for the spectral region of our interest (Hansen, 2005, personal communication).

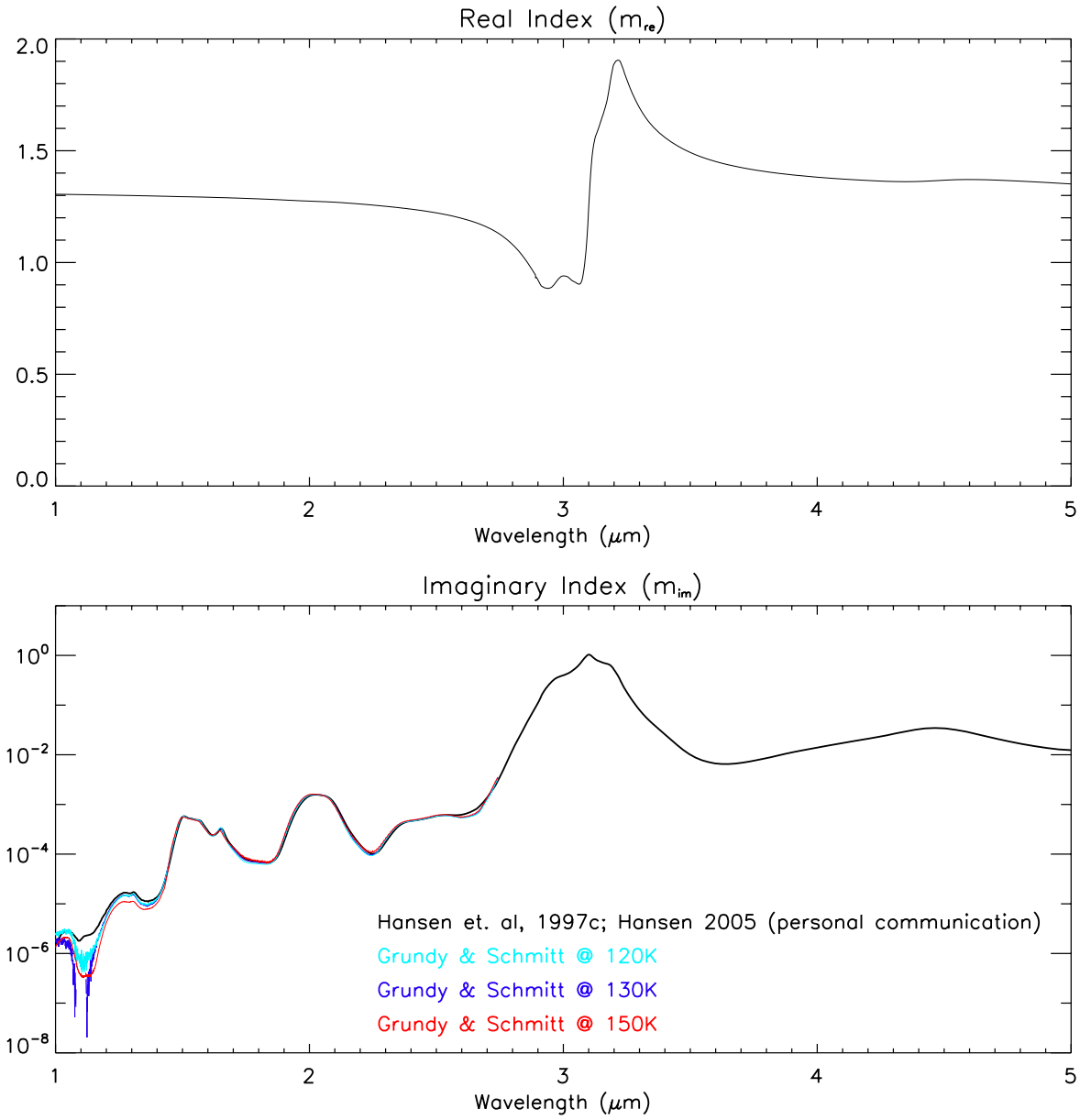

Figure 6.2. H_2O ice refractive indexes used in our work. *Top*: Real index of refraction. *Bottom*: Complex index of refraction used in our work (*black*, entire range) compared to those by Grundy and Schmitt, 1988, for three different temperatures (*coloured*, up to ~2.7 μm). See text for details.

6.1.3 Optical constants of Martian dust

Until recently, Martian aerosol spectra have been fit only with modelled laboratory spectra of terrestrial analogs (e.g. the *montmorillonite-basalt* dust composition by Toon *et al.*, 1977; and the *palagonite-like* composition by Clancy *et al.*, 1995 and more recent Ockert-Bell *et al.*, 1997, based on the Roush *et al.*, 1991, palagonite sample). When these optical constants were used in models of dusty CO_2 ice, poor fits to polar spectra in the 20–50 μm region resulted (Hansen, 1999). To model the mixture of dust and ice in the Martian polar caps, optical constants which best fit the measured spectra are desired.

Model dust optical properties that are based on spectra of Mars aerosols have been recently obtained using both Mariner 9 infrared spectra (Snook *et al.*, 1999) and Mars Global Surveyor (MGS) Thermal Emission Spectrometer (TES) spectra (Snook *et al.*, 2000).

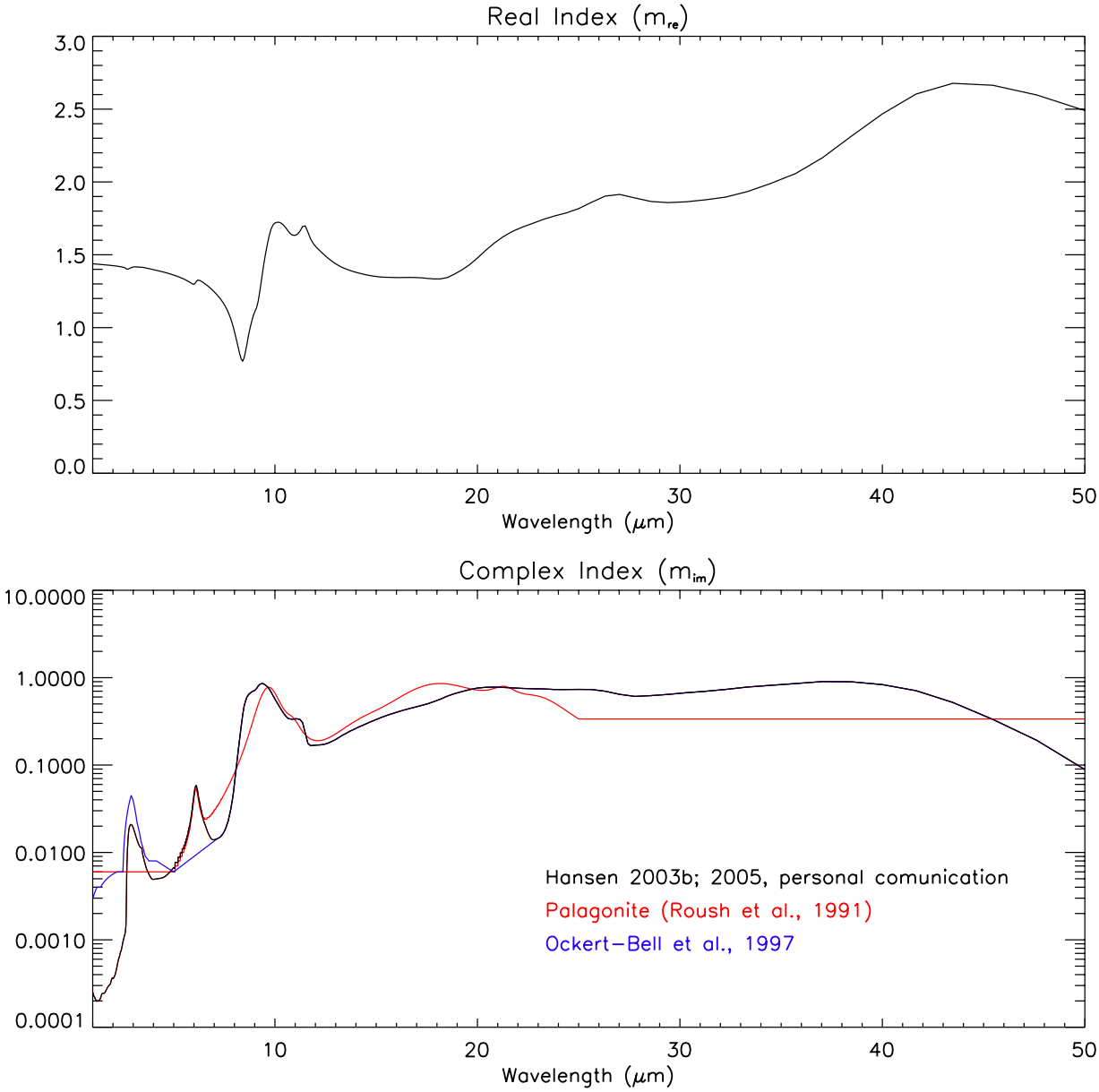

Figure 6.3. Refractive indexes of Martian dust used in our work. *Top*: Real index of refraction. *Bottom*: Complex index of refraction used in our work (*black*) compared to original palagonite sample (*red*) and that by Ockert-Bell, 1977 (*blue*).

More recently, an independent study of the infrared dust signature in the Mariner 9 spectra has been performed by G. B. Hansen (2003b), with particular emphasis on the high precision results necessary for the analysis of high spectral resolution data. Using the optical constants derived from this study, fits to polar ice spectra are greatly improved (Hansen, 2003b). These are the optical constants for Martian dust used in our work, and are shown on Figure 6.3 (Hansen, 2005, personal communication).

6.1.4 Size distributions of Martian aerosols

Martian aerosols are essentially dust and water ice. Excellent reviews and summaries of existing works on Martian aerosol properties can be found in the literature (e.g., Clancy *et al.*, 2003), and thus comprehensive duplication here is not repeated.

For dust, a thorough discussion may be found in the combination of several key works (e.g., Clancy and Lee, 1991; Murphy *et al.*, 1993; Clancy *et al.*, 1995; Pollack *et al.*, 1995; Ockert-Bell *et al.*, 1997; Tomasko *et al.*, 1999, and references therein), while work on water ice is somewhat less voluminous (e.g., Pearl *et al.*, 2001; Glenar *et al.*, 2003, and references therein).
For the purposes of our work, it is sufficient to briefly mention the results relevant to particle size and variations thereof. These results will be used in our single-scattering computations and represent a key parameter for the calculation of synthetic spectra to best-fit the PFS observations of the Martian polar caps. They will be presented here in chronological order. The distribution functions recalled below have been introduced in paragraph 5.2.2.2; the same notation of the parameters has been kept.

Dust
Toon *et al.* (1977) used the infrared spectra obtained from the Mariner 9 spacecraft during the 1971–1972 dust storm to derive information on the composition and particle size distribution of the dust. They found a best fit of the observations for a *montmorillonite-basalt* dust composition and a modified gamma size distribution with r_m = 0.4 μm, α = 2 and γ = 0.5, which correspond to an effective radius of r_{eff} = 2.75 μm and effective variance of ν_{eff} = 0.4 μm.

Pollack *et al.* (1995) analyzed three sets of Viking Lander 1 and 2 images of the Martian atmosphere to better evaluate the radiative properties of the atmospheric dust particles. The properties of interest were, among others, the first two moments of the size distribution of the particles. By using a lognormal particle size distribution, the geometric cross-section weighted mean radius r_{eff} was found to be 1.85 μm at VL2 during northern summer when dust loading was low and 1.52 μm at VL1 during the first dust storm. In both cases the best cross-section weighted mean variance ν_{eff} of the size distribution was equal to 0.5 μm.

Clancy *et al.* (1995) proposed key modifications to the Toon *et al.* (1977) model of the particle size distribution and composition of Mars atmospheric dust, based on a variety of spacecraft and wavelength observations of the dust (Mariner 9, Viking, and PHOBOS). A much broader ($\nu_{eff} \sim$ 0.8 μm), smaller particle size (r_{eff} = 1.8 μm, corresponding to a mode radius for the modified gamma distribution of $r_m \sim$ 0.02 μm) distribution coupled with a '*palagonite-like*' composition (based on the Rousch *et al.*, 1991, palagonite sample) was argued to fit the complete ultraviolet-to-30-μm absorption properties of the dust better than the dust model of Toon *et al.* (1977). Essentially, the nanocrystalline structure of palagonite coupled with the smaller, broader distribution of dust particle sizes provides a more consistent fit than the Toon *et al.* model of the dust to the IRIS spectra, the observed visible/9-μm dust opacity ratio, the Phobos occultation measurements of the dust particle sizes (Chassefiere *et al.*, 1992), and the weakness of surface near IR absorptions expected for clay minerals (Bell and Crisp, 1993).

K. Snook, 1999, reanalyzed the Mariner 9 observations of the global Martian dust storm in 1971-1972; theoretical spectra of the emergent intensity from Martian dust clouds were generated using a 2-stream source-function radiative transfer code (see subsection 5.3.3). The particle size distribution corresponding to the best fit was a lognormal distribution with a mean particle radius, r_m = 0.66 μm, and variance, σ^2 = 0.412 (r_{eff} = 1.85 μm, ν_{eff} = 0.51 μm), in close agreement with the size distribution found by Clancy *et al.*, 1995.

The Imager for Mars Pathfinder (IMP) returned sequences of images of the Martian sky characterizing the size distribution, optical constants, and nature of the aerosols suspended in the atmosphere of Mars. These data were analyzed by Tomasko *et al*, 1999. Results included the following: the geometric cross-section-weighted mean particle radius

was r_{eff} = 1.6 μm, almost independent of the assumed width (variance) of the size distribution; the variance of the gamma size distribution v_{eff} was difficult to constrain from the observations alone, since good fits were possible from less than 0.2 to 0.5 μm or more. Overall, the results for the mean cross-section-weighted size are in remarkably good agreement with the revised analysis by Pollack *et al.*, 1995, of the observations made by the Viking lander 20 years earlier.

New insights into Martian dust distribution may be found in Montmessin *et al.*, 2002, where a direct method which combines microphysics and photometric simulations of the Martian atmosphere is used. This approach allowed to reproduce vertical profiles of the light scattered by the haze at the limb of Mars. Subsequent results were compared to a multiple-color image provided by the Viking Orbiter camera. One of the "free parameters" of this study was dust size distribution. Except for an unlikely distribution of submicron particles (r_{eff} ~ 0.2 μm), no consistent fit could be obtained. The results were not in agreement with the size distributions of dust suggested by previous studies. This apparent discrepancy could be resolved by adding a separate peak of submicron particles to the size distribution previously extracted from Viking Lander images. Only in that case could spectral and vertical structures of haze be successfully matched. As the authors pointed out, while a bimodal distribution would change the current picture of Martian dust, such distribution is a common representation of soil-derived aerosol size function in Earth deserts.

Recently, aerosol particle sizes independently determined from TES observations by quantitatively accurate visible/IR optical depth ratios (Clancy *et al.*, 2003) and IR spectral fits (Wolff and Clancy, 2003) have been compared, providing particularly sensitive definitions of particle size and variations thereof of Mars ice and dust aerosols. The typical dust particle sizes found in these works is r_{eff} = 1.5 μm (and v_{eff} = 0.4 μm, same as in Toon *et al.*, 1977), in agreement with Pathfinder measurements (Tomasko *et al.*, 1999) and reanalyses of Viking observations (Clancy *et al.*, 1995; Pollack *et al.*, 1995). However, dust particle sizes also exhibit significant variations, contrary to previous inferences (e.g., Toon *et al.*, 1977; Tomasko *et al.*, 1999). In particular, very small dust particle sizes (r_{eff} = 1.0 μm) appear common over northern latitudes for the seasonal ranges Ls = 40–200° and 320–340°, and significantly larger dust particle sizes (r_{eff} = 1.8–2.5 μm) were found at southern latitudes during the 2001 global dust storm.

Essentially, the most recent (i.e., 1995-present) work is consistent in deriving an average size (r_{eff}) of 1.5–1.7 μm, with the most precise retrievals coming from Pathfinder data (Tomasko *et al.*, 1999) and seasonally-dependent particle size variations proposed by Clancy *et al.*, 2003, and Wolff and Clancy, 2003.

Water Ice

The most recent and comprehensive results on ice particle size distribution have been obtained by a cross comparison of two distinct methods of particle size measurement for Mars ice aerosols. By using TES data, particle size determinations based on the solar band to thermal IR optical depth ratios (Clancy *et al.*, 2003) are compared to ice particle sizes determined from the relative depths of 12 and 18 mm ice absorptions (Wolff and Clancy, 2003). Taken together, the two techniques provide the first-time seasonal/latitudinal distributions particle sizes. The combined angular and wavelength coverage enabled identification of two distinct ice cloud types over 45°S–45°N. *Type 1* ice clouds exhibit small particle sizes (r_{eff} = 1–2 μm, with the most commonly observed particle size being 1.5 μm) and a distinctive backscattering increase. They are most prevalent in the southern hemisphere during aphelion, but also appear more widely distributed in season and latitude as topographic and high-altitude (≥ 20 km) ice hazes. *Type 2* ice clouds exhibit larger particle sizes (r_{eff} = 3–4 μm, with the most commonly observed particle size being

3.2 μm), a distinct side-scattering minimum at 90–100° phase angles (characteristic of a change in particle shape relative to the type 1), and appear most prominently in the northern subtropical aphelion cloud belt. v_{eff} = 0.1 μm in both

Atmospheric water ice particle size retrievals are somewhat rare in the literature. Prior to above mentioned work, the most direct measurement of size in the published literature was the Mariner 9 IRIS determination of r_{eff} = 2.2 μm (Curran *et al.*, 1973). Although the large (regional-size) field of view may potentially include different cloud types (and sizes), the dominant cloud observed in this work was tentatively identified as a discrete, orographic cloud of the type commonly reported during the Mariner 9 and Viking epochs (Smith and Smith, 1972; French *et al.*, 1981). Other direct measurements of r_{eff} through a combination of scattering and radiative transfer analyses occur in only a handful of refereed publications: Petrova *et al.*, 1996, Titov *et al.*, 1997, and Montmessin *et al.*, 2002. These authors arrive at r_{eff} ~ 1 μm, 0.7–1.0 μm, and 1.3–1.8 μm respectively. Although precision is either not reported or not well established in the aforementioned studies, one may view the reported values as being consistent with each other. A more indirect determination of r_{eff} = 2.3 μm is derived by Rodin *et al.* [1997] via a synthesis of Phobos data and a microphysical model.

The seasons and locations sampled by the cited works correlate very well with the retrievals of similarly sized particles of Type 1 ice cloud observations. However, the seasonal phenomenon often referred to as the Aphelion Cloud Belt (ACB), in which *Type 2* ice has been found, was not recognized prior to the mid-1990's (Clancy *et al.*, 1996). Thus, previous evidence of Type 2 water ice clouds is even scarcer than that for Type 1. In fact, only Glenar *et al.*, (2003) have previously reported statistically significant retrievals of the larger ice particle sizes. More specifically, Glenar *et al.*, 2003, find their observations of the aphelion cloud belt during the 1999 season (Ls = 130°) to be consistent with Clancy *et al.*, 2003, and Wolff and Clancy, 2003. In addition, although their size bins are quite coarse, they highlight systematic local time progression in particle sizes, from smaller particle sizes near 12:00 Local Time (~ 2 μm) to larger ones (~4 μm) by their final time step (~ 15:00 LT).

6.1.5 Intimate mixtures

Intimate mixtures are also called *homogeneous* and *microscopic mixtures*. In an intimate mixture the surface consists of different types of particles mixed homogeneously together in close proximity. In this case the averaging process is on the level of the individual particle, and the parameters that appear in the equation of radiative transfer are averages of the properties of the various types of particles in the mixtures weighted by cross-sectional area. Because the parameters enter into the reflectance equation nonlinearly, the reflectance of an intimate mixture is a nonlinear function of the reflectances of the pure end members.

The mixing formula for each parameter follows from the definition of that parameter, as given in Chapter 5. Because these formulas follow from the definitions in the radiative-transfer equation, they are independent of the method or type of approximation used to solve that equation.

Mixtures are often specified by the fractional mass of each component, rather than by the number of particles, and this is true for our case, as we will see in the next Chapter. Assume that the particles are equant, and let the subscript i refer to any property of the particles, such as size, shape or composition. Then the cross-sectional area of the i-th type of particle is $\sigma_i = \pi r_i^2$, where r_i is the radius if the i-th type of particle. The bulk density of the i-th component is

(6.1) $$M_i = N_i \frac{4}{3} \pi \, r_i^3 \rho_i$$

where N_i is the number of particles of type i per unit volume, and ρ_i is their solid density. Then

(6.2) $$N_i \sigma_i = \frac{3}{4} \frac{M_i}{\rho_i r_i}$$

The average single-scattering albedo is

(6.3) $$\omega = \frac{S}{E} = \frac{\sum_i N_i \sigma_i Q_{Si}}{\sum_i N_i \sigma_i Q_{Ei}} = \left(\sum_i \frac{M_i Q_{Si}}{\rho_i r_i} \right) \Big/ \left(\sum_i \frac{M_i Q_{Ei}}{\rho_i r_i} \right)$$

Where Q_E and Q_S are, respectively, the extinction and scattering efficiency factors defined in Eq. (5.e). Because we are assuming that individual particles are randomly oriented, the probability of scattering through a given angle depends only on the scattering or phase angle, not on the direction of the incident radiation. Hence the average particle phase function is

(6.4) $$p(g) = \frac{G(g)}{S} = \frac{\sum_i N_i \sigma_i Q_{Si} p_i(g)}{\sum_i N_i \sigma_i Q_{Si}} = \left(\sum_i \frac{M_i Q_{Si}}{\rho_i r_i} p_i(g) \right) \Big/ \left(\sum_i \frac{M_i Q_{Si}}{\rho_i r_i} \right)$$

If there is a continuous distribution of properties, the summatories in these definitions may be replaced by integrations.

If Eq. (6.5) is multiplied by $(1/4\pi)\cos g$ and integrated over solid angle, the following equations for the average cosine asymmetry factor is obtained:

(6.5) $$\xi = \frac{\sum_i N_i \sigma_i Q_{Ei} \omega_i \xi_i}{\sum_i N_i \sigma_i Q_{Ei} \omega_i} = \left(\sum_i \frac{M_i Q_{Ei}}{\rho_i r_i} \omega_i \xi_i \right) \Big/ \left(\sum_i \frac{M_i Q_{Ei}}{\rho_i r_i} \omega_i \right)$$

In our work we model the snowpack of the Martian polar caps as an intimate mixture of two or three elements, namely CO_2 ice, H_2O ice and dust. We can then rewrite the above expression in a more convenient form for three types of particles, as follows:

(6.6) $$w = \frac{Q_{E1} \varpi_1 + K_2 Q_{E2} \omega_2 + K_3 Q_{E3} \omega_3}{Q_{E1} + K_2 Q_{E2} + K_3 Q_{E3}}$$

(6.7) $$p(g) = \frac{Q_{E1} \varpi_1 p_1(g) + K_2 Q_{E2} \omega_2 p_2(g) + K_3 Q_{E3} \omega_3 p_3(g)}{Q_{E1} \varpi_1 + K_2 Q_{E2} \varpi_2 + K_3 Q_{E3} \varpi_3}$$

(6.8) $$\xi = \frac{Q_{E1} \varpi_1 \xi_1 + K_2 Q_{E2} \omega_2 \xi_2 + K_3 Q_{E3} \omega_3 \xi_3}{Q_{E1} \varpi_1 + K_2 Q_{E2} \varpi_2 + K_3 Q_{E3} \varpi_3}$$

where the subscripts *1*, *2* and *3* refer to the three components of the mixture (*1* refers to the main component, e.g., CO_2 ice), and K_2 and K_3 are defined as follows:

$$K_2 = \frac{M_2 \rho_1 r_1}{M_1 \rho_2 r_2} \quad , \quad K_3 = \frac{M_3 \rho_1 r_1}{M_1 \rho_3 r_3} \tag{6.9}$$

The ratios M_2/M_1 and M_3/M_1 are the mass fractions (wt%) of the secondary elements (e.g., H_2O ice and dust) that can be used as free arbitrary input parameters in the calculations. Binary mixtures are obtained for $K_3 = 0$.
In the following figures we present examples of single-scattering albedo and asymmetry factor for different binary mixtures of CO2 ice and dust or H2O ice.

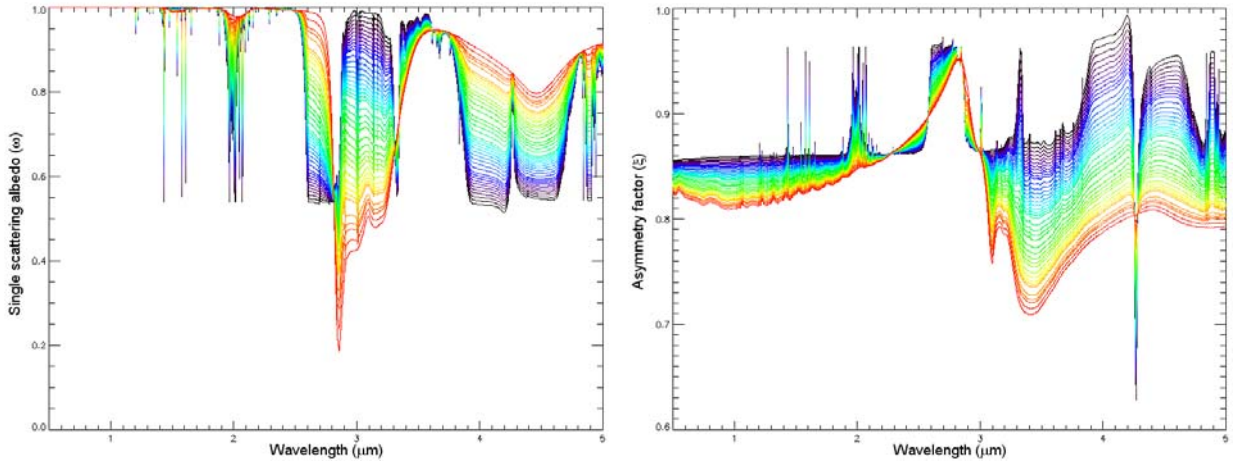

Figure 6.4. Single-scattering albedo (*left*) and asymmetry factor (*right*) of a 5-mm sized particle of CO_2 ice intimately mixed with different fractions of water ice. *Black*: Pure CO_2 ice. *Red*: 0.9 wt% of H_2O ice. Minimum water ice mass fraction is $M_{ice}/M_{CO2} = 1{\cdot}10^{-5}$ (0.0001 wt%).

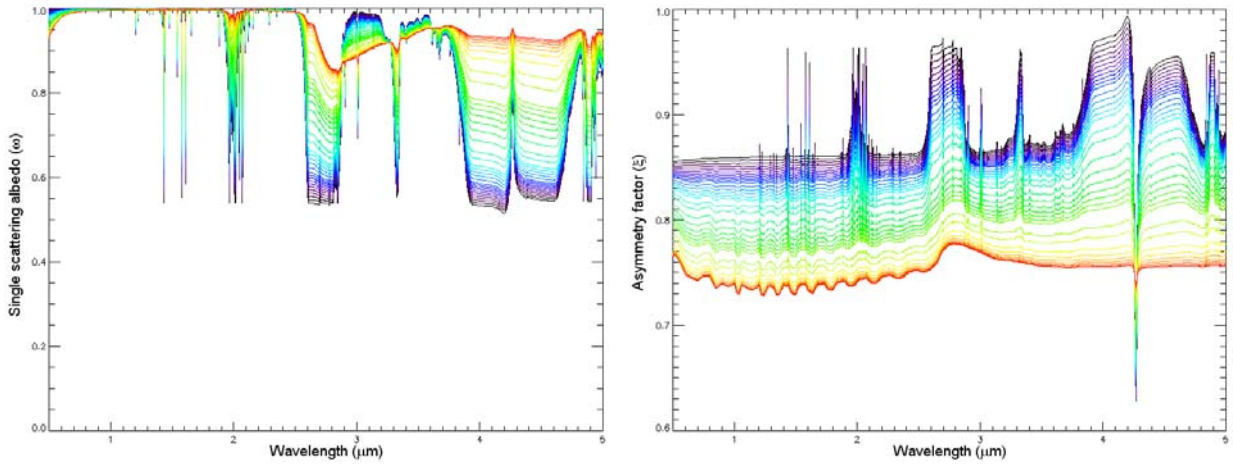

Figure 6.5. Single-scattering albedo (*left*) and asymmetry factor (*right*) of a 5-mm sized particle of CO_2 ice intimately mixed with different fractions of Martian dust. *Black*: Pure CO_2 ice. *Red*: 0.9 wt% of dust. Minimum dust mass fraction is $M_{dust}/M_{CO2} = 1{\cdot}10^{-4}$ (0.001 wt%).

6.2 Multiple scattering Solutions for Angular Reflectance

We describe here different approaches for calculating multiple scattering from particulate media. The three categories of solution are approximate, numerical, and geometric optical. For each approach, we describe the model that has revealed to be the most suitable and useful in the contest of this work and, more in general, for calculating spectral reflectance of soil and snow.

In the geometric optical modelling, mathematical expressions are used to describe the geometry of a surface, and the bidirectional reflectance is calculated from parameterization of the reflectance and transmittance of three-dimensional objects that make up the scattering medium. There have only been a few applications of geometric optical modelling that apply strictly to a soil surface, and none to snow. In all of these works, soil is modelled as a set of regularly-spaced equally-sized opaque spheroids on a horizontally flat surface. The models predict directional reflectances in the principal plane (the plane that includes both the Sun and the target) by calculating the areas of sunlit facets, shaded facets, and their radiant existence, but do not accurately predict soil bidirectional reflectance factors in all Sun-viewing geometries. In our work we are mainly interested in bidirectional reflectances if icy surfaces. Therefore, geometric optical models will not be discussed.

6.2.1 Approximate solutions

The multiple scattering of light from both soil and snow can be calculated using Chandrasekhar's (1960) radiative transfer equation or variants thereof. The radiative transfer equations used for snow are described by Wiscombe and Warren (Wiscombe and Warren, 1980; Warren and Wiscombe, 1980) and for soils by Liang and Townshend (1996a, 1996b). The basic form is exactly the same as Eq. (5.10). Most analytic radiative transfer models that simplify multiple scattering are based on the two-stream approximation (see subsection 5.3.3). For flux calculations only, a two-stream approximation to the analytic solution for the equation of radiative transfer allows us to quickly solve for the diffuse upwelling flux from either snow or soil.

6.2.1.1 Directional Hemispherical Reflectance

For snow, a delta-Eddington approximation has been widely used (Wiscombe and Warren 1980) that characterizes the strong forward scattering of snow throughout the optical region. The physical depth and bulk density of the snowpack affect scattering and absorbing properties via the optical depth τ. Optical depth is a dimensionless quantity and, for snow, is related to the snowpack density, depth, snow grain size, and wavelength of the observation:

$$\tau = \frac{3W_{\text{eq}}Q_{\text{ext}}}{4r\rho_{\text{ice}}} = \frac{3\rho_{\text{snow}}zQ_{\text{ext}}}{4r\rho_{\text{ice}}} \tag{6.10}$$

where W_{eq} is the water equivalent depth of the snowpack, defined as the geometric depth z times the snow density, Q_{ext} is the extinction efficiency factor defined in Eq. (5.e). The density of ice ρ_{ice} is about 917 kg/m^3. For the optical depth to be dimensionless, W_{eq} is in kilograms per cubic meter and r, the radius of the equivalent snow grain, is in meters. Dozier (1989b) gives a practical definition of an optically semi-infinite snowpack as one whose directional hemispheric reflectance is within 1% of the reflectance of that for $\tau = \infty$.

Wiscombe and Warren (1980) applied the delta-Eddington approximation, one of the two-stream approximations discussed in subsection 5.3.3, to calculate the directional hemispheric reflectance (i.e., planar albedo) $A(\theta_o)$ at the solar zenith angle θ_o. The formula is expressed for total optical depth τ under the direct-beam illumination at the top of the snow surface:

$$A(\theta_o) = \frac{2\gamma_2\alpha \exp\left(-\frac{\tau^*}{\mu_0}\right)\left(r_L - \frac{\omega^* R^*}{1-\alpha^2\mu_0^2}\right) + \varpi^*\left(Q^+P^+ - Q^-P^-\right)}{Q^+\left(\gamma_1+\alpha\right) - Q^-\left(\gamma_1-\alpha\right)} \tag{6.11}$$

Where the scaled optical depth τ^*, single scattering albedo ω^*, and asymmetry parameter ξ^* are related to their original parameters as follows:

$$\begin{aligned} \tau^* &= \left(1-\omega\xi^2\right)\tau \\ \omega^* &= \frac{\left(1-\xi^2\right)\omega}{1-\xi^2\omega} \\ \xi^* &= \frac{\xi}{1+\xi} \end{aligned} \tag{6.12}$$

The parameters $\gamma_1 \ldots \gamma_4$ characterizing the Eddington approximation are given in table 5.2. The remaining parameters are given by

$$\begin{aligned} Q^{\pm} &= \exp\left(\pm\alpha\tau^*\right)\left[\gamma_2 - r_L\left(\gamma_1 \pm \alpha\right)\right] \\ P^{\pm} &= \frac{\alpha_2 \pm \alpha\gamma_3}{1 \pm \alpha\mu_0} \\ R^* &= \mu_0\left(r_L\alpha_1 - \alpha_2\right) + r_L\gamma_4 + \gamma_3 \\ \alpha &= \sqrt{\gamma_1^2 - \gamma_2^2} \\ \alpha_1 &= \gamma_1\gamma_4 + \gamma_2\gamma_3 \\ \alpha_2 &= \gamma_2\gamma_4 + \gamma_2\gamma_3 \end{aligned} \tag{6.13}$$

where r_L is the Lambertian reflectance of the underlying snow, defined in Eq. (5.n).

If snowpacks are very deep, the directional hemispheric reflectance can be calculated from the "semi-infinite" medium:

$$A(\theta_o) = \frac{\omega^*\left[\gamma_3\left(\alpha+\gamma_1-\gamma_2\right)+\gamma_2\right]}{\left(\alpha+\gamma_1\right)\left(1+\alpha\mu_0\right)} \tag{6.14}$$

For a snow surface under a natural condition, both direct and diffuse radiation will be illuminated. Thus, the total albedo is the weighted average

(6.15) $$\overline{R} = w\overline{A} + (1-w)A(\theta_o)$$

were w is the fraction of diffuse radiation and

(6.16) $$\overline{A} = 2\int_0^{90°} A(\theta_0)\cos\theta_0 \sin\theta_0 d\theta_0$$

The following figures show the spectral characteristics of the reflectance of snow using the two-stream approximation by Wiscombe and Warren (1980).

Figure 6.6 shows the spectral direct albedo of semi-infinite pure snow at the visible and near-infrared wavelengths, for snow grain radii of 50–1000 μm. In general, increasing the grain size affects the albedo much more in the near-IR spectrum than in the visible region. The albedo is sensitive to grain size mainly at 1.0–1.3 μm. The solar zenith angle θ_o = 60°. Figure 6.7 illustrates the snow direct albedo dependent on the solar zenith angle. The snow depth is assumed to be semi-infinite. It is evident that the increased solar zenith angles lead to larger snow reflectance.

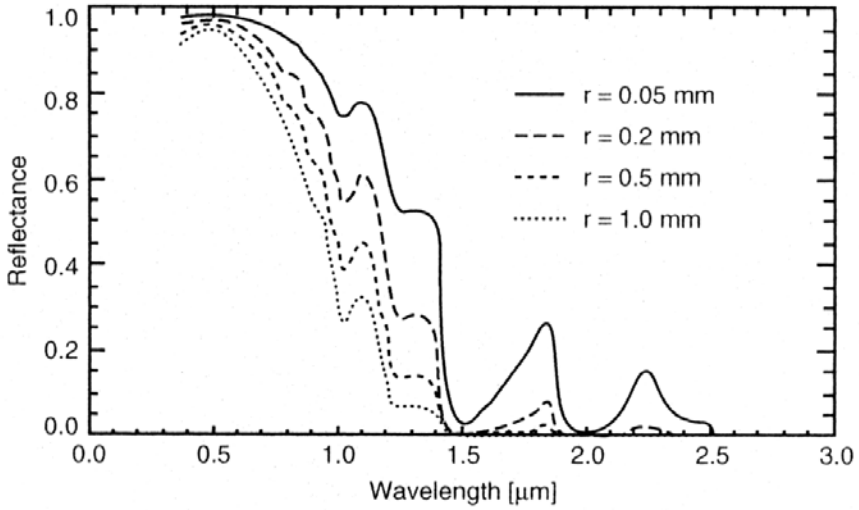

Fig. 6.6 Snow albedo dependent on snow grain size (modified from Wiscombe and Warren, 1980).

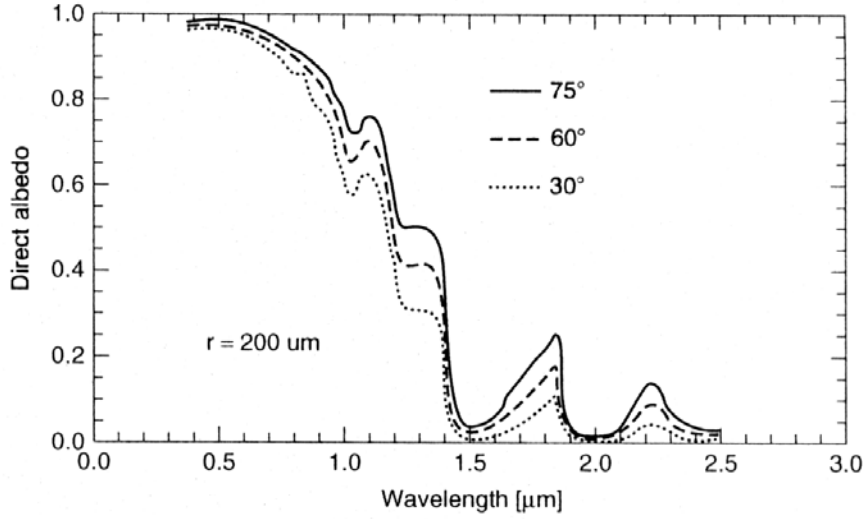

Fig. 6.7 Snow reflectance dependent on the solar zenith angle.

It should be pointed out that while the two-stream approach can give reasonably accurate estimates of the change in directional hemispherical reflectance with the solar zenith angle (Wiscombe and Warren 1980, Choudhury and Chang 1981, Dozier 1989a, 1989b), it does not provide the angular reflectance values needed to characterize the snow BRDF.

6.2.1.2 Bidirectional Reflectance

HIMSA

A widely used model of surface reflectance in this category of approximate solutions to the equation of radiative transfer is the Hapke model of bidirectional reflectance (Hapke 1993). The Hapke's isotropic multiple-scattering approximation (HIMSA) solves the single scattering exactly and approximates the multiple scattering as isotropic:

$$BDR(\mu_0, \mu, g) = \frac{\varpi}{4\pi} \frac{\mu_0}{\mu_0 + \mu} \{[1 + B(g)]P(g) + H(\mu_0)H(\mu) - 1\} \tag{6.17}$$

where μ_0, μ and g are the cosine of the incident zenith, the cosine of the viewing zenith, and the phase angle, respectively. *P(g)* is the single-scattering phase function (normalized to 4π), ω is the single-scattering albedo, and *H(x)* is an approximation to the Chandrasekhar *H* function:

$$H(x) = \frac{1 + 2x}{1 + 2\sqrt{1 - \omega x}} \tag{6.18}$$

B(g) is the enhanced backscattering correction factor due to the shadow-hiding opposition effect

$$B(g) = \frac{B_0}{1 + \frac{1}{h}\tan\frac{g}{2}} \tag{6.19}$$

where B_0 and h are the empirical parameters related to the height and width of the hotspot. In the Hapke model [Eq. 6.8], the single scattering component (the first term of the right side of the equation) is modified to account for the hotspot effect, and the multiple scattering radiance is assumed to be isotropic and is expressed by the approximate Chandrasekhar *H* function. The hotspot effect is represented by a semi-empirical formula based on the shadow-hiding principle.

The shadow-hiding opposition effect (SHOE) is caused by the fact that the shadow cast by one particle of the medium on another can be seen at all angles except zero phase, when each particle hides its own shadow, causing a relatively broad surge in brightness at small phase angles. The SHOE involves only the singly scattered rays. To understand why the SHOE acts only on the singly scattered light it is necessary to discuss the detailed processes that can occur when light is scattered from a complex medium like a planetary regolith. In the radiative transfer theory, a scattering event is considered to result from the interaction of a wave with a particle as a whole, and multiple scatterings are considered to occur only between entire particles. If the particle is complex because of inclusions, voids, or surface irregularities, these are accounted for by their effect on *P(g)*. However, in theories of the opposition effect a scattering is any event that changes the direction of a photon. The event must be treated as if it occurred at a point and, thus, involves only a small portion of a

particle. Hence, in models of the opposition effect in a medium consisting of large complex particles, multiple scatterings can occur between different parts of a single particle as well as between particles.

In the SHOE a ray of light seen by a detector after scattering from a particle embedded in a particulate medium has been exponentially attenuated twice, once on the way in and once on the way out, except in the backscatter direction. For rays that are scattered back toward the source, the incident ray has, in effect, preselected an open path, so that backscattered rays can escape unattenuated. This gives rise to the SHOE peak. However, this is true only for rays that leave the particle close to the same point at which the incident ray encountered the particle, such as rays that are specularly reflected from the surface or scattered by a subsurface imperfection close to the entry point. Typical rays are shown schematically in Fig. 6.8 as ABC and ABDEF.

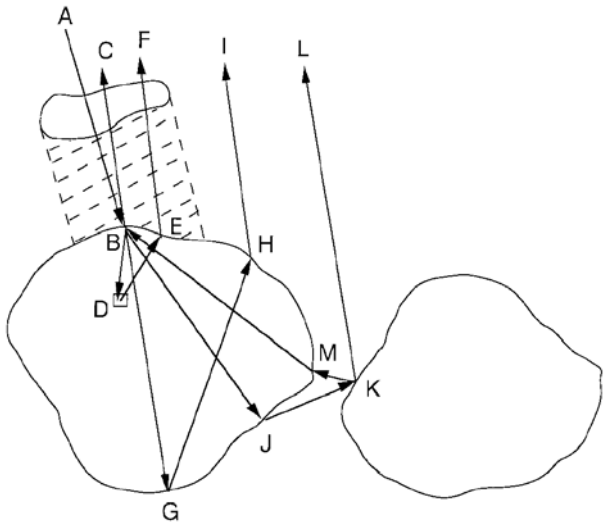

Fig. 6.8 Schematic diagram showing some of the wavepaths involved in the Opposition Effect.

In Fig. 6.8 the cross-hatched area is intended to denote schematically the clear volume that has been preselected by ray AB, and the square D denotes an imperfection such as an internal scatterer or a surface scatterer located close to point B.

Rays that are refracted into the particle and then leave it from a point located some distance away from the entry point, such as ray ABGHI, have a finite probability of being blocked, even if they are headed in the direction of the source. Hence, only part of the light backscattered by a particle contributes to the SHOE peak. A multiply scattered ray such as ABJKL will be too far from the preselected clear path to avoid being partially blocked and will not contribute. Aray such as ABJKMBC will contribute to the peak, but not only does such a ray scatter twice off of the first particle, but the second exit point must be very close to the initial entry point B. The fraction of rays that follow such restricted paths compared to all of the other multiply scattered rays is assumed to be so small that these rays can be neglected. Thus, the SHOE multiplies only the single-scattering term.

One approximation made in the Hapke model is that the multiple scattering component is isotropic regardless of the actual phase function of the medium. Hapke (1993) inferred that backscattering from planetary particulate surfaces indicated a negative value for the single-particle asymmetry parameter. Mischenko (1994) and Mishchenko and Macke (1997) have questioned the accuracy of the Hapke model based on laboratory measurements and Monte Carlo simulations. Their measurements and model output indicate that Hapke's negative asymmetry parameters (backscattering) are the result of numerical inaccuracies that are generated through Hapke's inversion approach.

HAMSA

In the anisotropic version of the Hapke model (HAMSA), a more accurate expression of the *H* functions, a more accurate multiple-scattering term for anisotropic scatterers and the inclusion of the Coherent Backscatter Opposition Effect (CBOE) represent important improvements of the bidirectional reflectance model. In the HAMSA (Hapke, 2002) the single-scattering part remains the same while the multiple-scattering part is replaced by a more anisotropic term:

$$BDR(\mu_0,\mu,g)=\frac{\varpi}{4\pi}\frac{\mu_0}{\mu_0+\mu}\{B_{SH}(g)P(g)+M(\mu_0,\mu)\}B_{CB}(g) \tag{6.20}$$

The CBOE is accounted by multiplying the entire reflectance by the function

$$B_{CB}(g)=1+B_{C0}B_C(g) \tag{6.21}$$

where B_{Co} is the amplitude of the CBOE and is constrained by physical considerations to be ≤ 1,

$$B_C(g)=\frac{1+\dfrac{1-e^{-(1/h_c)\tan((g/2)}}{(1/h_c)\tan(g/2)}}{2\left[1+(1/h_c)\tan(g/2)\right]^2} \tag{6.22}$$

$$h_c=\lambda/4\pi\Lambda \tag{6.23}$$

λ is the wavelength, and Λ is the transport mean free path in the medium.
The transport mean free path may be thought of as the mean distance a photon travels in the medium before its direction is changed by a large angle, say 1 radian. The conventional expression for Λ is

$$\Lambda=\left[n\sigma Q_s\left(1-\langle\cos\theta\rangle\right)\right]^{-1} \tag{6.24}$$

where n is the number of particles per unit volume, σ is the mean particle cross-sectional area, Q_S is the mean particle scattering efficiency, and $\langle\cos\theta\rangle$ is the mean cosine of the scattering angle.
The multiple-scattering term is given by

$$M(\mu_0,\mu)=\Pi(\mu_0)\left[H(\mu)-1\right]+\Pi(\mu)\left[H(\mu_0)-1\right]+\Delta\left[H(\mu)-1\right]\left[H(\mu_0)-1\right] \tag{6.25}$$

where:

$$\Pi(x)=1+\sum_{n=1}^{\infty}A_n b_n P_n(x) \tag{6.26}$$

$$\Delta=1+\sum_{n=1}^{\infty}A_n^2 b_n \tag{6.27}$$

(6.28) $$A_n = \frac{(-1)^{\frac{n+1}{2}}}{n} \frac{1\times 3\times 5\times \cdots \times n}{2\times 4\times 6\times \cdots \times (n+1)}, \; n \text{ odd} \qquad \text{and} \qquad A_n = 0, \; n \text{ even.}$$

H(x) is the Chandrasekar's function approximated by:

(6.29) $$H(x) \approx \frac{1}{1-\varpi x\left(r_0 + \frac{1-2r_0 x}{2}\ln\frac{1+x}{x}\right)}, \qquad r_0 = \frac{1-(1-\varpi)^{1/2}}{1+(1-\varpi)^{1/2}}$$

and the terms b_n are the Legendre expansion coefficients of the phase function

(6.30) $$P(g) = 1 + \sum_{n=1}^{\infty} b_n P_n(\cos g)$$

The coherent backscatter opposition effect (CBOE) results from the fact that portions of waves traveling in opposite directions along the same multiply scattered paths within a scattering medium interfere constructively with each other as they exit the medium near zero phase and cause a relative peak in brightness there. The CBOE can act on both the singly scattered and multiply scattered light. That the CBOE acts on all the light, and not just on the multiply scattered component, as is commonly believed, was first recognized by Helfenstein *et al.* (1997) in their analysis of the lunar opposition effect.

To contribute to the CBOE not only must a ray be scattered more than once, but the point at which it is first scattered within the medium must be separated by a finite distance from the last point from which it is scattered as it leaves the medium. The closer together the two points are, the larger the range of phase angles at which constructive interference occurs. If the two points coincide, such as ray ABJKMBC in Fig. 6.8, waves that travel in opposite directions over the same path will be in phase for all phase angles so that the coherently scattered light will contribute to the continuum intensity, and no discrete CBOE peak will occur. In media made up of large, physically complex particles the entrance and exit points can be located on the same particle, as is the case for rays ABDEF and ABGHI. If a large fraction of such backscattered rays have end points that are separated by only a few wavelengths the CBOE peak can be several degrees wide. Note that some of the rays that are treated in the radiative transfer equation as singly scattered contribute to the CBOE, including some of the rays that also contribute to the SHOE, as well as those that the equation treats as multiply scattered, such as ray ABJKL. Thus, the CBOE multiplies the singly scattered component of the scattered light, including the SHOE, as well as the multiply scattered component.

6.2.2 Numerical solutions

Unlike the radiative transfer approximations, methods such as discrete ordinates and adding-doubling are numerical methods for determining bidirectional reflectance quantities of snow and soil. The adding-doubling method was first introduced by van de Hulst (1980). It assumes superimposed plane parallel layers with solar illumination entering the top layer. The angular reflectance of the combined layers is the sum of the reflectances of each very thin individual layer for which the single scattering properties have been calculated. The discrete ordinates method allows numerous computational streams for calculation of angular radiance quantities. Its basic principles are discussed in Paragraph 5.3.2.1. Originally designed and used for cloud scattering problems, DISORT (Stamnes *et al.* 1988) has also been effective for modeling angular reflectances from snow

and soil. Mishchenko *et al.* (1999) recently developed a numerical code (refl.f) for calculating bidirectional reflectance of soil and snow.

6.3 Discussion

One question that arises when applying Mie theory to snow (and soil) is whether the particles behave as independent scatterers (i.e., as completely incoherent scatterers). If they do act as separate spheres, then classical Mie theory may be used to define the angular scattering pattern. For snow grains to behave as independent scatterers, they need to be randomly organized and sufficiently distant from one another that they do not interfere with each others illumination or scattering. Wiscombe and Warren (1980) found that the single scattering albedo of snow was insensitive to close packing. This can be explained by the fact that light refraction through the ice particles dominates scattering in snow and refraction is not sensitive to dense packing. The authors also demonstrated from some limited measurements that any near-field effects would be relatively minor. However, complete tests of this assumption remain to be performed.

The nature of snow grain metamorphism creates a tendency toward spherical grains. Indeed, for equitemperature metamorphism in which the surface free energy of the snow grain is minimized, the equilibrium shape is a sphere (Colbeck 1982). In wet snow, crystals rapidly become very rounded, often forming clusters. Conditions where snow grains are markedly non-spherical include the transient case of fresh snow (hexagonal crystals, needles, etc.), surface hoar created by condensation of water vapour on the snow surface (faceted, cup-shaped crystals), and depth hoar induced by strong temperature gradients (faceted, cup-shaped crystals). Surface hoar occurs under restricted surface energy balance conditions and is not common, while the more common depth hoar would have virtually no effect on albedo if the hoar layer is buried by more than 10 cm (as is typically the case).

Jin and Simpson (1999) have demonstrated the differences between using the exact Mie phase function for an ice particle and the Henyey-Greenstein phase function. They found that, although both result in the same asymmetry parameter, the exact Mie phase function predicts a smaller backscattering peak and a slightly smaller forward scattering peak than does the Henyey-Greenstein phase function. However, this backscattering peak typically does not appear in measurements, and it remains unclear if its inclusion in a model gives a more accurate result. Mishchenko (1994) demonstrated that for moderately and non-absorbing particles that are large relative to the wavelength, the asymmetry parameter may be used without modification. He emphasized that for grain radius-to-wavelength ratios (r/λ) between 0.01 and 10, the asymmetry parameter value is sensitive to the density of the particulate medium. On terrestrial snow, the minimum value of r/λ is about 20 (where $r = 50$ μm and $\lambda = 2.5$ μm), indicating that, for virtually all combinations of grain size and wavelength, snowpack density does not influence the asymmetry parameter. According to Mishchenko (1994), effects of particle non-sphericity are also quite small in that range and may be neglected. Thus, for snow grains in the optical region, problems associated with dense packing of particles and non-sphericity have a negligible effect on the asymmetry parameter.

7 PFS/MEX OBSERVATIONS OF THE MARTIAN POLAR CAPS

In this Chapter we present the scientific results achieved in our work through the analysis of PFS/MEX observations.

The first three Sections concern the South Polar Cap. In Section 7.1 we propose a new and accurate method to track the edges of the seasonal caps of Mars based on Thermal Infrared observations, and apply it to the SPC during the fall and winter seasons. In Section 7.2 we use PFS SWC spectra in the Near Infrared recorded over the permanent ice cap to study its composition and microphysical state in terms of CO_2 ice, H_2O ice and dust. A detailed analysis of the condensing CO_2 south polar cap is presented in Section 7.3. Atmospheric thermal fields have been used to compute thermal winds and to characterize the complex dynamical processes that occur in the polar night. Air vertical temperature profiles are retrieved by PFS LWC thermal observations and compared to CO_2 condensation curves to study the mechanisms of ice accumulation. Our results also provide new insights in the explanation of the residual south polar cap asymmetry, a major Martian curiosity from many decades.

In the last Section we present the first comprehensive study of the north polar cap in middle-spring. Models are fitted to the observed data, allowing for composition, microphysical state, coexistence modes and thickness of the seasonal deposits.

Most of the results presented in this Chapter have been published on international scientific journals. The papers are available in the Appendix of this book.

7.1 Tracking the edge of the south seasonal polar cap of Mars

In this study, we track the south seasonal cap edges as a function of season and longitude for the fall and winter seasons (MY27), using data from PFS LWC. As discussed in Chapter 1, the polar caps have gained significance in that they are one of the driving forces of the Martian climate, with approximately 25% of the atmosphere being cycled through the polar caps annually. The Martian seasonal caps have been monitored by both satellite and telescopic observations for many years. Most of these studies utilized visible imaging to determine the albedo contrast between the edge of the seasonal cap and the uncovered soil. This contrast is practically undetectable where the CO_2 cap is dark, as in the South polar cryptic region (Kieffer *et al.*, 2000), and during the polar night (Titus and Kieffer, 2001). The visible method also fails to distinguish between CO2 and H2O ices. In this study we used the surface temperatures retrieved from the PFS Long Wavelength Channel to monitor the CO_2 ice cap evolution. Adopting the very general formalism of Bayesian analysis, an algorithm for the scientific analysis of individual calibrated PFS LWC

measurements has been developed, allowing the simultaneous retrieval of several parameters, including the surface temperatures used for this work, with an error in the order of 1K. A full description of the adopted method can be found in Grassi *et al.* (2005). The cases presented in this study were carefully selected imposing a value of χ^2-test close to 1 in the indicative range 400–800 cm^{-1}. The adopted retrieval method assumes no CO_2 ice clouds in the atmosphere and surface emissivity equal to one in the entire thermal range. The above-mentioned data acceptance criteria implies, therefore, the rejection of possible cases where:

1) CO2 ice deposits show a departure from unit emissivity leading to radiance variations greater than noise level;
2) CO2 ice clouds are present in a meaningful amount in condition of non-null lapse rate.

Both effects should be evident as bands (only in absorption for surface, in emission or absorption depending on dT/dz for clouds) in the region of 400 cm^{-1} (Warren *et al.*, 1990). The effective modeling of this spectral region with our assumptions implies, in our opinion, the unit emissivity behaviour of ice as well as the absence of clouds. A possible exception is represented by an almost isothermal atmosphere, where thermal emission of clouds is possibly fully compensated by their absorption. The retrieval of surface temperature in the entire range ensures anyway that the almost transparent region around 550 cm^{-1} is able to provide a reliable estimate of surface temperature even if 400 cm^{-1} would be affected by possible cloud presence.

In this study we have collected and analyzed a huge set of 467 PFS orbits acquired during the first 2 years of activity. This dataset covers more than a half Martian year, from Ls 330° to 194°, with some gaps and lacks, such as the 39°–49° and 80°–90° Ls ranges. Nevertheless, the data allow a detailed study of the CO_2 south seasonal polar cap advancing and retreating speeds during the fall and winter seasons. The results have been published on *Planetary and Space Science* (Giuranna *et al.*, 2007a); the paper is available in the Appendix A.4 of this book.

7.1.1 Surface temperature maps

By applying the retrieval scheme discussed in the previous Section to the PFS LWC thermal spectra, we produced several mosaics of tracks of the surface temperatures for different Ls ranges during the fall and winter seasons. The maps are shown in Fig. 7.1.

The surface temperature map of the early-fall South polar cap (Ls 0°–25°) reveals that the well known asymmetry of the summer residual cap (see Subsection 1.3.3) has already vanished and the CO_2 cap appears symmetric. It extends down to –70° latitude, as implied by the fact that, poleward from that latitude, the surface temperature is well stable around the CO_2 condensation temperature of ~ 145 K. The maps clearly show that, during the fall season, the South polar cap edges are advancing towards lower latitudes. The cap remains symmetric during the whole first half of the fall season (Ls 0°–45°, top-left and top-right panels of Fig. 7.1), when the cap edges are as low as –60° latitude. In the 50°–70° Ls range (Fig. 7.1, middle-left panel) the cap appears strongly asymmetric. We will see in the next Section that this asymmetry is mainly due to the presence of the two major Martian basins, Hellas and Argyrae. Very few data are available in the 72°–97° Ls range (actually, the 80°–90° Ls range is totally missing) but it is clear from the surface temperature maps (and from the results discussed in the next Section) that, at the winter solstice, when the edges

of the polar night start going back poleward, the cap recession has already started. If we compare the first two maps of Fig. 7.1 we see that the cap edges have grown by 10° of latitude in about 15 degrees of Ls.

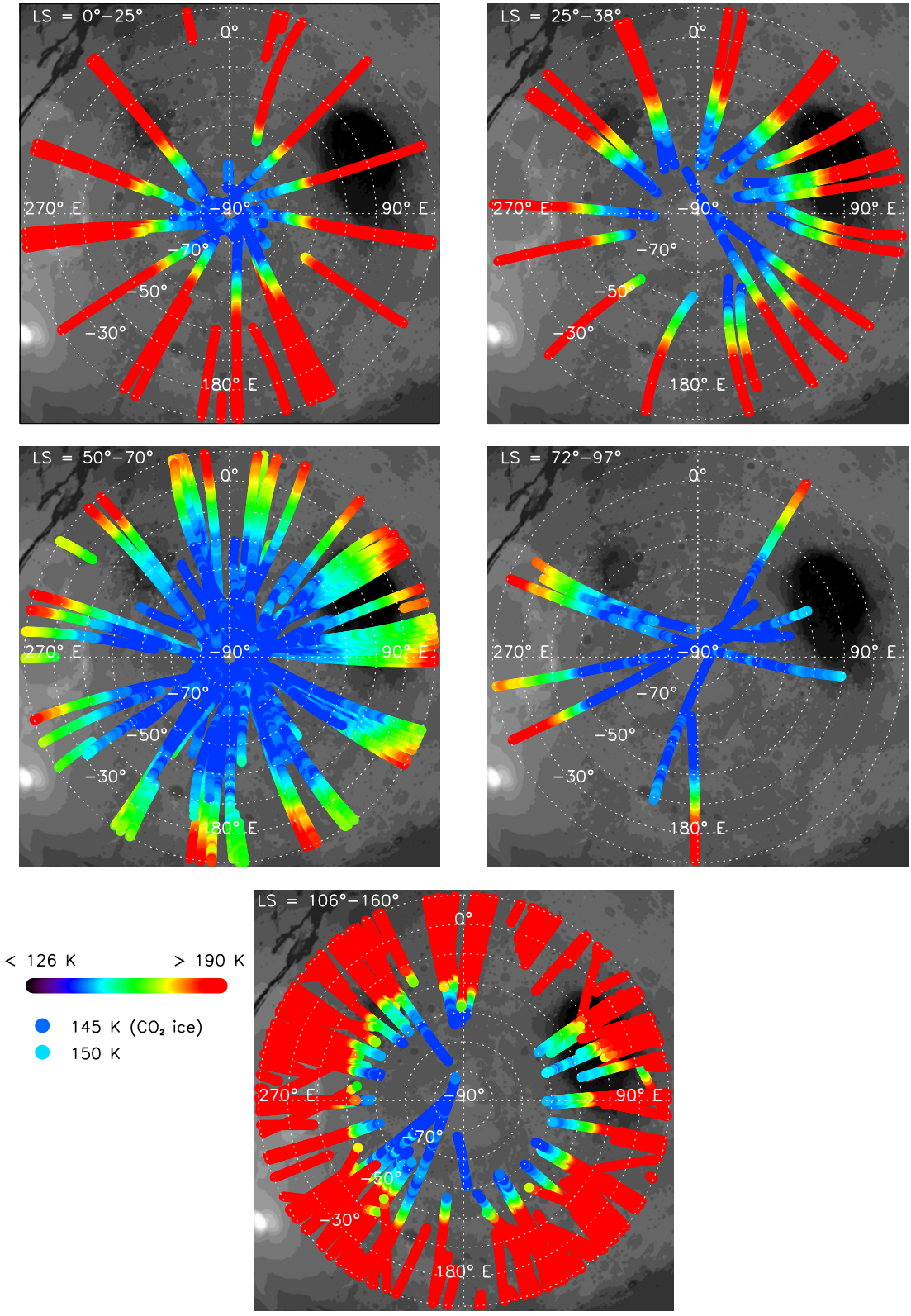

Fig. 7.1 Surface temperature mosaics of tracks of the South polar region for five Ls ranges covering the fall and winter seasons. During the fall season, the south polar cap edges are advancing towards lower latitudes. During the 50°–70° Ls range the cap appears strongly asymmetric.

The PFS south pole observations pause at 38° Ls and start again at 50° Ls, when a huge amount of polar spectra have been acquired up to 70° Ls. At these Ls the cap reaches the maximum observed extension, with CO_2 ice deposits as low as 40° S latitude. This is exactly the latitude we would get if we assume a constant progression rate over the whole 25°–70° Ls period. These simple considerations lead us to a first estimation of the cap progression speed of about 10° of latitude per 15 degrees of Ls during the expansion phase, that is most of the fall season, up to Ls ~ 70° when the cap stops its expansion and eventually starts to shrink. The colored symbols used in the maps are of fixed size and are not representative of the actual footprints.

The MEX orbit is elliptical, with a precession of the pericentre. To help the reader understanding the effect of this precession on the spatial resolution of PFS measurements, we show on Fig. 7.2 the actual size (diameter) of the footprints as a function of Ls, for six different South polar latitudes.

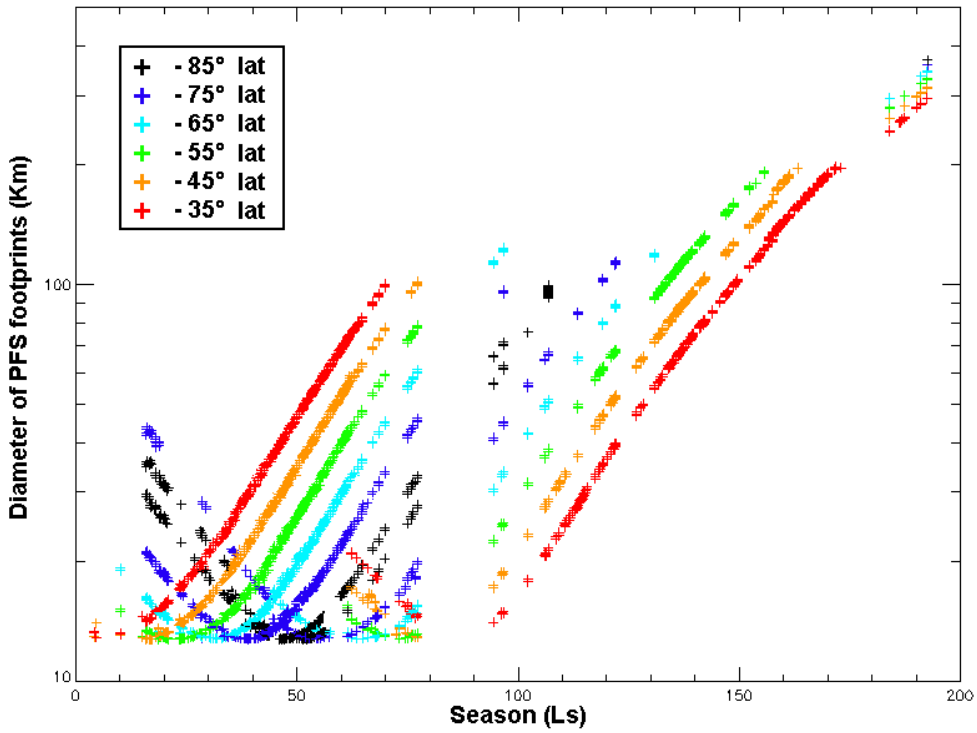

Fig. 7.2 Actual footprint of the PFS measurements used in this study as a function of season, for six different latitudes. The LWC IFOV is 2.8° (see Section 2.3), which corresponds to a footprint of ~12 km at the pericentre (250 km).

Since the spacecraft is orbiting Mars in a polar orbit, during a same orbit (i.e. fixed Ls) we may observe the same latitudes twice (of course at different longitudes), but with different spatial resolutions. As can be seen from Fig. 7.2, this only happen in the Ls range 15°–80°, and only for latitudes lower than –75° (if Ls < 60°; black and blue colors) or higher than –55° (if 60° < Ls < 80°; green, orange and red colors). In early fall (Ls = 20°) the pericentre is around 55° S latitude and the cap edges are close to –70° latitude, where the PFS footprint is less than 20 km. At Ls = 50° the pericentre is close to the south pole, while the cap edges are around –50° latitude, which corresponds to a footprint of ~ 30 km. In early winter (Ls = 110°), the pericentre is close to the equator, and the PFS footprint at the polar

edges (around –50° latitude) is ~ 40 km. At Ls = 190°, the pericentre is close to the North pole and the footprint is now close to 350 km. The most favorable condition occurs at Ls~30°, where the pericentre is essentially at the same latitude as the polar edges (–65°), allowing a better accuracy in the edge detection.

7.1.2 South polar cap progression/regression speeds

7.1.2.1 First approach: fixed temperatures

A tracking of the cap edges can be done exploiting the rapid rise (decrease) in surface temperature that occurs when CO_2 ice is removed (deposited). We defined the advancing cap edge to be where the surface temperature drops below 150 K (which is essentially the CO_2 condensation temperature for average Martian conditions), and the retreating cap edge where the surface temperature rises above 160 K; this threshold temperature is high enough to ensure that essentially no CO_2 ice/frost is present in the IFOV.

In Fig. 7.3, we present typical surface temperature profiles (solid lines) along several orbits over the South polar region for different Ls. The orbits have similar local time (7–9 a.m.). The threshold temperatures used in this analysis and described above are also plotted (dot–dashed lines). When present, the CO_2 ice acts as a thermostat in equilibrium with the atmospheric pressure and the surface temperatures may vary in a limited range of temperatures (approximately in the 140–150 K range), depending on the local conditions (mainly the local CO_2 partial pressure).

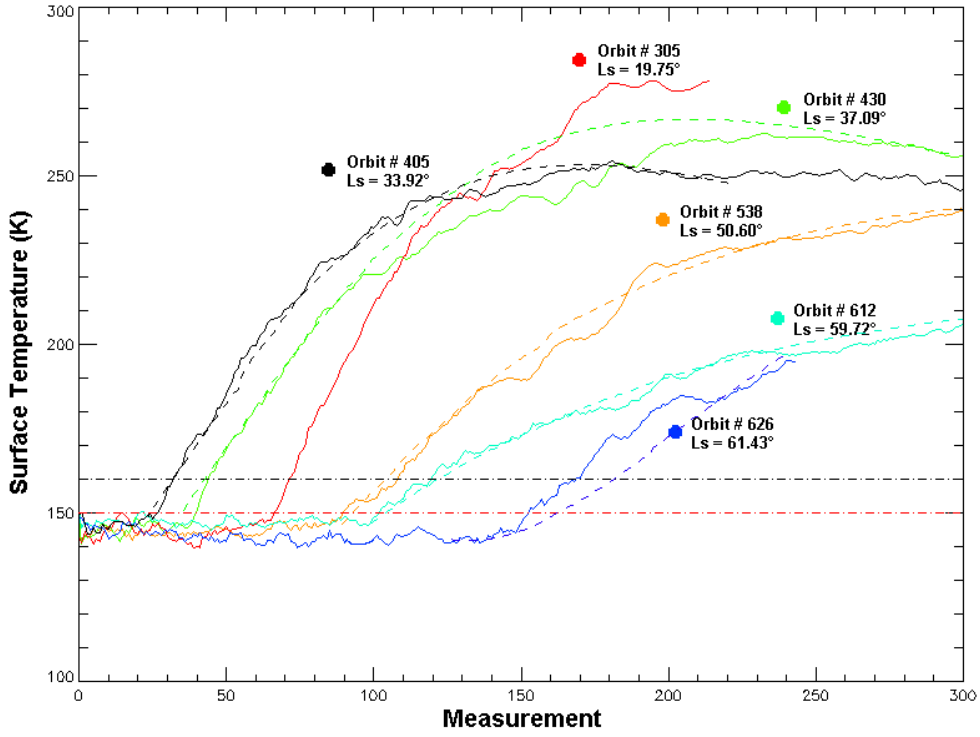

Fig. 7.3 Typical surface temperature profiles (solid lines) along several orbits over the South polar region, for different Ls. The dot–dashed lines indicate the threshold temperatures used for the cap edge detection. Dashed lines are Sun elevation vs. latitude (measurement) curves.

Note that a retrieved temperature of ~ 150 K implies that the whole PFS FOV is filled by CO_2 ice. Outside the CO_2 ice cap, the surface temperature is allowed to rise above 150 K and the surface temperature profiles follow essentially the slope of the Sun elevation vs. latitude curves. In a recent analysis of TES data, the springtime threshold temperature is set to 165 K, due to effects from atmospheric dust that are common during the cap retreat (Titus, 2005). In our case, as described in Section 7.1, the integrated dust content is one of the parameters retrieved by our self-consistent retrieval scheme (Grassi *et al.*, 2005).

Our results are shown in Fig. 7.4, where we plot the latitude of the edges of the South polar cap versus the solar longitude Ls. A comparison with TES data is also shown (solid lines; Titus, 2005).

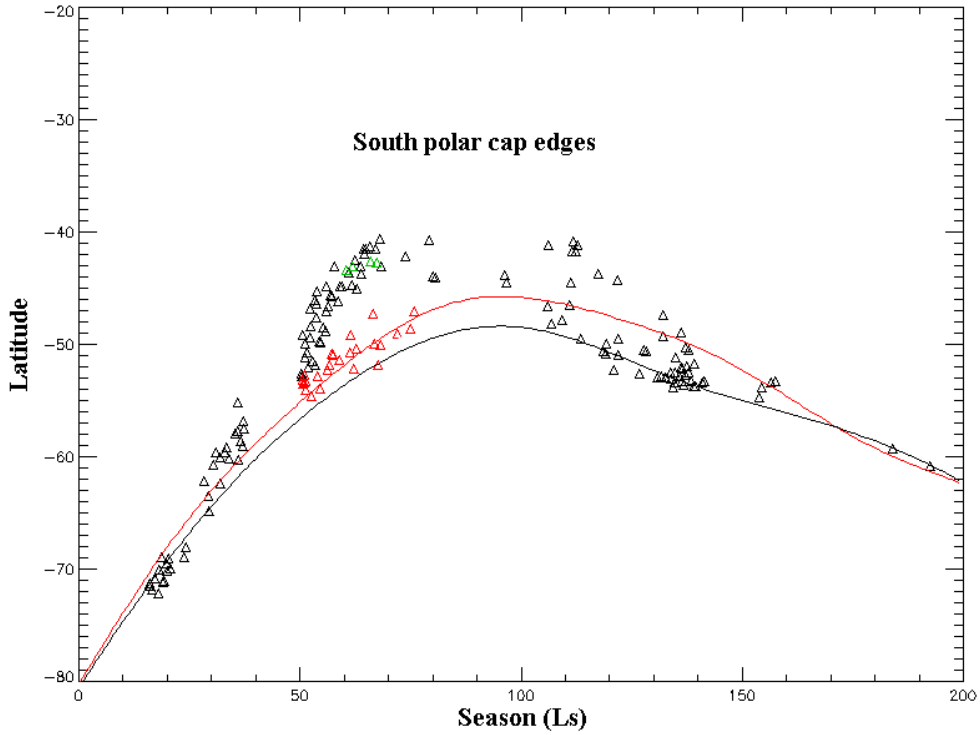

Fig. 7.4 South cap edge latitude vs. season — first approach. See text for details. Horizontal positions of triangles give also the actual Ls sampling grid of the measurements used in the different Ls ranges of Fig. 7.1. Solid lines represent the south polar cap edges measured by TES during MYs 24–25 and 25–26 (Titus, 2005). Black curve is for 180° E longitude and red curve is for 70° E longitude.

In the 0°–50° Ls range the data are well displaced along a straight line, independently from the longitude, showing that the cap is symmetrically expanding toward lower latitudes at a constant speed of 10° of latitude per 15 degrees of Ls. When we first looked at the 50°–70° Ls range, we noted a huge increase of the data scattering, the edges being no longer aligned along a straight line. A closer look at the 50°–70° Ls range surface temperature map (middle-left panel of Fig. 7.1) reveals that the cap is indeed asymmetric during this period and, assuming that only temperatures below 145–150 K allow the presence of solid CO_2, no CO_2 ice appears to be present inside the two major Martian basins, namely Hellas and Argyrae. The latter are the main responsible for the cap asymmetry and hence for the increase of the data scattering observed in this range of Ls.

For this particular Ls range, we then grouped the data in two sets: one for the hemisphere that extends from the eastern limit of the Hellas basin (~ 110° E) to the western limit of the Argyrae basin (~ 70° W) and containing the two basins (red triangles), and one for the other hemisphere (black triangles). This study revealed that, starting from Ls ~ 50°, the edge progression speed start to be longitude-dependent; in the hemisphere containing the two Martian basins the edges progression speed is about a half than that of the other hemisphere.

The fact that, apparently, no CO_2 ice is present inside the basins (see Fig. 7.1), especially for Hellas, is rather unexpected and suspicious: the CO_2 pressure increases with decreasing altitude (i.e. inside Hellas) and, in turn, the CO_2 condensation temperature increases, following the Clausius–Clapeyron's law. This makes the CO_2 frost more likely to form and be stable in the high-pressure areas inside the basins than in the adjacent lower-pressure regions outside the basins; Fig. 7.4 shows an opposite behaviour instead: the green triangles belong to the narrow range of longitudes [25° W–25° E,] that is in the same hemisphere containing Hellas and Argyrae, but outside the basins. The cap in this lower-pressure region seems to be more extended (i.e. the CO_2 frost is still present at higher latitudes) than in the higher-pressure regions inside the basins. Thus, the cap edge detection technique used in this approach may not be sufficiently accurate to track the seasonal variations of the cap edges.

For a more accurate analysis, it is necessary to keep into account the actual CO_2 partial pressure at the surface from which depends the actual CO_2 condensation temperature at the surface. To support this idea, we investigated the presence of any correlation between the altitude and the surface temperature inside the seasonal cap. As a result, we found that almost every orbit show an anti-correlation between these two parameters. The degree of this anti-correlation varies from orbit to orbit, being barely visible in some and very strong and defined in some others. As an example of a strong anti-correlation, in Fig. 7.5 we show the surface temperature profile during MEX orbit #538, together with the corresponding altimetry for the first 100 PFS observations.

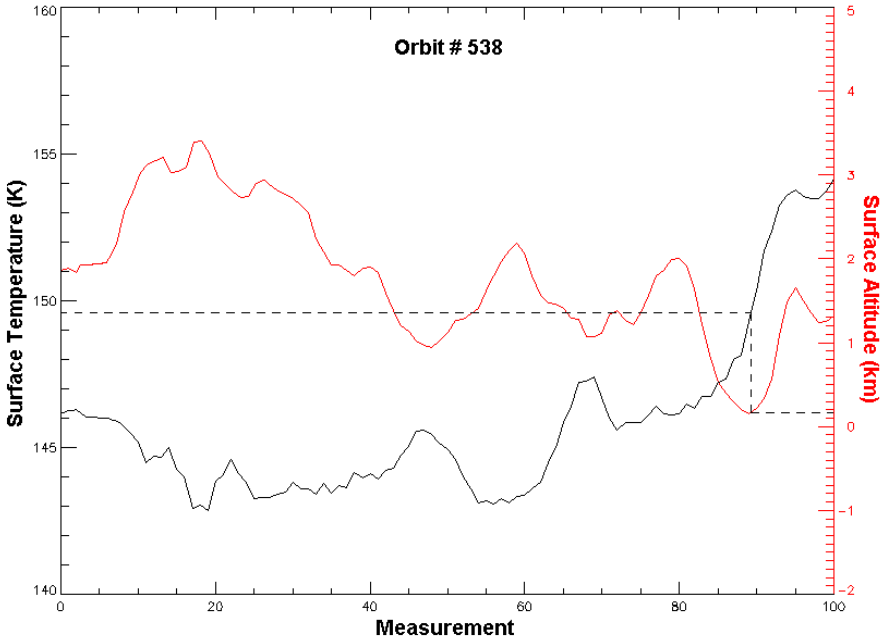

Fig. 7.4 The anti-correlation between the altitude (red curve) and the surface temperature (black curve).

Where the CO_2 ice is present (i.e., for T ≤ 150 K) the strong anti-correlation between the altitude and the surface temperature is clearly visible. Generally, this effect may be reduced or hidden by several occurrences, as the presence of warmer H_2O ice patches or uncovered soil (or both) in the IFOV (i.e., spatial mixtures of different objects with different temperatures); local departures of the CO_2 mixing ratio from its usual average value; a non-thermodynamic equilibrium of the CO_2 deposits with the atmosphere. Nevertheless, note that, where the surface altitude is close to 0 km, the surface temperature is close to 150 K (minimum of red curve in Fig. 7.5, dashed line), as expected for the CO_2 ice temperature for average Martian conditions.

7.1.2.2 Second approach: pressure-dependent temperatures

As discussed in the previous Section, defining the advancing and retreating cap edges to be where, respectively, the surface temperatures drop below or rise above certain fixed temperatures, may lead to noteworthy errors in the latitudes of the cap edges, due to the variations of the CO_2 condensation temperatures as a consequence of variations of the local surface pressure which, in turn, varies with the altimetry. Therefore, the higher the discrepancies of the pressure from the average 6.1mbar value (which corresponds to a CO_2 condensation temperature of ~ 150 K at the surface), the higher the errors in the cap edge tracking. The worst cases occur where big variations of the altimetry occur, that is, in our case, inside Hellas and Argyrae basins. For a more accurate tracking of the advancing polar cap edges, the CO_2 condensation temperature that corresponds to the actual value of the local surface pressure must be considered, rather than a fixed value. This can be done by using the Clausius–Clapeyron's law, which for our purposes can be written as follows:

$$T_{cond}^{surf}(h) = \frac{b}{a - \ln(P^{surf}(h) \cdot m)} \tag{7.1}$$

where $T_{cond}^{surf}(h)$ is the CO_2 condensation temperature (in Kelvin) at the surface as a function of the altimetry h; a and b are the Clausisus-Clapeyron's coefficients for the CO_2; P^{surf} is the surface pressure (in millibar), and m is the CO_2 mixing ratio. The Clausisus-Clapeyron's coefficients for the CO_2 are known parameters (a = 23.102; b = 3148 K), as well as the average CO_2 mixing ratio (m = 0.9532). For the surface pressure determination P^{surf} (h), we use a specific routine (pres0) developed by the LMC-AOPP-IAA team, which is able to take into account the MOLA topography at higher resolution (0.03125° × 0.03125°, Smith *et al.*, 2003). The surface pressure determination is carried out with a typical uncertainty of 0.2–0.3 millibar (Grassi *et al.*, 2005).

Now, the advancing cap edges are defined where the surface temperatures drop below the CO_2 condensation temperature for the actual surface pressure values, given by Eq. (7.1). The retreating cap edges are defined in the same way as in the previous section. The results are shown in Fig. 7.5. It is now evident that the cap actually expands with a constant speed of about 10° of latitude per 15 degrees of Ls during the most part of the fall season (up to Ls ~ 70°) at every longitude (black and green triangles).

The maximum extension of the South polar cap occurs somewhere in the 80°–90° Ls range, when the cap edges are as low as –40° latitude. At the winter solstice, when the

edges of the polar night start moving poleward, the cap recession has already started, in response to seasonal changes in insolation. The CO_2 ice South polar cap will recede with a constant speed of ~5° of latitude every 25 degrees of Ls during the whole winter. Inside the Hellas and Argyrae basins (red triangles), due to the higher pressure values, the CO_2 condensation temperature is several degrees higher than that of the rest of the South polar region, so that the CO_2 frost can be stable at higher latitudes (and temperatures), extending down to (and occasionally below) –30° latitude, and causing the cap to be asymmetric.

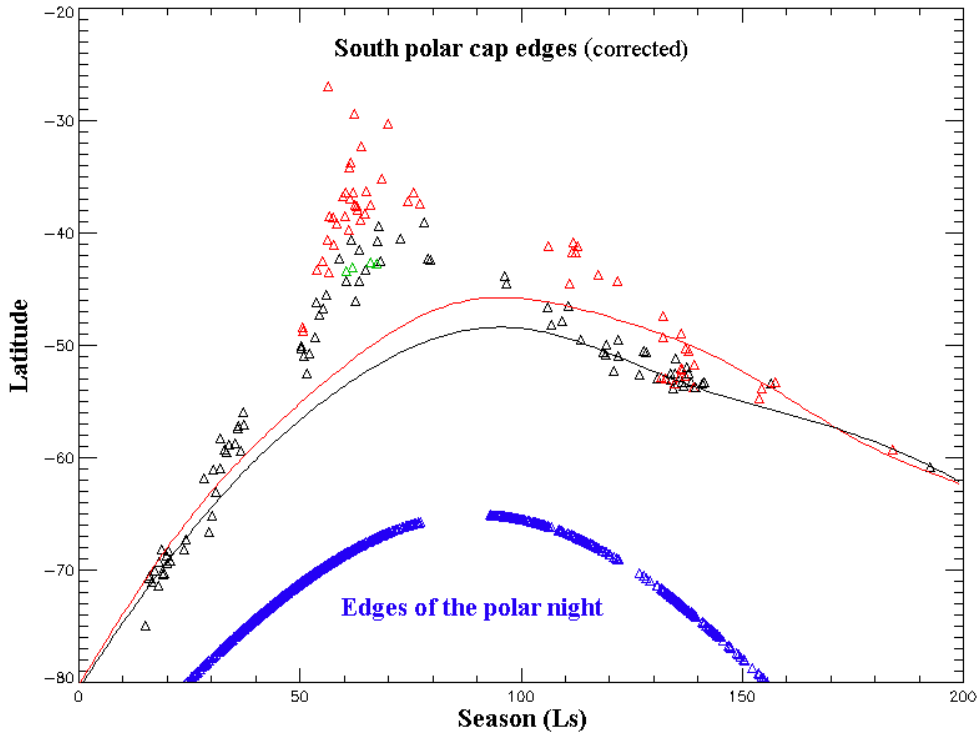

Fig. 7.5 South cap edge latitude vs. season — second approach. See text for details.

We looked for any corresponding observations by TES during previous Martian years: solid lines on Fig. 7.5 represent the South polar cap edges vs. Ls as measured by TES during MYs 24–25 and 25–26 (Titus, 2005). Black curve is for 180° E longitude and red curve is for 70° E longitude (i.e. inside Hellas). The latter is also the highest-latitude curve at every Ls (at least up to Ls ~ 170°); in other words, in agreement with our results, also the TES data indicate that the cap is asymmetric, with its maximum extension being inside the Hellas basin, around 70° E longitude. Nevertheless, the actual extension of the South seasonal polar cap differs dramatically between the two experiments, especially in the 50°–100° Ls range, with PFS data showing a much more extended cap. The reason for these big discrepancies has still to be investigated. Possible reasons may be:

- actual interannual variations (PFS data here used have been acquired during MY 27);
- differences in the data set and treatment. The TES maps of the date when all the CO_2 ice in a particular region of the cap has sublimated were constructed on the basis of relative albedo and diurnally corrected brightness temperature, by means of a diurnal planar model (Kieffer *et al.*, 2000). The band at 30 μm (T_{30}) was selected as the

primary band for thermal cap edge mapping and only daytime temperature data were used;

- different techniques adopted for the cap edge detection. Details on the technique used to estimate the cap edge from TES data can be found in Kieffer *et al.* (2000), and Kieffer and Titus (2001).

The longitudinal asymmetries reduce during the cap retreat, as the CO_2 ice/frost inside the basins sublimates, and completely disappears around 145° Ls. Then the cap continues to recede symmetrically. Note that, although the night edge and the cap border move roughly with similar speeds, the latter is always at least 10° of latitude (up to 25° outside the basins and up to 35° inside them) more extended than the first, allowing stable CO_2 ice deposits in illuminated conditions. This is valid for both fall winter seasons as can be seen from the blue triangles in Fig. 7.5.

7.2 The Residual South Polar Cap of Mars

As discussed in Chapter 4, surface temperatures and spectral information about the composition of surface materials and polar deposits can be obtained by spectra acquired by both PFS channels. In this Section, we present a preliminary report on observations of the perennial south polar cap showing many absorption lines of solid CO_2, but requiring also some admixture of condensed H_2O and mineral dust to match the observed spectra.

Except for some spatially unresolved 10–50 μm IRIS spectra (Paige *et al.*, 1990) and TES spectra (Kieffer *et al.*, 2000), the spectral characteristics of the south residual ice cap have not been published from any of the previous missions. Our results have been published on *Planetary and Space Science* (Hansen *et al.*, 2005); the paper is available in the Appendix A.3 of this book.

7.2.1 Dataset and models

Mars Express started observing during the end of summer in the southern hemisphere. We have analyzed south polar observations in three of the first 100 orbits (acquired in the first three weeks of PFS operation): 30, 41, and 61. The solar longitude of these observations was 336°, 338°, and 341°, respectively. Orbits 30 and 41 show clear spectral signatures of the residual polar cap. Viking orbiter data 25 yr ago verified that the perennial south and north polar caps currently have different compositions; the former consists of CO_2 ice, while the latter of H2O ice (see Subsection 1.3.3). CO_2 ice in the residual south polar cap was proposed on the basis of its low infrared brightness temperature, since the spectral characteristics of the south residual ice cap in the NIR have not been published from any of the previous missions. The IRS (infrared spectrometer) on Mariner 7 showed near-infrared CO_2 ice features in only the seasonal south polar cap (Fig. 1.9), before the exposure of the residual cap. The spectra of these spring seasonal deposits show effective CO_2 ice grain sizes of 3–10 mm, and less than 1% dust or water ice contamination. South pole residual cap observations from the Mars Express OMEGA instrument at 2 km spatial resolution, made simultaneously with the PFS observations, show that the CO_2–rich deposits are surrounded by extensive water ice covered regions (Bibring *et al.*, 2004). Bibring *et al.*

model the CO_2-rich deposits as an intimate molecular mixture of 15% water with the CO_2 ice.

Here, we present several SW PFS spectral averages and models that fit the spectra. The spectra have been smoothed over seven points to reduce the noise to an acceptable level for this analysis. This smoothing has the effect of muting some sharp spectral lines that are in the data and models but are not well seen here. The measured and simulated spectral reflectance is shown in Fig. 7.6a in a short spectral interval from 2300 to 4350 cm^{-1} (2.3–4.35 μm). In the polar regions, the thermal radiation emitted is comparable to the solar reflected radiation at 6–8 μm. Therefore, in this spectral range, the energy measured is entirely from reflected sunlight. In the case of a large soil fraction with the soil much warmer than the frost, the thermal component of the spectrum will be less than 0.01 at 2400 cm^{-1} and less than 0.02 at 2200 cm^{-1} (this worst case for a soil fraction of 0.3 with soil emissivity 0.8 and soil temperature 230 K). The spectrum of the residual polar cap in Fig. 7.6a is scaled and offset for easy comparison to albedo models. The measured spectrum shows the distinctive features of solid CO_2, indicated by arrows in. There are no narrow water ice lines in this range but the overall shape of the spectrum and the relatively low level of reflectance imply the presence of ice also.

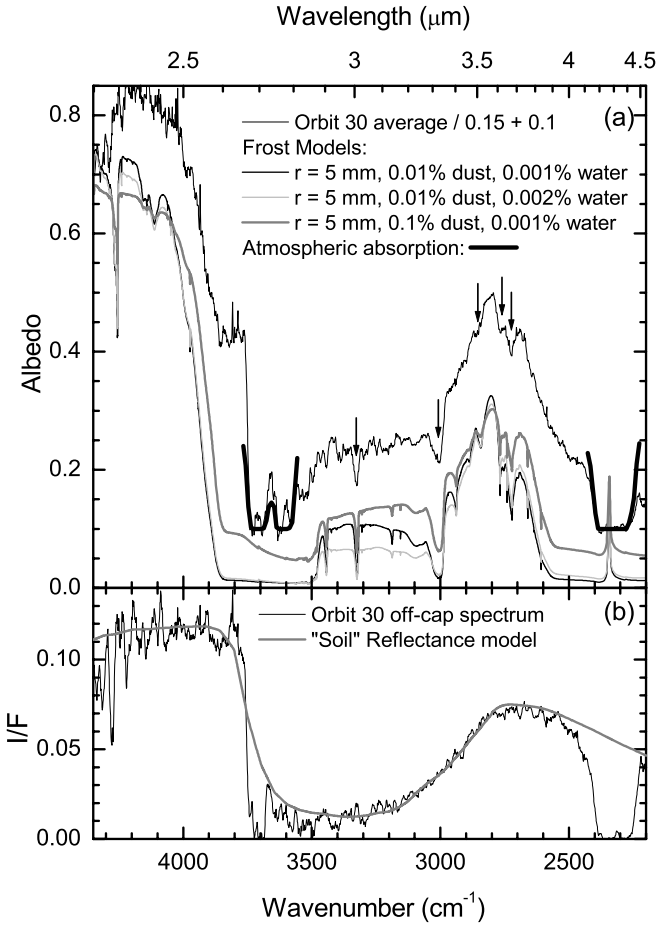

Fig. 7.6 (a) Sample PFS polar spectrum and CO_2 frost models. The PFS data is scaled and offset for clarity. The models show the spectral sensitivity to variations in CO_2 grain size, dust content, and water ice content. (b) Off-cap PFS spectrum used to define soil model for spatial mixtures.

We have modeled the observations by using optical constants of CO_2 and H_2O ices from Hansen (1997) and Hansen (1999), and dust from the palagonite measurements of Roush *et al.* (1991), as described in Section 6.1 and shown in Figs. 6.1, 6.2 and 6.3 respectively. We employed the same computational approach as used by Warren *et al.* (1990). The surface is described as semi-infinite layer of particulate medium. Mie theory is used to compute the scattering and absorption of individual particles, and a two-stream delta-Eddington multiple scattering theory for reflection of the whole layer. In our case the models include the linear (spatial) contribution of a fraction of unfrosted soil (with a spectral shape taken from PFS spectra of nearby regions outside the residual polar cap is seen in Fig. 7.6b), and a fraction covered with a neutral dark material, which could be shade or large-grained water ice. The polar cap ice is modeled as an intimate mixture of CO_2 ice and dust and water ice grains with radii on the order of 1–2 μm. The input to the model includes the CO_2 ice grain radius, the water ice mass fraction, and the dust mass fraction. Mie theory has been discussed in details in Chapter 5 (Subsection 5.2.1); the multiple-scattering approximation used in this work is described in Subsection 5.3.3 and, more in details, in Paragraph 6.2.2.1. Intimate mixtures and mass fraction definitions and formulas are given in Subsection 6.1.5. Details of the adopted size distributions for ice and dust are given in Subsection 6.1.4.

The output of the model is a hemispherical albedo, which is typically much brighter than the examples with extreme lighting geometry studied here and must be scaled to match these observations. Four albedo models showing spectral variations due to variations in ice content, dust content, and grain size are shown in Fig. 7.6a. Another input to the model is the illumination incidence angle, which is set to zero for these models, because we are using a pre-computed set of 1400 models built for conversion to thermal infrared normal emissivity. To determine the effect of this limitation, we ran 32-stream bidirectional reflectance models using the actual lighting geometry of the observations. We used the discrete ordinates radiative transfer model (DISORT) developed by Stamnes *et al.* (1988) described in Paragraph 5.3.2.1 and discussed in Subsection 6.2.2. The results of these models are discussed below.

In the spectral region investigated here, the models are most sensitive to the amount of water ice included, such that a change of 5% in water concentration will make a notable change in the spectrum. The model is similarly sensitive to grain size, bringing about significant spectral variance at a 10% change in grain size, while it is least sensitive to dust concentration, where a 50% change is needed to produce a notable spectral change. These sensitivities are illustrated by the model spectra in Fig. 7.6a.

We have made five spectral averages of the radiance factor (I/F) of the residual south cap plus one of an adjoining region with the spectral features of fine-grained water snow. The location of the spectra used in these averages is depicted in Fig. 7.7.

7.2.2 Perennial south polar cap ice composition

The average of eleven spectra from Orbit 30 (yellow outlines on Fig. 7.7) is shown in Fig. 7.8, along with a scaled albedo model. The scaling given in Table 7.1 is relative to the albedo times the cosine of the incidence angle (~0.18 in this instance), so the numbers are closer to relative abundances and have the same relative units as the soil spectra. There are inaccuracies and uncertainties that cause the sum of the parts in Table 7.1 to be different

from 1.0, such as surface roughness and surface photometry, which are known to be significant factors at large incidence angles.

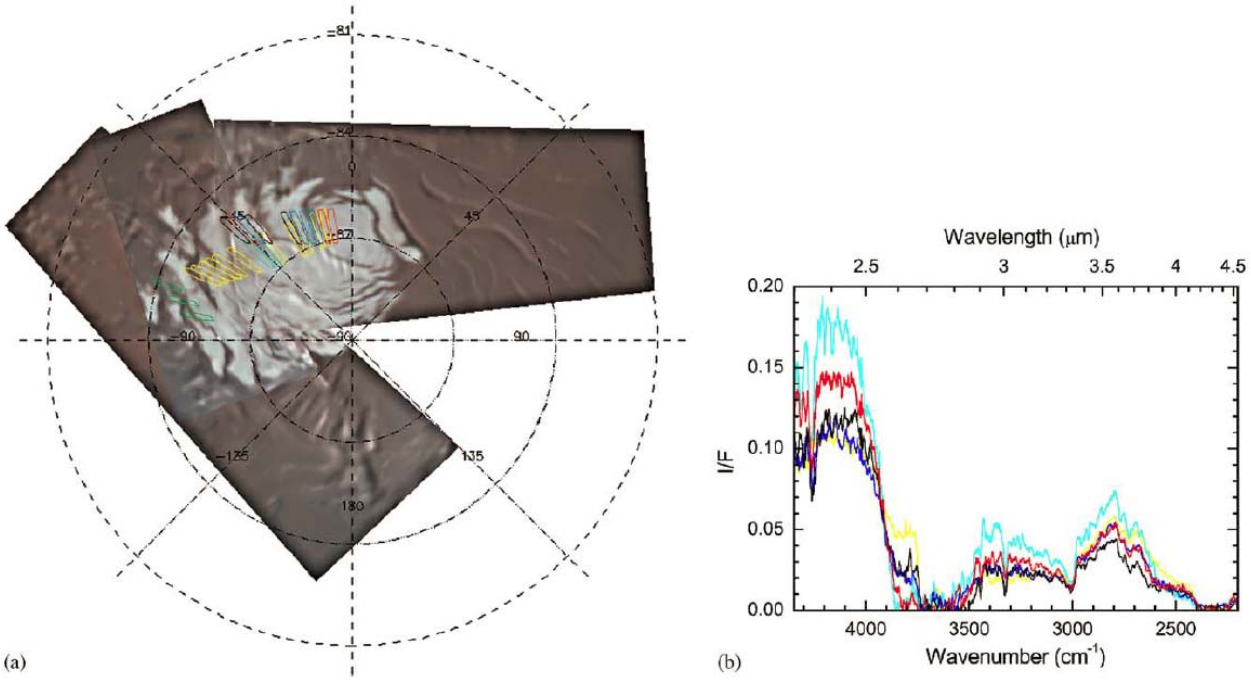

Fig. 7.7 (a) Mosaic of Mars Express OMEGA images, with the outline of individual PFS LWC footprints for the data used in this study plotted over it. The separate colors indicate groups of spectra that are averaged to produce the PFS spectra shown in Figs. 7.7b, 7.8–7.12, 7.14 and 7.15. (b) PFS average spectra for the five regions sampled over the residual polar cap frost deposits. The plot colors correspond to the colors of the outlines in Fig. 7.7a.

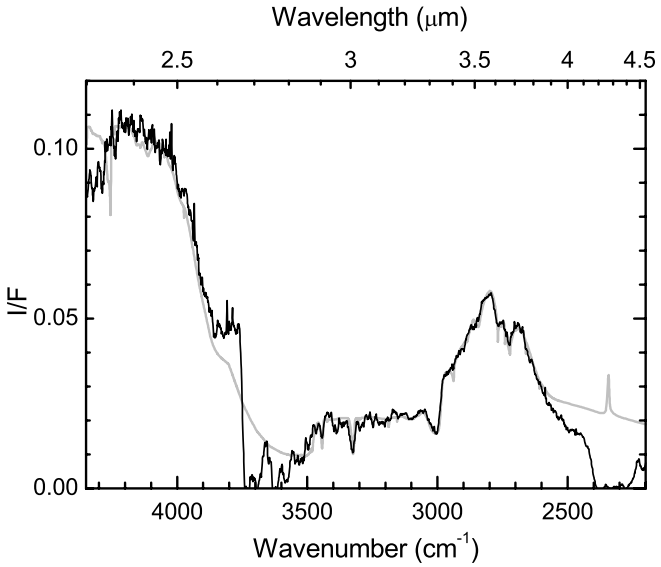

Fig. 7.8 The large average for Orbit 30 (black line) is shown along with a scaled albedo model fit (grey line). The average is from the 11 yellow footprints in Fig. 7.7. The model parameters are specified in Table 7.1.

The fit is very good to this low-noise average, at least up to 4300 cm^{-1}, except in the regions where the solid CO_2 absorption edge is outside the atmospheric absorption bands near 2500 and 3800 cm^{-1}. Here the level of reflectance is near zero for pure CO_2 ice, and is elevated by the intimately and spatially mixed impurities, mainly dust. The exact level and shape of the spectra in these regions is determined by the dust optical constants. In this spectral region we use those for terrestrial palagonite given in Fig. 6.3, which is not an exact analog for Martian dust. This large average requires about 40% of the area to consist of soil with a spectrum similar to that outside the polar cap.

The average of two especially bright spectra from Orbit 30 (cyan outlines on Fig. 7.7) is shown in Fig. 7.9. Here the model fit is optimized to fit the spectrum at wavenumbers below ~3200 cm^{-1}, because this is the region which has been calibrated using a blackbody radiator. It was not possible to fit the data at wavenumbers > 3300 cm^{-1} without significantly losing the fit < 3300 cm^{-1}. This kind of misfit is common when averaging only two or three spectra, and perhaps would be improved if we had more spectra to average. This example is larger grained and requires no soil spatial fraction, implying 100% frost coverage in these areas. It is also 30% brighter than a Lambertian plane of frost. This is partly explained by the typical increase in albedo of bright materials at high incidence angles, and partly by non-Lambertian behavior of the frost scattering.

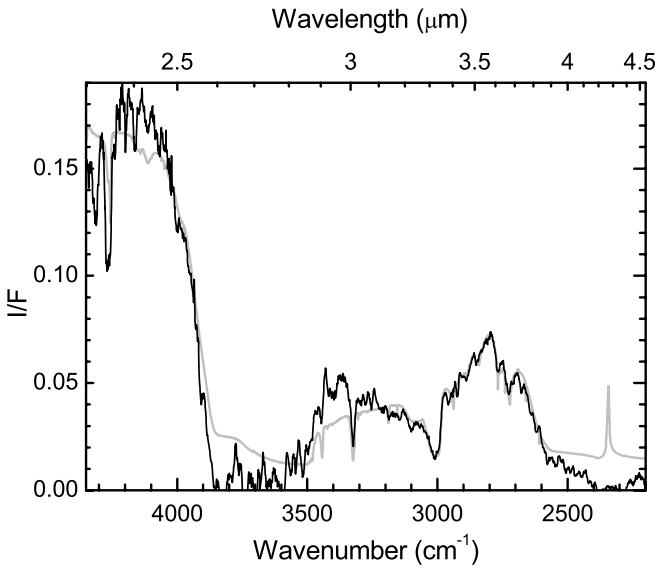

Fig. 7.9 The bright average for Orbit 30 (black line) is shown along with a scaled albedo model fit (grey line). The average is from the 2 cyan footprints in Fig. 7.7. The model parameters are specified in Table 7.1.

Three sets of spectra were selected from the available Orbit 41 data, based on their similarity across the spectral range investigated here. The first average consisting of four spectra (colored blue in Fig. 7.7) is similar to the large average of Orbit 30. The second average of three spectra (black outlines in Fig. 7.7) is slightly brighter at large wavenumbers and darker at small wavenumbers than the first average. The final average consisting of three spectra (colored red on Fig. 7.7) is similar to the bright average of Orbit 30. These three averages are plotted, respectively, in Figs. 7.10, 7.11 and 7.12, along with model fits. In all three cases, for the same reason as before, the fit was held tightly below 3200 cm^{-1}, with some misfit at larger wavenumbers appearing in averages two and three.

The fits are generally better in the first two than any of the others from either orbit. The model grain sizes are slightly larger than those from Orbit 30, and all present fields-of-view more filled by frost (≤ 10%soil area) than the large Orbit 30 average.

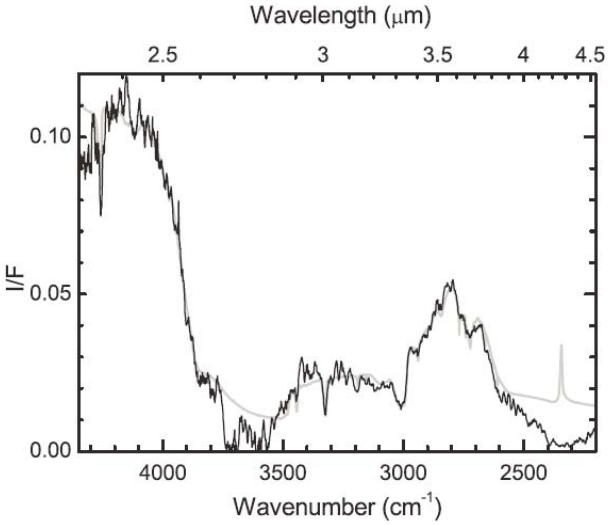

Fig. 7.10 The A (darkest) average for Orbit 41 (black line) is shown along with a scaled albedo model fit (grey line). The average is from the 4 blue footprints in Fig. 7.7. The model parameters are specified in Table 7.1.

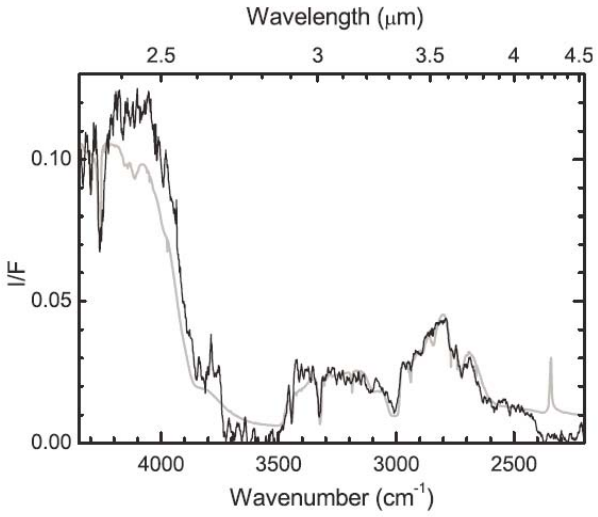

Fig. 7.11 The B (brighter) average for Orbit 41 (black line) is shown along with a scaled albedo model fit (grey line). The average is from the 3 black footprints in Fig. 7.7. The model parameters are specified in Table 7.1.

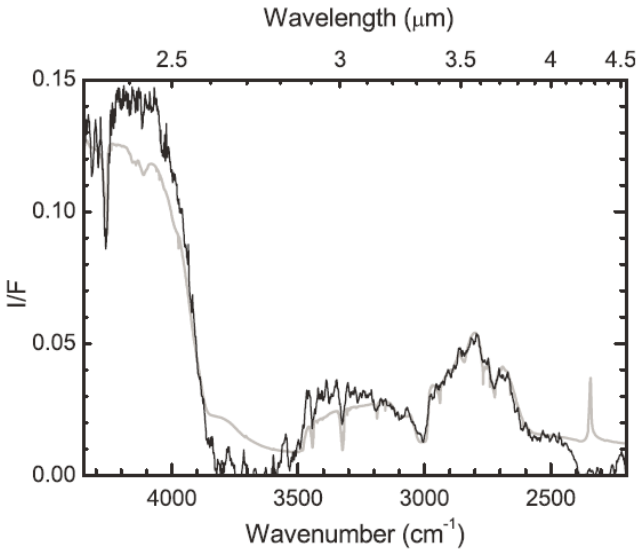

Fig. 7.12 The C (brightest) average for Orbit 41 (black line) is shown along with a scaled albedo model fit (grey line). The average is from the 3 red footprints in Fig. 7.7. The model parameters are specified in Table 7.1.

To investigate the sensitivity of the models to the lighting geometry, bi-directional reflectance (BDR) models were run to compare to the scaled albedo models. The results of this study are shown in Fig. 7.13. Here are plotted the albedo at incidence angles of 0° and 79°, and the BDR (scaled by π/0.18) for an incidence angle of 79° and an emission angle of 2°, all for r = 5 mm CO_2 ice with 0.02% dust and 0.005% water ice. Also plotted are the albedo at normal incidence for r = 2 mm CO_2 ice with 0.01% dust and 0.001% water ice (similar to the model for the Orbit 30 large average). Note that the BDR spectrum looks

more like the normal albedo spectrum with a factor of 2–5 less dust and water ice. The normal albedo with the same impurity amounts as the high incidence models is too dark in the 2800–3500 cm^{-1} region, and the albedo model at 79° incidence looks even purer than the BDR.

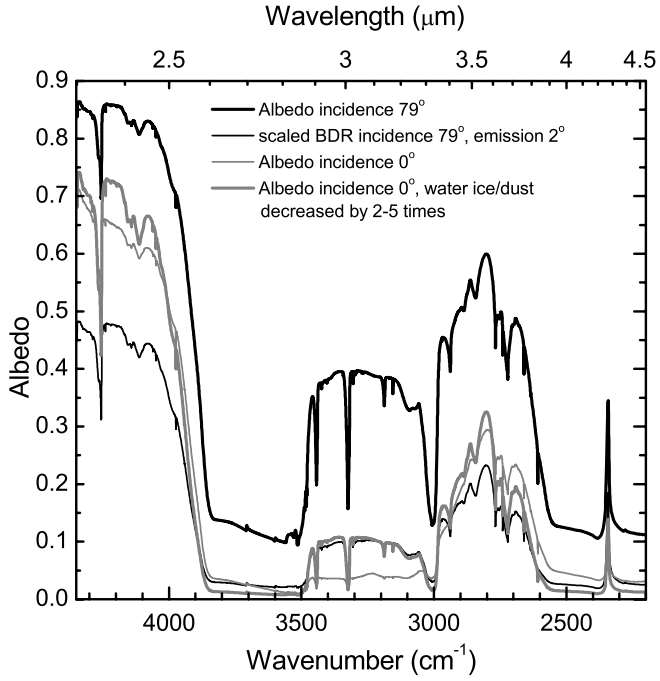

Fig. 7.13 This figure shows the effect of lighting geometry on models with the same properties. The thick black, thin black, and thin grey models all have the same grain size and dust and water ice content, but the thick grey model is for albedo at incidence angle 0° while the black spectrum is albedo at incidence angle 79°. There are major differences in apparent impurity content between these spectra. The thin black line is a BDR model for the geometry of the observation (incidence 79°, emission 2°) scaled by pi and the reciprocal of the cosine of the incidence angle. The thick grey line is the albedo at 0° incidence, but with 2–5 times less water and dust content. This albedo is closer to the scaled BDR in the middle section, implying that the 0° incidence albedo models underestimate the content of water ice and dust in the frost by 2–5 times.

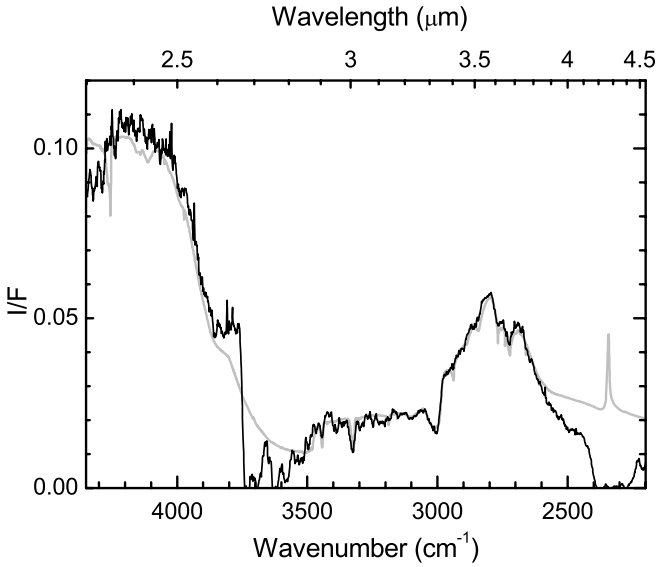

Fig. 7.14 The large (dark) average for Orbit 30 (black line) is shown along with a scaled BDR model fit (grey line). The model parameters are specified in Table 7.1.

A BDR model (multiplied by π) described in Table 7.1 is adjusted to fit the Orbit 30 large average in Fig. 7.14, with a fit comparable to the scaled normal albedo model. The implication is that the measured spectra are consistent with 2–5 times more dust and water than given in the albedo models described in Table 7.1.

On Orbit 61, a region at the edge the south polar residual cap was found which looked very much like a fine-grained water frost. Fig. 7.15 shows the average of three spectra (indicated by the green outlines in Fig. 7.7), smoothed over wavenumbers because there are no fine-resolution features in the spectrum of water snow. Also shown in Fig. 7.15 is a model that fits it. The model is based on a bi-directional reflectance model of water snow at ~150 K at the lighting geometry consistent with the observation. The model is adjusted to fit the peak reflection at 2800 and 4000 cm^{-1}, and the height of the Fresnel reflectance peak of water ice at 3220 cm^{-1}. The model consists of a spatial mixture of fine-grained water ice (to match the high reflectance) and large-grained water ice (to match the Fresnel peak). The relative abundance of fine-grained (r = 3 μm) snow and coarse-grained (r ≥ 50 μm) snow is about equal and the model is scaled by a factor of about 0.8 (implying a small amount of shadow in the footprints).

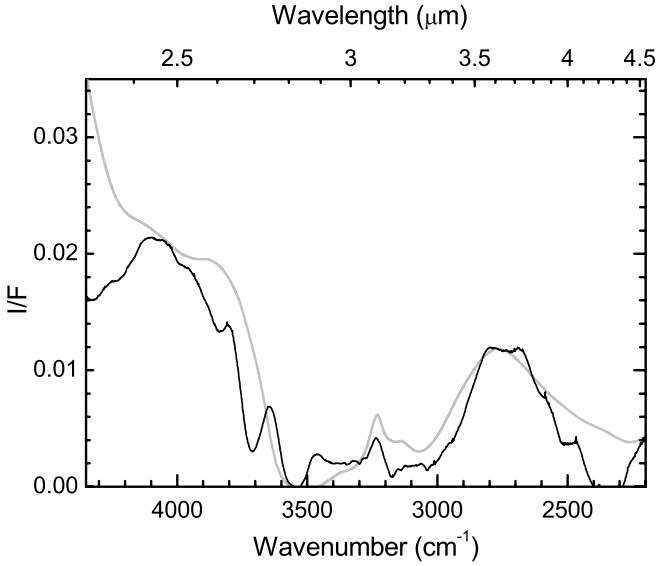

Fig. 7.15 Water ice spectrum at the edge of the residual polar cap. This average is from the areas indicated by the three green outlines in Fig. 7.7. The scaled BDR model is shown in grey. It is a linear combination of large and small grained ice that mimics the height of the reflecting regions around 4000 and 2750 cm^{-1}, and the relative height of the Fresnel reflection peak near 3220 cm^{-1}. The mixture consists of about 50% 3 μm and 50% 50 μm snow.

Table 7.1 Parameters for CO_2 frost models that fit specified PFS residual south polar cap averages

Spectra description	CO2 grain radius, mm	Mixed water, wt.%	Mixed dust, wt.%	Frost model scaling	Soil spatial fraction	Dark neutral spatial I/F
Orbit 30 average (Fig. 7.8)	3.5	0.001	0.01	0.50	0.30	0.004
Orbit 30 bright spot (Fig. 7.9)	8.4	0.0005	0.06	1.38	0.0	0.0
Orbit 41 A (Fig. 7.10)	7.0	0.0007	0.05	0.77	0.095	0.004
Orbit 41 B (Fig. 7.11)	10.0	0.0003	0.03	0.77	0.09	0.0
Orbit 41 C (Fig. 7.12)	10.0	0.0005	0.05	1.00	0.05	0.0
Orbit 30 avg. BDR (Fig 7.14)	5.0	0.005	0.02	0.76	0.30	0.003

7.2.3 Discussion

PFS very first observations occurred during the late southern summer (Ls 330°). PFS observations of the RSPC in the 2.3÷4.8 μm wavelength range have been here used for a detailed study of its composition, in terms of CO_2 ice grain sizes, and water ice and dust contents, showing that the principal component of ice is indeed solid carbon dioxide, but some admixture with water ice amounting to not more than several tens of ppm by mass is always present. The effective grain sizes are typically 5–10 mm, and the dust content is 1–$6 \cdot 10^{-4}$ (see Table 7.1). A very different estimate of 15% for the H_2O/CO_2 mixing ratio (in the form of a molecular mixture) was published by Bibring *et al.* (2004), on the basis of spectra obtained by OMEGA-MEX in the 2.0–2.6 μm wavelength range. It seems the discrepancy is mainly related to the models: a later re-analysis of the OMEGA data by Douté *et al.* (2007), make use of an intimate granular mixture model (the same as used in our work), showing better fits of the data than those in Bibring *et al.* (2004), and results much closer to our results given in Table 7.1, although the estimated water ice and dust content are still one order of magnitude higher than those from PFS data. It must be said that the 2.4–4.2 μm range is the most diagnostic spectral range for investigating the water ice contamination. Below 2.4 μm the spectra are much less sensitive on this parameter, allowing greater uncertainties in the results. Moreover, a high spectral resolution is needed to resolve all the narrow features of the CO_2 ice in the NIR, which are diagnostic of the grain size. These considerations may explain the differences in the water ice content and the ~5 cm coarse CO_2 ice grain sizes obtained by Douté *et al.*, 2007 (OMEGA has a spectral resolution of 20-30 cm^{-1} in the 2.6–2.0 μm spectral range). On the other side, PFS has a lower spatial resolution than OMEGA and the contributions of uncovered soil and dust contamination may be difficult to separate, allowing higher uncertainties in the dust content.

7.3 The condensing CO_2 south polar cap of Mars

In this Section we present a study of the south polar cap during the fall and winter seasons. With this work we have been able to fill some of the lacks of information about the condensing CO_2 south polar cap of Mars studying, in particular, the progression (recession) rate of the CO_2 ice deposits towards lower (higher) latitudes, and the complex dynamical processes that occur in the polar nights and determine the nature and mechanisms of CO_2 ice accumulation. The southern fall season has been found to be extremely important in the explanation of the residual south polar cap asymmetry.

Results from selected PFS orbits have also been compared with the results provided by the Martian general circulation model (GCM) of the Laboratoire de Météorologie dynamique (LMD) in Paris. The comparison presented in this work is far from being exhaustive, and further work will be devoted to a more complete analysis of the differences between the model and the observations. Nevertheless, this first attempt of cross-validation between PFS measurements and the LMD GCM shows how tricky is modeling the condensing CO2 south polar cap.

At the time of writing, the results presented in this Section are in press to the scientific journal *Icarus*.

7.3.1 Background and rationale

Despite the large number of studies on the southern spring and summer polar cap recession, with both satellite and ground-based observations, only few studies are available in the literature describing the seasonal progression of the Martian south polar cap (SPC) during the fall and winter seasons; in addition, most of them make use of model predictions rather than measurements. This is mainly due to limitations in the visible imaging technique which is used to determine the contrast of albedo between the edge of the seasonal cap and the volatile free soil. As discussed in Section 7.1, such contrast is practically undetectable where the CO_2 cap is dark. Because a large portion of the atmosphere condenses in and sublimes from the seasonal caps in a cyclic way during the year, the frost deposits play a significant role in the regional and global atmospheric circulation. Understanding the nature of the seasonal polar caps is essential if we want to understand the current Martian climate with high degree of confidence.

We have seen in Chapter 1 that as much as 30% of the Martian atmosphere condenses every year to form polar caps in both hemispheres inducing large variations of the surface pressure over the entire planet, as first observed by the Viking landers (see also Prettyman *et al.*, 2003),. At first glance, this phenomenon may seem straightforward, but several previous works on the thermal structure and thermal IR observations of the polar night by the NASA Mars Global Surveyor (MGS) and Mars Odyssey missions, suggest that this event is very complex, expecially in the southern hemisphere (Titus and Kieffer, 2001; Banfield *et al.*, 2003; Hinson *et al.*, 2003; Colaprete *et al.*, 2005). Traveling weather systems (transient eddies) are prominent in both hemispheres (J. R. Barnes, 2003; Banfield *et al.*, 2004; Hinson and Wilson, 2002), while the large-amplitude and strongly upper-level disturbances observed for the first time in the northern hemisphere by the Viking Meteorology Experiment (J. R. Barnes, 1980, 1981) have not been observed in the south yet, despite they are predicted by Mars GCM experiments (Barnes *et al.*, 1993). A peculiar and very prominent component of the southern winter circulation, as revealed by the Thermal Emission Spectrometer (TES) and Radio Occultation observations from MGS (Hinson *et al.*, 2003), is a large-amplitude quasi-stationary wave pattern. At lower altitudes this wave can show a fairly strong wavenumber-2 pattern, but at upper altitudes it is dominated by wavenumber-1. This planetary wave and the complex dynamical processes that occur in the atmosphere during the southern polar night have important effects on the regional climate of the southern hemisphere in winter time (Colaprete *et al.*, 2005).

Whether the CO_2 ice accumulation in the polar caps is the result of a direct vapour condensation at the ground (frost), or of atmospheric condensation and precipitation (snow), cannot be easily addressed. The formation of CO_2 ice clouds and snowfall in the Martian polar night is far from being completely understood, and the direct condensation of the main atmospheric constituent (carbon dioxide) in the polar regions during fall and winter is one aspect of the Martian meteorology that has no terrestrial counterpart.

In this work we try to fill, at least partially, the lack of information about the condensing CO_2 south polar cap of Mars, studying in particular, the progression (recession) rate of the CO_2 ice deposits towards lower (higher) latitudes and the mechanisms of the CO_2 ice accumulation. To this purpose, we have analysed the PFS spectra which have been acquired during the first two years of activity of the MEX mission. We also provide new insights in the explanation of the residual south polar cap asymmetry which has been proposed by Colaprete *et al.* (2005).

7.3.2 Data set and treatment

The PFS experiment and its calibration have been described in Chapters 2 and 3. Detailed information on the calibration campaign performed in laboratory, space and with the spacecraft orbiting mars are available in the Appendix A.2 and A.3 of this book (Giuranna *et al.*, 2005a, 2005b). Essentially, only the LWC spectra were used in this work, since during the polar night the SWC is "blind": there is no reflected sun light to measure and only negligible thermal emission from the cold CO_2 ice (temperature ~ 145 K) in the thermal range of the SWC.
The observed LWC radiance depends on several parameters of the atmosphere and surface of Mars, as described by the radiative transfer theory: the surface temperature, the column density of dust and water ice aerosols in the atmosphere, the air temperatures as a function of altitude, the surface pressure, and the column density of water vapour and carbon monoxide. Adopting the very general formalism of Bayesian analysis, an algorithm for the scientific analysis of individual calibrated PFS measurements has been developed, allowing the simultaneous retrieval of the above mentioned parameters. A full description of the adopted method can be found in Grassi *et al.*, 2005. The cases presented in this study were carefully selected imposing a value of chi-square test close to 1 in the indicative range 400–800 cm^{-1}. The typical quality of the modeling is presented in figure 7.16 for different thermal conditions of the atmosphere. In our retrieval scheme, the entire range 400–1100 cm^{-1} is used simultaneously for the self-consistent retrieval of the following parameters (state vector elements):

e) surface temperature;
f) air temperature profile (in the indicative range 1-50 km);
g) integrated silicate dust content;
h) integrated water ice content.

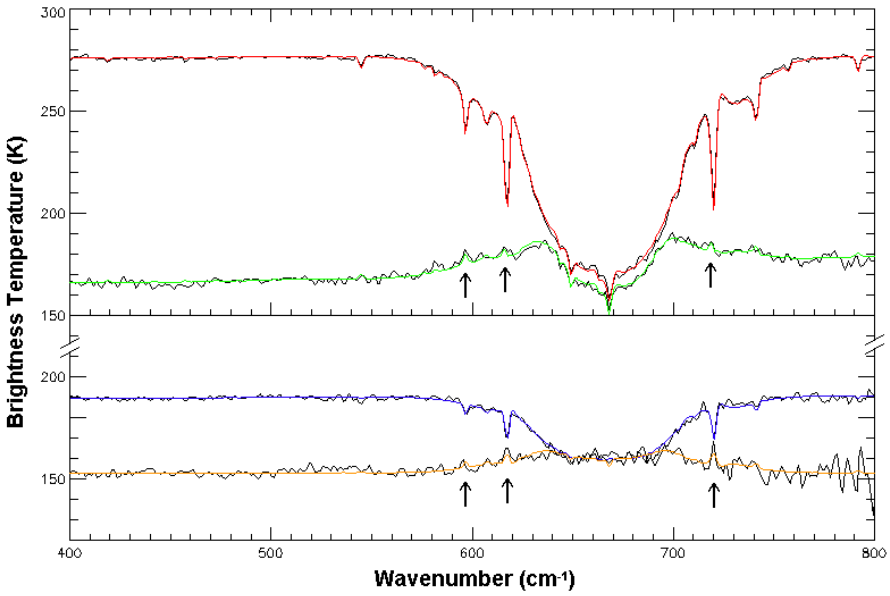

Fig. 7.16 Typical quality of PFS spectra modeling for different thermal condition of the atmosphere. *Black curves*: PFS measured single spectra. *Colored curves*: synthetic spectra computed by the algorithm for the scientific analysis of individual calibrated PFS measurements, developed by Grassi *et al.* (2005). Black arrows point to the CO_2 Q-branches.

Noteworthy, the high spectral resolution of PFS allows the detection of several different thermal gradients in the atmosphere, as demonstrated by the effective modeling in the same spectrum of absorbing and emitting Q-branches (lower curves of both panels of figure 7.16, black arrows).

The general retrieval code adopted for the analysis of PFS calibrated data (Grassi *et al.*, 2005) was designed for being used for general purposes. In this perspective, an important characteristic is given by its robustness against possible run-time errors due to occasional residual instrumental features in calibrated data and intimate numerical instability of the retrieval inverse problem. Therefore, the physical parameters of the Martian atmosphere computed from PFS data are constrained to lie within realistic ranges. For air temperature, the lower limit was fixed - quite arbitrarily - to the CO_2 condensation temperature. This choice is partially justified by

1. the need to avoid extrapolation of gaseous absorbing coefficients outside the temperature range for which they have originally been tabulated, and
2. the ambiguity to define a more realistic lower limit without introducing a complete condensation microphysical scheme inside the retrieval code.

This constraint implies that, in our retrievals, any physical situation consistent with a supersaturated CO_2 atmosphere is actually represented with a temperature profile coinciding with the condensation profile. For this reason, one must be careful in the interpretation of the results; whether is the radiative or the adiabatic cooling to control the CO_2 condensation in the atmosphere cannot be addressed by the vertical temperature profiles themselves.

The Hamming apodization has been applied to all the interferograms used in this study; the effective spectral resolution is thus ~2 cm^{-1}.

In this study we have collected and analyzed a set of 467 orbits acquired during the first two years of PFS activity. This dataset spans more than half a Martian year, from Ls~330° to Ls~194°, although there are some gaps and lacks. For instance, during the whole winter season the orbit geometry is such that we rarely observe latitudes lower than –60°, making it impossible to compute longitude cross-sections of the vertical profiles of (T – Tsat) at polar latitudes, which are needed for a comprehensive study of the mechanisms of the CO_2 ice accumulation. Some other short Ls range is also missing, such as the 39°-49° range. Nevertheless, the data allow a detailed study of the CO_2 south polar cap formation rates and mechanisms, especially during the fall season which has been found to be extremely important for the explanation of the residual south polar cap asymmetry.

7.3.3 CO_2 ice clouds and snowfalls: theoretical considerations

Before showing the vertical structure of the atmospheric temperature above the southern polar cap during the polar night as measured by PFS, and discuss the possible implications on the Martian climate and the mechanisms of the CO_2 ice accumulation, it is important to analyze the various processes which lead to cooling and condensation of the atmosphere, and thus to CO_2 snowfall. Although it is a general idea that most of the dry ice condenses directly on the surface, a fraction should also condense in the atmosphere, strongly influencing its radiative properties.

Since CO_2 ice clouds essentially form in the polar night, the evidence of their existence has remained theoretical or indirect. It is only recently that a variety of cloud shapes varying over space and time has been observed by the MGS laser altimeter MOLA (Pettengill and Ford, 2000; Colaprete and Toon, 2002). The radiative effect of snow would strongly alter the radiative balance of the condensing polar caps and thus the CO_2 cycle and the global climate. As discussed in Subsection 1.3.2, Forget *et al.* (1995) showed that the low emission zones observed by the infrared thermal mapper (IRTM) instrument aboard Viking (Fig. 1.6) and by Mariner 9 IRIS (Paige *et al.*, 1990a), were likely to be created by the radiative properties of CO_2 snowfalls (falling snow particles or fresh snow deposits). CO_2 snowfall has never been directly observed on Mars. Nevertheless, climate simulation with general circulation models (GCMs) showed that a fraction of the total CO_2 condensation could take place in the atmosphere, especially when it is dust laden, because of the increased atmospheric emissivity (Pollack *et al.* 1990). In this case, atmospheric condensation is the result of *radiative cooling*. Atmospheric condensation may also result from *adiabatic cooling* in upward motions (Forget *et al.*, 1998b). This latter process can be very efficient locally.

Radiative cooling

During the polar night, the radiative balance of surface CO_2 is negative, barring an extraordinarily warm atmosphere. The radiative budget is reduced to cooling due to the emission of thermal infrared radiation from the ground. When the surface is cooled to the frost point, its temperature is kept constant by the latent heat released by surface condensation, while the atmosphere is radiatively warmed by the surface infrared emission. Gierash and Goody (1968) and, more recently, Paige (1985) pointed out that the radiative equilibrium of a surface + atmosphere column is always colder than the condensation temperature profile. Thus, in the polar night, the atmospheric column may rapidly cool and condense out. The latent heat released by condensation would then balance the radiative cooling to keep the temperature at the frost point value everywhere in the atmosphere (actually, everywhere the condensation is in act). As Forget *et al.* (1998b) have shown, in such conditions, the cooling and condensation rates depend only on the radiative properties (emissivity and transmittivity) of the ground and the atmosphere, being the lowest for a clear atmosphere ($\tau = 0$) above a blackbody surface ($\varepsilon = 1$): only 3% of the CO_2 condenses in the atmosphere in that case. The presence of dust strongly increases the emissivity of the atmosphere and thus the cooling rate. The radiative properties of the surface also affect the equilibrium of the atmosphere: when the cap surface emissivity is lower than one, the infrared heating of the atmosphere by the ground is reduced, and the condensation increases. With surface emissivity $\varepsilon = 0.7$ and $\tau = 1$, the fraction of CO_2 condensing in the atmosphere reaches 25% (Forget *et al.*, 1998b).

Adiabatic cooling

The atmospheric circulation affects the thermal structure of the polar atmosphere. It is well known that the atmosphere transports heat from the insolated latitudes to the polar regions (Pollack *et al.*, 1990; Hourdin *et al.*, 1995). In addition, the circulation can locally warm or cool adiabatically the atmosphere. Cooling occurs in upward motions. Forget *et al.* (1998b) have simulated both the heat advection and the large-scale adiabatic effects during the southern winter ($Ls = 120°$), using a 1D version of the LMD Martian GCM radiative transfer code (Hourdin *et al.*, 1993 and 1995) with 25 layers. As a result, they

found that, according to the model, the atmospheric condensation rate reaches more than ten times the value corresponding to the radiative cooling alone in two special condensation zones around (75° S, 135° W) and (67.5° S, 20° W). These areas are created by a dynamic mechanism originating around two low-pressure zones located at about 60° W and 300° W and related to the Argyrae and Hellas basins. This is a typical effect of the southern winter stationary waves which are forced by topography (Hollingsworth and Barnes, 1995; Banfield *et al.*, 2003; Hinson *et al.*, 2003).

7.3.4 The Residual South Polar Cap (RSPC)

In Section 7.2 we have analyzed the composition of the RSPC. As we demonstrated, the carbon dioxide survives all year long in the south residual cap (see also Bibring *et al.*, 2004; Hansen *et al.*, 2005; Douté *et al.*, 2005); this behaviour is surprisingly different from what has been observed in the north, where the CO_2 completely sublimes by the beginning of the summer season. Paige and Ingersoll (1985) calculated the annual radiative budgets and infer the annual CO_2 frost budgets, showing that the CO_2 sublimation rates are much smaller in the south than in the north, and this is due to the higher albedo of the RSPC relative to the north cap. This difference in albedo, added to the difference in subsurface heat conduction – which is rather high on the residual north cap and close to zero on the RSPC where the temperature is constant all year long (Jakosky and Haberle, 1990) – explains why the north and south residual polar caps are so different.

What still has to be explained is the position of the south permanent cap. Figure 7.7a shows the RSPC in a mosaic of three OMEGA images. The residual south polar cap is approximately 400 Km across and the cap center is displaced by about 3° from the geographic pole. Mars eccentricity or local topographic irregularities cannot straightforwardly account for this asymmetry, nor the above mentioned energy balance models can reproduce it. In fact, this has been a major issue in Mars science for many years. A possible explanation has been recently suggested by Colaprete *et al.* (2005). In this work, we provide new insights in the explanation of the RSPC asymmetry.

7.3.5 Ls=0°-25°: the early-fall south polar cap

Direct observations of frost deposition are generally difficult to obtain due to the fact that most of the frost at high latitudes is deposited when the region is in darkness. However, radiometry data by MOLA suggest that frost at the higher latitudes starts to form on the surface before the end of (southern) summer, when the sun is approaching the equator but the pole is still illuminated (M. T. Zuber and D. E. Smith, 2003). Indeed, in the range of Ls examined in this section, soon after the end of summer (Ls=0°-25°), the asymmetry observed in the residual cap is completely vanished; the cap appears symmetric and extends already up to –70° latitude, as we can see from the mosaics of tracks of the surface temperatures in figure 7.1 (top-left panel). It is important to note that, in our work, we focus our interest only in the CO_2 cap and the mechanisms of CO_2 ice accumulation. Nevertheless, the actual extension of the polar ices, including the water ice cap, may be found at lower latitudes than –70°, this value being the bound only for the CO_2 ice deposits. Hereafter, we will always refer to the polar cap as the CO2 ice polar cap.

Whether the CO2 ice at these values of Ls is frost or snow cannot be addressed only on the basis of the surface temperatures. In both cases these temperatures are similar, forced by the vapor pressure equilibrium with the atmosphere (see Section 7.1, or Giuranna *et al.*, 2007a in Appendix A.4). In principle, a first discrimination may be done on the basis of the grain sizes. CO_2 snow grain sizes are expected to be smaller than those derived by a continuous vapor deposition. Unfortunately, the cap is in the night side and the PFS Short Wavelength Channel, which has shown great capabilities of retrieving ice grain sizes with its NIR spectra (see Sections 7.2 and 7.4, or Hansen *et al.*, 2005, and Giuranna *et al.*, 2007b in Appendix A.3 and A.4), is unusable. Nevertheless, a detailed study of the temperatures in the atmospheric column over the cap can be done using the thermal infrared radiation measured by the PFS Long Wavelength Channel, allowing us to straightforwardly answer the question. As anticipated in section 7.3.1, this may not be an easy task; nevertheless, if the atmospheric temperatures are always above the CO_2 condensation temperature (at a given altitude) in the whole column, the snowfall hypothesis can be undoubtedly rejected. As discussed in Subsection 7.3.2, the algorithm developed by Grassi *et al.* (2005) allows, among other things, the simultaneous retrieval of surface temperature, integrated content of water ice and dust suspended in the atmosphere, and, most important for the issue we want to address, the air thermal fields up to an altitude of about 50 Km. By comparing the measured vertical temperature profiles with the CO_2 condensation temperature at different altitudes we can establish if, where and at which altitudes CO_2 snow falls may be allowed.

Our results show that, at these values of Ls, the south polar cap essentially consists of CO_2 frost deposits. A typical situation is depicted in figure 7.17, where we show the study for a single representative orbit. The orbit number is 287 and Ls is 17°, right in the middle of the Ls range examined here. The surface temperatures (top-right panel) reveal the presence of CO_2 ice up to −70° latitude, which is essentially frost. This can be evinced by monitoring the vertical profiles of $\delta T_{sat}(z) = T(z) - T_{sat}(z)$ (where z is the atmospheric altitude): as shown in the bottom panel of figure 7.17, the atmospheric temperatures are far above the saturation value in the entire column and at every altitude, with only one exception in a narrow region centered around −85° latitude (mid-right panel; this is one of the very few $\delta T_{sat} < 0$ occurrences in the Ls range here examined). If we repeat this study for the whole set of orbits, and thus for the whole Ls = 0°−25° range, we can confirm that the situation described for orbit 287 is indeed the typical early-fall south pole situation. In figure 7.18 we show the $\delta T_{sat}(z)$ profile for a longitude cross-section at −85° latitude as a function of altitude: the CO_2 condensation in the atmosphere is forbidden almost everywhere, the atmospheric temperature being always few or several degrees above the CO_2 condensation temperature at any altitude. The wavenumber-1 planetary wave is not clearly marked yet, but still the 40°−220° longitude eastern hemisphere appear warmer than the western hemisphere and CO_2 snow falls, although only occasionally, are allowed exclusively in the latter.

Consequently, we can conclude that the early-fall south polar cap consists essentially of CO_2 frost deposits. Atmospheric condensation is allowed only occasionally and only for latitudes ≤ − 84°. Thermal inversions are present almost everywhere, especially in most of the eastern hemisphere, and centered around 5 Km above the surface.

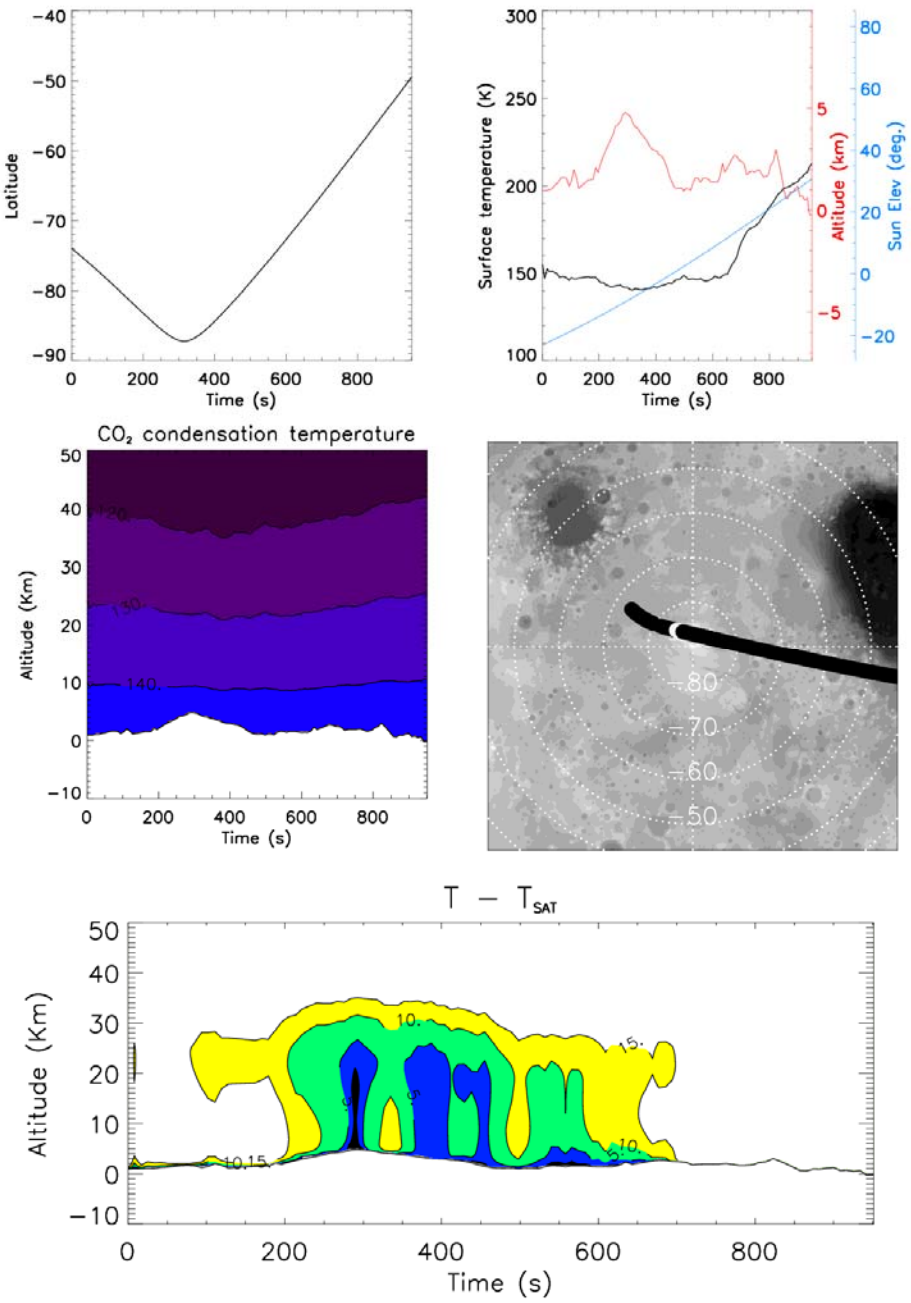

Fig. 7.17 Orbit # 287 (Ls 17°), a typical early-fall south pole scenario (see text for details). *Top-left*: latitude versus time (in seconds) elapsed from the beginning of the acquisition of the first spectrum. Use this to obtain latitudes for the other panels. *Top-right*: the surface temperatures (black curve) are "frozen" to the CO_2 condensation temperature (140-147 K, depending on the surface altitude – i.e. surface pressure – given by the red curve) up to -70° lat, where they finally increase roughly following the sun elevation gradient (light blue curve). *Middle-left*: CO_2 condensation temperature profiles. *Middle-right*: track of PFS observations; white spots indicate when and where CO_2 snow fall is allowed, according to the vertical profile of $T - T_{sat}$ shown on *bottom panel*, where the black area is where the atmospheric temperature, at a given altitude, goes below the CO_2 condensation temperature for the same altitude.

7.3.6 Ls=25°-38°: the early/mid-fall cap and evolution speed

Unfortunately, as can be seen in figure 7.1 (top-right panel), during this Ls range we observed latitudes poleward of –80° only twice, namely during orbit 371 and 378. It is,

therefore, impossible to study in detail the mechanisms of the CO_2 ice accumulation as we did in the previous Subsection for the early-fall season, that is by computing longitudinal cross-sections of $T(z) - T_{sat}(z)$ at polar latitudes as in figure 7.18.

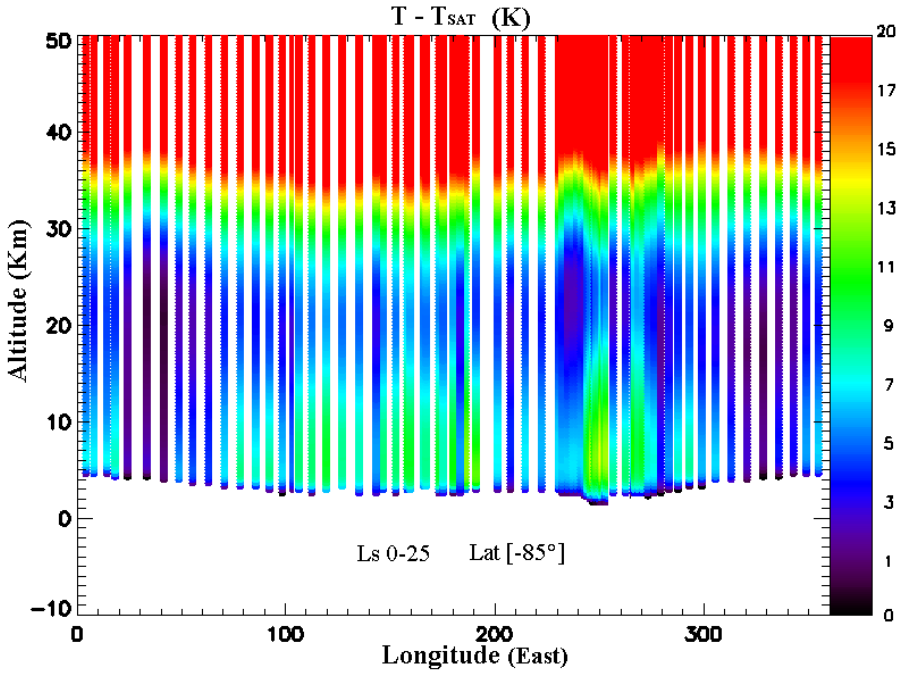

Fig. 7.18 Ls 0°-25°. Longitude cross-section at −85° latitude showing $T - T_{sat}$ as a function of altitude. Red color is used for $T - T_{sat} \geq 20$ K.

Nevertheless, repeating the same study as in figure 7.17 for these two orbits, and for all the other orbits within this Ls range, we found that, at least for the observed latitudes and longitudes, no CO_2 condensation zones were present anywhere in the atmosphere, suggesting a scenario similar to the one described in the previous section, with a cap mainly consisting of CO_2 frost deposits.

The south polar cap edges are advancing towards lower latitudes throughout the autumn. In Section 7.2 we performed a detailed tracking of Mars' south polar cap edges. The dataset used for the edge tracking is exactly the same as the one used for the present study. As shown in Fig. 7.5, the cap expands with a constant speed of about 10° of latitude per 15 degrees of Ls during most of the fall season (until Ls ~ 70°) at every longitude. The maximum extension of the south polar cap occurs sometime in the 80° – 90° Ls range, when the cap edges are as low as – 40° latitude. The CO_2 ice south polar cap will then recede with a constant speed of ~ 5° of latitude every 25 degrees of Ls during the whole winter. As discussed in Paragraph 7.1.2.2, inside the Hellas and Argyre basins (red triangles in Fig. 7.5) the CO_2 condensation temperature is several degrees higher than that of the rest of the south polar region (according to the Clausius-Clapeyron's law), due to the higher pressure values. Therefore the CO_2 frost can be stable at lower latitudes (and higher temperatures), extending up to −30° latitude (occasionally even at lower latitudes), causing the cap to be asymmetric. Thus, the two major Martian basins appear to be responsible for a south polar cap asymmetry. The longitudinal asymmetries reduce during

the cap retreat, as the CO_2 ice/frost sublimates, and disappear completely around Ls ~ 145°. Afterwards, the cap continues to recede symmetrically.

7.3.7 Ls 50°-70°: two distinct regional climates

7.3.7.1 Two distinct regional climates close to the pole

In the two previous Subsections we have shown that, during the first half of the southern fall, the cap consists of CO_2 frost deposit, the atmospheric temperatures being always above the CO_2 condensation temperature in the whole column, at every latitude and longitude (with few sporadic exceptions in the western hemisphere). A detailed study of the vertical temperature profiles above the cap, retrieved by the PFS LWC spectra, reveals that the mid-late fall season offers a much more complex and interesting scenario.

In figure 7.19 we show the $\delta T_{sat} = T - Tsat$ for a longitudinal cross-section in a narrow stripe of latitude (84°-86° S) as a function of altitude. In this selected season range (50° – 70° Ls) two distinct regional climates clearly characterize the south polar cap. CO_2 snow falls are now allowed, but they occur exclusively in the western hemisphere. In the eastern hemisphere (more precisely, in the 30° – 210° east-longitude range), the whole atmospheric column is several degrees above the saturation temperature; here, the direct vapor deposition is the only allowed mechanism for the CO_2 ice accumulation in the South polar cap. In the western hemisphere, instead, atmospheric condensation is allowed in the entire 0-30 km column; here, surface ice accumulation may be dominated by precipitation. This is especially true in two particularly cold regions, located around 260° E and 320° E longitude, where the CO_2 condensation is allowed to a large extent in the atmosphere, from the surface up to 20 km and 30 km, respectively.

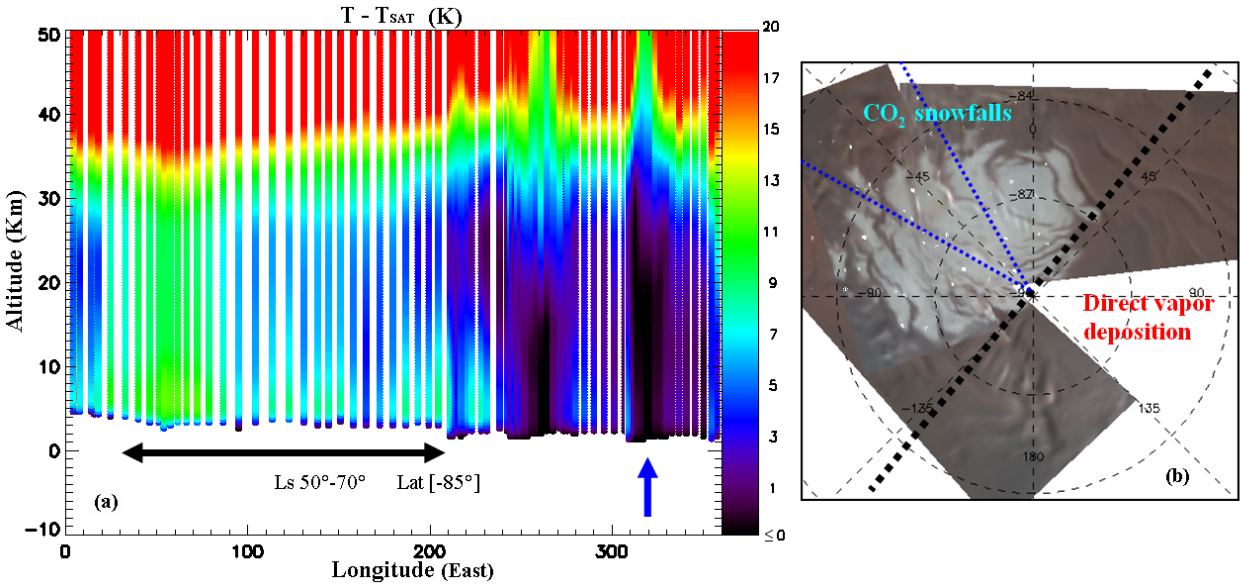

Fig. 7.19 (a) Ls 50°-55°. Longitude cross-section at –85° latitude showing the vertical profile of $T - T_{sat}$. At these Ls the wavenumber-one planetary wave is already well defined and so are the two distinct climates on either side of the pole. (b) CO_2 snowfalls are allowed exclusively in the western hemisphere. The coldest region (blue arrow in figure 7.19a) is located right around the center of the south residual cap (blue dotted line).

It is very interesting to note that the coldest region (blue arrow in figure 7a) is located right around the center of the south residual cap (blue dotted line in Fig. 7b; the south residual cap extends roughly from 250° E to 45° W longitude, and is centered around 320° E longitude). Note that both the high-condensation rate zones predicted by the 1D GCM simulations described in Subsection 7.3.3 are in the "cold" hemisphere, and are somehow in agreement with the two cold regions observed by PFS. In particular, the coldest one, which is predicted by the models to be around 340° E longitude, is only 10° longitude far from the one we have found in the present work. Note also that the warmest region is located in the 40° – 90° east-longitude range, i.e. right below the Hellas basin. An increase of the atmospheric temperatures below Hellas and poleward of -60° latitude is also predicted by the Mars GCM model, as a result of dynamical forcing by the largest southern impact basin (Forget et al., 2006; EMCD 4.1 pre-computed version, available online at http://www-mars.lmd.jussieu.fr).

The residual cap lies in the cold region, where CO2 snowfalls occur. The black dotted line in figure 7.19b separates the two hemispheres as defined in figure 7.19a, where the black double-arrow indicates the extension and the edges of the warm region. These two distinct regional climates produce differences in the nature of the surface ice deposits during the whole second half of the fall season, and are the main responsible for the residual south polar cap asymmetry. The scenario depicted in figure 7.19a starts around Ls = 50°-55°, and remains essentially unaltered until the end of the fall. The only exception is that, after Ls = 70°, the atmospheric temperatures above the polar regions are generally lower, therefore CO_2 condensation in the atmosphere occurs in a wider area and, occasionally, also in the western hemisphere (see Subsection 7.3.8). It is interesting to understand how this very peculiar scenario can form; we will show in the following Paragraph that the observations from PFS confirm that it is essentially the result of dynamical forcing by the largest southern impact basins, Argyre and Hellas.

7.3.7.2 Hadley circulation, winds and planetary waves from PFS nadir observations

In the last thirty years observations by instruments onboard rovers, landers, and spacecrafts have provided detailed insights in the thermal structure and dynamics of the martian atmosphere. The vertical temperature profiles inferred from measurements of thermal emission by instruments aboard orbiting spacecrafts, such as the MEX/PFS LW Channel, represent the best available way to get indirect information on the atmospheric circulation. These data can provide more complete spatial and temporal coverage of Mars than direct measurements from landers or rovers on the surface, and can be used to infer winds. The vertical variation of the horizontal wind components (i.e., the wind shears) can be computed from global temperature fields, using the geostrophic or higher-order approximations (Zurek et al., 1992), while the zonal-mean (longitudinal average) meridional and vertical winds can be calculated by combining the thermodynamic energy and mass continuity equations. The zonal-mean component of the zonal wind can be derived in a rather straightforward way from the observed temperature field, by using the thermal wind relation (see, e.g., Holton, 1979; Andrews et al., 1987):

$$\frac{\partial}{\partial z}\left[\left(f+\frac{\overline{u}\tan\theta}{a}\right)\overline{u}\right]=-\frac{R}{ma}\frac{\partial\overline{T}}{\partial\theta} \qquad (7.2)$$

where $\overline{T}$ is the zonal mean temperature, $\bar{u}$ is the zonal mean eastward wind component, θ is the latitude, f is the Coriolis parameter, a is the planetary radius, R is the gas constant, z is the relative pressure, and m is the atmospheric mean molecular weight. This relation cannot be used close to the equator; here the gradient winds cannot be computed since the assumed force balance is not valid at low latitudes (Holton, 1979). The computation of the gradient winds requires a boundary condition for the zonal wind speed. It is assumed here that $\bar{u} = 0$ at the planetary surface and Eq. (7.2) is integrated upward, yielding the baroclinic component of the wind field. Any nonzero surface wind must be added to the result to obtain the total wind speed. On the Earth, the contribution of the surface wind to the total wind in the mid-troposphere is usually small, and integration of Eq. (7.2) with $\bar{u} = 0$ at $z = 0$ provides a good approximation to $\bar{u}(z)$. It is reasonable to expect this approximation to be valid on Mars (Leovy, 1969 and 2001). Although the calculation of $\bar{u}$ from Eq. (7.2) is simple in principle, care must be taken because of the required numerical differentiation of the temperature with respect to latitude. For this purpose the temperatures were smoothed in latitude using a 4° wide window centered on latitudes evenly spaced by 2°.

The zonal-mean thermal structure as retrieved from the PFS LWC thermal spectra in the 50°-70° Ls range, and the corresponding zonal-mean eastward wind field derived from thermal gradient wind balance (7.2) are shown in figure 7.20. For the temperature cross-section in the meridional plane (figure 7.20a) an adequate coverage in longitude and latitude is ensured by the large set of available PFS observations. Air temperatures from the individual retrievals were binned in latitude (two-degrees wide bins) and then averaged to obtain mean air temperature fields. This has been done for each of the pressure levels at which temperatures were retrieved. Generally speaking, the changes in the atmospheric temperature fields and, consequently, in the thermal wind fields, are a consequence of the different solar heating with seasons. In the winter hemisphere we have the minimum solar heating at the corresponding solstice, when the atmospheric temperatures reach minimum values. The highest atmospheric temperatures occur instead during the summer solstice. Despite this, we observe from figure 7.20a that the temperature field shows a local maximum at an altitude of about 40 km in the polar night hemisphere, i.e. the temperature field is warmer than the thermodynamic equilibrium. The reason of this polar warming is dynamic: it is caused by adiabatic heating produced by the mean meridional residual circulation (Zurek, 1992). This type of circulation can be described in terms of an ascending branch, near 30° latitude in the warm northern hemisphere, and a descending branch near 60° latitude in the cold southern hemisphere. It is similar to the Earth's Hadley circulation, with the difference that the cells are much stronger and displaced far from the equator (Leovy, 2001). The local temperature maximum in the latitude belt 50-60° of the winter hemisphere shown in figure 7.20a results from adiabatic warming associated to the descending branches of the Hadley cell. Although the Hadley circulation on Mars is stronger near the solstices, we observe that it is already prominent during the mid-late southern fall season. The resulting steep gradient gives rise to strong zonal eastward winds. It is known (Zurek et al., 1992; Conrath et al., 2000; Leovy, 2001) that the general circulation of Mars is characterized by strong eastward winds in the winter hemisphere. Our results show that this is also true for the mid-late fall season (50°-70° Ls range), as Figure 7.20b shows. The strongest winds, as expected, are in the hemisphere of the polar night, where the polar vortex is well developed. Indeed, in this region the horizontal temperature gradient between the local maximum and the cold polar night is

steeper than in any other region. Winds reach 110 m/s at roughly 55° S and 0.1 mbar. The interaction of this flow with zonally varying topography excites stationary waves, which take the form of planetary (Rossby) waves for forcing at the largest horizontal scales.

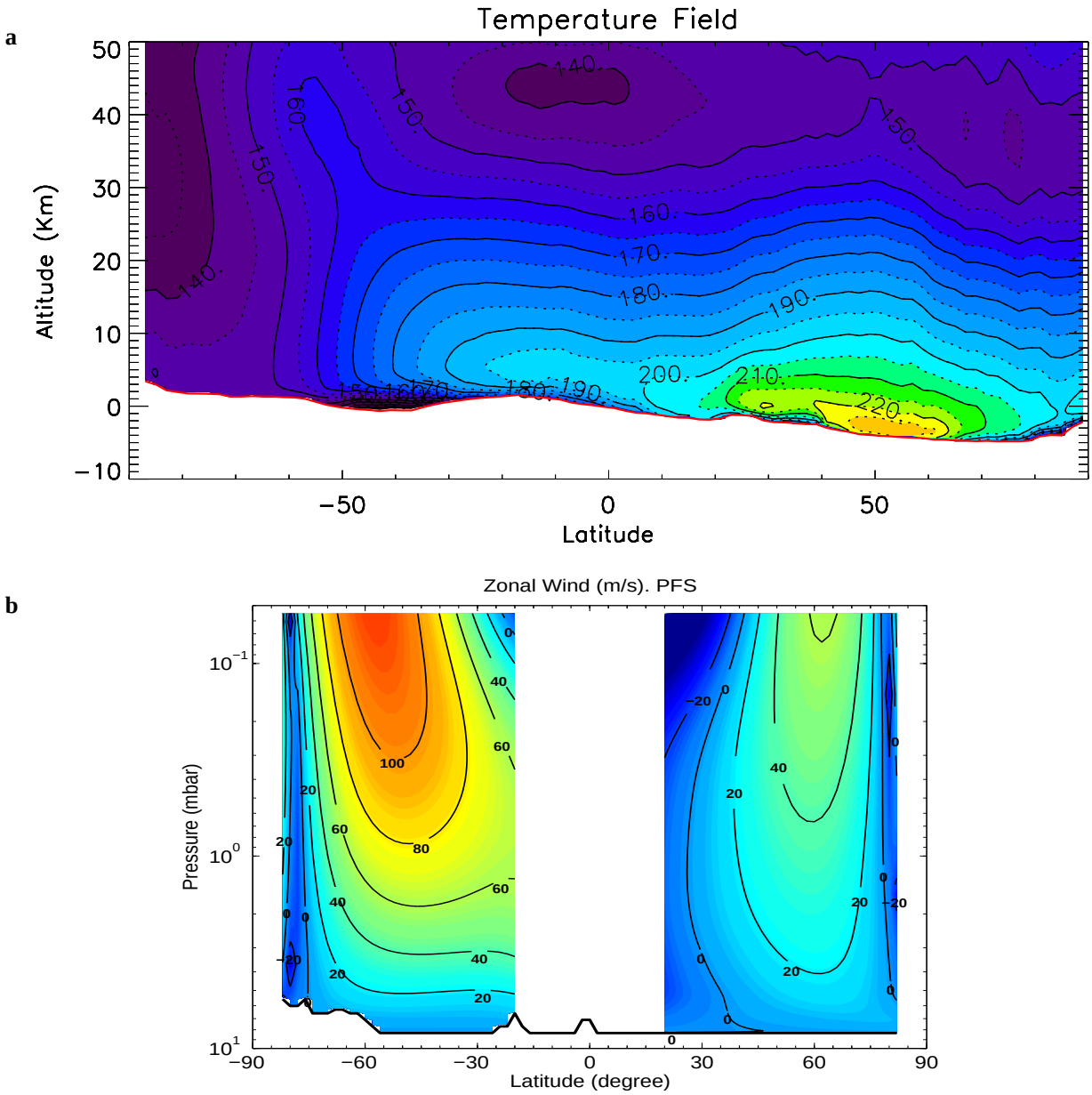

Fig. 7.20 *a*. Zonal-mean thermal structure of Martian atmosphere in the 50°-70° Ls range, from the surface up to 50 km. *b*. Zonal-mean component of the zonal wind derived by Eq. (7.2) for the same range of solar longitudes as of Fig. 7.20a.

Evidence of planetary-scale, wavelike disturbances in the Mars winter atmosphere was first provided by Mariner 9 and Viking spacecraft observations (J. L. Hollingsworth and J. R. Barnes, 1995). Possible sources of the wave activity were suggested to be dynamical instabilities (e.g. barotropic and/or baroclinic instabilities), and quasi-stationary planetary waves, that is waves that arise predominantly via zonally-asymmetric orography. Banfield *et al.* (2003) have characterized their global structure and seasonal evolution analyzing nadir observations from the MGS Thermal Emission Spectrometer, and have confirmed

that these are stationary planetary waves with significant amplitudes at zonal wavenumbers s =1 and 2. The s = 1 stationary planetary wave is likely the dominant mechanism for eddy meridional heat transport for the southern winter. Hinson *et al.* (2003) provided favorable and complementary results with respect to those of Banfield *et al.* (2003), by combining MGS Radio Science and TES limb data. In addition to an enhancement of the vertical resolution and an extension of the vertical range, they obtained a unique measure of the geopotential field as well as the implied meridional winds and the poleward eddy heat flux. According to Hinson *et al.* (2003), the geopotential field of the s = 2 component is "barotropic" in character, while the s = 1 component propagates vertically, as reflected by a westward tilt with increasing height in the geopotential and temperature fields and a net poleward eddy flux. These upwelling and downwelling motions in the atmosphere cause expansions and compressions of air masses which, in turn, reflect in variations in the temperatures. Thus, an indirect way to detect and characterize such a complex dynamical process is to study the effects on the atmospheric temperatures.

A general view of the planetary wave that characterizes the south polar region of Mars during the mid-late fall season as seen by PFS is given in figure 7.21, where we show the atmospheric temperature of the polar region at an altitude of 40 km. We remark here that the data used to produce the results in figure 7.21 where highly selected in local time, in order to avoid diurnal effects. All the measurements in the latitude belt 50°-60° S are within the narrow range 7:00-7:30 local time.

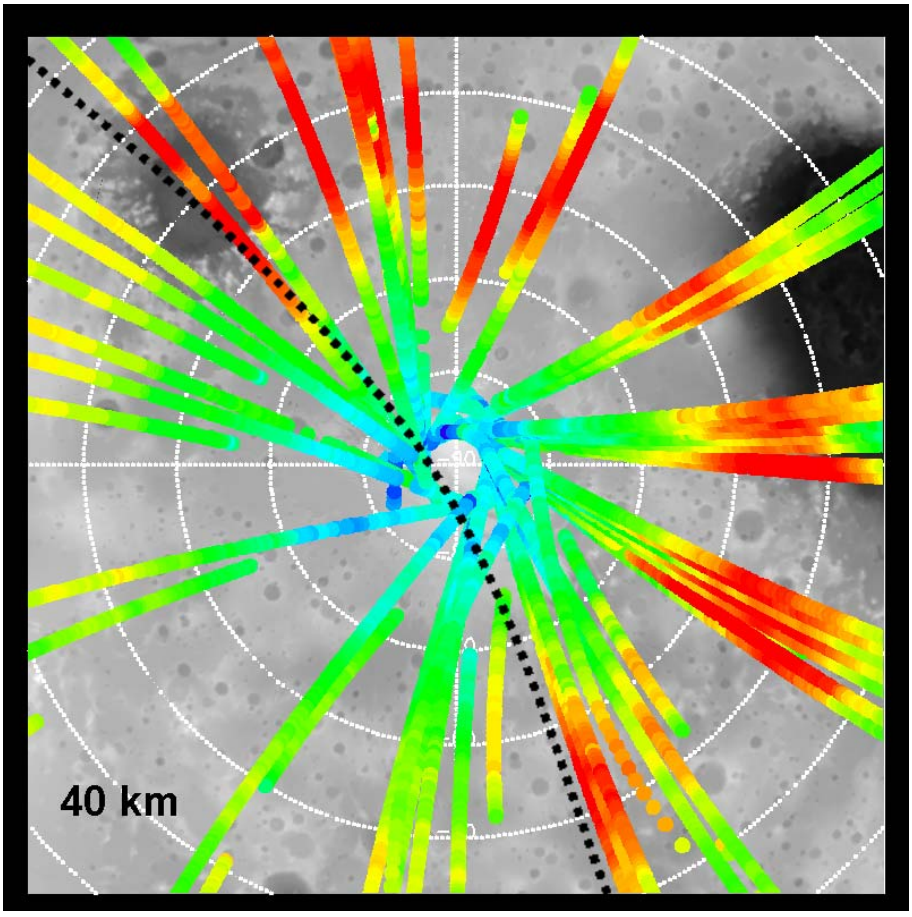

Fig. 7.21 Effects of the wavenumber-one planetary wave on the atmospheric temperature of the polar region at an altitude of 40 km.

The south polar circulation is controlled by a wavenumber-one quasi-stationary planetary wave that produces longitudinal variation in the circulation and climate. The black dotted line in figure 7.21 separates the polar region into two parts. One has a strong increase of the atmospheric temperature around the latitude belt 50°-60° S, which is associated with adiabatic warming produced by downwelling of air masses. The other part is where upwelling occurs, resulting in adiabatic cooling. The eastward phase shift with increasing distance from the equator observed by Hinson *et al.* (2003) may explain the non-coincidence of the cold and warm hemispheres in figure 7.21 with respect to those found at 85° S latitude. In fact, the longitudinal thermal asymmetries between the western and eastern hemispheres observed at southern high latitudes (figure 7.19a) are a result of this planetary wave that is excited primarily by the middle-latitude surface topography, namely the basins of Hellas and Argyre. Our results should be viewed in the context of the broad description of stationary waves derived from TES nadir measurements by Banfield *et al.* (2003). Within the southern hemisphere they report significant amplitudes at both s = 1 and 2 throughout the fall and winter seasons. There is a notable difference in the seasonal evolution of the two modes. The s = 1 amplitude has a distinct maximum around southern winter solstice (Ls = 90°), while the s = 2 amplitude is relatively weak at the solstice and strongest in midfall and midwinter. For a better characterization of the planetary wave, such as amplitude and phase of the component with zonal wavenumber one, we analyzed in details each of the vertical temperature profile inside the interested area. The results are well summarized in figure 7.22, where we show the vertical temperature profiles along a single representative PFS orbit. The orbit is number 695 (Ls = 70°), where the PFS observations cross entirely the polar cap, being half in the warm hemisphere, and half in the cold one. Orbit starts from latitude 40° N and moves southward; it crosses the Hellas Basin, right over its center (~ 70° E longitude), passes close to the south pole at a minimum latitude of 86.67° S, and then moves northward up to 30° S latitude. Strong differences in the atmospheric temperature in the two hemispheres are clearly visible.

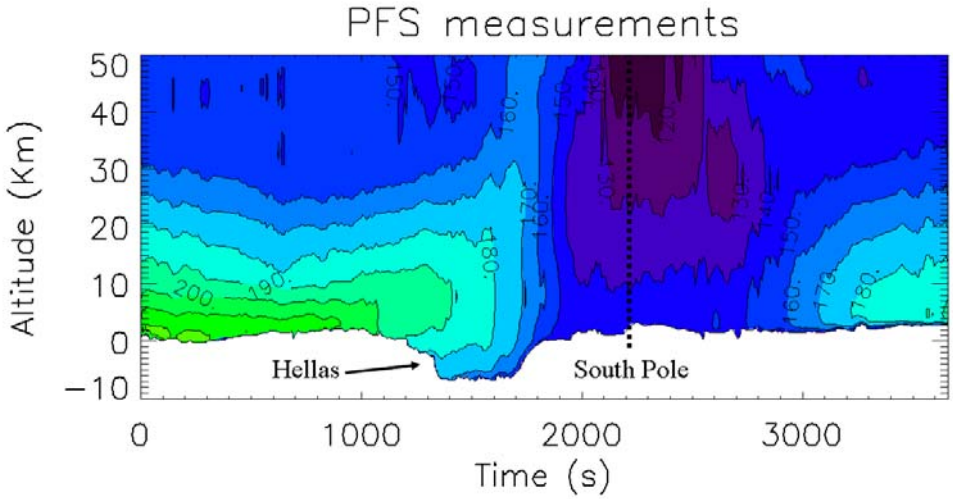

Fig. 7.22 Thermal field along orbit 695 (Ls = 70°). The temperature asymmetry between the two hemispheres is clearly visible. Horizontal axis are seconds elapsed from the beginning of the acquisition of the first spectrum.

Once again, these differences are not due to differences in local times, but are a consequence of the dynamic processes associated with the planetary wave. The increase of

temperatures in the whole atmospheric column observed in correspondence of the southern edge of the Hellas basin cannot be attributed (at least not exclusively) to the descending branch of the Hadley cell. An extra heating is due to downward motions and high pressure zones associated with the planetary wave. Atmospheric cooling is present in the other hemisphere, due to upward motion and low pressure zones, and the effect of the descending branch of the Hadley circulation is essentially canceled out. This will be also confirmed by the comparison with GCM model results in the next paragraph. We note here that, if we ignore the possible effects caused by differences in the soil albedo and thermal inertia, for a flat, perfectly spherical planet, the effect of the Hadley circulation should be longitude-independent, i.e. the same for a given latitude at a given local time. At s=1 the phase is defined as the east longitude of the maximum in temperature. The wave achieves its largest amplitude of about 10-15 K near 45 km altitude and 55° S where the phase is about 50° E. Hence, the peak of positive temperature perturbation is located above the southwest edge of Hellas. This is in good agreement with the 7 K peak found by Hinson *et al.* (2003) near 10 Pa and 60° S, with a phase of ~ 40° E. The differences in the peak amplitude may be due to the fact that we are considering the absolute difference between the peak temperature and the adjacent regions, while Hinson *et al.* (2003) report the wave amplitude after the zonal average has been subtracted.

All the elements summarized in this section allow us to suggest an explanation for the results in figure 7.19a: a wavenumber-one planetary wave establishes a high-pressure zone over much of the eastern hemisphere, preventing CO_2 condensation in the atmosphere during the fall season. Upward motions occur in the western hemisphere, establishing a cold, low-pressure zone. This makes the CO_2 precipitation very likely to occur in the western hemisphere. As explained in Subsection 7.3.3, upward motions result in an efficient adiabatic cooling, allowing high CO_2 condensation rate in the interested areas. The two climates established by the topographically forced circulation produce differences in the nature of the surface ice deposits. Thus topography, through its influence on the circulation, is ultimately responsible for the nature and location of the RSPC. As discussed in Subsection 7.3.9, these results confirm and extend what has been recently proposed by Colaprete *et al.* (2005).

7.3.7.3 Model comparison

Modeling the Martian climate at high latitudes during the fall and winter seasons with a high degree of accuracy is one of the most challenging task of the general circulation models. Nevertheless, it is also one of the most crucial task in order to provide reliable results, for instance, on the dynamics of non-condensable gases such as Argon, Nitrogen and Oxygen. It is also essential in order to account for the correct spatial and temporal distribution of water ice and CO_2 ice clouds. In this respect, the comparison between the results from the GCMs and the observations provides a necessary validation of the former, which is particularly welcome in the case of the Martian polar nights. During these periods on Mars, in fact, observations are generally more difficult to obtain and the details of the physical processes involved (including the microphysics of the CO_2 condensation) are not yet completely understood.

From the purely numerical point of view, moreover, the modeling of the general circulation near the poles feels the effects of using different schemes for the integration of

the dynamical equations, and different filters for the numerical stability in the vicinity of the poles. As a consequence, the details of the climate predicted by GCMs at high latitudes can differ from model to model, and only the comparison to observations can provide a reliable validation. On the other hand, GCMs provide a global picture of all atmospheric variables, which can be essential to put the observations (especially those which are unevenly distributed in space and time) in the right context.

For these reasons, we have performed a comparison of selected PFS orbits with the results provided by the Martian GCM of the Laboratoire de Météorologie Dynamique (LMD) in Paris (Forget *et al*, 2006), which is an adaptation to Mars of the Terrestrial LMDZ model in use at LMD since the 80's (Sadourny and Laval, 1984). The comparison presented in this paper is far from being exhaustive, and further work will be devoted to a more complete analysis of the differences between the model and the observations, and included in a forthcoming paper. Nevertheless, this first attempt of cross-validation between PFS measurements and the LMD GCM shows how tricky is the modeling of the condensing CO_2 south polar cap, for the reasons exposed above.

Figure 7.23 shows several PFS retrievals in the "cold" hemisphere (solid curves) and in the "warm" hemisphere (dashed curves) at 85° S latitude for different longitudes, in the range of areocentric longitude 50°-70°. The two hemispheres show very different profiles at this time of year. As it has already been pointed out using Figure 7.19a, in the cold hemisphere we have areas (longitudes) where the atmospheric temperature is close to (but above) the CO_2 condensation temperature (black solid curves), and areas where CO_2 condensation in the atmosphere is allowed at several altitudes (colored solid curves). The dash-dotted curve in Figure 7.23 is the CO_2 condensation profile for the average atmospheric condition of the areas where CO_2 condensation in the atmosphere is allowed. With referring to Figure 7.23, there are cases in which condensation is allowed from the ground up to 10 km (blue curve), 15 km (orange curve) and 20 km (red curve); we may also have condensation areas located around 15 km (yellow and green curves) and, occasionally, from ~15 to 30 km (cyan curve).

In the warm hemisphere (30° – 210° east-longitude) the atmospheric temperatures are always far above the CO_2 condensation temperatures and three types of profiles can be distinguished. Moving eastward we observe the following situations:

a) The warmest region (red-dotted curves in figure 11) is located in the 40° – 90° E longitude range which corresponds essentially to the margins of the Hellas basin. The whole atmospheric column is warm (at least 10-15 K above the CO_2 condensation temperature), with strong temperature inversions around 5-10 km altitude.
b) A wide area (80° – 180° E longitude) shows weaker inversions at 5-10 km and a colder atmospheric column (light-blue-dotted curves in figure 11). These are the "typical" profiles in the warm hemisphere.
c) A narrow area at the eastern limits of the warm region (180° – 210° E longitude) shows strong temperature inversions around 5 km altitude and a higher temperature gradient (and consequently lower temperatures at 30-35 km altitude).

In all these cases, the polar warming starts at 30-35 km altitudes.

Figure 7.24 shows a profile-to-profile comparison between observations and model results at Ls = 52.21° and 86° S in the "cold" hemisphere, where the solid profiles are PFS retrievals at different longitudes in the coldest region (indicated by a blue arrow in figure 7.19a) and the dot-dashed ones are the corresponding model profiles. The general agreement among the profiles is very good for most of the atmospheric column where PFS

is mostly sensitive. Even the small inversions between 4 and 5 mbar are in good agreement, as well as the more pronounced polar warming inversions higher than 0.1 mbar (although, at that particular altitude, they are not observed by PFS at all longitudes). For the purposes of this paper, the good agreement in the "cold" hemisphere shows that CO_2 snowfall may indeed occur in a large range of atmospheric altitudes, other than by direct condensation on the ground.

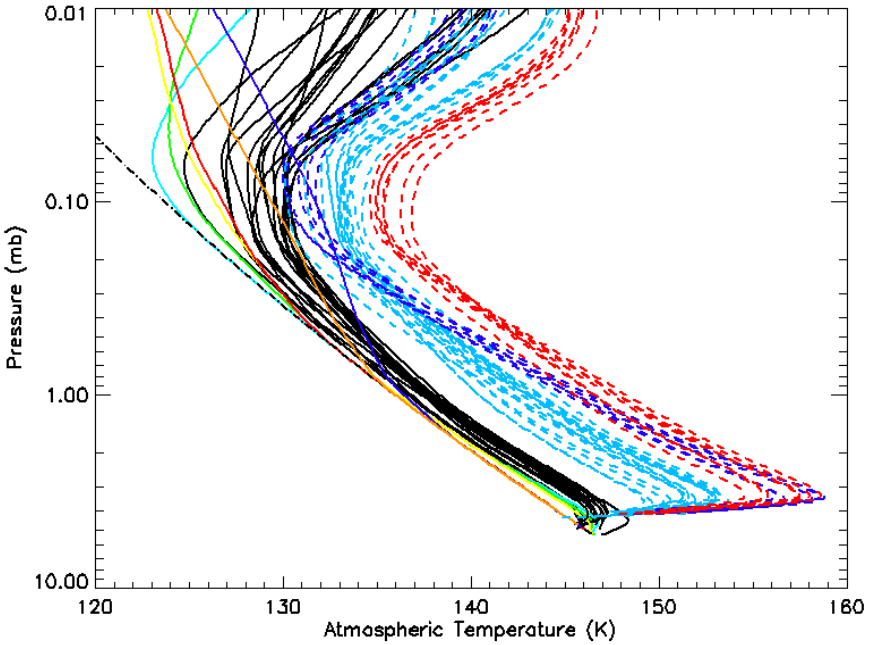

Fig. 7.23 PFS retrievals of air temperature profiles at 85° S latitude in the 50°-70° Ls range in the "cold" hemisphere (solid curves) and in the "warm" hemisphere (dashed curves). Dash-dotted curve is the CO_2 condensation profile (see text for more details).

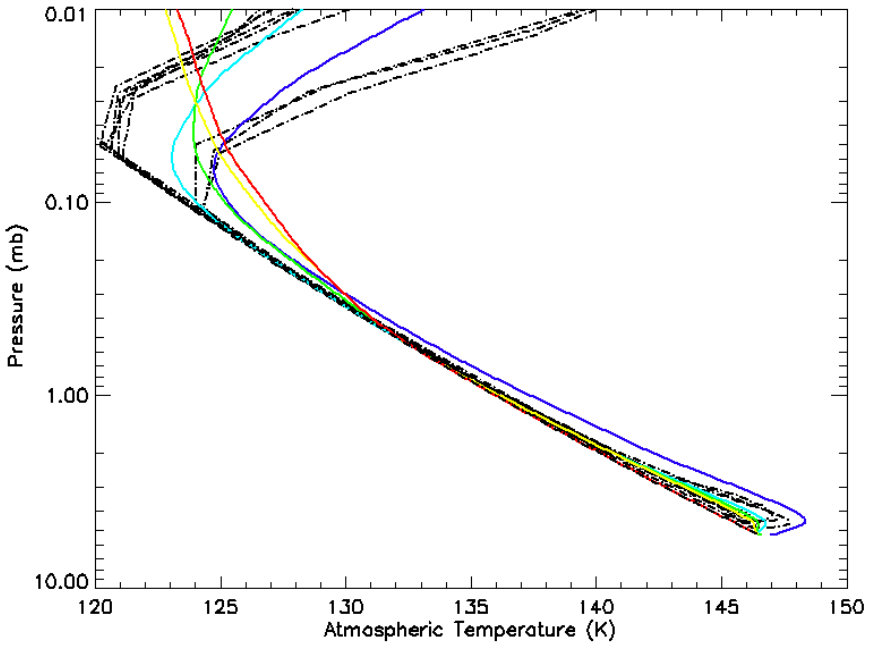

Fig. 7.24 profile-to-profile comparison between observations at different longitudes (solid curves) and corresponding model results (dot-dashed curves) in the "cold" hemisphere. Latitude is 86° S and Ls = 52.21° (see text for more details).

Figure 7.25 shows the same kind of comparison for the "warm" hemisphere at Ls = 52.46° and 86° S. This case highlights that the GCM predicts CO_2 condensation in the whole atmospheric column from the ground up to 0.1 mbar (dot-dashed profile), whereas the PFS retrievals are much warmer (up to 10 degrees). The altitude of the polar warming inversion is in good agreement, but neither its temperature nor the inversion at the ground is close to the observations. The GCM, in this configuration, does not show any asymmetry between the eastern and western hemispheres, predicting CO_2 snowfall at all longitudes during the southern polar night.

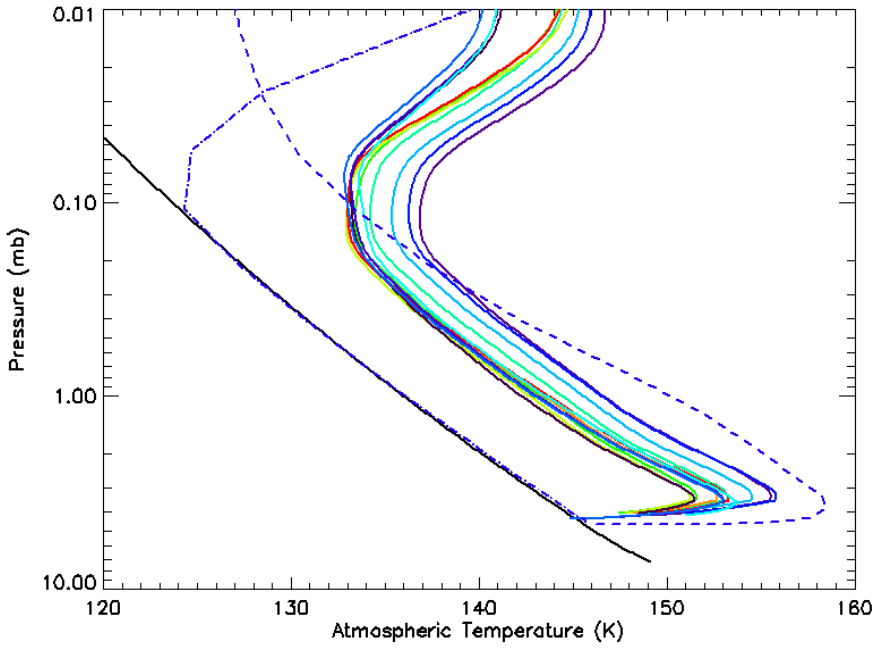

Fig. 7.25 profile-to-profile comparison between observations at different longitudes (solid curves) and corresponding model results using the new dynamical core (dashed curve) and the old one (dot-dashed curve) in the "warm" hemisphere. Latitude is 86° S and Ls = 52.46° (see text for more details).

The effect of having different atmospheric dust loading has been taken into account, but did not change the results significantly. What does change the model results is the use of a different implementation for the integration of the dynamical equations, together with the use of a different filter for the numerical stability around the pole. The dashed curve in Fig. 7.25 is the GCM profile produced by using a later version of the (finite differences) dynamical core of the LMDZ model (LMDZ-3), equivalent to the dot-dashed profile which is produced instead with the dynamical core in use in the version LMDZ-2. The former lies within 5 degrees from the average of the PFS retrievals at most altitudes, although the polar warming starts at higher altitude than the observations. The GCM based on the new dynamical core is able to take into account warm temperatures in the eastern hemisphere, but fails to predict cold atmospheric temperatures in the western one, thus preventing CO_2 snowfall. Work is in progress to understand the role played by the different dynamical cores and the numerical stability filters in the two versions of the model, in order to properly simulate the observed hemispherical asymmetry. This work in progress includes also a comparison with a Martian GCM based on a spectral dynamical core (the UK

MGCM), which is less sensitive to filtering around the poles. Results from this study will be reported in a forthcoming paper.
Figure 7.25 shows also that the GCM based on the new dynamical core predicts the strong inversion at the ground in the "warm" hemisphere. This particular feature is not very robust even in the PFS retrievals though, as the sensitivity of the instrument does not extend so close to the ground. Different retrieval methods which make use of different *a priori* profiles show different results around 4 mbar for the curves in Fig. 7.25 (not shown here). Nevertheless, at higher altitudes the retrievals are robust and do not depend on the chosen *a priori* profile, therefore the warm temperatures are consistently observed no matter which retrieval method is used. This confirms that in the western Martian hemisphere CO_2 snowfall does not occur in the bulk of the atmosphere, and can be only allowed very close to the ground.

When extending the comparison between observations and model results at several latitudes, it appears clear that it is at high latitudes where the disagreement is more pronounced, confirming the fact that modeling the circumpolar region during the period of the polar night is a crucial task for the GCMs.

Figure 7.26 shows (as in Fig. 7.22) the temperature observed by PFS during one of its orbit (orbit 695) which crosses entirely the south pole, extending from 40° N in the "warm" hemisphere (~70° E longitude) to 30° N in the "cold" one (~250° E longitude), and gets as close to the south pole as 86.67° S. Together with the observations, this figure shows the temperature fields provided by the two versions of the GCM and the fields of the differences between observations and model. This orbit is at Ls = 70°, thus the temperatures in the polar vortex are more representative of the late-fall situation described in the next section rather than of the early-fall distinction between two regional climates, but this comparison with the model highlights the general agreement between what is observed and what is simulated, and the areas where we expect some disagreement.
The structure of the two hemispheres, as described in Fig. 7.22, appears remarkably similar in the observations and in the model, thus providing further evidence for the conclusions which have been drawn in the previous Paragraph. The asymmetry between the longitudes around the Hellas basin and the western longitudes is evident also in the model, independently from the version which is used. Although the model is not able to reproduce the asymmetry between eastern and western longitudes in the polar night, as shown in Figs. 7.24 and 7.25, the agreement with the observations at latitudes outside the polar night supports the hypothesis of a wavenumber-one planetary wave induced by the presence of the underlying topography.
On the other hand, when comparing observations and model in detail, one can appreciate that the most prominent differences are located around the polar vortex and around the equator. The underestimation of temperatures at the equator and above 0.2 mb in the two versions of the model might be caused (at this time of the year and at these altitudes) by the presence of water ice clouds in the tropics, an effect which is not taken into account in the simulations (see Wilson *et al.*, 2007, for details on this topic). The structure of the polar vortex, though, is profoundly different in all the panels of Fig. 7.26. The observations from PFS show that the periphery of the polar vortex is highly barotropic, with little or no entrainment of polar warming at high latitudes, almost at all altitudes. The model, on the contrary, predicts that the polar warming breaks the vertical extension of the vortex even at very high latitudes. This, in turn, would imply quite different properties in the transport of tracers at high latitudes during the polar night. Two remarkable differences between the

two versions of the model are the stronger polar warming predicted by the version LMDZ-2 (old dynamical core) in both hemispheres, and the colder temperatures shown in the polar vortex, especially at low altitudes and near the ground (as already described for Figs. 7.24 and 7.25).

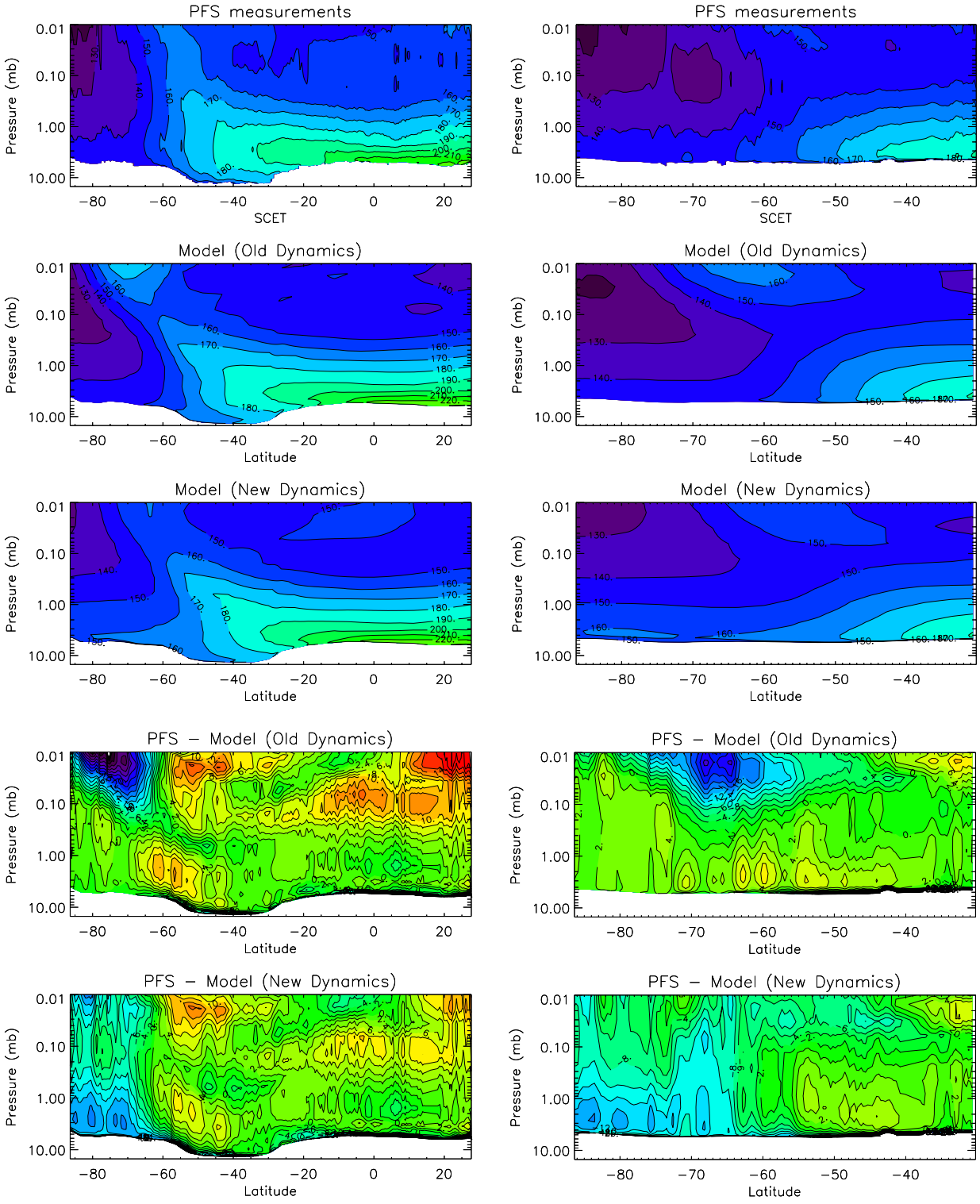

Fig. 7.26 Comparison between PFS vertical profiles retrieved for orbit 695, and temperature fields provided by the two versions of the GCM for the same geometries and conditions as the observations. The orbit has been divided in two parts, one in the warm hemisphere (left panels) and one in the cold one (right panels).

These differences are not limited to this particular orbit, but are a general feature which characterizes the two versions of the LMD Martian GCM examined here, as it is evident in Figure 7.27, where we plot the time-averaged zonal means of temperature in the range of areocentric longitude 50°-70°, comparing with the PFS observations at two local times (7 a.m. and 7 p.m).

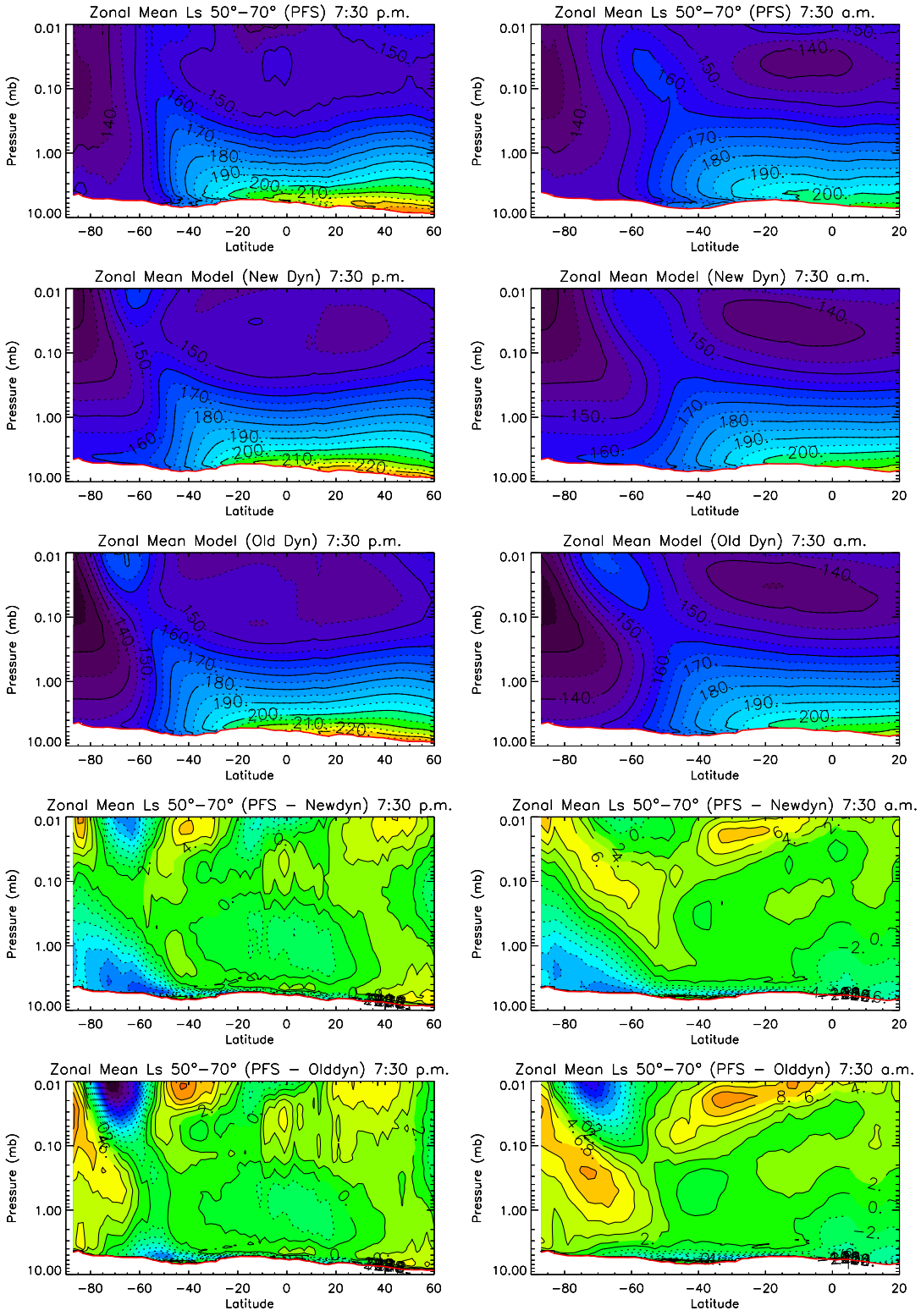

Fig. 7.27 Comparison between zonal-mean temperature fields retrieved by PFS and predicted by the two versions of the LMD Martian GCM, in the 50°-70° Ls range and for two different local times: 7:30 p.m. (left panels) and 7:30 a.m. (right panels).

Polar night and polar vortex apart, observations and model agree very well at all other latitudes, thus confirming 1) the validity of the considerations made in the previous paragraph, and 2) the ability of the LMD Martian GCM to model the atmospheric dynamics outside the polar night, as already inferred with previous validations carried out using several other dataset (MGS/TES and MGS/radio occultation, for instance).

7.3.8 The late-fall and winter polar cap

At the end of the fall season, the atmosphere above the polar region cools down and evolves toward the situation described in Colaprete *et al.* (2005) for the winter season. The polar cap reaches its maximum extension end eventually starts to shrink. CO_2 condensation in the atmosphere is now allowed at lower latitudes as well as in the eastern hemisphere. As an example, we show in figure 7.28 the air temperature field difference $\delta T_{sat}(z) = T(z) - T_{sat}(z)$ for orbit 755 (Ls = 78°). The track of the PFS measurements is depicted in the top-right panel. White circles highlight the areas where the CO_2 condensation is allowed, according to the vertical profiles shown in the bottom panel.

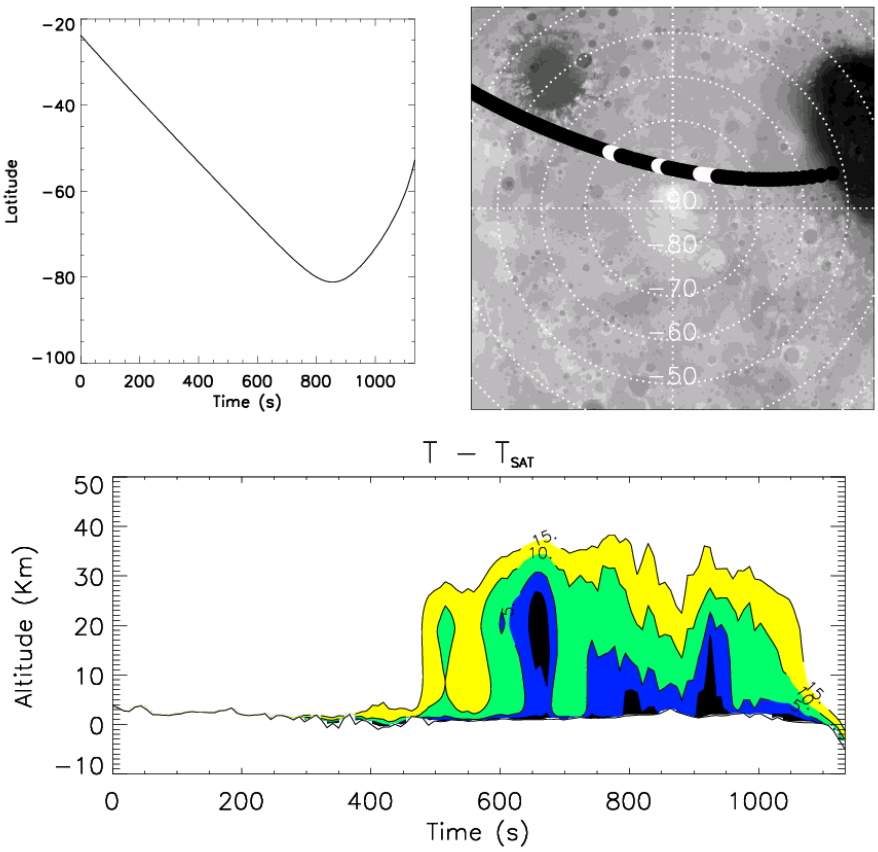

Fig. 7.28 Orbit # 755 (Ls 78°), a typical late-fall south pole scenario (see text for details). *Top-left*: latitude versus time (in seconds) elapsed from the beginning of the acquisition of the first spectrum. Use this to obtain latitudes for the bottom panel. *Top-right*: track of PFS observations; white spots indicate when and where CO_2 snow fall is allowed, according to the vertical profile of $T - T_{sat}$ shown on *bottom panel*, where the black areas are where the atmospheric temperature, at a given altitude, goes below the CO_2 condensation temperature for the same altitude.

The key observational aspects of the southern hemisphere winter weather have been recently summarized by Barnes and Tyler (2007). During the winter, the atmosphere frequently chills to below the condensation temperature of the CO_2 and becomes supersaturated. The largest and most persistent supersaturation occurs in a region which extends eastward from the areas southward of the Tharsis plateau up to the vicinity of the Argyre basin. More broadly, the western hemisphere exhibits much stronger storm activity than the eastern hemisphere, and is also substantially colder at a given altitude, on average. In other words, CO_2 condensation in the atmosphere is now allowed in both hemispheres, but the low-pressure zone established by the planetary wave over much of the western hemisphere allows a higher CO_2 condensation rate than in the eastern one.

7.3.9 Discussion

The explanation suggested by Colaprete *et al.* (2005) for the RSPC asymmetry involves a different CO_2 condensation rate in the atmosphere in the two hemispheres above the south polar region during the southern winter, the higher condensation rate occurring in the western hemisphere. PFS observations shown in this paper reveal that an important role is also played by the fall season, especially during the 50°-70° Ls range. In this period, in fact, CO_2 precipitation occurs exclusively in the western hemisphere, and particularly in the longitudinal corridor of the RSPC. Prettyman *et al.* (2003) have shown that the measured inventory of CO_2 frost in the southern seasonal cap achieves a maximum value of 8×10^{18} g between 160° and 170° Ls, which is slightly more than 30% of the established value for total atmospheric mass (2.5×10^{19} g). They have also shown that, by Ls=70° at 85° S latitude, more than a third of such amount of CO_2 ice has been already deposited in the polar cap. As a consequence of the results discussed in the previous Subsection, we can reasonably assume that most of this CO_2 ice is deposited within the western hemisphere and in correspondence of the RSPC longitudinal corridor. We note here that all the CO_2 ice clouds and precipitations phenomena previously reported (Formisano *et al.*, 2006; Montmessin *et al.*, 2006; Montmessin *et al.*, 2007) were forming inside supersaturated pockets of air created by upward propagating thermal waves. In fact, upward motions in the atmosphere cause the temperature to rapidly decrease to a supersaturation level, allowing CO_2 condensation in the atmosphere. Unfortunately, due to the limitations in the retrieval scheme described in section 1.2, we cannot state with the current version of the PFS retrievals whether the atmospheric temperature goes below the saturation point or not; nevertheless, the considerations described above, the model predictions, and the strong upward motions associated with the planetary wave in the colder hemisphere make the condensation and precipitation scenario very likely. Therefore, the different amounts of CO_2 ice deposited in the two hemispheres during the fall and winter seasons, together with the difference in albedo (due to different grain sizes) and sublimation rates between CO_2 (fresh) snow and frost, may explain the asymmetry observed at the end of the southern summer: the dry ice sublimes entirely in the eastern hemisphere, while in the western hemisphere it survives all year long as the RSPC.

7.4 The mid-spring North Polar Cap

In this Section we present the first comprehensive analysis of the north polar cap during the mid-spring. Composition, microphysical state, coexistence modes and thickness of the seasonal cap have been studied through the comparison of PFS SWC Near Infrared spectra of the polar ices with bidirectional reflectance and hemispherical albedo models, fitted to the observed data. The results have been published on *Planetary and Space Science* (Giuranna *et al.*, 2007b); the paper is available in the Appendix A.5 of this book.

7.4.1 Background and rationale

The spring north polar cap has not been observed in detail for several reasons. First, the north polar hood clouds usually shroud the high northern latitudes during the first part of the spring. Second, only limited synoptic imaging by spacecraft is available, since spacecraft orbits imposed a limited areal coverage for Viking Orbiter 2 and undesirably large emission angles for Orbiter 1. Third, terrestrial observations must be acquired during aphelic oppositions when Mars is relatively small in diameter. As we have discussed several times throughout this thesis, the seasonal polar caps are a major element of Mars' climate and circulation, for more than a fourth of the CO_2 in the atmosphere condenses each year in the seasonal caps. In addition, water has a great importance to human interest in exploration of Mars, making it important to minimize any confusion between the occurrence of CO_2 and H_2O ice. The similarity in reflectance of fresh CO_2 and H_2O snow makes them difficult to distinguish in monochrome or multiband reflectance imaging, unless coverage extends longward of about 1 μm. Thermal infrared observations may partially resolve the composition of the seasonal and permanent polar caps on Mars: the condensation temperatures of CO_2 and H_2O differ by several tens of degrees, with solid CO_2 not occurring on Mars above 150 K; temperature measurements can be used to determine the ice composition (Neugebauer et al., 1971; Hanel et al., 1972; Kieffer et al., 1976b; Kieffer, 1979), limited by knowledge of the spatial mixtures present in the field-of-view (FOV).
Recently, TES data have been used to track the behavior of surface and atmospheric temperatures over the seasonal north polar cap, the distribution of condensed CO_2 and H_2O, and the occurrence of dust storms (Kieffer and Titus, 2001). Nevertheless, to unambiguously and comprehensively resolve the Mars' polar cap ice composition, the CO_2 snow/frost grain sizes as well as the water ice and dust contamination, it is necessary to investigate the near-infrared spectral region. More precisely, the 2.15–5 μm spectral range is among the most diagnostic for polar studies on Mars: both water ice and CO_2 ice have a rich spectral structure in this region that is diagnostic of their abundance and grain size. In fact, with the exception of the northern summer, the seasonal exposed Martian polar caps are mainly composed by CO_2 ice, with some level of contamination by water ice and dust. Furthermore, the strongest absorption bands of both ices (2.7-μm and 4.3-μm for CO_2 ice, and 3-μm for water ice) and dust (around 3 μm) are in this region, with characteristic spectral features, therefore allowing detection of even small quantities. Most of the CO_2 narrow absorption features, which are very diagnostic for the snow grain size, occur in this region (triangles in Fig. 7.35). Spectral resolutions as high as ~1 cm^{-1} are needed to resolve many of the narrow CO_2 lines (see Chapter 4). The extent of water ice at the surface and

the size evolution of ice grains for the north summer polar cap has been recently monitored as a function of time by Langevin *et al.* (2005a). NIR spectral characteristics of the seasonal north CO_2 ice cap have not been published from any of the previous missions. PFS has the unique capability to accurately measure the ices composition and properties, combining thermal-infrared spectra with NIR spectra, and a high spectral resolution.

7.4.2 Data set and treatment

The North polar region has been observed several times by PFS in its first two years of activity. There have been many previous studies focusing on the shape of the north cap during the recession and on the latitude of the cap edge. These include spacecraft visual imaging data (James and North, 1982), infrared data (Christensen and Zurek, 1984; Kieffer and Titus, 2001) and telescopic data (Iwisaki et al., 1982; James et al., 1987, 1994). These observations indicate that during its recession the cap edge usually "pauses" for at least 60 Martian days at about 65° N latitude during mid-spring, from Ls = 20° to 50°, and that the water ice clouds seem to be absent during the "standstill", only reappearing when the recession resumes. This short Ls range is then the best period for the north cap observations. Orbit number 452 of the MEX occurs at Ls = 39.9°, in the middle of the spring season and just inside the above mentioned Ls range. Fifty-six spectra from this orbit have been selected and examined in detail. In this selection, the PFS observations cross entirely over the polar cap, going from 61.3° N up to 84.2° N latitude and then down again to 65.6° N latitude. All the spectra were acquired on the day side.

Actual footprints of the orbit for latitudes > 60° N are depicted in Fig. 7.29, on top of an RGB image obtained from the spectra in the visible range acquired by OMEGA during the same orbit session. The decrease in albedo in the middle-top part of the figure is due to the high solar incidence angles near the terminator. The different colors mark the five different regions in which the spectra have been grouped and averaged. White color indicates spectra not used in this study, being either in transition regions (i.e. where the spectral features are not homogeneous in contiguous spectra) or in critical regions (i.e. very close to the terminator and near-grazing incidence angles). The black arrow indicates the advancing direction of the measurements. Standard MEX orbits are nadir-pointing. Occasionally limb-pointing and inertial orbits are planned, the latter being the case for the orbit 452. In this particular orbit the spacecraft pointing direction is fixed, in a way that the emission angle (that is the angle between the spacecraft pointing direction and the perpendicular to the surface) increases with increasing latitude. This, and the fact that the spacecraft distance from the surface increases along the orbit (at this Ls the pericentre is around −75° lat; see Fig. 7.2) causes the area of the PFS footprints to increase with latitude. The unusually large spacecraft distance from the planet (~5000 km) explains the low (~140 Km) spatial resolution of these observations; nevertheless, the spectra are spatially quite close to one another, allowing great spectral homogeneity within every selected region. Since our model computes the bi-directional reflectance (BDR) (see next Subsection), for a direct comparison, every single PFS spectrum has been divided by the continuum of the solar Irradiance at Mars, calculated for the actual distance of Mars to the Sun which, during this orbit, is equal to 1.6418 AU. We redirect the reader to Figure 2 of Giuranna *et al.* (2007b), available in Appendix A.5 of this book, for a detailed description of the 56 sequential spectra that constitute the spectral set used in this work.

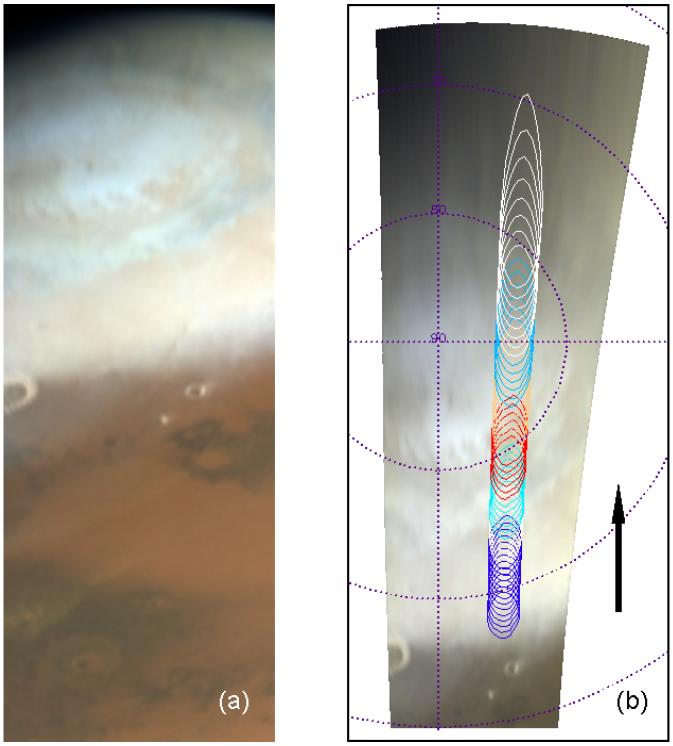

Fig. 7.29 (a) RGB image of the north polar cap, obtained from OMEGA visible spectra acquired during the same orbit 452. (b) Blow-up of the North polar cap region, polar projected and with the outline of individual PFS SWC footprints for the data used in this paper plotted over it. The separate colours indicate the five different regions in which the spectra have been grouped and averaged to produce the PFS spectra to be fitted by the model. White colour indicates spectra not used in this study (see text for details). The black arrow shows the advancing direction of the measurements. The decrease in albedo that occurs in the upper part of the images is due to the high solar incidence angles near the terminator.

In Subsection 2.4.5 it has been shown that, after the launch, the PFS pointing mirror was contaminated by the degassing oil of the ball-bearings of the mirror. Thus, in the 2800–3000-cm^{-1} spectral range, the SWC spectra show the features of the stretch transitions of the CH_2 and CH_3 groups. The general shape and strength of these bands has been verified to be essentially constant during the whole period of PFS activity. A special procedure to remove the contamination has been developed and applied to the spectra used in this work. An example is shown in Fig. 7.30, where the correction has been applied to a single PFS spectrum of region IV (orange footprints in Fig. 7.29). The features still present in the above-mentioned spectral range after the correction are not residuals of the contamination, but are real features of the CO_2 ice, as will be shown later on in Subsection 7.5.4, where all these features have been reproduced and fitted by a model. PFS SWC spectra also show a modulation from 4200 to 6000 cm^{-1}, due to the external mechanical vibrations of the spacecraft, which causes a spurious minimum around 5000 cm^{-1} in the spectra. It has been inferred (Comolli and Saggin, 2005) that such vibrations affect the level of the continuum of the spectra, leaving unaltered the relative depth (with respect to the continuum) of the atmospheric lines and, particularly in our case, of the CO_2 narrow absorption lines. In other words, if we "correct" the continuum, we have the absolute depth of the absorption lines. A simple procedure to correct for this spectral modulation has been devised: above 4200 cm^{-1} the continuum of the measured spectra is replaced by the

continuum of a 5-mm pure CO_2 snow synthetic spectrum, scaled to the level of the measured spectrum at 4200 cm^{-1}. For $\nu \geq 4200$ cm^{-1}, we first divide the measured spectrum by its own continuum, preserving all the narrow features, and then multiply by the scaled continuum of the synthetic CO_2 spectrum. With this procedure, the possible contribution to the continuum due to water ice contamination (dust is spectrally flat in this spectral region) is clearly lost, for we force the continuum to be that of a pure CO_2 snow. Nevertheless, the only intent of this procedure is to be able to compare the relative depth of the measured CO^2 ice absorption lines with those of the model. For a direct comparison above 4200 cm^{-1}, we thus apply the same procedure to the synthetic spectra used for the best-fits. Optimal results are obtained up to 4650 cm^{-1} and thus wavenumbers above this value are ignored in this work. The fact that, as we will see, the intensities of the CO_2 lines in the measured spectra are reproduced by the synthetic best-fit spectra in the whole spectral range considered (i.e. up to 4650 cm^{-1}) is a further confirmation that the relative depth of such lines is not altered by the mechanical disturbances.

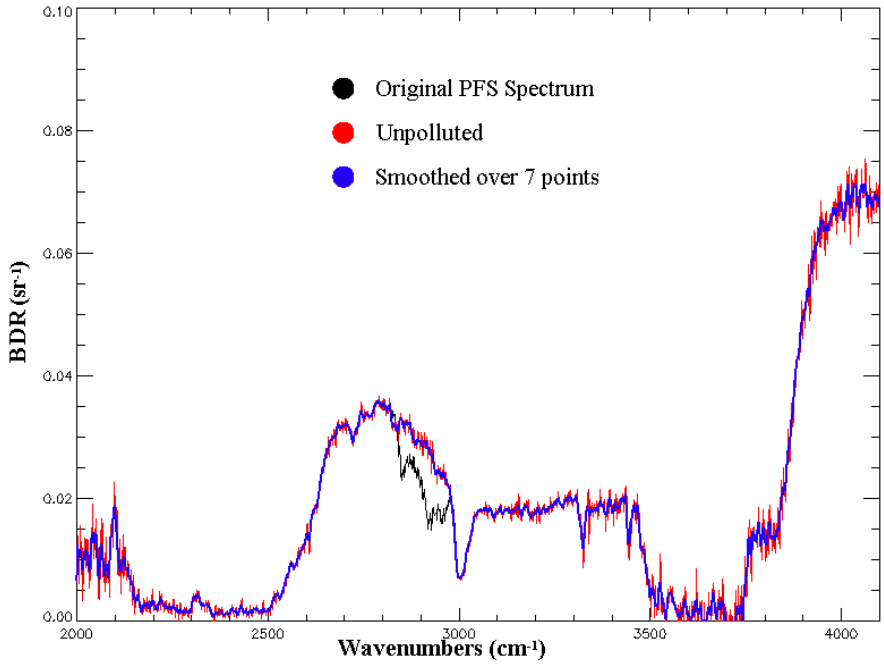

Fig. 7.30 Data treating for all the spectra used in this work. First, the spectra are divided by the continuum of the solar Irradiance at Mars; then the procedure to remove the pollution is applied and, finally, the spectra are smoothed over 7 points to reduce the apparent instrumental noise (the spectrum used in this example relates to the central of the orange spots of Fig. 7.29).

7.4.3 The BDR model

As described above, the orbit number 452 of the MEX mission used for this work is not a standard nadir-pointing orbit, but an inertial orbit instead. As a consequence, while the phase angle remains fixed around 36.36° during the whole orbit, both the incidence and the emission angles vary noticeably from one spectrum to another, ranging from, respectively, 63.5° and 52.9° for the first spectrum to 80.8° and 75.2° for the last one. This makes the computation of synthetic spectra even more difficult than usual, requiring a

different lighting geometry for each spectrum. In other words, a spectrum of a same mixture (i.e. same grain sizes and CO_2 ice/H_2O ice/dust ratios) may need to be computed several times, one for each couple of incidence and emission angles, to properly reproduce the observations and fit the data. For this reason, a fast and yet accurate multiple scattering computation algorithm is needed. A two-stream delta-Eddington multiple scattering computational approach, as described in Subsection 6.2.1 and used in Section 7.2 to study the RSPC, although fast, may not be enough accurate, especially for the extreme lighting geometries of these measurements (incidence angles as high as 80°). A plane-parallel discrete ordinates radiative transfer code such as DISORT (Stamnes et al., 1988), described in Subsections 5.3.2 and 6.2.2, although extensively tested and validated, needs a very long computational time for a single spectrum. We then developed our own multiple-stream BDR model following Hapke's theory of reflectance. Hapke's isotropic multiple-scattering approximation (see paragraph 6.2.1.2) solves the single scattering exactly and approximates the multiple scattering as isotropic. This approximation is not suitable for our case. We then adopted the anisotropic version of Hapke's formula given in Eq. (6.20), where the single-scattering part remains the same and the multiple-scattering part is replaced by a more anisotropic term; since the CO_2 snow grains considered in this work are very large spheres, where coherent backscattering is unlikely to be observable (see Mishchenko, 1992, 1996; Hapke, 2002 and the discussions in paragraph 6.2.1.2), we adopt Hapke's anisotropic multiple-scattering approximation without the coherent backscattering correction term.

Although Hapke's backscattering correction factor $B(g)$ given in Eq. (6.19) due to the shadow-hiding opposition effect can increase the BDR value's single-scattering part at a 0° phase angle by a factor as great as 2, its B_0 parameter seems hard to predict. The theoretical derivation of the opposition effect assumes that the ray is scattered by a point; that is, the finite size of the particle is neglected. However, the refracted rays and the internally reflected, backscattered rays may enter and leave the particle at points that are separated by up to nearly the entire particle diameter, and for this light the opposition effect is negligible and $B_0 \sim 0$ (Hapke, 1993). Moreover, the $B(g)$ function decreases rapidly as g increases. For the high 36.36° phase angle of PFS observations and for values of B_0 as high as 0.5, we found the contribution of this effect being less than ~8% of the total BDR even for large monodisperse CO_2 ice particles ($h \sim 0.26$). If the snowpack has a wide range of sizes, then h can be much smaller, reducing the opposition effect (a surface without voids does not have a shadow-hiding opposition effect). This term has thus been neglected in our model. If needed, one may still approximately account for the shadow effects by adding small constant values to the computed BDR (as we did in Section 7.2; see Table 7.1 and Hansen *et al.*, 2005 available in appendix A.3 of this book), but this has never been necessary in our fits.

We used optical constants of CO_2 ice from Hansen (1997). H2O ice optical constants are from Hansen (1999); dust optical constant are from Hansen (2003). The optical constants and size distributions here used are reviewed in Section 6.1. The surface is described as semi-infinite layer of particulate medium. The polar caps ice have been modeled as an intimate granular mixture (Fig. 7.31) of CO_2 ice with different grain sizes, and dust and water ice with radii on the order of 1–3 μm, consistent with measurements of atmospheric aerosols of these materials (Wolff and Clancy, 2003). More precisely, the geometric cross-section weighted mean particle radius adopted for dust size distribution is $r_{eff} = 1.6$ μm, with a variance of the gamma size distribution $v_{eff} = 0.35$ μm [Eqs. (5.42) and

(5.48)]. For water ice, we used a modified gamma size distribution [Eqs. (5.43) and (5.50)] with r_m = 0.4 μm, α = 2 and γ = 0.5, which correspond to an effective radius of r_{eff} = 2.75 μm and effective variance of v_{eff} = 0.4 μm (Toon et al., 1977). The main input parameters are the CO_2 ice grain radius, the water ice mass fraction and the dust mass fraction, as well as the incidence, emission and phase angles. The output is the BDR. For the CO_2 monodisperse spheres we determine first the single-scattering quantities of the particles including the phase function, single scattering albedo, asymmetry parameter, and scattering and extinction efficiencies by using Mie theory (see Subsection 5.2.1). Then we introduce these single-scattering quantities into the BDR model and compare results with the measurements. In an intimate mixture the surface consists of different types of particles mixed homogeneously together in close proximity (Fig. 7.31). In this case the averaging process is on the level of the individual particle, and the parameters that appear in the radiative-transfer equation (RTE) are averages of the properties of the various types of particles in the mixture weighted by cross-sectional area.

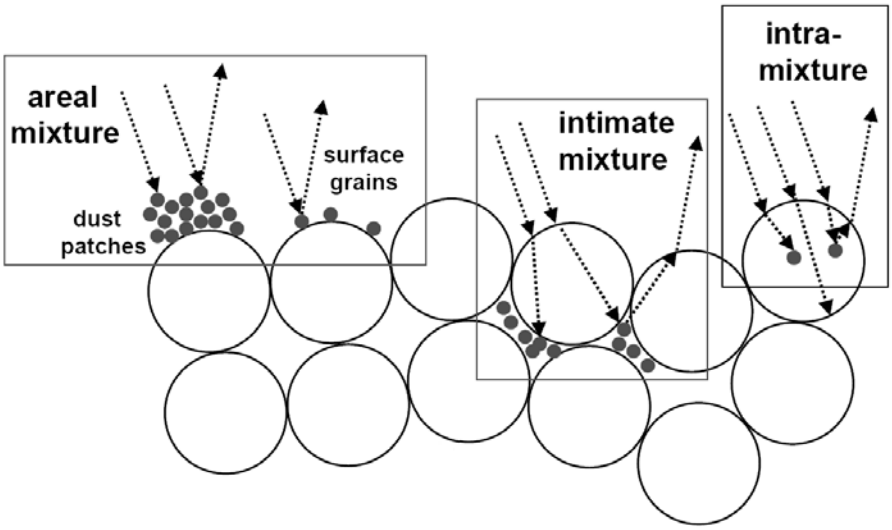

Fig. 7.31 Different CO_2/dust mixtures (modified from Langevin *et al.*, 2005b).

More than 17000 32-stream [the sums in Eqs. (6.26), (6.27) and (6.30) stop at n = 32] BDRs have been computed with our model at the full resolution of the optical constants (typically better than 0.1%), then convolved to PFS resolution and used to best-fit the PFS observations. To compute the multiple-scattering term, we adopted the δ-fit scheme developed by Hu *et al.* (2000) described in Paragraph 5.2.4.1, which is a robust technique that performs a least-square fitting to generate coefficients of the Legendre polynomial expansion of the phase function given by Eq. (6.30). To test and validate the model, we compared our results with the strict numerical RTE solution provided by DISORT for some specific mixtures. An example is shown in Fig. 7.32, where the mixture consists of 5mm CO_2 ice with 0.2 wt % of dust and 0.005 w t% of water ice; emission angle is 0° and both incidence and phase angles are 60°. The agreement is extremely good in the entire spectral range considered for this study, the discrepancies being less than 3%.

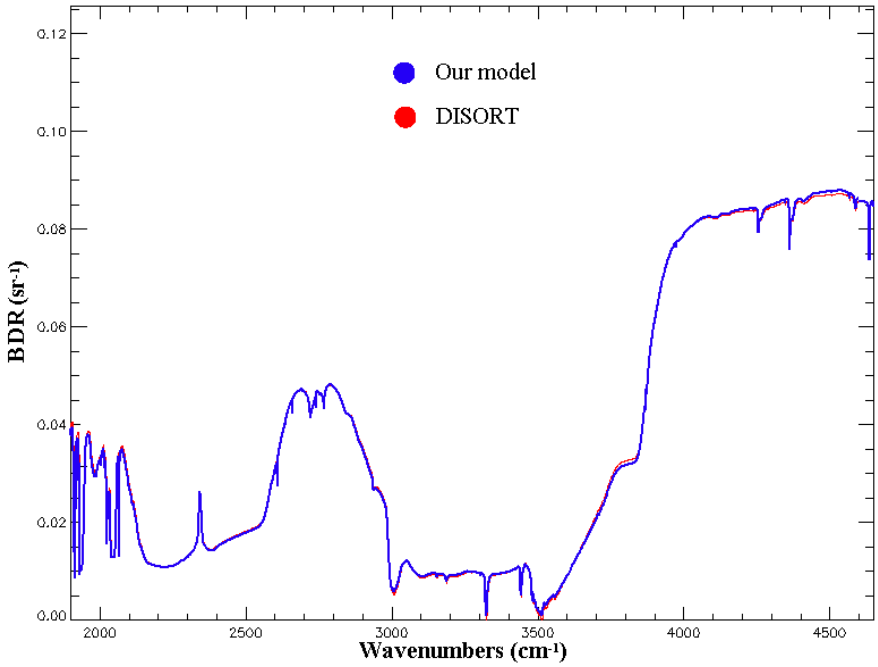

Fig. 7.32 Comparison between our model (blue curve) and DISORT (red curve).The agreement is extremely good in the entire spectral range considered, the discrepancies being less than 3%.

7.4.3.1 Sensitivity

The Hapke model described above only accounts for the energy scattered by the Martian surface. In order to account for the effect of the Martian atmosphere we apply to the synthetic BDR spectra the Mars' atmospheric transmittance, computed by means of the ARS program (Ignatiev *et al.*, 2005), a fast radiative transfer model specially developed for PFS/MEX. The final synthetic spectra thus obtained are directly compared with the PFS spectra. The effect of the atmospheric transmittance, mainly due to the gaseous CO_2, is shown in Fig. 7.33, together with the effect of the main input parameters for the mixtures, namely the H_2O ice and dust contamination. It is well known (Calvin and Martin, 1994; Warren *et al.*, 1990) that in the spectral region considered in this study the band depths of the CO_2 ice features increase with increasing grain sizes, while the reflectance decreases leaving the slopes practically unaltered. Much different is the effect of H_2O ice contamination, as shown in Fig. 7.33b. The inclusion of water ice introduces strong slopes in the spectral region from 2750 to 3000 cm^{-1}. In addition, in the 3100–3500 cm^{-1} spectral Range, water ice has an absorption coefficient that is over 4 orders of magnitude greater than that of CO_2 ice, so even small quantities can have a significant effect; the spectrum is flattened with a slow slope that raises with increasing wavenumbers. An opposite slope in the same spectral region is caused by dust contamination (Fig. 7.33c) with the reflectance showing a decrease with increasing wavenumbers. Dust also impacts the overall reflectance level and suppresses the CO_2 features around 4300 cm^{-1}. Note that in the regions where the solid CO_2 strong-band absorption edge is outside the atmospheric absorption bands (i.e., near 2500 and 3800 cm^{-1}; see Fig. 7.33a), the level of reflectance is near zero for pure CO_2 ice, and is elevated by the mixed impurities, especially dust. This consideration will be used later on in this paper to account for the possible effects of a

layered surface. The distinct effects of grain sizes and impurities on the CO_2 ice reflectance allow an accurate and simultaneous retrieval of all these quantities by fitting the measured spectra.

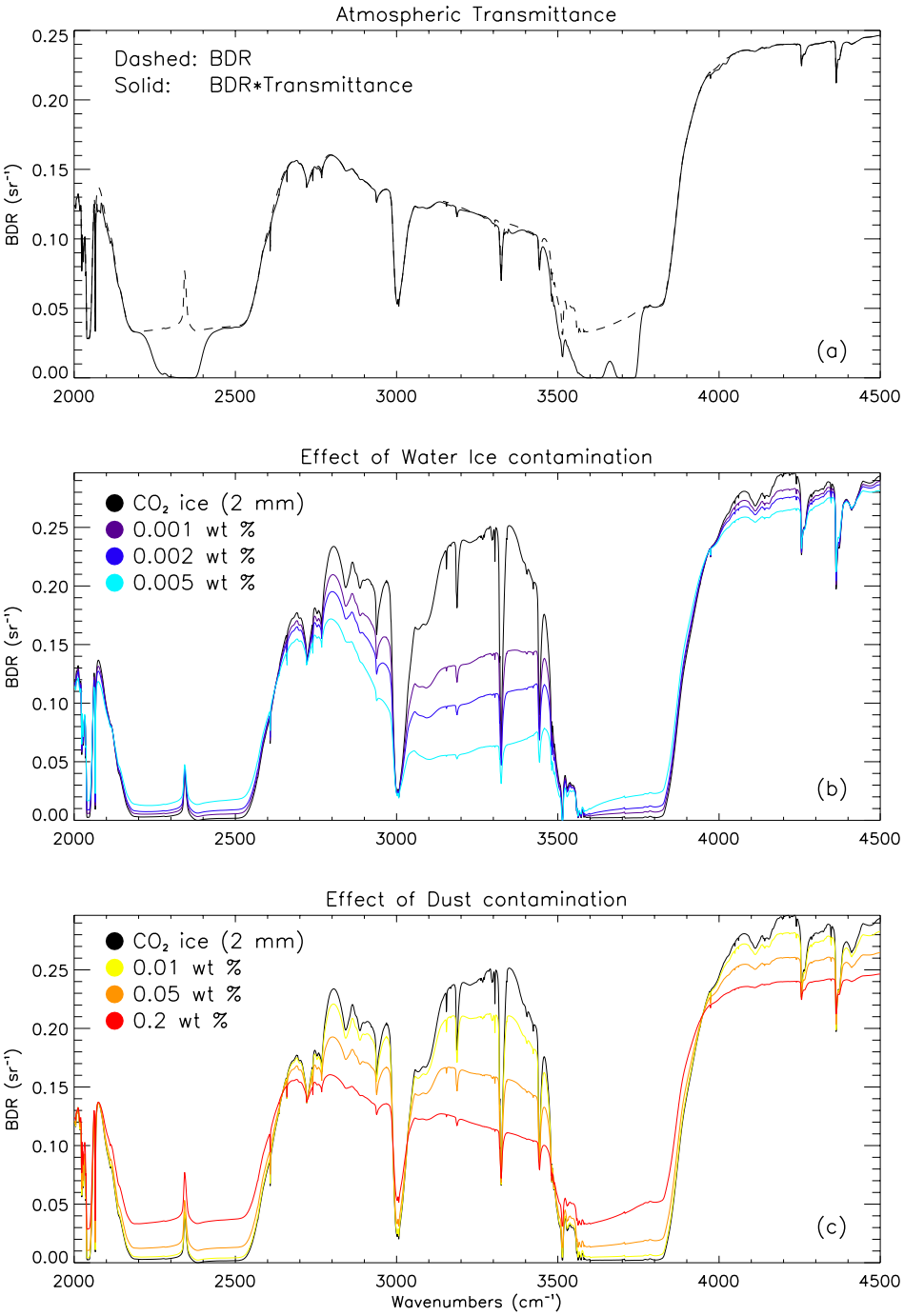

Fig. 7.33 (a) Effect of the Martian atmospheric transmission. (b) Calculated reflectance of CO_2/H_2O mixes. (c) Calculated reflectance of CO2/dust mixes. See text for more details.

As mentioned above, to compute the BDR of CO_2 snow containing dust or water ice, Mie calculations are done separately for the dust particles and the ice particles and then averaged using the respective cross-sectional areas per unit volume as weighting factors.

The calculation assumes that the dust particles are separate from the ice particles. If the dust particles are instead located inside the ice particles (condensation nuclei, whether in H_2O ice or CO_2 ice), they may be more effective at absorbing radiation (intra-mixtures; see Fig. 7.31), such that the effects we attribute to a particular concentration of dust may actually result from only half that concentration (Bohren and Huffman, 1983; Chylek *et al.*, 1983; Bohren, 1986). BDR spectra are computed with the same spectral resolution of PFS.

7.4.4 The Albedo Model (snowpack thickness)

The BDR model described in previous Subsection has been used to fit the PFS spectra. As we will see, the data show strong indication that the inner cap has a layered structure with a thin CO_2 layer on top of an H_2O ice underneath ground.

Layered structures are not accounted for on our BDR model, where the surface is described as semi-infinite layer of particulate medium. To investigate the effects of a finite snowpack thickness, we use a model for the spectral albedo of snow originally developed by Wiscombe and Warren (1980) for terrestrial snow, and subsequently extended to the case of carbon dioxide snow on Mars (Warren *et al.*, 1990). This two-stream delta-Eddington model is described in Paragraph 6.2.1.1; it was designed specifically to handle strongly forward-directed scattering (i.e. asymmetry factor $0.6 \le \xi \ge 1$) such as we have in the case of a snowpack (both H_2O and CO_2 snow; see, e.g., Figs. 6.4 and 6.5). The analytical formula for albedo, for parallel-beam incidence, is given by Eqs. (6.11) (for a thin snowpack) and (6.14) (for the semi-infinite limit). It depends on single scattering albedo, asymmetry factor, and the cosine of the solar zenith angle and, for a thin snowpack only, on the albedo of the underlying surface and the snow optical depth

$$\tau = N\sigma^{ext}d \tag{7.3}$$

where N is the number density of snow grains, σ^{ext} the extinction cross section, and d the snowpack thickness.

For a mixture, the total optical depth of the snowpack is given by the sum of the optical depths of the single components:

$$\tau_{mix}^{\text{snowp}} = \sum_i (N_i \sigma_i^{\text{ext}}) \cdot d \tag{7.4}$$

where the subscript i refers to any property of the i-th type of particle in the mixture.

In our work, mixtures are specified by the fractional mass m (given in wt%) of each component, rather than by the number of particles (see Subs. 6.1.5). The bulk density of the i-th component is

$$M_i = N_i \frac{4}{3} \pi \, r_i^3 \rho_i \tag{7.5}$$

where r_i is the radius of the i-th type of particle, and ρ_i its solid density (g cm^{-3}).

For a snowpack of pure CO2 we can then write

$$\tau_{CO_2}^{\text{snowp}} = \frac{M_{CO_2}\sigma_{CO_2}^{\text{ext}}}{\frac{4}{3}\pi\, r_{CO_2}^3 \rho_{CO_2}} \cdot d = \frac{3}{4}\left(\frac{Q_{CO_2}^{\text{ext}}}{r_{CO_2}\rho_{CO_2}} \right) \cdot L \tag{7.6}$$

where in the last equality we used the fact that $\sigma^{ext} = \pi r^2 Q^{ext}$, where Q^{ext} is the dimensionless extinction efficiency given by Eq. (5.e). In our calculations, the depth of the snowpack will be expressed as mass per unit area (g cm^{-2}), that is in terms of $L = Md$. The density of pure CO_2 ice is ρ_{CO_2} = 1.56 g cm^{-3}.

Equation (7.6) indicates that, because of the inverse dependence of optical depth on grain radius r, radiation will penetrate deeper into a snowpack of larger particles if the density M is kept fixed. In other words, the semi-infinite limit requires greater depths for larger grain sizes. Warren *et al.* (1990) shown that, for a snowpack of pure CO_2 with grain radii of 100 μm, the semi-infinite limit is reached already at 0.1 g cm^{-2} in the absorption bands and at 0.5 g cm^{-2} in most parts of the thermal infrared. However, the CO_2 grain sizes we are dealing with in our study are of several millimetres, that is 1–2 order of magnitudes larger than those in Warren *et al.* (1990); we thus expect the semi-infinite limit to be reached for greater depths.

Warren and Wiscombe (1980) showed that two centimeter liquid equivalent of soot-containing snow is effectively semi-infinite, whereas the same depth of pure snow is not. This is because light does not penetrate as deeply in the dirty snow as it does in the pure snow. In our mixtures, the millimeter-sized CO_2 ice is mixed with impurities of much smaller particles, such as dust with r_{eff} = 1.6 μm, and water ice with r_{eff} = 2.75 μm. In this condition, we can reasonably assume that the CO_2 bulk density (or, equivalently, the number of CO_2 particles per unit volume) is the same in the pure and in the dust-contaminated snowpack (in the form of intimate mixture; see Fig. 7.31). Thus, for a snowpack of CO_2 ice mixed with dust (mass fraction m), we can write:

$$\tau_{mix}^{\text{snowp}} = \frac{M_{CO_2}\sigma_{CO_2}^{\text{ext}}}{\frac{4}{3}\pi\, r_{CO_2}^3 \rho_{CO_2}} \cdot d + \frac{(m \cdot M_{CO_2})\sigma_{dust}^{\text{ext}}}{\frac{4}{3}\pi\, r_{eff}^3 \rho_{dust}} \cdot d = \frac{3}{4}\left(\frac{Q_{CO_2}^{\text{ext}}}{r_{CO_2}\rho_{CO_2}} + m\frac{Q_{dust}^{\text{ext}}}{r_{eff}\rho_{dust}} \right) \cdot L \geq \tau_{CO_2}^{\text{snowp}} \tag{7.7}$$

Equation (7.7) indicates that, for a given depth L, the dust-contaminated snowpack is optically thicker than its pure-CO_2 ice correspondent. The same applies for water ice contamination. In other words, if a snowpack is contaminated by some impurities, in the given assumption that the bulk density of the main component remains the same, the semi-infinite limit requires lesser depths. In our calculations, we assume the dust has a density r_{dust} = 2.7 g cm^{-3}, typical of clay minerals, while the density of water ice is r_{ice} = 0.917 g cm^{-3}.

The albedo model we just described allows us to determine how thick a snowpack must be to be effectively semi-infinite. Fig. 7.34 shows albedo for various depths of CO_2 snow, where depth is expressed as mass per unit area, and for three different levels of contamination:

a) pure CO_2 snow, grain radius 5 mm. As expected [Eq. (7.6)], this large-grains pure CO_2 ice snowpack requires great depths to be considered as semi-infinite (i.e. albedo at all

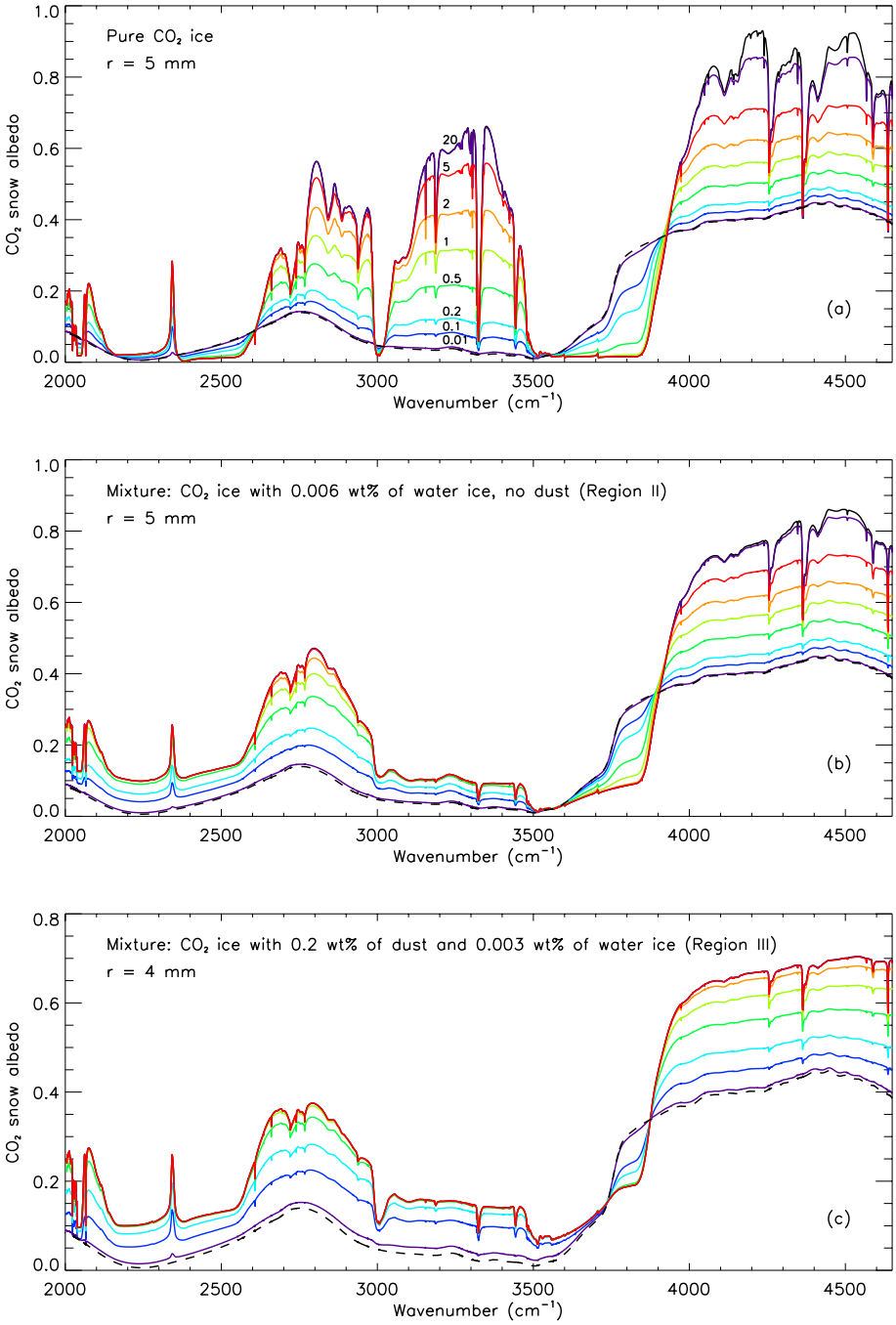

Fig. 7.34 Direct-beam spectral albedo of a thin snowpack, for a variety of snow depths, for pure and contaminated CO_2 snow over a surface of dirty water ice (the underlying albedo is shown as a dashed line). The black solid curve in each case is the semi-infinite depth. Numbers in the top-panel represent depth of the snowpack, expressed as mass per unit area (g cm^{-2}). Same colours mean same depths.

wavenumbers within 2% of that for an infinitely thick snowpack). In the considered spectral range, the semi-infinite limit is reached at 50 gcm^{-2}. Below 3500 cm^{-1}, 20 gcm^{-2} are sufficient for the thickness to be considered as semi-infinite, while in the absorption band the semi-infinite limit is reached already at ~1 g cm^{-2}. This is because the higher

the absorption coefficients, the more the incoming radiation is absorbed, and therefore the less transparent the snowpack. The opposite limit, that is a snowpack totally transparent, will require a depth of only 0.01 g cm^{-2}.

b) 5-mm CO_2 ice, mixed with 0.006 wt% of H_2O ice. We will see (Paragraph 7.4.5.2) that this is the best-fit composition of region II. With respect to the pure CO_2 case, the semi-infinite limit is reached for lower thickness.
c) 4-mm CO_2 ice, contaminated by 0.2 wt% of dust and mixed with 0.003 wt% of H_2O ice. This is the composition of region III, as indicated by the best-fit of the data (see Paragraoh 7.4.5.3). The presence of dust make the snowpack optically much thicker than its uncontaminated correspondent with the same depth L (g cm^{-2}). Inside the absorption band, the snowpack is effectively semi-infinite for depths as low as 0.5 gcm^{-2}. In the entire spectral range considered, the semi-infinite limit is reached at 5 gcm^{-2}, that is for a layer 10 times thinner than that of pure CO_2 snow. At the same time, 0.01 g cm^{-2} are not sufficient to reach the totally transparent limit.

For all the above cases, the spectral albedo of the underlying surface is that of a 20-μm H_2O ice contaminated by 0.15 wt % of dust. We will see in Paragraph 7.4.5.1 that this is the best-fit composition of region I. In general, outside the 2.7-μm CO_2 absorption band, the effect of finite snow depth is to decrease the albedo, and smooth the CO_2 ice narrow features. On the contrary, inside the absorption band, the albedo is raised-up by the brighter underneath layer. Further considerations, and implications on the results related to the effects of the snowpack thickness shown in Fig. 7.34, will be discussed in Subsection 7.4.6.

Note that the spectra in Fig. 7.34 are calculated for a spectral resolution much higher than that of PFS; consequently, for a same mixture, the CO_2 narrow features may appear more pronounced in the albedo models than in the observations. However, this will not affect the considerations we will derive by these calculations.

7.4.5 Model results

The averaged spectra of each of the five regions are shown in Fig. 7.35, after being divided by the cosine of the incidence angle. This simple correction assumes Lambertian scattering on the surface and has been used to give an idea on how the spectra would appear if they were acquired with a same incidence angle. All the CO_2 ice absorptions are marked with triangles. The BDR model described in Subsection 7.4.3 has been used to fit these PFS averaged spectra. The composition, the grain sizes and the dust content have been resolved for each of the five regions, allowing comprehensive characterization of the seasonal north polar cap. Here we present the best-fit models of the observations and the parameters used in the models. The results will be discussed in the next Subsection and are summarized in Table 7.2. The data suggest that the inner cap has a layered structure (see below). As anticipated, layered structures are not accounted for on our current reflectance models. The ice beneath the top layer has been considered as a spatial mixture. The results are still very good everywhere in the spectral range, except where the CO_2 ice absorption coefficients are such that even a thin layer is enough to totally absorb the incoming radiation (i.e. the band is saturated). This only happens around 3800 cm^{-1}, inside the strong 2.7-μm CO_2 ice absorption band. The discrepancies are higher when the observed radiation around 3800 cm^{-1} is near zero, which happens when no dust is present. In these

cases, the spatial mixture with water ice is unable to reproduce the observations because it increases the signal in that region. The radiance inside this band is instead well reproduced by the models in the spectra with high contents of dust, being either on-top of or well mixed with the ices, because the snowpack is optically thicker and shields the ground underneath [Eq. (7.7); Fig. 7.34c]. Quantitative analysis of the thickness of the upper layer can be performed exploiting the results of the albedo model presented in the previous section. This will be discussed in Subsection 7.4.6.

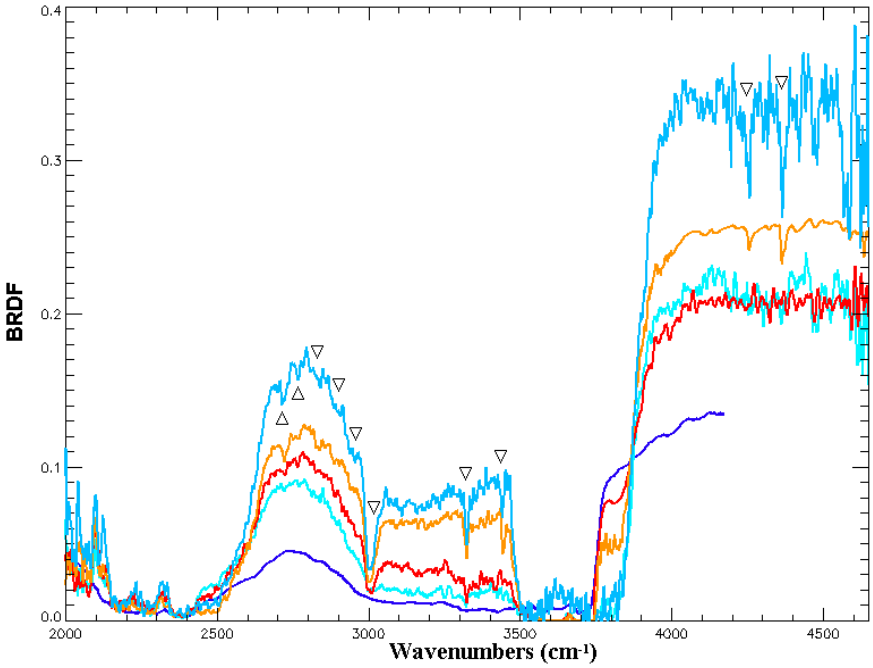

Fig. 7.35 Averaged spectra of the five regions. Colours are the same as in Fig. 7.29. The main CO_2 ice absorptions are marked with triangles. The spectra have been divided by the cosine of the incidence angle to give an idea of how the spectra would appear if they were acquired with the same incidence angle.

Before running our models, we predicted a possible composition for each region, based on a series of preliminarily considerations that one may argue by simply looking at the data. These considerations will be discussed at the beginning of the five following Paragraphs (one for each region); they provided a practical and useful contribution for the determination of the initial input parameters to be used in the model for each region. The colours used in Fig. 7.29 (and preserved in Fig. 7.35) to indicate the five regions in which the spectra have been grouped are not random, but follow from the above considerations: dark blue resembles the colour of water and thus the blue colour for region I indicates that we expect water ice; Martian dust is red, so the red and orange colours for regions III and IV stand for different amounts of dust expected in the mixtures; finally, light blue and cyan colours for regions II and V predict the presence of pure CO2 ice. All the expectations have been eventually confirmed by the models.

7.4.5.1 Region I: dirty water ice at the cap edges

This is the lowest-latitude region and extends from 65° N to 72° N. Thirteen spectra have been acquired by PFS in this range of latitudes during orbit 452, from observation number 275 to 287. The total lack of narrow features in the low-noise average of these spectra suggests the absence of CO_2 ice (see Fig. 7.36); this is also supported by the surface temperatures retrieved from the LWC spectra which, in this region, are always far above the CO_2 condensation temperature (Fig. 7.42). The overall spectral shape and the Fresnel reflection peak clearly visible around 3230 cm^{-1} indicate that it is water ice and the slow-decreasing slope with increasing wavenumbers in the 3100–3500 cm^{-1} spectral range suggests the presence of dust. To fit this spectrum we then ran special BDR models of a mixtures of only two elements, H_2O ice and dust, for different ice grain sizes and dust contents. The fit is shown in Fig. 7.36, where the blue curve is the spectrum measured by PFS and the black curve is a BDR model of an intimate admixture of medium sized H_2O ice (20 μm) and 0.15 wt % of dust. The procedure described in Subsection 7.4.2 for the correction of the spectral modulation above 4200 cm^{-1} is useful only when the main component of the snowpack is the CO_2 ice. Therefore, it has not been applied to this average, and the fit stops at 4150 cm^{-1}.

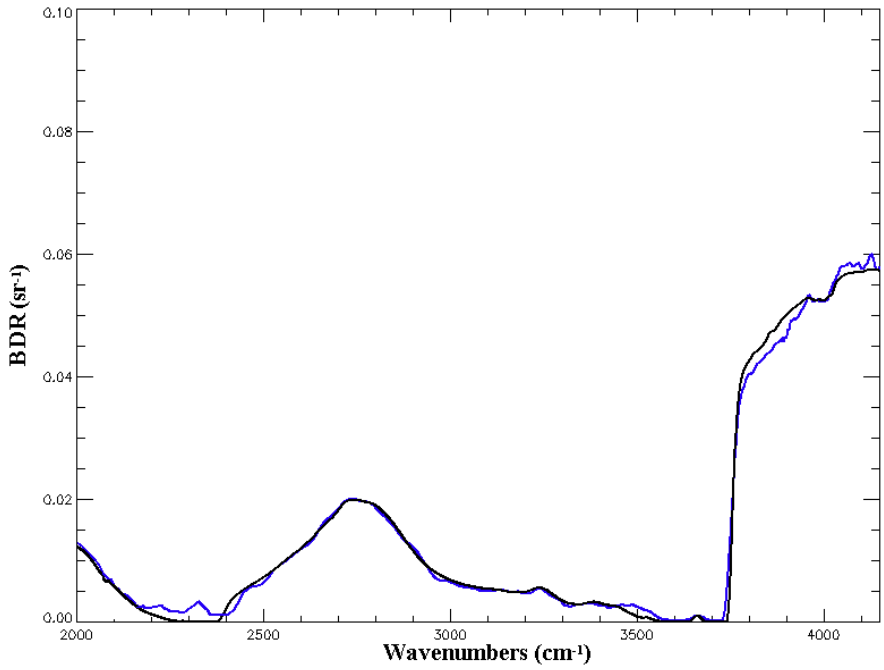

Fig. 7.36 Best-fit of region I PFS averaged spectrum. The blue curve is the spectrum measured by PFS; the black curve is a BDR model of an intimate admixture of H_2O ice (20-μm) and 0.15 wt % of dust.

7.4.5.2 Region II: thin CO_2 ice layer

Region II is a narrow region (76–79° N) just at the edge of the structural layered terrain cap (see Fig. 7.41). The averaged spectrum of this region (observation number 292 to 297) shows very weak CO_2 ice features, except for the 2.7 μm band which causes the radiation to

be near zero up to ~3850 cm^{-1} (see Fig. 7.37); it is low in brightness, except above 4000 cm^{-1}, and the Fresnel reflection peak is barely visible around 3230 cm^{-1}. As discussed in Subsection 7.4.4, this suggests a layered ground, with a thin CO_2 layer on top of an optically thick H_2O ice layer. A simple CO_2+H_2O ice intimate mixture would require too much water ice to suppress the CO_2 ice features as observed in the data, which would raise the level of the fringe around 3800 cm^{-1} far above the measured signal (see Fig. 7.33b). The averaged spectrum (cyan curve) and its best-fit (black curve) are shown in Fig. 7.37. The model is a spatial mixture of 30% CO_2 ice (5 mm grain size) and 70% of the same water ice as in region I. The CO_2 ice, in turn, is intimately mixed with 0.006 wt% of H_2O ice. No dust is present in the thin overlying mixture. The level of the bright fringe around 3800 cm^{-1} tells us how much dust is present in the top-layer (Fig. 7.33c). The CO_2 ice band is almost saturated. Adding some dust in the mixture would make it impossible to have a good fit everywhere below 3500 cm^{-1}, and would raise the level of the fringe around 3800 cm^{-1}. Before we add the spatial contribution of H_2O ice, the level of the fringe is well reproduced by the model. Adding more dust and/or H_2O ice would reduce the quality of the fit.

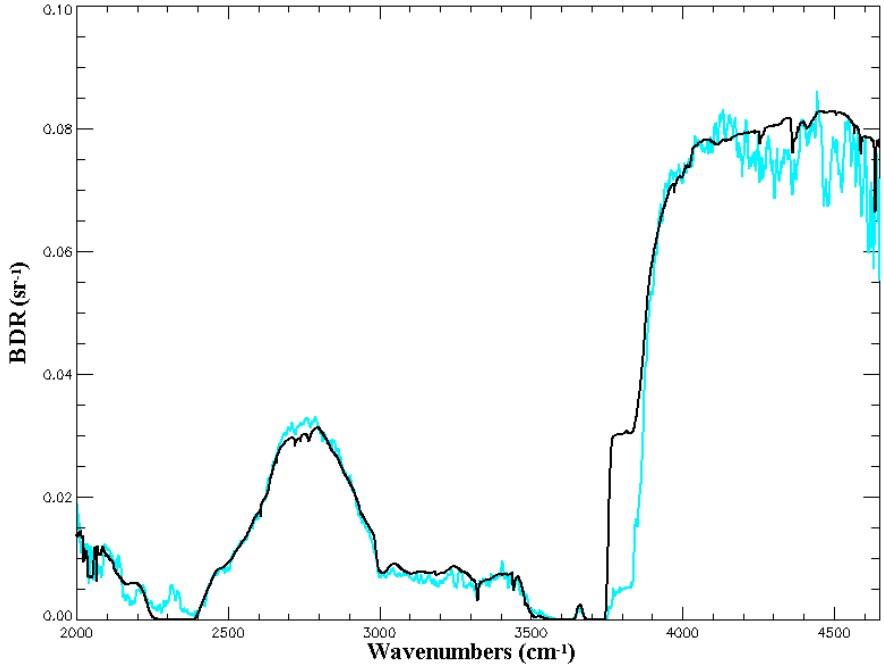

Fig. 7.37 Best-fit of region II PFS averaged spectrum. Cyan curve is the spectrum measured by PFS; black curve is the BDR model. See Table 7.2 for model parameters, and text for details.

The lobes around 2250 cm^{-1} in the measured spectrum are due to the non-LTE emission (Formisano et al., 2006) of the gaseous CO_2 that occur in the atmospheric column above the cap.

Despite the high level of noise present in this spectrum, the fit is quite good everywhere, except for the bright fringe around 3800 cm^{-1}, where we know the level of reflectance is near zero for pure CO_2 ice (see Paragraph 7.4.3.3 and Fig. 7.33). This is because, rather than spatially mixed, the water ice is actually "seen" underneath a CO_2 surface layer. The data show the 2.7 μm band almost saturated up to 3850 cm^{-1}. With a spatial-mixture model such that used in our fit, this cannot be possible for it assumes a

percentage of uncovered water ice (very bright in this spectral region) that raises the reflectance around 3800 cm^{-1}. The actual situation is likely the following: a thin layer of CO_2 ice covers the same water ice as region I. This statement is supported by the layered albedo model of region II, shown in Fig. 7.34b. The albedo of a CO_2 snow layer, on top of an underlying surface with the same water ice as in region I, is shown for various depths of the top-layer. The CO_2 ice absorption coefficients for the 2.7-μm band are so strong that even a thin layer is enough to absorb the incoming radiation. Outside this band, the CO_2 ice layer is optically thin (i.e. transparent to the radiation, for depths ≤ 2 g cm^{-2}) and the spectra are dominated by the underlying H_2O ice layer.

Above 4000 cm^{-1} the spectrum is very noisy; the CO_2 features appear more pronounced in the data than in the modelled spectrum. It is difficult to establish whether these discrepancies are true or due to the instrumental noise. Nevertheless, we note that deep CO_2 lines in this spectral region would be in contrast with the rest of the spectrum, where the features are suppressed by both the water ice contamination of the mixture (Fig. 7.33b) and the finite optical thickness of the snowpack (Fig. 7.34b).

7.4.5.3 Region III: dusty CO_2 ice

As shown in Fig. 7.38, a bright fringe around 3800 cm^{-1} (just outside the CO_2 atmospheric absorption band), a low overall reflectance and no CO_2 features around 4300 cm^{-1} are observed in the six-spectra average of region III (observations 298–303); this are the typical effects of dust contamination (see Paragraph7.4.3.3 and Fig. 7.33c). In addition, as can be seen from Fig. 7.29, the footprints of these measurements (red spots) occur in a brown area from visible data, which also may be interpreted as a higher content of Martian dust.

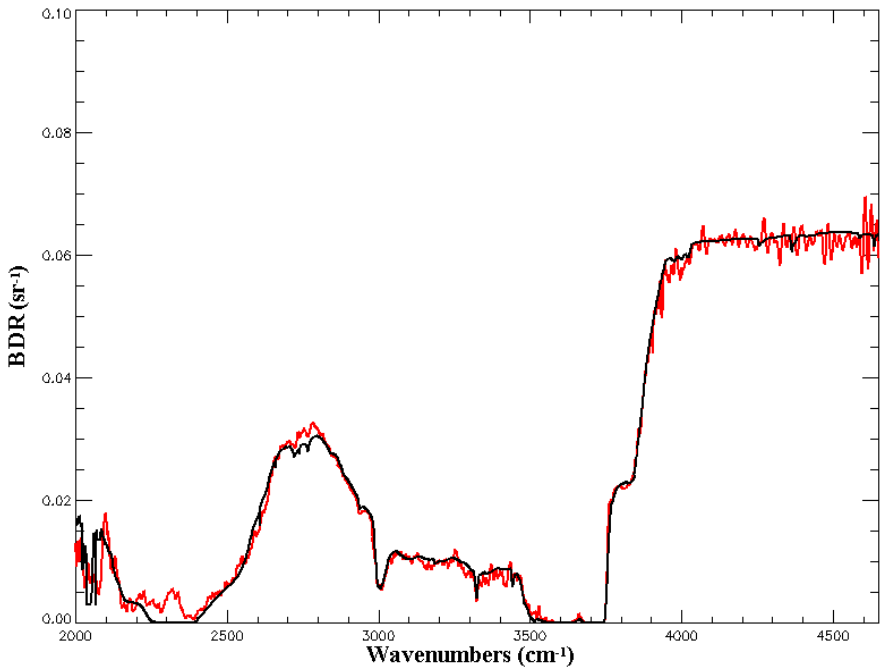

Fig. 7.38 Best-fit of region III PFS averaged spectrum. Red curve is the spectrum measured by PFS; Black curve is the BDR model. See Table 7.2 for model parameters, and text for details.

Indeed, the model confirms a very high dust content: the observed spectrum is best-fitted by a mixture of CO_2 ice, with 0.003 wt% of water ice and 0.23wt% of dust, which is one order of magnitude higher of that observed for the south residual polar cap in Section 7.2. A 30% spatial mixture with same water ice as in region I is also needed. Note that each time the ice of region I has been used for a spatial mixture, it has been scaled for the actual lighting geometry of the current observations. This time the fit is very good in the entire spectral range and the bright fringe around 3800 cm^{-1} is well reproduced by the model. Thanks to the presence of a high content of dust, the snowpack is optically thicker [see Eq. (7.7)], the underlying layer is barely visible and the effect of the lower layer is small, even for a thin layer, especially in the absorption band, as can be noted by the layered albedo model of region III shown in Fig. 7.34c.

Now, the 30% spatial mixture with same water ice as in region I is not only to account for mimicing the underlying layer: this region is actually a spatial mixture of dusty CO_2 and H_2O ices as in the model. This is suggested by the increase of the surface temperatures inside this region, measured from the LWC thermal-infrared spectra, only attributable to spatial mixtures of cold CO_2 ice and warmer dust/H_2O ice, as we will discuss in the next Subsection. The level of the signal around 3800 cm^{-1} is raised up by both the dust mixed with the CO^2 ice and the regions of exposed H_2O ice, which both scatter back the radiation before it is totally absorbed by the CO_2-ice top layer (contrary to what is seen in region II).

7.4.5.4 Region IV: a thick CO2 ice layer near the top of the polar terrain

Region IV is close to the top of the polar cap (see Fig. 7.41) and extends from 81° N to 85° N (observations 304–310). The same fringe around 3800 cm^{-1}, as seen in region III, is present in the averaged spectrum, but it is much less pronounced indicating a lower, but still not negligible, dust content. The spectrum is bright and strong CO_2 features are present, especially the 3.3 μm band (around 3000 cm^{-1}), which may indicate a layer of CO_2 ice much thicker than that in region II. The best-fit is shown in Fig. 7.39; CO_2 grain size is 3 mm and the dust content 10 times lower than that of region III (0.02 wt%). Water ice is present as 0.0018 wt% in the intimate mixture, and as a 50% spatial fraction with the same composition as in region I, which we know is actually due to the underlying layer. The fit is extremely good for this high signal-to-noise average; the overall reflectance and the shape and the depth of all the CO_2 lines and bands have been reproduced by our model. The fit of the bright fringe around 3800 cm^{-1} is poor for the same reasons expressed in the last two Paragraphs: in the data, the level is raised by the presence of dust which scatters the radiation before it is totally absorbed by the strong 2.7 μm band of the CO_2 ice top layer; in the model, it is over-enhanced by the bright uncovered water ice of the linear mixture that emulates the second layer. The higher the dust content and/or the thickness of the upper layer (that is, the higher the optical thickness of the snowpack; see Subsection 7.4.4), the lower the spatial fraction of H_2O ice needed in the model (the underlying layer is shielded) and the better the fit around 3800 cm^{-1}.

7.4.5.5 Region V: a pure CO_2 ice thick layer on the top of the polar terrain

As can be seen in Fig. 7.40, the average spectrum of region V (observation number 311 to 316) has the 2.7 μm band almost completely saturated (i.e. the radiance is zero up to ~3850 cm^{-1}) as that of region II, but is much brighter and has very pronounced CO_2 features, indicating a pure CO_2 ice.

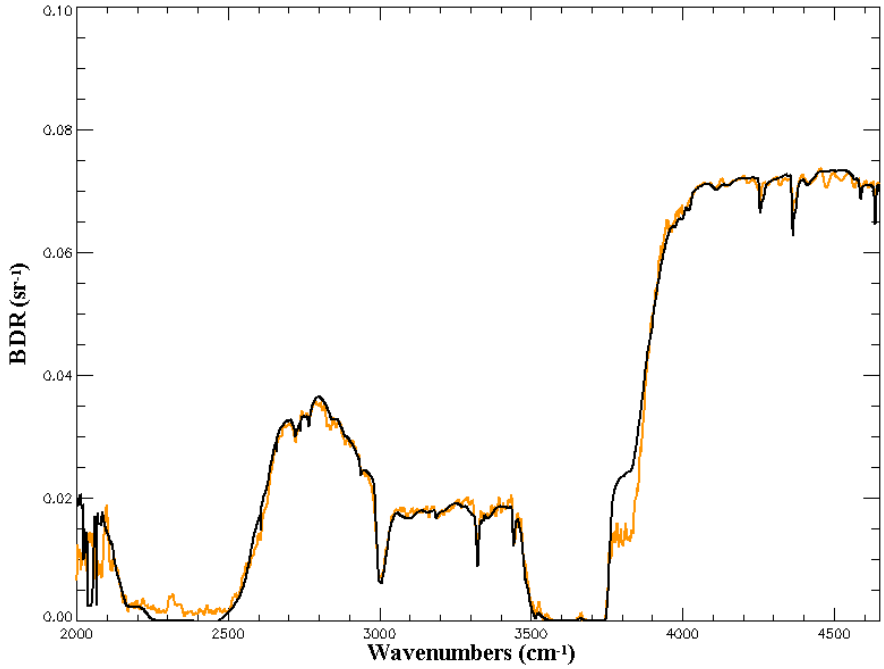

Fig. 7.39 Best-fit of region IV PFS averaged spectrum. Orange curve is the spectrum measured by PFS which is best-fitted by the model (black curve). See Table 7.2 for model parameters, and text for details.

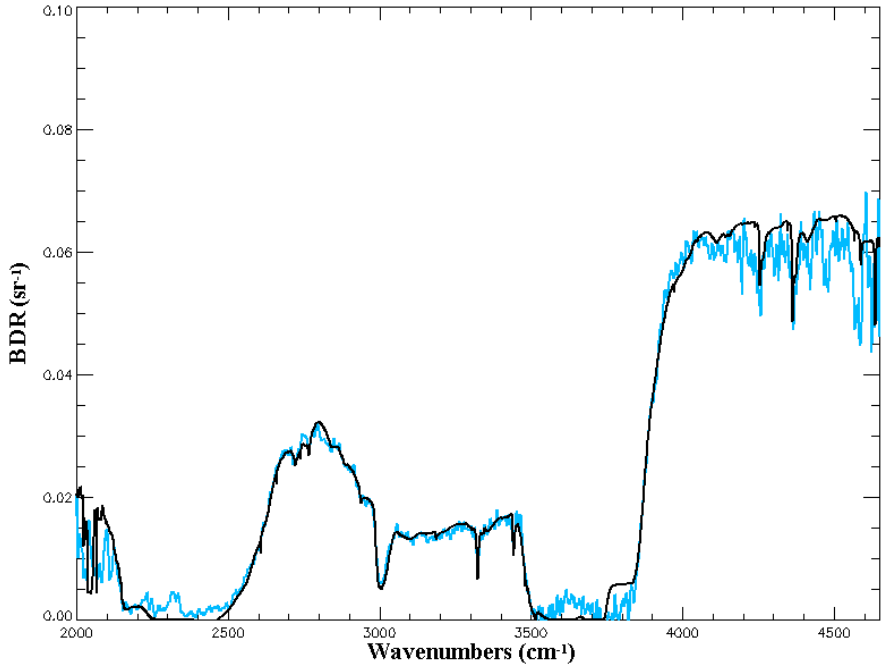

Fig. 7.40 Best-fit of region V PFS averaged spectrum. Light blue curve is the spectrum measured by PFS; Black curve is BDR model. See Table 7.2 for model parameters, and text for details.

The spectrum is best-fitted by a mixture of 5-mm sized CO_2 ice and 0.003 wt% of water ice. No dust is required, as expected following the above considerations. Only a 15% spatial fraction of water ice (same water ice as region I) is needed to emulate the underlying layer, indicating a thick layer. This is also supported by the strong CO_2 ice features, whose depth increases with increasing path lengths of the radiation in the CO_2 ice surface. This is the most poleward region (latitudes ≥ 84° N) and it is placed right on the top of the north polar cap, as can be seen in Fig. 7.41. We recall that, during this orbit, the spacecraft was very far from the Martian surface (~5000 Km); moreover, this region has been observed with the most extreme lighting geometry (incidence and emission angles as high as 80.2° and 75.2°, respectively). Thus, the air mass that the radiation goes through (twice, once prior and then after being scattered by the surface) is large.

Table 7.2 - Summary

Description	composition	Grain size	Dust content (wt%)	H2O ice content (wt%)	Thickness
Region I (65° N – 72° N)	H2O ice	20 μm	0.15	-	Decreases with latitude
Region II (76°N – 79°N)	CO2 ice	5 mm	0	0.006	0.5–1 g cm-2 (1–2 cm)*
Region III (79°N – 81°N)	CO2 ice	3.7 mm	0.23	0.003	0.2–0.5 g cm-2 (0.4–1 cm)*
Region IV (81°N – 84°N))	CO2 ice	3 mm	0.02	0.0018	1–2 g cm-2 (4–10 cm)*
Region V (≥ 84°N)	CO2 ice	5 mm	0	0.003	> 20 g cm-2 (≥ 60–80 cm)*

*Assuming a snowpack density of 0.5 g cm^{-3}

7.4.6 Discussion

We have determined the physical state and coexistence modes of the ices and dust composing the seasonal condensates of the north polar cap. Results are summarized in table 7.2. In the middle of the north spring (Ls ~40°) the polar cap is regressing; nevertheless, CO_2 ice has not yet entirely sublimated, being still present at latitudes higher than 76° N. From the North pole toward lower latitudes, a continuum evolution of the seasonal ice deposits has been observed. The sublimation of CO_2 ice leads to the progressive enrichment in water ice and dust of the CO_2-rich seasonal deposits. At the lowest latitudes, a spatial segregation of dusty water ice from the CO_2 ice occurs to finally form a thin CO_2-free dusty water ice layer.

Fig. 7.41 shows a 3D surface plot of the Martian north polar cap; RGB colours have been obtained from the spectra in the visible range acquired by OMEGA at the same time of the PFS observations used in this study, and the altimetry is retrieved from MOLA data. The actual altimetry values are related in Fig. 7.42b. The five regions investigated in this work are indicated. Region I is the lowest latitudes region. It is a wide annulus of dusty H_2O ice that extends from 65° N to 76° N latitude, which corresponds to approximately 450 km, and surrounds the entire CO_2 seasonal cap.

A second annulus, this time made of CO_2 ice, surrounds the cap (region II). This region is clearly identifiable in the RGB image of Fig. 7.41 as a thin bright stripe at the foot of the

cap. It is only degrees of latitude wide (76–79° N) which corresponds to about 150 km. Our results showed that it consists of a thin layer of CO_2 ice covering the same ice as region I. The CO2 ice has not yet entirely sublimated in this little-higher latitude region (with respect to region I). The grain size is large (5 mm) and the composition is quite different from that of the adjacent region III (mainly the dust content).

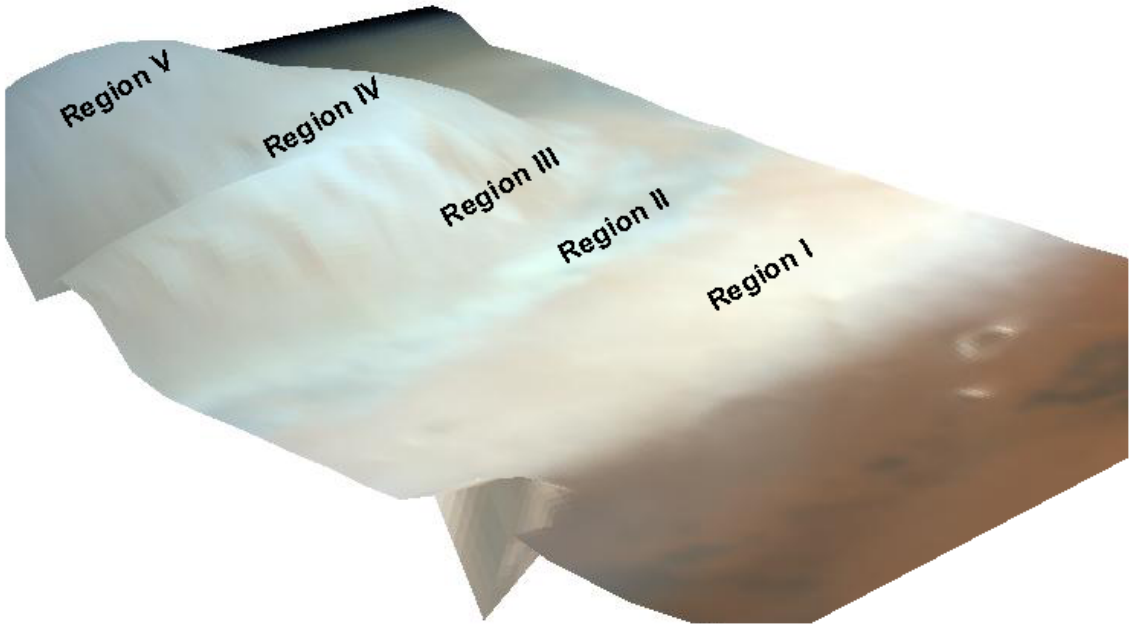

Fig. 7.41 3D surface plot of the Martian north polar cap at Ls ~40° (MEX orbit 452). The RGB colours have been obtained from the spectra in the visible range acquired by OMEGA. The altimetry is retrieved from MOLA data. The five regions investigated in this work are marked.

By means of the LWC thermal-infrared spectra we were able to retrieve the surface temperatures within the five regions (Fig. 7.42). The CO_2 condensation temperature (~150 K) is first reached within region II, which confirms the presence of an exposed CO_2 ice layer. Unexpectedly, region III shows increases of the surface temperature as high as 3°. This region is placed along the shoulders of the cap and extends for 1.5 km in altitude. Since CO_2 ice is present everywhere in this region and the altitude increases, we rather expected the surface temperatures to decrease, following Clausius–Clapeyron's law (see Giuranna *et al.*, 2007a, in Appendix A.4). On top of the 2 km high cap, the CO2 ice temperature is indeed around 145 K as expected (Fig. 42). This increase of temperatures within region III cannot be explained by a recent deposition of "warm" dust on-top of the ice, transported by winds circulation or by a local/regional dust storm. This may be for two reasons: first, even if regional dust storms have been previously observed in the north polar region during its regression (Cantor et al., 2001; James and Cantor, 2001), preferential deposition of dust on this spatially limited region III is unlikely. Second, the CO_2 ice acts as a thermostat in equilibrium with the atmospheric pressure; hot dust landing on it will sublime some CO_2 until it cools to ~150 K. Where CO_2 spectral features are clearly visible, as in our case, and T > ~150 K, it is very likely to be a spatial mixture of cold CO_2 and warmer, dusty H_2O ice. Region III is a region of increased slopes. As the slopes have more or less southern orientation, they receive a higher solar exposure and

sublime earlier compared to the other regions (for instance, compared to region II, even if it is lower in latitude). At Ls = 40°, part of the CO_2 snow of region III remains. Perhaps the CO_2 ice is on flatter regions and the dirty water ice is exposed on the higher slopes. The result is an enhancement of the dust content.

Similar considerations about the slopes and the CO_2 sublimation may be applied to region IV, explaining the higher dust content and the lower grain sizes (3–4 mm) of these two regions with respect to the adjacent regions II and V (5 mm both).

Model results presented in the previous section indicate that the inner cap has a layered structure, with a thin CO_2 layer with varying concentrations of dark dust, on top of an H_2O ice layer. The layered albedo model presented in Subsection 7.4.4 can be used to obtain information on the actual thickness of the layers. Fig. 7.34c shows that 0.2–0.5 g cm^{-2} is most likely the thickness of the dirty CO_2 layer of region III. Indeed, such a depth is thin enough for the underneath layer to be seen, and thus suppress the CO_2 narrow features and shape the continuum of the spectrum, as observed for region III (Fig. 7.38). At the same time, it is thick enough not to rise the level of the radiance of the bright fringe around 3800 cm^{-1}. Similar considerations would lead to a thickness of 0.5–1 gcm^{-2} for region II, as can be deduced from Fig. 7.34b. We ran layered albedo models also for regions IV and V (not shown in Fig. 7.34), indicating a snowpack depth of 2–5 gcm^{-2} for region IV. The optical thickness of the top CO_2 ice layer of region V is close to the semi-infinite limit; for a 5-mm CO_2 snow with 0.003 wt% of water ice, this means a snowpack depth ≥ 30–40 gcm^{-2}. The mean thickness of seasonal CO_2 frost that covers the north pole of Mars during the winter and spring seasons has been recently studied by Feldman *et al.* (2003) using gamma ray and neutron data measured by the gamma ray spectrometer suite of instruments aboard Mars Odyssey. They found an average CO_2 frost thickness of about 45 gcm^{-2} at Ls = 40° (as in our case) for a latitude of 85° N. This is essentially the value needed to be effectively semi-infinite, according to our models. Our data are always equatorward of that latitude, with region II being as low as 76° N latitude. In addition, as discussed above, the higher slopes of regions III and IV may increase the CO_2 sublimation rates within these regions. Thinner depths of that in Feldman *et al.* (2003) are thus expected in our case. Furthermore, the snow may be blown by the wind to leave regions of thin snow (James *et al.*, 1979, thought this to be responsible for the variability of observed visible snow albedo across the polar cap). Therefore, the finite-depth condition may reasonably apply over large areas of the mid-spring north polar cap.

On Earth, the bulk density of fluffy new snow is about 0.1 gcm^{-3}, while for old melting snow is ~0.4 gcm^{-3}. The CO_2 solid density is ρ_{CO_2} = 1.56 gcm^{-3}, which is about 1.7 times greater that that of water ice (0.917 g cm^{-3}). Thus, one may lead to a first approximation of the bulk density of pure CO_2 fresh and melting snow of about, respectively, 0.2 and 0.7 gcm^{-3}. The upper limit density of the Martian seasonal deposits of carbon dioxide has been estimated by Smith *et al.* (2001) to be 0.91 ± 0.23 gcm^{-3}. Feldman *et al.* (2003) have shown that, at Ls = 40°, this value leads to a snowpack thickness about 75% higher than measured by the gamma ray spectrometer aboard Mars Odyssey, and than predicted by all three major Mars General Circulation Models presently in use. As the authors noted, this discrepancy can be explained if the actual density of CO_2 snow is in fact lower than the upper limit of 0.91 g cm^{-3} estimated by Smith *et al.* (2001).We here note that, to solve the discrepancies found in Feldman *et al.* (2003), one should assume an intermediate snowpack density of ~0.52 gcm^{-3}. Interesting enough, recent global-scale, volumetric

measurements of the distribution of condensed CO_2 combined with measurements of the deposited column mass density, derived from the neutron spectrometer on board Mars Odyssey, yielded an estimate of the density of the seasonally exchanging material of 0.5 ± 0.1 gcm^{-3} (Aharonson *et al.*, 2004), just the same value we derived from the above considerations. Assuming such a density for the snowpack, we get a thickness of 1–2 cm for the top layer of region II; 0.4–1 cm for region III; 4–10 cm for region IV; and ≥ 60–80 cm for region V. These values are consistent with those inferred from neutron spectrometry (Aharonson *et al.*, 2004), laser altimetry (Prettyman *et al.*, 2005), and NIR observations (Langevin et al., 2006) for the south seasonal polar cap. No similar studies have been done before for the north seasonal polar cap; these results should provide new, useful constraints in models of the Martian climate system and volatile cycles.

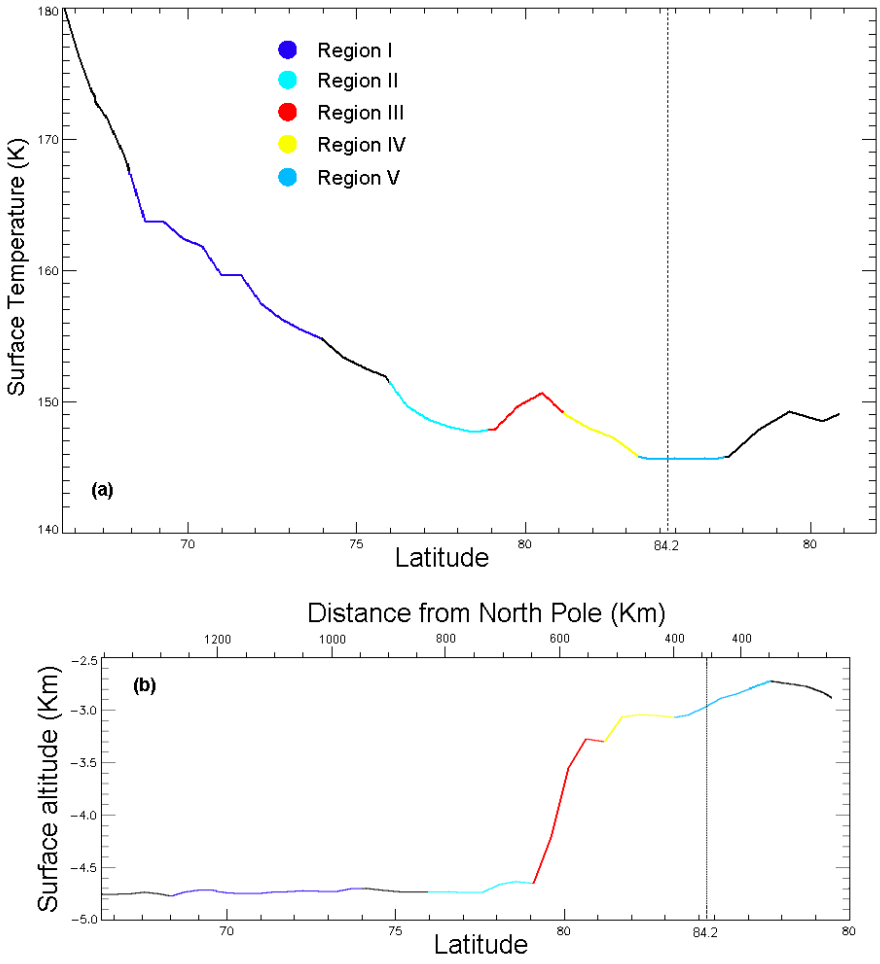

Fig. 7.42 (a) Surface temperatures of the five region retrieved from the thermal-infrared spectra of the PFS LWC channel. The temperatures above ~76° N latitude (beginning of region II) are consistent with the presence of CO_2 ice. Note the increase of temperatures within region III. (b) Surface altitude vs. latitude and distance from the North pole.

REFERENCES

Aharonson, O., Zuber, M.T., Smith, D.E., Neumann, G.A., Feldman, W.C., Prettyman, T.H. (2004) Depth, distribution, and density of CO_2 deposition on Mars, *J. Geophys. Res.*, **109** (E5), E05004.

Banfield, D., Conrath, B. J., Smith, M. D., Christensen, P. R., and John Wilson, R. (2003) Forced waves in the Martian atmosphere from MGS TES nadir data, *Icarus*, **161**, 319–345.

Banfield, D., Conrath, B. J., Gierasch, P. J., Wilson, R. John, Smith, M. D. (2004) Traveling waves in the martian atmosphere from MGS TES Nadir data, *Icarus*, **170**, 365–403.

Barnes, J. R. (1980) Time Spectral Analysis of Midlatitude Disturbances in the Martian Atmosphere, *J. Atmos. Sci.*, **37**, 2002–2015.

Barnes, J. R. (1981) Midlatitude Disturbances in the Martian Atmosphere: A Second Mars Year, *J. Atmos. Sci.*, **38**, 225–234.

Barnes, J. R., J. Pollack, R. Haberle, C. Leovy, R. Zurek, H. Lee, and J. Schaeffer (1993) Mars atmospheric dynamics as simulated by the NASA Ames general-circulation model. 2. Transient baroclinic eddies, *J. Geophys. Res.*, **98**, 3125– 3148.

Barnes, J. R. (2003) Mars Weather Systems and Maps: FFSM Analyses of MGS TES Temperature Data. The Sixth International Conference on Mars, Pasadena, California, 20 – 25 July, abstract no.**3127**.

Bell, J. F., and D. Crisp (1993) Ground-based imaging spectroscopy of Mars in the near infrared: preliminary results, *Icarus*, **104**, 2–19.

Bibring, J.-P., Langevin, Y., Poulet, F., Gendrin, A., Gondet, B., Berthe, M., Soufflot, A., Drossart, P., Combes, M., Bellucci, G., Maroz, V., Mangold, N., Schmitt, B. (2004) Perennial water ice identified in the south polar cap of Mars, *Nature*, **428**, 6983–6986.

Bohren, C. F. (1986) Applicability of effective-medium theories to problems of scattering and absorption by nonhomogeneous atmospheric particles, *J. Atmos. Sci.* **43**, 468–475.

Bohren, C. F., and D. Huffman (1983) Absorption and Scattering of Light by Small Particles, New York: Wiley.

Born, M., and E. Wolf (1980) Principles of optics, 6th ed. New York: Pergamon Press.

Bortolino, S., Comolli, L., Formisano, V. (2007) Mechanical disturbances in Fourier spectrometers, *Appl. Opt.*, **46**, Issue 22, 5248–5256.

Briggs, G. A. (1974) The nature of the residual Martian polar caps, *Icarus*, **23**, 167–191.

Briggs, G. A., and C. B. Leovy (1974) Mariner 9 observations of the Mars north polar hood, *Bull. Am. Meteorol. Soc.*, **55**, 278–296.

Briggs, G., K. Klaasen, T. Thorpe, and J. Wellman (1977) Martian dynamical phenomenon during June-November 1976: Viking orbiter imaging results, *J. Geophys. Res.*, **82**, 4121–4149.

Butler, B., D. Muhleman, and M. Slade (1995), The difference in the residual ice caps on Mars as deduced from VLA/Goldstone radar images, Abstract for the "Solar System Ice" international symposium, Toulouse, France.

Calvin, W. M. (1990) Additions and corrections to the absorption coefficient of CO2 ice: applications to the Martian south polar cap, *J. Geophys. Res.*, **95,** 14743–14750.

Calvin, W. M., and T. Z. Martin (1994) Spatial variability in the seasonal south polar cap of Mars, *J. Geophys. Res.*, **99**, 21143–21152.

Cantor, B.A., James, P.B., Caplinger, M., Wolff, M.J. (2001) Martian dust storms: 1999 Mars Orbiter Camera observations, *J. Geophys. Res.*, **106**, 23,653–23,687.

Chandrasekhar, S. (1960), *Radiative Transfer*, Dover Publications.

Chassefiere, E., J. E. Blamont, V. A. Krasnopolsky, O. I. Korablev, S. K. Atreya, and R. A. West (1992) Vertical structure and size distributions of Martian aerosols from solar occultation measurements, *Icarus*, **97**, 46–69.

Choudhury, B. and Chang, A. (1981) On the angular variation of solar reflectance of snow, *J. Geophys. Res.*, **86**, 465–472.
Christensen, P. R., and R. W. Zurek (1984) Martian north polar hazes and surface ice: Results from the Viking survey/completion mission, *J. Geophys. Res.*, **89**, 4587–4596.
Christensen, P.R., D.L. Anderson, S.C. Chase, R.T. Clancy, R.N. Clark, H.H. Kieffer, R.O.Kuzmin, M.C. Malin, J.C. Pearl, T.L. Roush, and M.D. Smith (1998) Results from the MarsGlobal Surveyor thermal emission spectrometer, *Science*, **279**, 1692–1698.
Chylek, P., Ramaswami, V., Srivastava, V. (1983) Albedo of soot-contaminated snow, *J. Geophys. Res*, **88**, 10837–10843.
Clancy, R. T., and S. W. Lee (1991) A new look at dust and clouds in the Mars atmosphere: Analysis of emission-phase-function sequences from global Viking IRTM observations, *Icarus*, **93**, 135–158.
Clancy, R. T., S. W. Lee, G. R. Gladstone, W. W. McMillan, and T. Rousch (1995) A new model for Mars atmospheric dust based upon analysis of ultraviolet through infrared observations from Mariner 9, Viking, and Phobos, *J. Geophys. Res.*, **100**, 5251–5264.
Clancy, R. T., A. W. Grossman, M. J. Wolff, P. B. James, D. J. Rudy, Y. N. Billawala, B. J. Sandor, S. W. Lee, and D. O. Muhleman (1996) Water vapor saturation at low altitudes around aphelion: A key to Mars climate?, *Icarus*, **122**, 36– 62.
Clancy, R. T., M. J. Wolff, and P. R. Christensen (2003) Mars aerosol studies with the MGS TES emission phase function observations: Optical depths, particle sizes, and ice cloud types versus latitude and solar longitude, *J. Geophys. Res.*, **108**(E9), 5097–5120.
Clark, R. N., and T. B. McCord (1982) Mars residual polar cap : Earth-based spectroscopic confirmation of water ice as a major constituent and evidence for hydrated minerals, *J. Geophys. Res.*, **87**, 367–370.
Colaprete, A., and O. B. Toon (2002) Carbon dioxide snow storms during the polar night on Mars, *J. Geophys. Res.*, **107**, 5051.
Colaprete, A., Barnes, J. R., Haberle, R. M., Hollingsworth, J. L., Kieffer, H. H., Titus, T. N. (2005) Albedo of the south pole of Mars determined by topographic forcing of atmosphere dynamics, *Nature*, **435**, 184–188.
Colbeck, S. C. (1982) An overview of seasonal snow metamorphism, *Rev. Geophys. Space Phys.*, **20**, 45–61.
Colburn, D. S., J. B. Pollack, and R. M. Haberle (1989) Diurnal variations in optical depth at Mars, *Icarus*, **79**, 159–189.
Comolli, L., and Saggin, B. (2005) Evaluation of the sensitivity to mechanical vibrations of an IR Fourier spectrometer, *Rev. Sci. Instr.*, **76**, 123112–123120.
Conrath, B. J., J. C. Pearl, M. D. Smith, W. C. Maguire, P. R. Christensen, S. Dason, and M. S. Kaelberer (2000) Mars Global Surveyor Thermal Emission Spectrometer (TES) observations: Atmospheric temperatures during aerobraking and science phasing. *J. Geophys. Res.*, **105**, 9509–9519.
Curran, R. J., B. J. Conrath, R. A. Hanel, V. G. Kunde, and J. C. Pearl (1973) Mars: Mariner 9 spectroscopic evidence for H2O ice clouds, *Science*, **182**, 381–383.
Davies, D. W. (1979) Effect of dust on the heating of mars's surface and atmosphere, *J. Geophys. Res.*, **84**, 8289–8293.
Davies, D. W., C. B. Farmer, and D. D. LaPorte (1979) Behavior of volatile in Mars' polar areas : a model incorporating new experimental data., *J. Geophys. Res.*, **82**, 3815–3822.
Deirmidjian, D. (1964) Scattering and polarization properties of water clouds and hazes in the visible and infrared, *Appl. Opt.*, **3**, 187– 202,.
Ditteon, R., and H. H. Kieffer (1979) Optical properties of solid CO_2 : Application to Mars, *J. Geophys. Res.*, **84**, 8294–8300.
Dollfus, A. (1965) Etude de la plan`ete Mars de 1954 à 1958, *Ann. Astrophys*, **28**, 722–747.

Dozier, J. (1989a), Spectral signature of alpine snow cover from the Landsat Thematic Mapper, *Remote Sens. Envir.*, **28**, 9–22.
Dozier, J. (1989b), Remote sensing of snow in visible and near-infrared wavelengths, in *Theory and Applications of optical Remote Sensing*, G. Asrar, ed., Wiley, pp. 527–547.
Douté, S., B. Schmitt, Langevin, Y., Bibring, J-P., Altieri, F., Bellucci, G., Gondet, B. Poulet, F., and the MEX OMEGA Team (2007) South Pole of Mars: Nature and composition of the icy terrains from Mars Express OMEGA observations, *Planet. Space Sci.*, **55**, 113–133.
Eluszkiewicz, J. (1993) On the microphysical state of the Martian seasonal caps, *Icarus*, **103**, 43–48.
Eluszkiewicz, J., and T. N. Titus (2002) Application of a Sintering Model to the Analysis of TES Spectra of the Seasonal Caps, *Bull. American Astron. Soc.*, **34**, 866.
Fanale, F., Postawko, S., Pollack, J., Carr, M. and Pepin, R. (1992) Mars: Epochal climate change and volatile history, Chapter 32, in *Mars* (H. H. Kieffer et al., eds.), Univ. Arizona Press, Tucson, 1135–1179.
Feldman, W.C., Prettyman, T.H., Boynton, W.V., Murphy, J.R., Squyres, S., Karunatillake, S., Maurice, S., Tokar, R.L., McKinney, G.W., Hamara, D.K., Kelly, N., Kerry, K. (2003) CO2 frost cap thickness on Mars during northern winter and spring, *J. Geophys. Res.*, **108** (5103), 7.1–7.8.
Forget, F., J. B. Pollack, and G. B. Hansen (1995) Low brightness temperatures of Martian polar caps: CO_2 clouds or low spectral emissivity?, *J. Geophys. Res.*, **100**, 21119–21234.
Forget, F., and J. Pollack (1996) Thermal infrared observations of the condensing Martian polar caps: CO_2 ice temperatures and radiative budget., *J. Geophys. Res.*, **101**, 16865–16880.
Forget, F. (1998a) Mars CO_2 ice polar caps, *Review chapter from Solar System Ices*, 477–507.
Forget, F., F. Hourdin, O. Talagrand (1998b) CO_2 Snowfall on Mars: Simulation with a General Circulation Model, *Icarus*, **131**, 302–316.
Forget, F., E. Millour, S. Lebonnois, L. Montabone, K. Dassas S. R. Lewis, P. L. Read, M. Lopez-Valverde, F. Gon-zalez Galindo F. Montmessin, F. Lefevre M.C. Desjean and J. P. Huot (2006) The New Mars Climate Database, in 2nd workshop on Mars atmosphere modelling and observations abstract book, Granada, Spain.
Forman M.L., Steel W.H., Vanasse G.A. (1966) Correction of asymmetric interferograms obtained in Fourier spectroscopy; *J. of the Optical Soc. Of America.*, **56**, 59–63.
Formisano, V., et al. (1997) PFS: A Fourier Spectrometer for the Study of Martian atmosphere. *Adv. Space Res.*, **19**, 1277–1280.
Formisano, V., Fonti, S., Grassi, D., Orfei, R., Piccioni, G., Saggin, B., Hirsh, H., Orleanski, P., Rataj, M., Biondi, D., Mencarelli, E., Mattana, A., Nespoli, F., Malgoska, M., Patsaev, D., Moroz, V., Zasova, L., Ignatiev, N., Khatuntsev, I., Moshkin, B., Ekonomov, A., Maturilli, A., Giuranna, M., Rossi, M., Maggi, M., Di Lellis, A., Baldetti, P., Chionchio, G., Cerroni, P., Capaccioni, F., Gobbi, P., Capria, M.T., Angrilli, F., Bianchini, G., Colangeli, L., Palomba, E., Esposito, F., Orofino, V., Blanco, A., Cordini, A., Grigoriev, A., Nechaev, V., Kiselev, A., Nikolsky, Y., Gnedykh, V., Titov, D., Jurewicz, A., Blecka, M.I., Arnold, G., Lellouch, E., Marten, A., Encrenaz, T., Lopez, J., Moreno, S., Atreya, (2004) The Planetary Fourier Spectrometer (PFS) for Mars Express. In "*The Mars Express mission of ESA*". ESA SP.
Formisano, V.; Angrilli, F.; Arnold, G.; Atreya, S.; Bianchini, G.; Biondi, D.; Blanco, A.; Blecka, M. I.; Coradini, A.; Colangeli, L.; Ekonomov, A.; Esposito, F.; Fonti, S.; Giuranna, M.; Grassi, D.; Gnedykh, V.; Grigoriev, A.; Hansen, G.; Hirsh, H.; Khatuntsev, I.; Kiselev, A.; Ignatiev, N.; Jurewicz, A.; Lellouch, E.; Lopez Moreno, J.; Marten, A.; Mattana, A.; Maturilli, A.; Mencarelli, E.; Michalska, M.; Moroz, V.; Moshkin, B.; Nespoli, F.; Nikolsky, Y.; Orfei, R.; Orleanski, P.; Orofino, V.; Palomba, E.;

Patsaev, D.; Piccioni, G.; Rataj, M.; Rodrigo, R.; Rodriguez, J.; Rossi, M.; Saggin, B.; Titov, D.; Zasova, L. (2005) The Planetary Fourier Spectrometer (PFS) onboard the European Mars Express mission, *Planetary and Space Science*, **53**, issue 10, 963–974.

Formisano, V., Maturilli, A., Giuranna, M., D'Aversa, E., Lopez-Valverde, M. A. (2006) Observations of non-LTE emission at 4.5 microns with the planetary Fourier spectrometer abord the Mars Express mission, *Icarus*, **182**, 51–67.

French, R. G., P. J. Gierasch, B. D. Popp, and R. J. Yerdon (1981) Global patterns in cloud forms on Mars, *Icarus*, **45**, 468– 493.

Fung, A. K., Microwave Scattering and Emission Models and Their Applications, Artech House.

Gierasch, P. J., and R. M. Goody (1968) A study of the thermal and dynamical structure of the Martian lower atmosphere, *Planet. Space Sci.*, **16**, 615–646.

Giuranna, M., Formisano, V., Biondi, D., Ekonomov, A., Fonti, S., Grassi, D., Hirsch, H., Khatuntsev, I., Ignatiev, N., Michalska, M., Mattana, A., Maturilli, A., Moshkin, B. E., Mencarelli, E., Nespoli, F., Orfei, R., Orleanski, P., Piccioni, G., Rataj, M., Saggin, B., Zasova, L. (2005a) Calibration of the Planetary Fourier Spectrometer Short Wavelength Channel, *Planet. Space Sci*, **53**, issue 10, 975–991.

Giuranna, M., Formisano, V., Biondi, D., Ekonomov, A., Fonti, S., Grassi, D., Hirsch, H., Khatuntsev, I., Ignatiev, N., Malgoska, M., Mattana, A., Maturilli, A., Mencarelli, E., Nespoli, F., Orfei, R., Orleanski, P., Piccioni, G., Rataj, M., Saggin, B., Zasova L. (2005b) Calibration of the Planetary Fourier Spectrometer Long Wavelength Channel, *Planet. Space Sci.*, **53**, issue 10, 993–1007.

Giuranna, M., V. Formisano, D. Grassi and A. Maturilli (2007a) Tracking the edge of the south seasonal polar cap of Mars, *Planet. Space Sci.*, **55**, issue 10, 1319–1327.

Giuranna, M., Hansen, G., Maturilli, A., Zasova, L., Formisano, V., Grassi, D., Ignatiev, N. (2007b) Spatial variability, composition and thickness of the seasonal north polar cap of Mars in mid-spring, *Planet. Space Sci.*, **55**, issue 10, 1328–1345.

Glenar, D., R. E. Samuelson, J. C. Pearl, G. L. Bjoraker, and D. Blaney (2003) Spectral imaging of Martian water ice clouds and their diurnal behavior during the 1999 aphelion season (LS = 130°), *Icarus*, **161**, 297–318.

Gosse, S., Labrie, D., and Chylek, P. (1995) Refractive index of ice in the 1.4- to 7.8-μm spectral range, *Appl. Opt.*, **34**, 6582–6586.

Grassi, D., Ignatiev, N.I., Zasova, L.V., Maturilli, A., Formisano, V., Bianchini, G.A., Giuranna, M. (2005) Methods for the analysis of data from the Planetary Fourier Spectrometer on the Mars Express Mission, *Planet. Space Sci.*, **53** (10), 1017–1034.

Grundy, W. M., and B. Schmitt (1998) The temperature-dependent near-infrared absorption spectrum of hexagonal H_2O ice, *J. Geophys. Res.*, **103**, 25809–25822.

Haberle, R. M. (1995) Buried dry ice on mars, *Nature*, **374**, 595–596.

Hanel, R. A., Conrath, B., Hovis, W., Kunde, V., Lowman, P., Maguire, W., Pearl, J., Pirraglia, J., Prabhakara, C., Schlachman, B., Levin, G., Straat, P., Burke, T. (1972) Investigation of the Martian environment by infrared spectroscopy on Mariner 9, *Icarus*, **17**, 423–442.

Hanel, R. A., et al. (1992) Exploration of the Solar System by infrared remote sensing, Cambridge University Press.

Hansen, G. B. (1993) The spectral absorption of CO_2 ice in the thermal infrared, *Bull. Am. Astron. Soc.*, **25**, (3), 1034.

Hansen, G.B. (1997a) The infrared absorption spectrum of carbon dioxide ice from 1.8 to 333 μm, *J. Geophys. Res.*, **102**, 21569–21587.

Hansen, G.B. (1997b) Spectral absorption of solid CO_2 from the ultraviolet to the far-infrared, *Adv. In Sp. Res.*, **20**, issue 8, 1613–1616.

Hansen, G.B., McCord, T. B., and Galileo NIMS Team (1997c) Optical Properties of Water Ice Below 200 K, *28th Annual Lunar and Planetary Science Conference*, March 17-21, 1997, Houston, TX, p. 505.
Hansen, G.B. (1999) Control of the radiative properties of the Martian polar caps by surface CO_2 ice: Evidence from Mars Global Surveyor measurements. *J. Geophys. Res.,* **104**, 16471–16486.
Hansen, G. B. (2001) Eos Trans. AGU, 82, Fall Meet. Suppl., Abstract P12E-09.
Hansen, G. B. (2003a) Evolution of low-emissivity spots in the Martian winter polar caps: mobility of dust grains, *Third Mars Polar Science Conference*, October 13-17, Alberta, Canada.
Hansen, G. B. (2003b) Infrared Optical Constants of Martian Dust Derived from Martian Spectra, *Sixth International Conference on Mars*, July 20-25 2003, Pasadena, California, abstract no.3194.
Hansen, G.B. (2005) Ultraviolet to near-infrared absorption spectrum of carbon dioxide ice from 0.174 to 1.8 μm, *J. Geophys. Res.*, **110**, E11003.1–E11003.18.
Hansen, G. B., Giuranna, M., Formisano, V., Fonti, S., Grassi, D., Hirsh, H., Ignatiev, N., Maturilli, A., Orleanski, P., Piccioni, G., Rataj, M., Saggin, B., Zasova, L. (2005) PFS-MEX observation of ices in the residual south polar cap of Mars, *Planet. Space Sci.*, **53**, issue 10, 1089–1095.
Hansen, J. E., and L. D. Travis (1974) Light scattering in planetary atmospheres, *Space Sci. Rev.*, **16**, 527–610.
Hapke, B. W. (1993) Theory of Reflectance and Emittance Spectroscopy, *Cambridge University Press*, New York.
Hapke, B. W. (2002) Bidirectional reflectance spectroscopy. 5. Coherent backscatter opposition effect and anisotropic scattering, *Icarus*, **157**, 523–534.
Hart, H. M., and B. M. Jakosky (1986) Composition and stability of the condensate observed at the Viking lander 2 site on Mars, *Icarus*, **66**, 134–142.
Helfenstein, P., J. Veverka, and J. Hillier (1997) The lunar opposition effect: A test of alternative models, *Icarus*, **128**, 2–14.
Herr, K. C., and G. C. Pimentel (1969) Infrared absorptions near three microns recorded over the polar caps of Mars, *Science*, **166**, 496–499.
Herr, K. C., and G. C. Pimentel (1970) Evidence for solid carbon dioxide in the upper atmosphere of Mars, Science, 166, 496–499.
Herschel, W. (1784) On the remarkable appearance of the polar regions of the planet Mars, the inclination of its axis, the position of its poles, and its spheroidical figure; With a few hints relative to its diameter, *Philos. Trans.*, **24**, 233–273.
Hess, S. L. (1979) Static stability and thermal wind in an atmosphere of variable composition: Application to Mars, *J. Geophys. Res.*, **84**, 2969–2973.
Hess, S. L., Ryan, J. A., Tillman, J. E., Henry, R. M., Leovy, C. B. (1980) The annual cycle of pressure on Mars measured by Viking landers 1 and 2, *Geoph. Res. Lett.*, **7**, 197–200.
Hinson, D. P. and R.J. Wilson (2002) Transient waves in the southern hemisphere of Mars, *Geophys. Res. Lett.*, **29**(7), doi: 10.1029/2001GL014103.
Hinson, D. P., R. J. Wilson, M. D. Smith, and B. J. Conrath (2003) Stationary planetary waves in the atmosphere of Mars during southern winter, *J. Geophys. Res.*, **108**, E1, 5004.
Hollingsworth, J. L., and J. R. Barnes (1995) Forced Stationary Planetary Waves in Mars's Winter Atmosphere, *J. Atmos. Sci.*, **53**, 428–448.
Holton, J. R. (1979) An introduction to dynamic Meteorology, Academic, San Diego, Calif.
Hourdin, F., P. Le Van, F. Forget, and O. Talagrand (1993) Meteorological variability and the annual surface pressure cycle on Mars, *J. Atmos. Sci.*, **50**, 3625–3640.

Hourdin, F., F. Forget, and O. Talagrand (1995) The sensitivity of the Martian surface pressure to various parameters: a comparison between numerical simulations and Viking observations, *J. Geophys. Res.*, **100**, 5501–5523.
Hunt, G. E. (1980) On the infrared radiative properties of CO2 ice clouds: Applications to Mars., *Geophys. Res. Lett.*, **7**, 481–484.
Hu, Y. X., B. Wielicki, B. Lin, G. Gibson, S.C. Tsay, K. Stamnes, and T. Wong (2000) *δ*-fit: a fast and accurate treatment of particle scattering phase functions with weighted singular-value decomposition least-squares fitting, *J. Quant. Spectrosc. Radiat. Transfer*, **65**, 681–690.
Ignatiev, N.I., Grassi, D., Zasova, L.V. (2005) Planetary Fourier spectrometer data analysis: fast radiative transfer models, *Planet. Space Sci*, **53** (10), 1035–1042.
Iwisaki, K., Y. Saito, and T. Akabane (1982) Martian north polar cap: 1979-1980, *J. Geophys. Res.*, **87**, 10265–10269.
Jakosky, B. M. (1983) Comments on "Mars residual north polar cap : Earth-based spectroscopic confirmation of water ice as a major constituent and evidence for hydrated minerals" by R. N. Clark and T. B. McCord., *J. Geophys. Res.*, **88**, 4329–4330.
Jakosky, B. M., and E. S. Barker (1984) Comparison of ground-based and Viking Orbiter measurements of Martian water vapor: variability of the seasonal cycle., *Icarus*, **57**, 322–334.
Jakosky, B. M., and T. Z. Martin (1987) Mars: North-polar atmospheric warming during dust storms, *Icarus*, **72**, 528–534.
Jakosky, B. M., and R. M. Haberle (1990) Year-to-year instability of the Mars south polar cap., *J. Geophys. Res.*, **95**, 1359–1365.
Jakosky, B. M., B. G. Henderson, and M. T. Mellon (1993) The Mars water cycle at other epochs: recent history of the polar caps and layered terrain., *Icarus*, **102**, 286–297.
James, P. B., G. Briggs, J. Barnes, and A. Spruck (1979) Seasonal recession of Mars' south polar cap as seen by Viking, *J. Geophys. Res.*, **84**, (B6), 2889–2922.
James, P. B., and G. R. North (1982) The seasonal CO_2 cycle on Mars: An application of an energy balance climate model, *J. Geophys. Res.*, **87**, 10271–10283.
James, P. B. (1983) Condensation phase of the Martian south polar cap, *Bull. Am. Astron. Soc.*, **15**, 846–847.
James, P. B., M. Pierce, and L. J. Martin (1987) Martian north polar cap and circumpolar clouds: 1975-1980 Telescopic observation., *Icarus*, **71**, 306–312.
James, P. B., H. H. Kieffer, and D. A. Paige (1992) The seasonal cycle of carbon dioxide on Mars, in *Mars*, pp. 934–968, University of Arizona Press, Tucson.
James, P. B., R. T. Clancy, S. W. Lee, L. J. Martin, R. B. Singer, S. E., R. A. Kahn, and R. W. Zurek (1994) Monitoring Mars with the Hubble space telescope : 1990-1991 observations., *Icarus*, **109**, 79–101.
James, P. B., and Cantor, B.A. (2001) Martian north polar cap regression: 2000. Mars Orbiter Camera observations, *Icarus*, **154**, 131–144.
Jin, Z. and Simpson, J. (1999) Bidirectional anisotropic reflectance of snow and sea ice in AVHRR channel 1 and 2 spectral regions. Part I: Theoretical analysis, *IEEE Trans. Geosci. Remote Sens.*, **37**, 543–554.
Johnson, B. R., S. K. Atreya (1996) Feasibility of Determining the Composition of Planetary Ices by Far Infrared Observations: Application to Martian Cloud and Surface Ices, *Icarus*, **119**, 405–426.
Jones, K., R. E. Arvidson, E. A. Guiness, S. L. Braggs, S. D. Wall, C. E. Carlston, and D. G. Pidek (1979) One Mars year : Viking lander imaging observations, *Science*, **204**, 799–806.
Kaufman, Y. J., and Joseph, J. H. (1982) Determination of surface albedoes and aerosol extinction characteristics from satellite imagery, *J. Geophys. Res.*, **20**, 1287–1299.

Kerker, M. (1969) The scattering of light, New York: Academic Press.
Kieffer, H. H. (1970a), Interpretation of the Martian polar cap spectra, *J. Geophys. Res.*, **75**, 510–514.
Kieffer, H. H. (1970b), Spectral reflectance of CO_2-H_2O frosts, *J. Geophys. Res.*, **75**, 501–509.
Kieffer, H. H., S. C. Chase, E. D. Miner, F. D. Palluconi, G. M¨unch, G. Neugebauer, and T. Z. Martin (1976) Infrared thermal mapping of the martian surface and atmosphere: First results, *Science*, **193**, 780–786.
Kieffer, H.H., Chase Jr., S.C., Martin, T.Z., Miner, E.D., Palluconi, F.D. (1976b) Martian north pole summer temperatures: Dirty water ice, *Science*, **194**, 1341–1344.
Kieffer, H. H., T. Z. Martin, R. Peterfreund, B. M. Jakosky, E. D. Miner, and F. D. Palluconi (1977) Thermal and albedo mapping during the Viking primary mission, *J. Geophys. Res.*, **82**, 4249–4291.
Kieffer, HH (1979), Mars South Polar spring and summer temperatures: A residual Co_2 frost, *J.Geophys. Res.*, **84**, 8263–8288.
Kieffer, H. H. (1990) H_2O grain size and the amount of dust in Mars's residualnorth polar cap, *J. Geophys. Res.*, **95**, 1481–1493.
Kieffer, H. H., and A. P. Zent (1992) Quasi-periodic climate change on Mars, in *Mars*, edited by S. Kieffer, Jakosky and Matthews, pp. 1180–1218, University of Arizona Press, Tucson.
Kieffer, H. H., Titus, T. N., and Mullins, K.F. (2000) Mars south polar spring and summer behavior observed by TES: Seasonal cap evolution controlled by frost grain size, *J. Geophys. Res.*, **105**, 9653–9699.
Kieffer, H. H., and Titus, T. N. (2001) TES Mapping of Mars' North Seasonal Cap, *Icarus*, **154**, 162–180.
King, M. D., and Harshvardhan (1986) Comparative accuracy of selected multiple-scattering approximations, *J. Atmos. Sci.*, **43**, 784–801.
Kou, L., Labrie, D., and Chylek, P. (1993) Refractive indices of water and ice in the 0.65–2.5 μm spectral range, *Appl. Opt.*, **32**, 3531–3540.
Langevin, Y., Poulet, F., Bibring, J.-P., Schmitt, B., Douté , S., Gondet, B. (2005a) Summer evolution of the north polar cap of Mars as observed by OMEGA/Mars Express, *Science*, **307**, 1581–1584.
Langevin, Y., Douté , S., Vincendon, M., Poulet, F., Bibring, J-P., Gondet, B., Schmitt, B., Forget, F. (2006) No signature of clear CO_2 ice from the 'cryptic' regions in Mars' south seasonal polar cap, *Nature*, **442**, 790–792.
Larson, H. P., and U. Fink (1972) Identification of carbon dioxide frost on the Martian polar caps, *Astrophys. Jour.*, **171**, L91–L95.
Laskar, J., and P. Robutel (1993) The chaotic obliquity of the planets, *Nature*, **361**, 608–612.
Leighton, R. R., and B. C. Murray (1966) Behavior of carbon dioxide and other volatiles on Mars, *Science*, **153**, 136–144.
Lenoble, J. (1985) Radiative transfer in scattering and absorbing atmospheres: standard computational procedures, A. Deepak Publishing.
Leovy, C. (1969) Theoretical aspects of meteorology, *Appl. Opt.*, Vol. **8**, No. 7 , 1279–1286.
Leovy, C. (2001) Weather and climate on Mars, *Nature*, **412**, 245–249.
Liang, S., and Strahler, A. H. (1994a) Retrieval of surface BRDF from multiangle remotely sensed data, *Remote Sens. Envir.*, **50**, 18–30.
Liang, S., and Strahler, A. H. (1994b) A four-stream solution for atmospheric radiative transfer over a non-Lambertian surface, *Appl. Opt.*, **33**, 5745–5753.
Liang, S. and Townshend, J. R. G. (1996a), A parametric soil BRDF model: A four-stream approximation, *Int. J. Remote Sens.*, **17**, 1303–1315.

Liang, S. and Townshend, J. R. G. (1996b), A modified Hapke model for soil bidirectional reflectance, *Remote Sens. Envir.*, **55**, 1–10.
Lindner, B. L. (1990) The Martian polar cap : radiative effects of ozone, clouds and airborne dust, *J. Geophys. Res.*, **95**, 1367–1379.
Liou, K. N. (1974) Analytic two-stream and four stream solutions for radiative transfer, *J. Atmos. Sci.*, **31**, 1473–1475.
Liou, K. N. (1980) An introduction to atmospheric radiation, Academic Press.
Lumme, K. (1976) On the surface brightness and geometric albedo of some Martian areas., *Icarus*, **29**, 69.
Lumme, K., and P. B. James (1984) Some photometric properties of the Martian south polar cap region during the 1971 apparition, *Icarus*, **58**, 363–376.
Martin, T. Z., and H. H. Kieffer (1979) Thermal infrared properties of the Martian atmosphere, 2, the 15μm band measurements, *J. Geophys. Res.*, **84**, 2843–2852.
Martin, T. Z. (1981) Mean thermal and albedo behavior of the Mars surface and atmosphere over a Martian year, *Icarus*, **45**, 427–446.
Meador, W. E., and Weaver, W. R. (1980) Two-stream approximations to radiative transfer in planetary atmospheres: A unified description of existing methods and a new improvement, *J. Atmos. Sci.*, **37**, 630–643.
Mishchenko, M. I. (1991) Light scattering by randomly oriented axially symmetric particles, *J. Opt. Soc. Am.*, **A8**, 871–882.
Mishchenko, M.I. (1992) The angular width of the coherent backscatter opposition effect—an application to icy outer planet satellites, *Astrophys. Space Sci*, **194**, 327–333.
Mishchenko, M. I. (1993) Light scattering by size-shape distributions of randomly oriented axially symmetric particles of a size comparable to a wavelength, *Appl. Opt.*, **32**, 4652–4666.
Mishchenko, M. I. (1994) Asymmetry parameters of the phase function for densely packed scattering grains, *J. Quant. Spectrosc.* Radiat. Trans., **52**, 95–110.
Mishchenko, M.I. (1996) Diffuse and coherent backscattering by discrete random media. 1. Radar reflectivity, polarization ratios, and enhancement factors for a half-space of polydisperse nonabsorbing, and absorbing spherical particles, *J. Quant. Spectrosc. Radiat. Transfer*, **56**, 673–702.
Mishchenko, M. I. and Macke, A. (1997) Asymmetry parameters of the phase function for isolated and densely packed spherical particles with multiple internal inclusions in the geometric optics limit, *J. Quant. Spectrosc. Radiat. Trans.*, **57**, 767–794.
Mishchenko, M. I., Dlugach, J. M., Yanovitskijb, E. G., and Zakharovac, N. T. (1999) Bidirectional reflectance of flat, optically thick particulate layers: An efficient radiative transfer solution and applications to snow and soil surfaces, *J. Quant. Spectrosc. Radiat. Trans.*, **63**, 409–432.
Montmessin, F., P. Rannou, and M. Cabane (2002) New insights into Martian dust distribution and water-ice cloud microphysics, *J. Geophys. Res.*, **107**(E6), 5037.
Montmessin, F., Bertaux, J. L., Quemerais, E., Korablev, O., Rannou, P. , Forget, F., Perrier, S., Fussen, D. , Lebonnois, S, Reberac, A., Dimarellis, E. (2006) Subvisible CO_2 ice clouds detected in the mesosphere of Mars, *Icarus*, **183**, 403.
Montmessin, F., B. Gondet , J.P. Bibring, T. Fouchet, F. Forget, P. Drossart, Y. Langevin, T. Encrenaz (2007) Hyperspectral imaging of CO_2 ice clouds on Mars, *EGU General assembly 2007*, Vienna, Austria, 15 – 20 April.
Murphy, J. R., R. M. Haberle, O. B. Toon, and J. B. Pollack (1993) Martian global dust storms: Zonally symmetric numerical simulations including size-dependent particle transport, *J. Geophys. Res.*, **98**, 3197–3220.
Nakajima, T., and M. Tanaka (1988) Algorithms for radiative intensity calculations in moderately thick atmospheres using a truncation approximation, *J. Quant. Spectrosc. Radiat. Transfer*, **40**, 51–69.

Neugebauer, G., G. Münch, H. Kieffer, S.C. Chase Jr. and E. Miner (1971) Mariner 1969 infrared radiometer results: Temperatures and thermal properties of the martian surface, *Astron. J.*, **76**, 719–728.
Nussenzveig, H. M., and W. J. Wiscombe (1980) Efficiency factors in Mie scattering, *Phys. Rev. Lett.*, **45**, 1490–1494.
Ockert-Bell, M. E., J. F. Bell III, J. B. Pollack, C. P. McKay, and F. Forget (1997) Absorption and scattering properties of the Martian dust in the solar wavelengths, *J. Geophys. Res.*, **102**, 9039–9050.
Ockman, N. (1958) The infrared spectra and raman-spectra of ice, *Phil. Mag. Suppl.*, **7**, 199–220.
Ono, A., and D. A. Paige (1995) Martian polar frosts, Abstract for the "Solar System Ice" international symposium, Toulouse, France.
Paige, D. A. (1985) The annual heat balance of the Martian polar caps from Viking observations, Ph.D. thesis, Calif. Inst. of Technol., Pasadena
Paige, D. A., and A. P. Ingersoll (1985) Annual heat balance of Martian polar caps: Viking observations, *Science*, **228**, 1160–1168.
Paige, D. A., D. Crisp, and M. L. Santee (1990a), It snows on mars, *Bull. Am. Astron. Soc.*, **22**, 1075.
Paige, D. A., K. E. Herkenhoff, and B. C. Murray (1990b), Mariner 9 observations of the south polar cap of Mars : evidence for residual CO2 frost, *J. Geophys. Res.*, **95**, 1319–1335.
Paige, D. A., and S. E. Wood (1992) Modeling the Martian seasonal CO2 cycle: 2. interannual variability, *Icarus*, **99**, 15–27.
Parker, D. C., C. F. Capen, and J. D. Beish (1983) Exploring the martian artic., *Sky & Telescope*, **65**, 218–220.
Pearl, J. C., M. D. Smith, B. J. Conrath, J. L. Bandfield, and P. R. Christensen (2001) Observations of Martian ice clouds by the Mars Global Surveyor Thermal Emission Spectrometer: The first year, J. *Geophys. Res.*, **106**, 12,325– 12,338.
Petrova, E. H., U. Keller, W. J. Markiewicz, N. Thomas, and M. W. Wuttke (1996) Ice hazes and clouds in the Martian atmosphere as derived from the Phobos/KRFME data, *Planet. Space Sci.*, **44**, 1163–1176.
Pettengill, G. H. and Ford, P. G. (2000) Winter Clouds over the North martian Polar Cap. *Geoph. Res. Lett.*, **27**, 609–612.
Pimentel, G., P. Forney, and K. Herr (1974) Evidence about hydrate and solid water in the Martian surface from the 1969 Mariner infrared spectrometer, *J. Geophys. Res.*, **79**, 1623–1634.
Pollack, J. B., R. M. Haberle, J. Schaeffer, and H. Lee (1990) Simulations of the general circulation of the Martian atmosphere, I, Polar processes, *J. Geophys. Res.*, **95**, 1447–1473.
Pollack, J. B., R. M. Haberle, J. R. Murphy, J. Shaeffer, and H. Lee (1993) Simulation of the general circulation of the Martian atmosphere II: seasonnal pressure variations, *J. Geophys. Res.*, **98**, (E2), 3149–3181.
Pollack, J. B., M. E. Ockert-Bell, and M. K. Sheppard (1995) Viking lander analysis of Martian atmospheric dust, *J. Geophys. Res.*, **100**, 5235–5250.
Potter, J. F. (1970), The Delta Function Approximation in Radiative Transfer Theory, *J. Atmos. Sci.* **27**, 943–949.
Press, W. H., Flannery, B. P., Teukolsky, S. A., and Vetterling, W. T. (1989) Numerical Recipes. The art of scientific computing (Fortran Version), Cambridge Univ. Press.
Prettyman, T. H., Feldman, W. C., Murphy, J. R., Funsten, H. O., Lawrence, D. J., Linn, R. R., Maurice, S., Tokar, R. L. (2003) Seasonal Advance and Retreat of Mars' South Polar Cap as Measured by the Mars Odyssey Neutron Spectrometer, *Third International*

Conference on Mars Polar Science and Exploration, October 13 – 17, Alberta, Canada, abstract no.**8099**.
Rajaram, B., Glandorf, D. L., Curtis, D. B., Tolbert, M. A., Toon, O. B., and Ockman, N. (2001) Temperature-dependent optical constants of water ice in the near infrared: new results and critical review of the available measurements, *Appl. Opt.*, **40**, Issue 25, 4449–4462
Rizk, B., R. M. Haberle, D. Hunten, and J. B. Pollack (1995) Meridional transport and water reservoir in southern Mars during 1988-1989, *Icarus*, **118**, 39–50.
Rodin, A. V., O. I. Korablev, and V. I. Moroz (1997) Vertical distribution of water in the near-equatorial troposphere of Mars: Water vapor and clouds, *Icarus*, **125**, 212–229.
Roush, T., J. Pollack, and J. Orenberg (1991) Derivation of midinfrared (5–25 microns) optical constants of some silicates and palagonite, *Icarus*, **94**, 191–208.
Sadourny, R. and K. Laval (1984) January and July performance of the LMD general circulation model, in "New Perspectives in Climate Modeling", A.L. Berger and C. Nicolis (Eds.), Elsevier Press, Amsterdam, 173–197.
Saggin, B., Comolli, L., Formisano, V. (2007) Mechanical disturbances in Fourier spectrometers, *Appl. Opt.*, **46**, Issue 22, 5248–5256.
Singer, R.B. (1980) The dark materials on Mars, II. New mineralogic interpretations from reflectance spectroscopy and petrologic implications (abstract), in *Lunar and planetary science XI*, Lunar and Planetary Institute, 1048–1050.
Smith, S. A., and B. A. Smith (1972) Diurnal and seasonal behavior of discrete white clouds on Mars, *Icarus*, **16**, 509–521.
Smith, David E., Maria T. Zuber, Sean C. Solomon, Roger J. Phillips, James W. Head, James B. Garvin, W. Bruce Banerdt, Duane O. Muhleman, Gordon H. Pettengill, Gregory A. Neumann, Frank G. Lemoine, James B. Abshire, Oded Aharonson, C. David, Brown, Steven A. Hauck, Anton B. Ivanov, Patrick J. McGovern, H. Jay Zwally, and Thomas C. Duxbury (1999) The Global Topography of Mars and Implications for Surface Evolution, *Science*, **284**, 1495–1503.
Smith, D. E., Neumann, G., Arvidson, R.E., Guinness, E.A., Slavney, S. (2003) Mars global surveyor laser altimeter mission experiment gridded data record, NASA Planetary Data System, MGS-M-MOLA-5-MEGDR-L3-V1.0.
Snook, K. J. (1999) Optical properties and radiative heating effects of dust suspended in the Mars atmosphere, Ph.D thesis, Stanford Univ., Stanford, Calif..
Snook, K. J., J. L. Bandfield, F. Forget, and C. P. McKay (2000) Derivation of Infrared Optical Properties of Dust Suspended in the Martian Atmosphere from MGS-TES Data., *Bull. Am. Astron. Soc.*, **32**, 1094.
Soderblom, L.A., Wenner, D.B. (1978) Possible fossil water liquid-ice interfaces in the Martian crust, *Icarus*, **34**, 622–637.
Stamnes, K., Tsay, S. C., Wiscombe, W., and Jataweera, K. (1988) Numerically stable algorithm for discrete-ordinate-method radiative transfer in multiple scattering and emitting layered media, *Appl. Opt.*, **27**, 2502–2509.
Stratton, J. (1941) Electromagnetic Theory, New York: McGraw-Hill
Svitek, T., and B. Murray (1990) Winter frost at Viking Lander 2 site, *J. Geophys. Res.*, **95**, 1495–1510.
Takano, Y. and Liou, K. N. (1989a) Solar radiative transfer in cirrus clouds. Part I: Single-scattering and optical properties of hexagonal ice crystals, *J. Atmos. Sci.*, **46**, 3–19.
Takano, Y. and Liou, K. N. (1989b), Solar radiative transfer in cirrus clouds. Part II: Theory and computation of multiple scattering in an anisotropic medium, *J. Atmos. Sci.*, **46**, 20–36.
Takano, Y., K. N. Liou, and P. Minnis (1992) The effects of small ice crystals on cirrus infrared radiative properties. *J. Atmos. Sci.*, **49**, 1487–1493.

Takano, Y. and Liou, K. N. (1995), Solar radiative transfer in cirrus clouds. Part III: Light scattering by irregular ice crystals, *J. Atmos. Sci.*, **52**, 818–837.
Talagrand, O., F. Hourdin, and F. Forget (1991) The LMD Martian general circulation model: Results about the annual pressure cycle, *Bull. Am. Astron. Soc.*, **23**, 1217 (oral presentation at the 23rd annual DPS meeting (Palo Alto, California).
Tamppari, L. K., R. W. Zurek, and D. A. Paige (2000) Viking era water ice clouds, *J. Geophys. Res.*, **105**, 4087– 4107.
Thomas, G. E., and Stamnes, K. (1999) Radiative Transfer in the Atmosphere and ocean, Cambridge Atmospheric and Space Sciences Series, Cambridge Univ. Press.
Thomas, P., Veverka, J., Campos-Marquetti, R. (1979) Frost Streaks in the South Polar Cap of Mars, *J. Geophys. Res.*, **84**, 4621–4633.
Tillman, J. E. (1988) Mars global atmospheric oscillations: Annually synchronized transient normal-mode oscillations and the triggering of global dust storms, *J. Geophys. Res.*, **93**, 9433–9451.
Titov, D. V., V. I. Moroz, and Y. M. Getkin (1997) Aerosol component of the Martian atmosphere and its variability from the results of infrared radiometry in the Termoscan/Phobos-2 Experiment, *Planet. Space Sci.*, **45**, 637– 651.
Titus, T.N. and Kieffer, H. (2001) Slab ice and snow flurries in the Martian polar night, *J. Geophys. Res.*, **106** (23), 181.
Titus, T. N., H. H. Kieffer, K. F. Mullins, and P. R. Christensen (2001) TES premapping data: Slab ice and snow flurries in the martian north polar night, *J. Geophys. Res.*, **106**, 23,181–23,196.
Titus, T.N. (2005) Mars polar cap edges tracked over 3 full mars years, *36th Annual Lunar and Planetary Science Conference*, League City, Texas, abstract no.1993, March 14–18.
Tomasko, M. G., L. R. Doose, M. Lemmon, E. Wegryn, and P. H. Smith (1999) Properties of dust in the Martian atmosphere from the imager on Mars Pathfinder, *J. Geophys. Res.*, **104**, 8987– 9008.
Toon, O. B., J. B. Pollack, and C. Sagan (1977) Physical properties of the particles composing the Martian dust storm of 1971, *Icarus*, **30**, 663– 696.
Toon, O. B., Tolbert, M. A., Koehler, B. G., Middlebrook, A. M., and Jordan, J. , (1994) Infrared optical constants of water ice, amorphous nitric acid solutions, and nitric acid hydrates, *J. Geophys. Res.*, **99**, 25631–25654.
Van de Hulst, H. (1957) Light scattering by small particles, New York: Wiley.
Van de Hulst, H. (1980) Multiple Light Scattering, Tables, Formulas and Applications, Vols. 1, 2, Academic Pres..
Van de Hulst, H. (1981) Light scattering by small particles, New York: Dover Publications (unabridged and corrected republication of the work originally published in 1957 by J. Wiley and Sons, Inc.).
Wall, S. D. (1981) Analysis of condensates formed at the Viking 2 lander site : the first winter, *Icarus*, **47**, 173–183.
Ward, W. R., B. C. Murray, and M. C. Malin (1974) Climatic variations on Mars. 2. Evolution of carbon dioxide atmosphere and polar caps, *J. Geophys. Res.*, **79**, 3387–3395.
Warren, S. G. (1984) Optical constants of ice from the ultraviolet to the microwave, *Appl. Opt.*, **23**, 1206–1225.
Warren, S. G. (1986) Optical constants of carbon dioxide ice, *Appl. Opt.*, **25**, 2650–2674.
Warren, S. G. and Wiscombe, W. J. (1980) A model for the spextral albedo of snow. II. Snow containing atmospheric aerosols, *J. Atmos. Sci.* **37**, 2734–2745.
Warren, S. G., W. J. Wiscombe, and J. F. Firestone (1990) Spectral albedo and emissivity of CO_2 in Martian polar caps: model results, *J. Geophys. Res.*, **95**, 717–741.
Wiscombe, W. J. (1977) The delta-M method: rapid yet accurate radiative flux calculations for strongly asymmetric phase functions, *J. Atmos. Sci.*, **34**, 1408–1422.

Wiscombe, W. J. (1980) Improved Mie scattering algorithms, *Appl. Opt.*, **19**(9), 1505–1509.
Wiscombe, W. J. and Warren, S. G. (1980) A model for the spextral albedo of snow. I. pure snow, *J. Atmos. Sci.* **37**, 2712–2733.
Wiscombe, W. J. (1996) Mie Scattering Calculations: Advances in Technique and Fast, Vector-Speed Computer Codes." *NCAR Technical Note*, June 1979 (edited/revised August 1996).
Wolff, M. J., and R. T. Clancy (2003) Constraints on the size of Martian aerosols from Thermal Emission Spectrometer observations, *J. Geophys. Res.*, **108**(E9), 5097–5120.
Wood, S. E., and D. A. Paige (1992) Modeling the martian seasonal CO_2 cycle: fitting the Viking lander pressure curves, *Icarus*, **99**, 1–14.
Zurek, R., et al., Dynamics of the atmosphere of Mars (1992) In "*Mars*", eds Kieffer et al., 853–933.
Zurek, R. W., and L. J. Martin (1993) Interannual variability of planet-encircling dust storms on Mars, *J. Geophys. Res.*, **98**, 3247–3259.
Zuber, M. T., and Smith, D. E. (2003) Observations of the seasonal polar icecaps of Mars at 1064 nm, *Third Mars Polar Science Conference*, abstract no.**8032**.